

Evolution of the Sefidrud Delta (South West Caspian Sea) during the last millennium

A thesis submitted for the degree of Doctor of Philosophy

By

Safiyeh Haghani

Environmental Science

Brunel University London

July 2015

Declaration

This thesis is the result of the author's own work. Data or information from other authors contained herein, are acknowledge at the appropriate point in the text.

Abstract

The Sefidrud has developed a large delta in the south west of the Caspian Sea. Its delta is characterized by rapid sedimentation rate (20 mm/yr) in the delta plain and low sedimentation rate (1.67 mm/yr) in a very steep delta front. Sefidrud Delta evolution depends upon sediment supply by river and longshore current under rapid Caspian Sea Level (CSL) fluctuation and tectonic setting at the point of entry to the basin. The tectonic setting caused a very steep slope in the delta front. Sediment supply is variable and affected by river avulsion and dam construction. The CSL has undergone significant changes during the last millennium. Therefore, the Sefidrud Delta evolution during the last millennium is explained based on CSL fluctuations. This fluctuation has major impacts not only on coastal lagoons, but also more inland in wetlands when the CSL rose up to at least -21.44 m (i.e. >6 m above the present water level) during the early Little Ice Age. Although previous studies in the southern coast of the Caspian Sea have detected a high-stand during the Little Ice Age period, this study presents the first evidence that this high-stand reached so far inland and at such a high altitude. This study also examines the interdependence of different factors in the evolution of coastal lagoons as a part of delta evolution. Dam flushing operations and rapid sea-level rise (~3 m between 1977 and 1995) have accelerated the infilling of the coastal lagoon system. This rapid infilling (31 mm/yr) makes the whole system more prone to sediment encroachment in the short term. Because the lagoons are short-lived and have dynamic evolution, the impact of the Anthropocene is also visible in the delta evolution.

Contents

1	Introduction	1
1.1	Background.....	1
1.2	Aim and objectives of the research.....	3
1.2.1	Aim of the research	3
1.2.2	Objective of the research.....	3
1.3	Thesis structure	3
2	Literature review	5
2.1	The Caspian Sea basin	5
2.1.1	Caspian catchment area and river system	5
2.1.2	Caspian Sea Level (CSL) fluctuation.....	7
2.1.3	Deltas around the CS	9
2.1.4	Economic significance of deltaic deposits	11
2.2	Sefidrud Delta	13
2.2.1	Source of the sediments	14
2.2.2	Geology of the region	15
2.2.3	Coastal lagoons and wetlands	18
2.2.4	Climate and vegetation of the region	19
2.3	In conclusion for chapter two	19
3	Materials and methods.....	21
3.1	Remote sensing.....	21
3.2	GPR profiling	21
3.3	Coring	23
3.3.1	Gravity corer	25
3.3.2	Percussion corer	25
3.3.3	Livingstone corer	26
3.4	Sedimentology	27
3.4.1	Magnetic susceptibility	28
3.4.2	Core photography.....	29
3.4.3	Visual description	30
3.4.4	Loss on ignition (LOI)	30
3.4.5	Grain size analysis	31
3.5	Chronology	33
3.5.1	Radiocarbon dating	34
3.5.2	Radionuclide dating	35

3.5.3	Spheroidal carbonaceous fly–ash particles (SCPs)	36
3.6	Macro-remains analysis	36
3.7	Palynology	37
4	Results	39
4.1	Remotely sensed data	39
4.2	GPR profiles and sedimentary facies	40
4.2.1	Location A	41
4.2.2	Location B	43
4.2.3	Location C	45
4.2.4	Location D	49
4.3	Inland water bodies	52
4.3.1	Langarud	52
4.3.2	Astaneh (AAL13V)	61
4.4	Coastal lagoons	70
4.4.1	Zibakenar Lagoon	70
4.4.2	Kiashahr Lagoon	83
4.4.3	Amirkola Lagoon	87
4.4.4	AL11V3 sequence	95
4.5	Marine deposits	104
4.5.1	Sedimentology	106
4.5.2	Macro-remains	109
4.5.3	Chronology	112
5	Interpretation and Discussion	114
5.1	The development of the coastal lagoons using remotely sensed data	114
5.2	Radar profiles and sedimentary facies	116
5.3	Inland water bodies	116
5.3.1	Langarud	116
5.3.2	Astaneh (AAL13V)	122
5.4	Coastal lagoons	125
5.4.1	Zibakenar Lagoon	125
5.4.2	Amirkola Lagoon	131
5.4.3	AL11V3 sequence	132
5.5	Marine deposits	136
5.5.1	Steep slope setting	137
5.5.2	Sedimentation rate and sediment delivery to the basin	139
5.6	Evolution of Sefidrud delta during the last millennium	141
5.7	Contribution to CSL curve construction	144
5.8	Sediment accumulations within the Sefidrud Delta	144
6	Conclusions	146
6.1	Synopsis of key findings	146
6.2	Potential areas for further study	147

References.....	149
APPENDIX A (Length and location of the cores)	160
APPENDIX B (Publications).....	165
APPENDIX C (Paper accepted).....	166
APPENDIX D (Manuscript submitted).....	167

List of Abbreviations

<i>asl</i>	<i>above sea level</i>
<i>bsl</i>	<i>below sea level</i>
<i>CS</i>	<i>Caspian Sea</i>
<i>CSL</i>	<i>Caspian Sea Level</i>
<i>GIS</i>	<i>Geographical Information System</i>
<i>GPR</i>	<i>Ground Penetrating Radar</i>
<i>GSI</i>	<i>Geological Survey of Iran</i>
<i>INIOAS</i>	<i>Iranian National Institute for Oceanography and Atmospheric Science</i>
<i>LIA</i>	<i>Little Ice Age</i>
<i>MCA</i>	<i>Medieval Climate Anomaly</i>
<i>MCB</i>	<i>Middle Caspian Basin</i>
<i>MS</i>	<i>Magnetic Susceptibility</i>
<i>Mz</i>	<i>Macro-remain zone</i>
<i>NCB</i>	<i>North Caspian Basin</i>
<i>OM</i>	<i>Organic Matter</i>
<i>psu</i>	<i>practical salinity unit</i>
<i>Pz</i>	<i>Palynological zone</i>
<i>SCB</i>	<i>South Caspian Basin</i>
<i>Sz</i>	<i>Sedimentological zone</i>

Acknowledgements

Special acknowledgement is made to my first supervisor, Professor Suzanne Leroy, for her efforts to guide me towards achieving the aim of this research and also for performing palynology analyses on samples and writing the text for section of palynology. I acknowledge Mr David Finlayson, my second supervisor, for great assistance toward the process of this research work.

I would like to thank my sponsor, BP, especially Dr Greg Riley, for giving me this great opportunity to do my PhD research study and special thanks to Dr Simon Grant my BP supervisor for his guidance of support during the course of the project.

I am grateful to the Iranian National Institute for the Oceanography and Atmospheric Science (INIOAS) and Geological Survey of Iran (GSI) for providing technical facilities during several periods of field work. Professor Klaus Arpe is especially thanked for his support during the field campaign and especial thanks to Mr Vali Jahani (Gilan province Cultural Heritage and Tourism Organisation) and Dr Alireza Naqinezhad (University of Mazandaran) for the information on Langarud history.

I would like to acknowledge Professor Charlie Bristow (University College of London) for his guidance for interpretation of Ground Penetrating Radar profiles and Dr Frank Wesselingh for distinguishing species of bivalve and gastropod shells. I am grateful to Professor Neil Rose (University College of London) for analysing samples for Spheroidal carbonaceous fly-ash particles (SCPs) and Mr Jean-louis Reyss for radionuclide dating on offshore core.

I am very thankful to Dr Edwin Routledge, Deputy Head of Research, for his support during my research. I am also thankful to all the staff of Environmental Science Department: their logistical assistance is greatly appreciated.

Finally, a huge thank to my Mum, Dad and my husband Yashar for always being there for me.

1 Introduction

1.1 Background

The Caspian Sea (CS) with a surface area of 378,000 km², comparable in size with the British Isles, is the largest closed water body in the world. Although the CS is technically a lake, its 'sea-like' size and nature is reflected in the terminology (Caspian Sea). The Sefidrud located in the south west of the CS is one of the main sediment sources for the CS (Fig. 1.1 A). The Sefidrud means the White River; and white has a metaphorical meaning of life-giving in Persian. Therefore, the word Sefidrud is used instead of Sefidrud River to prevent repetition of the word river. The Sefidrud with its significant contribution in sediment supply for the CS has developed a large delta in its south coast (Fig. 1.1 A, B and C). Deltaic deposits, in general, are known as important sources of oil and gas and major hydrocarbon provinces are often formed in deltaic environment (Selley, 1996). According to the US Energy Information Administration, the CS region is one of the oldest oil-producing areas in the world (Eia report, 2013). Hydrocarbon reservoirs in the CS are fluvial-deltaic deposits (Kroonenberg et al., 2004). The U.S. Geological Survey (USGS) using published geologic information estimates a considerable amount of undiscovered oil and natural gas to be in the south of the CS basin (Eia report, 2013), which are deposited in a fluvio-deltaic system. Therefore, a fair understanding of present-day Sefidrud Delta characteristics is a key success factor in forecasting the location of oil bearing sediment. Currently, no significant Iranian production takes place in the CS; however, oil reserves, named Sardar Jangal (100 million bbl of oil), were discovered in 2011 in the South Western of the CS (Eia report, 2013, Fig. 1.1 A). Delta characteristics including gradient, palaeogeography setting and subsidence rate, fluvial and marine processes and sea level fluctuation are completely unique for each delta (Kroonenberg et al., 2005). Therefore, a detailed study of any delta that can be responsible for deposition of hydrocarbon reservoir is critically important.

In term of sea level fluctuation, the CS experienced dramatic fluctuations during the past. Therefore, the evolution of the Sefidrud Delta is best explained based in terms of CSL fluctuations. Since instrumental record hardly provides information for periods older than two centuries, a palaeo-environmental approach is required for reconstruction of the past CSL curve. Reconstruction of the CSL curve is essential to compile useful data for prediction of future CSL changes which has direct impact on populations and on onshore

and offshore hydrocarbon exploitation. However, the reconstructed curves are discontinuous and compilations show that they are often contradictory even for the last millennium (Naderi Beni et al., 2013a).

In this study, inland wetlands, coastal lagoons and offshore deposits are subjected to study using multi-proxy analyses of cores, and surface samples, seismic profiles and Ground Penetrating Radar (GPR) profiles to explain the evolution of the Sefidrud Delta (Fig. 1.1 C and Fig. 1.2). The present study focuses on evolution of inland wetlands (Langarud and Astaneh wetlands) and also coastal lagoons (Amirkola, Kiashahr, and Zibakenar lagoons) as a part of delta evolution and to contribute in reconstruction of CSL curve (Fig. 1.1 C). Despite the importance of offshore sediment in reconstructing of periods of sea level fall, the offshore sediments of the South Caspian Basin (SCB) are little studied (Fig. 1.1 B). Therefore, in this dissertation the offshore sediments are subjected to investigation using cores, surface samples and seismic profiles (Fig. 1.1 C).



Fig. 1.1. A: Location map of the Caspian Sea (white lines represent international boundaries.) and major rivers flowing to the Caspian Sea. Mt.: Mountains, red dots: location of lagoons and black dot location of Abeskun Town, Black line: the location of Manjil Dam B: Location of South Caspian Basin (Google Earth), red line: location of main faults in the study area, Green squares: location of the cores taken from SCB in other studies, yellow dots: location of offshore core in this study. C: The location of coastal lagoons: Zibakenar, Ushmak, Kiashahr and Amirkola (light blue bodies) and inland water bodies: Langarud and Astaneh (dark blue dots), yellow dots: location of offshore cores, purple dots: location of surface samples,

light blue dot: location of AL11V3 sequence, red lines location of seismic profiles, green boxes: location of GPR profiles, red dashed line represents submarine delta limit from Kazancı and Gulbabazadeh (2013) and purple line: Boujagh National Park (BNP) boundary from Naqinezhad (2012), red dots: the location of main towns.

1.2 Aim and objectives of the research

1.2.1 Aim of the research

The overall aim of this project is to study the evolution of the Sefidrud Delta during the last millennium, which includes important events such as river avulsion and lagoon formation under rapid CSL fluctuation. The goal of this research is to understand where sediment accumulation and erosion happen in the Sefidrud, the mechanism behind this and how fast the delta progrades into the sea and the sedimentation rates. The focus is on the main areas of deposition, inland wetland, the coastal lagoons, the offshore area, and along distributaries.

1.2.2 Objective of the research

The main objectives in this research are:

- I. Identifying the palaeo *coastlines* using published literature and dating the palaeo-beach and using GPR profiling to identify the mechanism of delta building.
- II. Using published literature to find the best locations for retrieving sediment cores from the *emerged delta* (e.g. coastal lagoons and inland wetlands). This will allow to delimit different sedimentary facies within the Sefidrud Delta and to understand the mechanism behind formation and erosion.
- III. Discovering new *coastal lagoons* deposits in the study area during the field work to study their evolution and examine effect of rapid CSL fluctuation on their formation.
- IV. Using seismic profiles to make a 3D morphology of *offshore* Sefidrud Delta and especially characterise its steep nature.
- V. Combining multiple dating approaches including radionuclide dating, radiocarbon dating, indirect biotic dating and evidence from spheroidal carbonaceous fly-ash deposits with remotely sensed data to understand the *deposition and erosion rates*, eg in coastal lagoons.

By reaching the previous objectives, it may become possible to contribute some new points in the CSL curve.

1.3 Thesis structure

This study describes the evolution of Sefidrud Delta based on geophysical data (seismic profiles and GPR profiles) and sediment cores within three sections including inland wetlands, coastal lagoons and marine deposits. The dissertation is divided into six chapters.

The background of study area and aims and objectives of the research are described in this chapter (chapter one: introduction). Chapter two (literature review) provides a general background about the CS and CSL changes followed by characteristics of the main deltas around the CS and their response to water level fluctuations. Also, Sefidrud Delta, its geology and possible sources of sediments have been discussed in this chapter. Chapter three describes materials and methods used for this research. Each method is presented individually and the aim of using each method is justified in chapter three. Chapter four (results) provides the results of material and methods used in this study (seismic profiles and remotely sensed data), followed by results of sedimentology (including visual description, magnetic susceptibility, grain size analyses, and loss on ignition), chronology, macro-remains analyses and palynological analyses for each section following concept of the three introduced sections: inland wetlands, coastal lagoons, and marine (offshore) deposits (Fig. 1.2). Chapter five (interpretations and discussions) presents the discussion of the main results for three introduced sections site by site, following the evolution of the delta, contribution of this study to CSL curve, and sediment accumulation within the delta. Finally, chapter six (conclusions) summarises the main findings of this research. Potential areas for further study are also proposed in this chapter.



Fig. 1.2. Schematic figure of different environments studied in this project.

2 Literature review

2.1 The Caspian Sea basin

The enclosed Caspian Sea (CS) is known as the largest brackish water body in the entire world, comprising ~40% of the earth's continental surface water (Dumont, 1998). Its surface area is 378,000 km² with a water volume of 78,000 km³, and its catchment area, 3.5 million km², is large especially in the north (UNEP, 2006).

The CS according to its morphology is divided into three distinct physical regions includes the northern, middle and southern basins (Fig. 2.1). The northern basin (known as North Caspian Basin: NCB) includes the Caspian shelf with an average depth of about 5 m and a maximum depth of 20 m. The northern basin occupies 27% of CS surface area and only 0.6% of the total volume due to its shallow origin. The CS noticeably drops off toward the middle basin, where the average depth of 190 m and a maximum depth of 790 m. The middle basin (Middle Caspian Basin: MCB) is separated by the Mangyshlak shelf from the NCB and occupies 39% of surface area and 36% of the total volume. The southern basin is the deepest region, with the average depth of 330 m and a maximum depth of 1025 m. The middle and southern basin (South Caspian Basin: SCB) are separated by Apsheron shelf which is continuation of Caucasus Mountains (UNEP, 2006). CS salinity in the MCB and SCB is brackish, around 10 and 13 psu, respectively; while it is nearly fresh in the northern basin (0.1 psu), especially near to Volga River (Kroonenberg et al., 1997; UNEP, 2006).

2.1.1 Caspian catchment area and river system

The CS with 3.5 million km² catchments area (~10 times larger than its surface area) is mainly located in littoral states of Iran, Turkmenistan, Kazakhstan, Russia and Azerbaijan, and small parts in Turkey, Armenia and Georgia (UNEP, 2006) (Fig. 2.1). The northern part of the basin is located in high latitude forests, middle Volga steppe and Pre-Caspian deserts. The western and southern parts of the basin are situated in high mountains of Caucasus and Elburz, respectively. The Kopet-Daq Mountains cover the south eastern part and the eastern part is dominated by wide area of deserts (Lahijani et al., 2008).

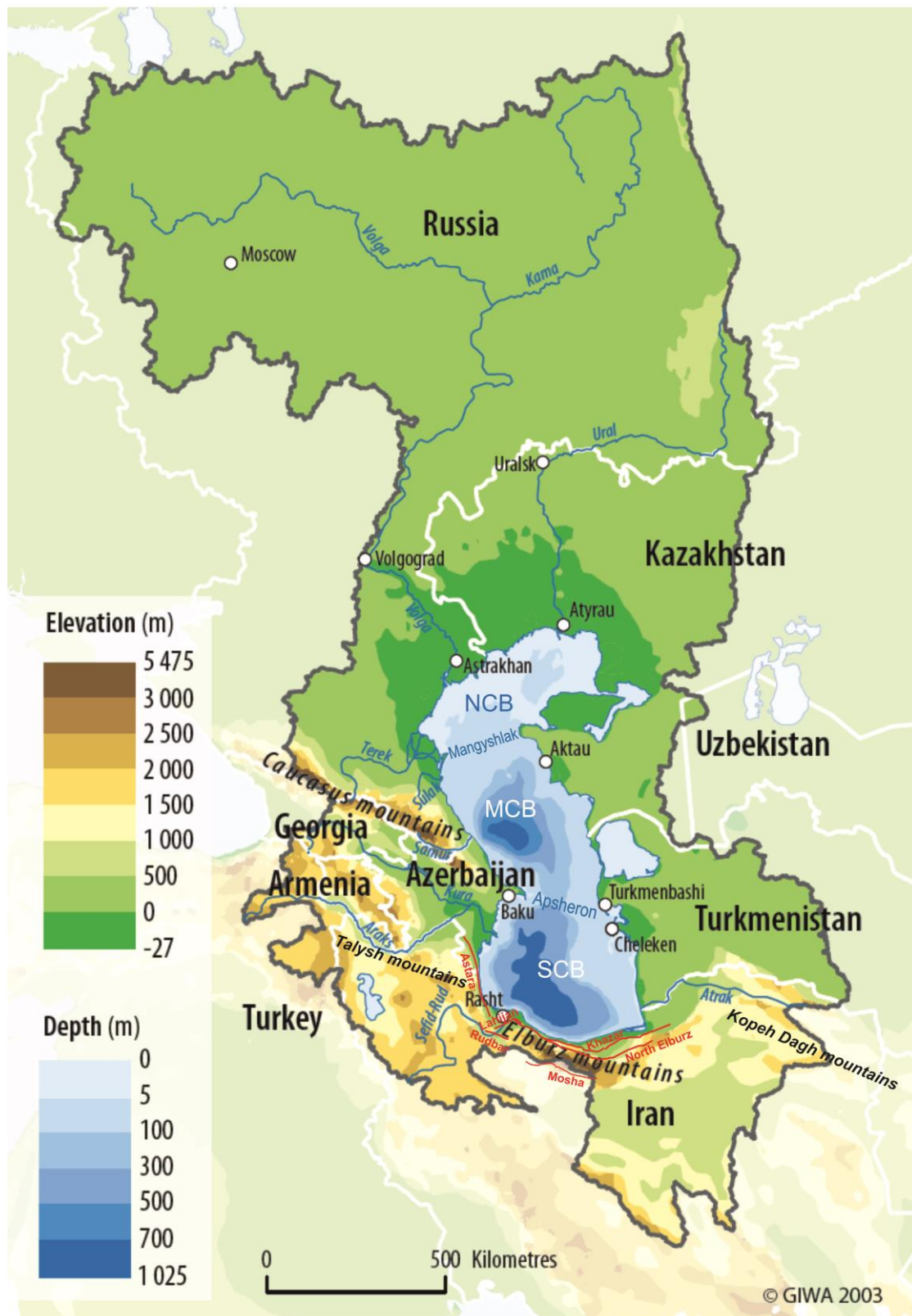


Fig. 2.1. The Caspian Sea catchment area (UNEP, 2006 with modifications). Red line represents location of the main faults in study area (southern CS). Location of the faults from Aghanabati (2004).

More than 130 rivers flow into the CS through the northern, southern and western coasts but there is no permanent river inflow from the desertic eastern area (UNEP, 2006) (Fig. 2.1). More than 88% of river inflow is supplied by the rivers of northern coast: Ural, Volga and Terek (UNEP, 2006). The Volga River itself contributes ~ 80% of the total inflow to the CS and it has a significant impact on water level of the Caspian Sea (Kroonenberg et

al., 1997; Arpe et al., 2014). Along the western coast, Sulak, Samur and Kura rivers account for 8% of total inflow. The remaining inflow is provided by river along the southern coast (Sefidrud and other rivers) where narrow coastal plain constrained them between the sea and the neighbouring mountains and the rivers travel only short distance before entering the CS (UNEP, 2006). Although most of the fresh water is provided by Volga River, the south-western rivers such as the Sefidrud, Kura, and Terek Rivers supply ~79% of sediment to the CS (41, 22, and 15%, respectively), due to their provenance in steep mountains with low vegetation (Lahijani et al., 2008).

2.1.2 Caspian Sea Level (CSL) fluctuation

The Caspian Sea, after separation from the Global Ocean, in Mid Pliocene (Varushchenko et al., 1987) has experienced dramatic water level fluctuations. In the Quaternary, during the Pleistocene, the CSL rose up at least +50 m asl. During the early Holocene, the CSL dropped to -113 m bsl (Varushchenko et al., 1987, Kroonenberg et al., 1997, 2000; Dolukhanov et al., 2010). During the last millennium CSL experienced two significant changes: a poorly identified drop and a slightly better known rise during the Medieval Climatic Anomaly (MCA, AD 950-1250) and the Little Ice Age (LIA, AD 1350-1850), respectively (dates defining these periods from Ruddiman 2008 and Mann et al. 2009) (Kroonenberg et al., 2007; Leroy et al., 2011). More recently, the CS has also experienced a c. 3 m rise and fall during the last century (Fig. 2.2), while the global sea level has fluctuated approximately 2 mm/year, in the same period (Kroonenberg et al., 2007).

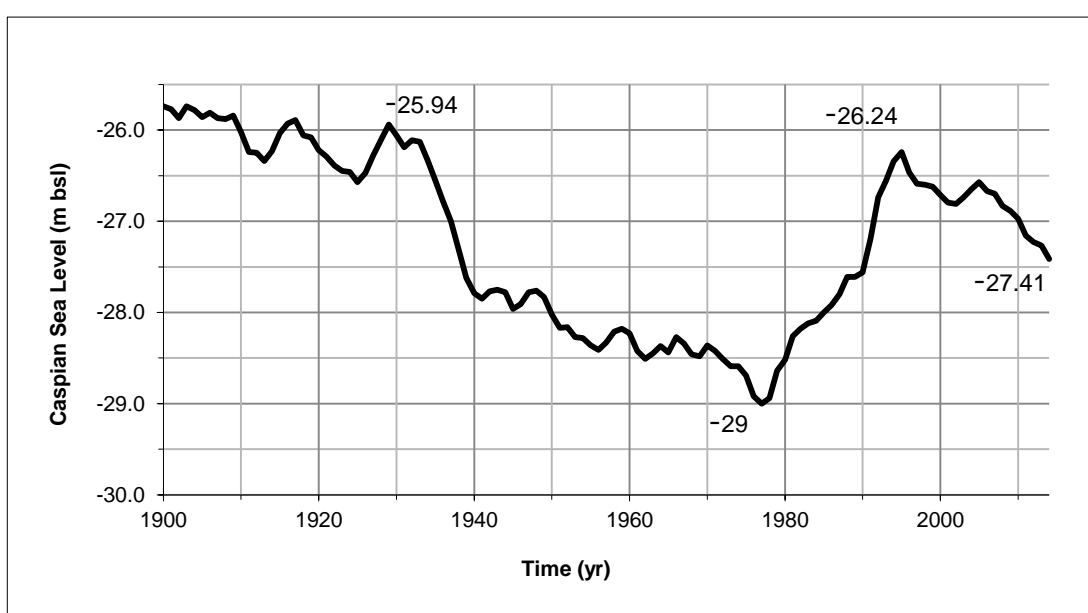


Fig. 2.2. Caspian Sea level (CSL) from 1900 to 1992 from Lepeshevkov et al. (1981); from 1992-2014 from USDA (2015)

These dramatic water level changes have affected the surrounding populations and their activities. The Italian traveller Marin Sanudo already documented that the early 14th century water-level rise destroyed many important towns around the CS (see Naderi Beni et al., 2013a). The recent and rapid CS level (CSL) changes have directly affected tens of thousands of people in the lowlands of Iran, Azerbaijan, Daghestan and the Volga Delta (Rucevska et al., 2006). The most important problems to be highlighted are urban facilities flooding, roads and railways destruction, industrial infrastructure damage (including oil and gas exploitation and fish farms), as well as salinization of agricultural land and destruction of beaches (Dolotov and Kaplin, 2005; Kosarev, 2005; Rucevska et al., 2006; Kroonenberg et al., 2007; Leroy et al., 2010; Naderi Beni et al., 2013a).

The importance of the effects of CSL rapid fluctuation on population and human activities requires research on prediction of future CSL changes. Although current models suggest that precipitation and evaporation seem to be the main factors influencing the CS hydrological budget (Arpe et al., 2000, 2012, 2014), mechanisms behind CSL changes are not still completely understood. Consequently, since the instrumental records hardly provide information for periods older than two centuries, a palaeo-environmental approach is required for unravelling past water-level changes in order to compile useful data for future modelling and forecasting. However, the reconstructed curves are discontinuous and compilations show that they are often contradictory even for the last millennium. Therefore, palaeo-environmental reconstruction even in one location is useful to contribute to the reconstruction of CSL curve.

Reconstruction of the past CSL oscillations and its driving forces has been the subject of many studies. Rychagov (1997) reconstructed the Holocene CSL curve based on altitude of several river terraces in mouth areas along Daghestan coast. His proposed curve is one of the most cited curves in literature. Hoogendoorn et al. (2005) have studied the sedimentary sequences of Kura delta in west coast of the CS and concluded that the CSL dropped to -38 m bsl during Derbent regression during MCA. Offshore deposits of the CS were studied by Leroy et al. (2007) to indicate salinity changes of the CS during the Holocene due to major river avulsion of Amu-Darya from Aral Sea into the CS. A combination of historical, archaeological and geological data was implemented by some researchers to reconstruct the past sea level changes (e.g. Varushchenko et al., 1987; Karpychev, 2001; Naderi Beni et al., 2013a). In the last attempt, Naderi Beni et al. (2013a) found that the CSL rose up to -19 m bmsl during the early LIA (Fig. 2.3).

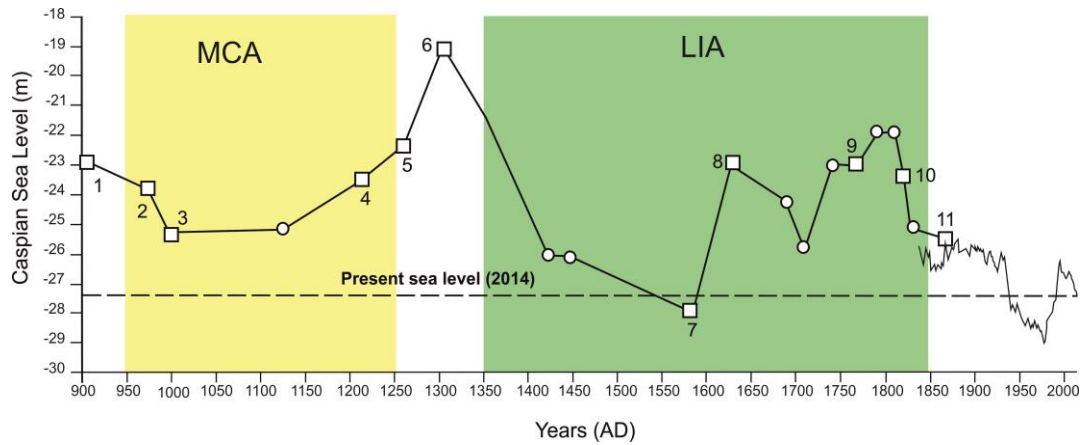


Fig.2.3. CSL curve for the last millennium, after Naderi Beni et al. (2013a). Data from 1900 to 1992 from Lepeshevkov et al. (1981); from 1992-2014 from USDA (2015)

It should be noticed that dating the lowstands are more problematic, as recording of lowstands along the coast is more difficult and also the dating is difficult (Kroonenberg et al., 2007). Deep sea cores without hiatus provide recording of lowstands (Leroy et al., 2007, 2013c and 2014). Based on CSL modelling the CSL curve during MCA could be even lower than the current CSL curve (K. Arpe, pers. comm.).

Although mechanisms behind CSL changes are not still completely understood, changes in water input, climatic changes and tectonic fluctuations are accepted as the main causes by many researchers (Arpe et al., 2000). As the Volga River supplies more than 80% of the river discharge into the CS, precipitation over the Volga River drainage area is the dominant factor on the CSL changes. In this regard, two major recent CSL changes (i.e. a drop in 1930 and a rise in 1977 in Fig. 2.2) have been linked to summer precipitation over the Volga River drainage area (Arpe and Leroy, 2007). Current models also suggest that precipitation and evaporation over the CS itself seem to be amongst the main factors influencing the CS hydrological budget (Arpe et al., 2000, 2012, 2014).

2.1.3 Deltas around the CS

The Greek letter delta (Δ) was applied for the first time to a triangular area where the Nile River loads its deposits into the Mediterranean in 454 B.C. Since that time this word is widely used for alluvial land formed by a river at its mouth without concerning about the deltaic geometry (Selley, 1996). When a river arrives at open water, the flow velocity of the river decreases abruptly. Hence the river's competence to carry sediment decreases and most sediment in transport is deposited, forming a delta. On the basis of gradient, the delta profile can be divided by three sections, by analogy with Gilbert-type deltas: (i) topset, with a low gradient which is partly subaerial and partly subaqueous, (ii) foreset, a relatively steep gradient, (iii) bottomset: low gradient subaqueous zone. This morphological terminology is now replaced by a process terminology: (i) delta plain: the largely subaerial zone dominated by river, (ii) delta front: the zone of interaction between

basinal and fluvial processes, (iii) prodelta: the zone of quiet sedimentation from suspension, disturbed only by gravity sliding and mass flow deposition (Reading, 2009).

The main Caspian deltas are distributed along the north, west and south coasts: Ural, Volga, Terek, Sulak, Samur, Kura and Sefidrud. Their shapes and morphologies are influenced by the shelf gradient, wave energy and sediment supply under variable CSL. At the point of entry to the basin, the Ural and Volga River enter into the NCB where the continental shelf is gently sloping. The gradient of the continental shelf toward the west side of the NCB gradually increases, where Terek and Sulak flowing into the basin. The continental shelf becomes very steep where the Samur, Kura and Sefidrud enter into the basin (Fig. 2.4) (Lahijani et al., 2008).

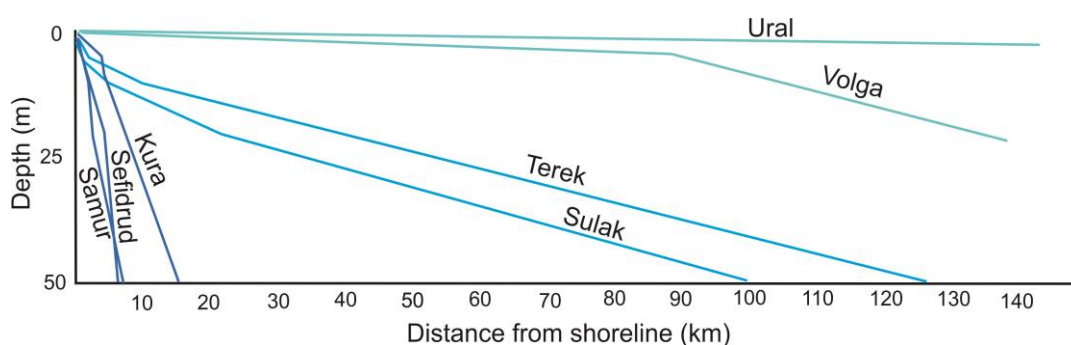


Fig. 2.4. Cross section of subaqueous part of the Caspian deltas (Lahijani et al., 2008, with modifications)

The shallow and wide shelf on the north Caspian prevents high wave development. Therefore, the role of wave energy in delta morphology in Ural and Volga deltas is negligible. In the west and south Caspian Sea, wave and wave induced currents are the main factors in delta configuration (i.e. Samur, Sulak, Kura and Sefidrud) (Krasnozhon, et al., 1999; Lahijani et al., 2008).

The difference in water and sediment discharges of these rivers has affected their delta type and size. The Sefidrud, Kura and Terek are the main sediment supplier for the CS, while other rivers (Ural, Volga, Samur and Sulak) are less important in terms of sediment load (Table 2.1) (Lahijani et al., 2008).

Table 2.1. Main Caspian deltaic rivers and their characteristics (Lahijani et al., 2008)

River	Length (km)	Drainage area (1000 km ²)	Water discharge (km ³ /yr)	Sediment discharge (mt/yr)
Ural	2430	237	6.6	-
Volga	3690	1360	233	6
Terek	623	43.2	8.4	11.9
Sulak	169	15.2	4.0	1.6
Samur	231	7.73	1.63	4.7
Kura	1360	188	15.5	17.1
Sefidrud	820	67	4	32

Sea level fluctuation can affect delta evolution. However, effect degree depends on the gradient of slope. Indeed, Volga and Ural deltas are sensitive to the short- and long-term sea-level changes and can be affected by a minor fluctuation, due to the low gradient of the north basin (Kroonenberg et al., 1997). In general, when sea-level rises, the deltas retrograde landward, and during sea-level fall they prograde into the sea. However, deltas can be affected by sea level fluctuation in different ways. Inundation, erosion and sand barrier formation and development of lagoons behind them are the main responses of coastal area to rapid sea level rise (Kaplin and Selivanov, 1995; Kroonenberg et al., 2000; Naderi Beni et al., 2013b). The CSL rise between 1979 and 1995 affected deltas by inundation and erosion. Ural, Volga and Terek deltas (gentle gradient coast) were subjected to passive inundation (drowning) and backstepping, while Sulak, Samur, Kura and Sefidrud (steep coast) were affected by erosion (Lahijani et al., 2008). Kroonenberg et al. (2000) showed that this period was characterised by erosion and development of sand barrier and lagoons behind them in western coast. Development of spit lagoons as a response to rapid sea level rise has been reported in moderate slope coasts (Voropaev et al., 1998; Kroonenberg et al., 2000; Storms and Kroonenberg, 2007; Lahijani et al., 2009; Kakroodi et al., 2012; Naderi et al., 2013b). Kroonenberg et al., (2000) discussed that the transgression on its own is not sufficient for barrier formation and wave energy is needed for mobilising the coarse sediments shore-wards to develop barrier ridge. Sand barriers also can be formed during sea level fall as small bars without lagoon development (Kroonenberg et al., 2000). During such a period, existing lagoons also became shallower and narrower (Kroonenberg et al., 2000) and some changes to marshland (Kaplin et al., 2010). Human activities such as reduction of sediments such as dam construction may cause intensive erosion of coasts and deltas (Ignatov et al., 1993; Lahijani et al., 2008) by sediment starvation.

2.1.4 Economic significance of deltaic deposits

Deltaic deposits are known as important sources of coal, oil and gas. Major hydrocarbon provinces are often formed in deltaic environment. The deltaic processes are excellent mean for transporting sand as potential hydrocarbon reservoir to marine basin with organic-rich mud as potential hydrocarbon source. Beside this, the deltas that form in areas of crustal instability structural deformation can form traps for hydrocarbon migration. Obviously, it is crucial to understand the sedimentology of deltas to predict the location and geometry of a hydrocarbon reservoir (Selley, 1996). However, fluvial and marine processes, gradient, sea level change, palaeogeography setting and subsidence rate vary and are completely unique for each delta (Kroonenberg et al., 2005). The Productive Series, the Lower Pliocene fluvial-deltaic deposits with up to 7000 m thickness, in the

northern part of SCB is one of the most promising hydrocarbon reservoirs in the world which is deposited by palaeo Volga, palaeo Amu Darya and palaeo Kura (Fig. 2.5; Kroonenberg et al., 2004, 2005). This reservoir also incorporates large volumes of sedimentary deposits contributed by other river systems, including the Sefidrud and other small palaeodeltas in Iran (Smith-Rouch, 2006).

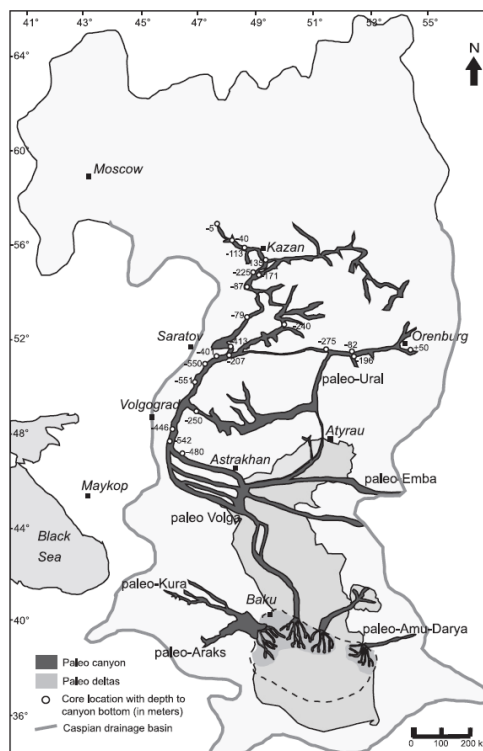


Fig. 2.5. Map of possible source of sediment deposited in palaeodeltas prograding into the SCB (Kroonenberg et al., 2005)

This hydrocarbon system is a product of unique palaeo-geographic and tectonic events that led to the deposition of organic-rich fluviodeltaic sediments, deposited at extremely high sedimentation rates (2-4 mm/yr), in the rapidly subsiding SCB concurrent with a huge supply of sediments and development of anticlinal traps (Kroonenberg et al., 2004, 2005; Abrams and Narimanov, 1997). High sedimentation rates help to decrease the burial time of organic matter (OM) in sediments; thus quickly removing the sediments from the oxygen-rich surface sediment layer, where OM degradation is most rapid. The result is increased preservation potential of OM with increasing sedimentation rates (Johnson Ibach, 1982). However, rapid burial also provides the relatively low geothermal gradients which result in favourable thermal conditions for the preservation of hydrocarbons (Nadirov, 1997).

The modern Sefidrud Delta continues to deliver sediments eroded from the Elburz Mountains to the SCB. If sediment was also being transported in the basin during the Pliocene and Pleistocene, by the Sefidrud, potential reservoir rocks could have been deposited in the southern SCB (Smith-Rouch, 2006). However, Kazancı and Gulbabazadeh

(2013) suggest that during Early Pleistocene, the Sefidrud was a short river and its catchment area was much smaller than at present and it increased its catchment area by capturing Kizilozen and Shahrud rivers in the Late Pleistocene (Fig. 2.6).

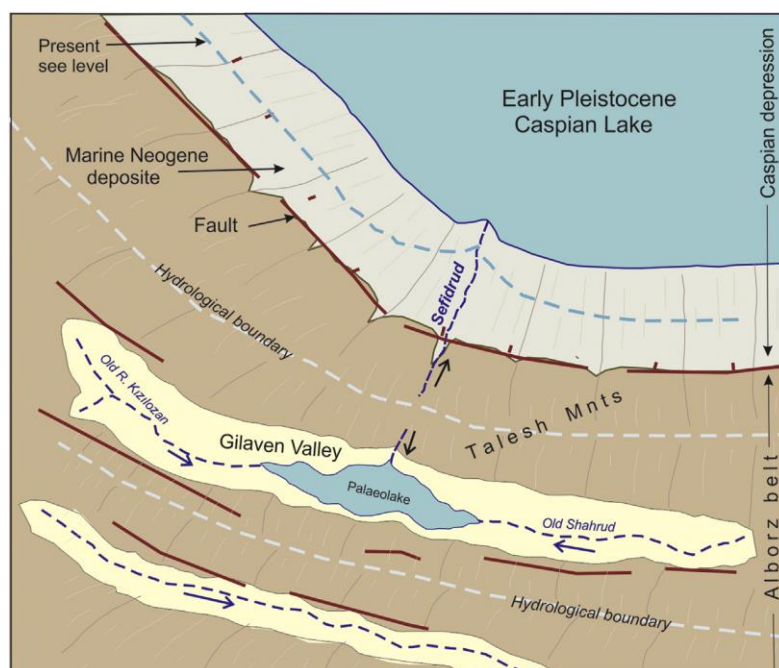


Fig. 2.6. Palaeogeography of the southern CS, from Kazancı and Gulbabazadeh (2013).

2.2 Sefidrud Delta

The Sefidrud, as the largest sediment supplier for the Caspian Sea, develops its delta under the influence of a complex of factors in a high energy and high gradient coastal area with strong littoral drift. The source of the 820 km long Sefidrud is in the metamorphic and igneous rocks of Zagros Mountains in western Iran. The river passes through a narrow passage within the Elburz Mountains to reach its large delta on the southern CS shore (Lahijani et al., 2008). The average water depth in the Sefidrud is ~2.5 m and its width in the delta varied between 250 and 400 m (Krasnozhon et al., 1999). Sefidrud has a meandering pattern after passing Astaneh Town (Fig. 1.1C). Kosari (1986) discussed that this meandering pattern is a result of reaching to the basement surface of the CS. However, Kazancı and Gulbabazadeh (2013) believed that the meandering pattern is due to the presence of different rock resistances in the area. Having high percent of heavy mineral, primarily ilmenite and magnetite, makes this river a source of heavy minerals for the south west CS and this river has been classified as a heavy-metal-dominated river (Lahijani and Tavakoli, 2012).

The Sefidrud Delta is wave-dominated during sea-level rise. During episodes of sea-level fall, the delta becomes river-dominated (Naderi Beni et al., 2013b). Based on terminology used in Reading (2009), fluvial-wave interaction delta is a better term to classify Sefidrud Delta system. The Sefidrud has repeatedly changed its course through the

area between the Anzali and Amirkola lagoons (Kousari, 1986). The last major avulsion is believed to have occurred around AD 1600 when the river diverted its course from the east, near Amirkola Lagoon, towards the west near Kiashahr Lagoon, shifting its outlet c. 23 km westwards (Krasnozhon et al., 1999; Lahijani et al., 2009; Leroy et al., 2011; Kazancı and Gulbabazadeh, 2013; Naderi Beni et al., 2013b). The Sefidrud before avulsion near Amirkola is known as Old Sefidrud and New Sefidrud (or Sefidrud) after avulsion. Although the age of this avulsion is widely accepted in publications, the timing evidence of this major event remains unclear. Sea level rise has been considered the main cause for river avulsion (Törnqvist, 1993; Törnqvist et al., 1996; Aslan and Autin, 1999; Jones and Schumm, 1999; Makaske, 2001; Overeem et al., 2003; Aslan et al., 2005; Hoogendoorn et al., 2005; Naderi Beni et al., 2013b; Ollivier et al., 2015). Avulsion can be caused by a decrease of river gradient as a result of several interacting processes such as subsidence, flood plain aggradation and sea level rise (Jones and Schumm, 1999; Overeem et al., 2003; Heyvaert and Baeteman, 2008). Furthermore, human activities, including channel diversion for irrigation through artificial and natural levee breaks and channel blockages, can also cause river avulsion (Heyvaert and Baeteman, 2008).

2.2.1 Source of the sediments

Most of the coarse sediments in the study area are transported to the coast by the Sefidrud. Passing through a barren plateau and steep mountains, the Sefidrud, with a mean sediment discharge of ~32 million tonnes per year, provides a huge amount of eroded sediments to the CS shoreline (Lahijani et al., 2008). Indeed, the south–western rivers including the Sefidrud, Kura, and Terek Rivers supply around 79% of sediment to the CS (42, 22, and 15%, respectively) (Lahijani et al., 2008). These sediments are redistributed mainly by waves and wave–induced longshore currents. The prevailing currents are southward in Azerbaijan and along the west Iranian coast (Lahijani et al., 2009). With the latter currents, sediments originating from the western river (e.g. Kura River) also contribute to the sediment supply in the area (Doriniana and Myakokin, 1972). These longshore currents supply sediment for the development of spit–barrier systems and associated lagoons (Kaplin and Selivanov, 1995; Kroonenberg et al., 2000; Lahijani et al., 2009) such as the Anzali, Zibakenar, Kiashahr and Amirkola Lagoons (Kousari, 1986; Lahijani et al., 2009; Naderi Beni et al., 2013b). Furthermore, the prevalent winds, combined with proximal availability of barren sand sources, drive dune formation in the delta (Kazancı et al., 2004; Lahijani et al., 2009).

The construction of the Manjil Dam (fig. 1.1 A and B) on the Sefidrud in 1962 caused a strong reduction of sediment supply to the lower reaches of the river. The dam, which is also known as the Sefidrud Dam, was constructed on the river in the Manjil area with the

purpose of irrigating downstream rice paddies during the summer (Morris and Fan, 1998; Khosronejad, 2009). Approximately 48 million tonnes of sediment enter the reservoir per year. Under normal condition (i.e. without flushing) only 14 million tonnes leaves the reservoir annually (Morris and Fan, 1998; Khosronejad, 2009). By 1978, 40% of the Manjil Dam reservoir capacity was choked with sediments and winter sediment flushing operations were initiated in 1980 (Morris and Fan, 1998; Khosronejad, 2009; Yamani et al., 2013). Sediment removal varies from year to year, with a maximum of 135 million tonnes of sediment removed in the flushing period of 1984–1985 (Table 2.2; Morris and Fan, 1998; Yamani et al., 2013). Since 1998, flushing operations have been suspended due to climate variations and increasing periods of drought in Iran (Yamani et al., 2013).

Table 2.2. Flushing operation statistics from 1980 to 1998, Water Research Institute, Ministry of Energy, Iran as in Yamani et al. (2013).

Flushing period	Sediment Discharge (10 ⁶ t)		Water Discharge (10 ⁶ m ³)	
	Flushing period	Normal condition (the rest of the year)	Flushing period	Normal condition (the rest of the year)
1980-1981	21.30	9.90	536	4926
1981-1982	10.30	3.8	390	3154
1982-1983	48.80	14.8	1513	4365
1983-1984	72.50	12.2	1017	3747
1984-1985	135.30	9.8	1606	4564
1985-1986	43.80	5.90	1084	3019
1986-1987	31.60	5.60	978	2902
1987-1988	59.10	35.30	1812	6577
1988-1989	55.20	4.70	1057	2636
1989-1990	31.9	1.50	681	2827
1990-1991	23.3	3.20	664	2473
1991-1992	18.6	9.30	664	4796
1992-1993	22.2	6.90	605	3996
1993-1994	52.9	5	2321	5447
1994-1995	46.1	7.70	2136	4489
1995-1996	12.5	10.30	812	4703
1996-1997	15.9	2.10	867	1815
1997-1998	11	3.40	374	3823

2.2.2 Geology of the region

The SCB is surrounded by the Elburz Mountains in the south, Talysh Mountains in the west and Kopeh Dagh Mountains in the east (Fig. 2.1). Elburz Mountains are composed of various lithologies such as volcanic, metamorphic and sedimentary rocks from the Palaeozoic to the Cenozoic Eras. Talysh and Kopeh Dagh mountains comprise sedimentary rocks (Berberian and King, 1981). Since the SCB is surrounded on all sides by mountain belts, the SCB itself contains the thickest sediment accumulations known on Earth (Jackson et al., 2002). These sediments contain a mud-prone sequence (Maykop Series) which is the most important regional source rock for hydrocarbons (Jones and Simmons, 1997). This mud sequence then was covered by sands that entered the basin through major delta systems known as the Productive Series. Abundant mud volcanoes and diapirs offshore and in the Kura Basin onshore is a consequence of the rapid sand deposition and

over pressuring of the underlying muds (Jackson et al., 2002). Brunet et al. (2003) indicated that an extraordinarily rapid subsidence of the SCB took place, during the Pliocene–Quaternary, which was coincident with the uplift of the Great Caucasus, Kopet Dagh and Elburz mountains. At the same time, the orogenic uplifts were intensely eroded, providing a large influx of sediments. These were transported towards the SCB by several major rivers and filled the SCB, allowing the formation of hydrocarbon system.

The study area is situated at the foot of the middle parts of Elburz Mountains which is known as coastal lowlands. The latter consists of Palaeocene to Quaternary intertwined marine and floodplain deposits (Fig. 2.7). The coastal plain is characterized by abundant distributary channels and extensive flood plain, on which local swamps are common. Sediments with marine characteristics are locally observed on the coastal plain, which reflect sea-level effects on the plain (Fig. 2.7; Lahijani et al., 2008). The Khazar Fault and the Lahijan Fault are the major tectonic features in the study area (Fig. 2.1). The Rudbar Fault and the Mosha Fault are located further south of the study area (Fig. 2.1) and caused two large-magnitude earthquakes in AD 1990 and 958, respectively. The latter blocked rivers and formed lakes in the area (Berberian and Yeats, 1999). The southern region of the CS is seismically active (Jackson et al., 2002; Vernant et al., 2004; Ritz et al., 2006). The rate of vertical movement (uplift/subsidence) on the coastal lowlands is negligible during the last millennium (Djamour et al., 2010). However, large-magnitude inland or sea-based earthquakes can be responsible for unexpected sudden sea level changes (Ozyavas et al., 2010; Naderi Beni et al., 2013a).

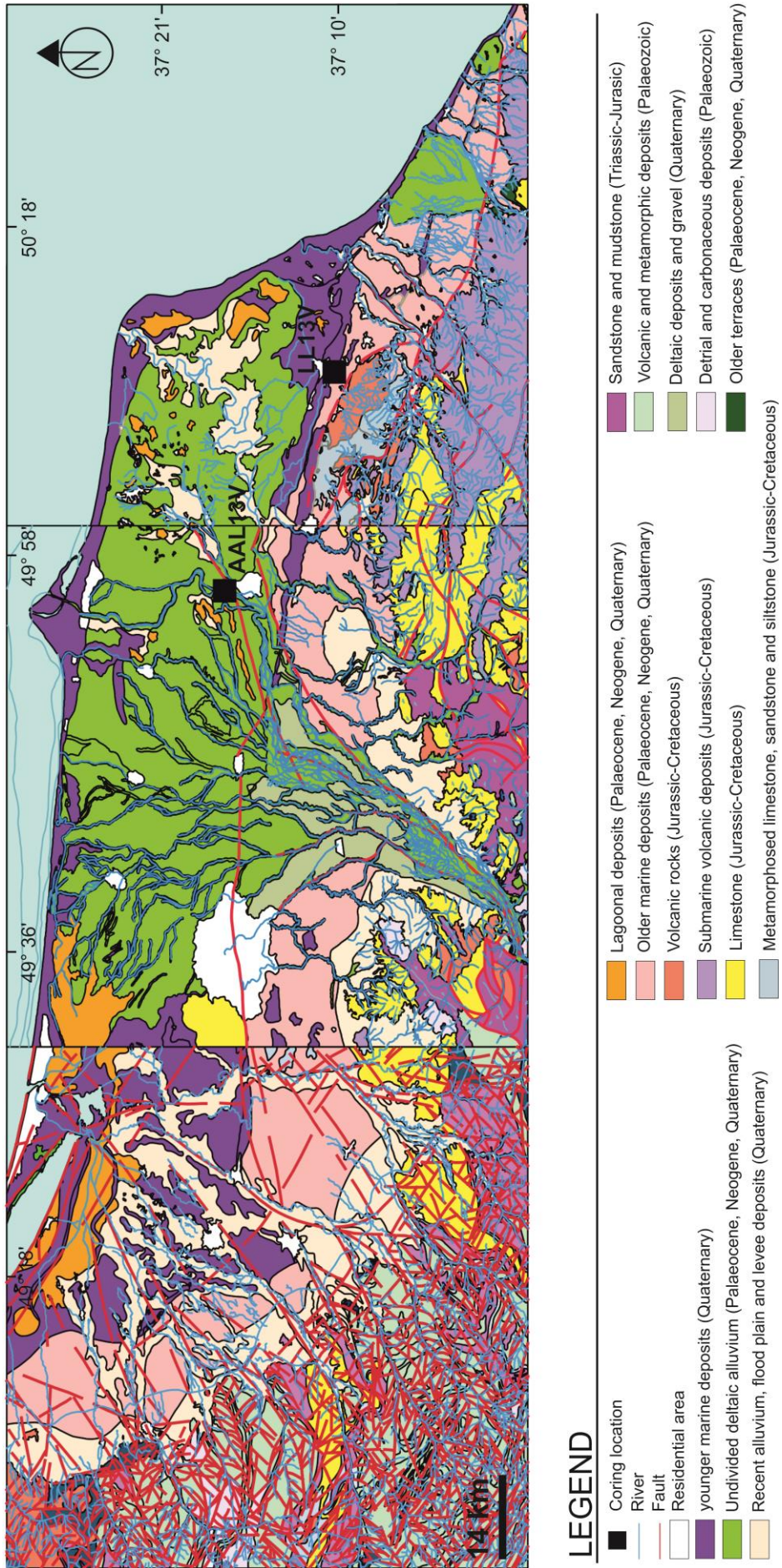


Fig. 2.7. Geological map of study area from Geological Map of Iran (scale: 1/100 000), series Sheet 5864 (Nazari and Omrani, 2004), 5964 (Khabbaz-nia and Sadeghi (2004), and 6064 (Rahmati Iikhchi et al., 2004).

2.2.3 Coastal lagoons and wetlands

Coastal lagoons are shallow inland water bodies, usually oriented parallel to the coast, separated by a barrier from the sea (Kjerfve, 1994). Wetlands are submerged lands that are including marshes, swamps, bogs, river banks, areas subjected to flooding, emergent and submergent plant communities in water bodies (Lefor and Kennard, 1977). Coastal wetlands are along the coastlines. Many of coastal wetlands can be included in the definition of coastal lagoon (Kjerfve, 1994). However, the coastal wetlands are above the highest high water (Bao et al., 2007).

Strong longshore drift and high sediment supply have created suitable conditions for coastal lagoon formation in the Sefidrud Delta. These water bodies and their sedimentary infill are ideal archives for the reconstruction of CSL fluctuations. Zibakenar, Ushmak, Kiashahr and Amirkola Lagoons are the main coastal lagoons which are subjected to study in this research. Zibakenar, Ushmak and Kiashahr Lagoons are associated with Sefidrud after avulsion of Old Sefidrud. Indeed, lateral immigration of Sefidrud has led to formation of these lagoons (Lahijani et al., 2009). Zibakenar Lagoon is located on the west side of Sefidrud, are part of a larger lagoon complex called Boujagh Lagoon (Fig. 1.1 C). Hence it is also known as the Boujagh (Boojagh, Bojagh) Lagoon. Kiashahr Lagoon (also called Farahnaz), is a shallow sea bay located on the east side of Sefidrud, together with Zibakenar and Ushmak Lagoons, forms part of Boujagh National Park (BNP) (Fig. 1.1 C) which was designated a Ramsar site in 1975. Ramsar site is an internationally important wetland habitat designated under the Convention on Wetlands, held in Ramsar, Iran in 1971. Most hunting activities have been banned since 1998 and the area is an important refuge for migratory birds (Naqinezhad et al., 2006). Since 2001, the area has also been designated a national park in order to decrease threats to its vegetation cover and to protect its biodiversity (Naqinezhad, 2012). The site is used for recreational and commercial fishing including aquaculture, livestock grazing, reed-cutting, limited hunting, rice farming and recreation/tourism (Annotated Ramsar List, 2011). The depth of water in these lagoons is usually less than 2 m, and controlled by freshwater input through precipitation and irrigation.

Amirkola Lagoon is associated with Old Sefidrud and has a maximum water depth of 2 meters (Naderi Beni, 2013 b). The lagoon has no river inflow and receives its fresh water by precipitation and surface water passing through rice fields that surround the lagoon. The Amirkola lagoon was formed by littoral drift of sediments supplied by the Old Sefidrud, during the LIA (around 1600 AD), as a result of sea level rise (Lahijani et al., 2009; Leroy et al., 2011; Naderi Beni et al., 2013b).

The Langarud wetland is located 11.5 km inland from the CS coastline (Fig. 1.1 C). Its name is variously spelled Langerud, Langroud, Langrood, Langarood, and Langaroud, but in this text it is standardised as Langarud. This wetland is known as the Kiakolayeh wetland as well. It is a freshwater wetland located in the south-east of Langarud town. It is not known when the town of Langarud appeared. However, the name of Langarud was already used in AD 1118 in historical books (Setudeh, 1970).

2.2.4 Climate and vegetation of the region

The CS area overlaps several climatic zones because of its great meridional extension. The western coast climate features are moderately warm. The northern part of the basin extends in a zone of temperate continental climate. Desertic climate is the dominant in the eastern coast, while the south-western and southern coasts have a subtropical climate (Leroy et al., 2007). The south western coastal plain where the Sefidrud Delta is located has a temperate humid climate and high precipitation. Annual precipitation in the study area is between 1850 mm (Anzali synoptic station) and 1344 mm (Rasht synoptic station). The mean annual temperature is ~16°C (in Anzali, Lahijan and Rasht synoptic station: Molavi–Arabshahi et al., accepted).

Most of the subaerial part of Sefidrud delta is intensively cultivated by tea plantations, citrus trees, and rice paddies. Therefore, the outcrops and geological features are covered by vegetation. Local vegetation in wetlands and lagoons are dominated by aquatic plants. The northern slopes of Elburz Mountains are parts of the Hyrcanian (Caspian mixed forest). In this study, palynology is also used as a proxy to reconstruct the history of coastal development. *Eucalyptus* and *Azolla filiculoides* are non-native plants found in the study area. *Eucalyptus* trees were introduced from the southern hemisphere not earlier than 1952 in the Hyrcanian forests, and only became abundant after 1970 (Akhani et al., 2010; Sagheb–Talabi, 2004). *Azolla filiculoides* is another invasive species introduced to Iran in 1986 from the Philippines (Hashemloian and Azimi, 2009). This aquatic fern is used as natural fertiliser in rice paddies.

2.3 In conclusion for chapter two

The main investigations in the Sefidrud delta are: Kazancı and Gulbabazadeh (2013), Naderi Beni et al. (2013b), Lahijani et al. (2009), Khoshraftar (2005), Krasnozhan et al. (1999) and Kosari (1986).

Kazancı and Gulbabazadeh (2013) focused on the initiation of the modern delta probably formed during the last three millennia and two older stages of the delta evolution in Late Khvalynian and Early Khvalynian. Their work is based on field work samples and data gathering and it is the first publication on the evolution of the Sefidrud Delta.

However, no age data were included. The authors proposed a concept of lobe evolution, partially based on a conceptual model.

Naderi Beni, et al. (2013) studied Kiashahr, Boujagh and Amirkola Lagoons using Ground Penetrating Radar (GPR) profiles supported by several radiocarbon age estimates on Kiashahr spit. They concluded that the development of these lagoons was a response to rapid CSL rise during the LIA. The results from the present study will show time hiatuses that complicate the evolutionary model of these authors.

Lahijani et al. (2009) studied the coastal evolution of the Sefidrud Delta including lagoon development in the area. The authors suggested that the Zibakenar and Kiashahr Lagoons developed during the past four centuries, yet new age data were not included.

Krasnozhon et al. (1999) used space imagery to determine the boundary between the ancient and modern deltas and the development of modern delta during the past 500 years. The main avulsion from the Old Sefidrud to the New Sefidrud was proposed to have occurred around AD 1600, but no age data to verify the age were presented. Their proposed timing became subsequently quoted in other studies (Lahijani et al., 2009; Leroy et al., 2011; Kazancı and Gulbabazadeh, 2013; Naderi Beni et al., 2013b).

Kousari (1986) documented the recent evolution of the Sefidrud delta by comparison of historical aerial photographs. This seminal work was later supplemented by other publications (i.e. Krasnozhon et al., 1999; Khoshraftar, 2005; Lahijani et al., 2008; Kazancı and Gulbabazadeh, 2013).

The exact timing of important events during the last millennium (e.g. the timing of avulsion of the Sefidrud and the timing of lagoon formation in relation to rapid CSL fluctuation) is incompletely understood. Moreover, no offshore investigations have been published so far. In the present work we aim to combine onshore and offshore sections and produce new age data in order to improve our understanding of the Sefidrud delta evolution. Moreover, considering the fact that existing CSL curves are often contradictory, any contribution of the present study in the reconstruction of CSL curve is helpful.

3 Materials and methods

This study is based on geophysical data and sediment samples acquired during three surveys. Field work was conducted in two parts including terrestrial (on land) and marine (onshore and offshore). On land, coastal lagoons and inland water bodies were subjected to study using cores during the field campaign organised by the Iranian National Institute for Oceanography and Atmospheric Science (INIOAS). Also, Ground Penetrating Radar (GPR) transects were obtained during these campaigns, and cores were specifically taken in order to confirm major reflections in GPR profiles. During the marine cruise organised by the Geological Survey of Iran (GSI), cores were retrieved from different depths. Also, surface samples were taken using a grab sampler by INIOAS from onshore where the water depth varied between 15 to 20 m. Materials including geological maps of the area (scale: 1/100,000), remotely sensed data, published literature and historical documents are also used in this study.

3.1 Remote sensing

Aerial photographs were used to observe coastal changes over time, in different places in the world, by various authors: Dolan et al. (1978), Leatherman (1983), Anders and Byrnes (1991), McBride et al. (1991) and De Stefano et al. (2013). In the CS area, the recent evolution of the Sefidrud delta has been documented by comparison of historical aerial photographs. The original work was made by Kousari (1986) and was later supplemented by other publications (i.e. Krasnozhan et al., 1999; Khoshraftar, 2005; Lahijani et al., 2008; Kazancı and Gulbabazadeh, 2013). Based on an updated compilation, our study especially focuses on the evolution of coastal lagoons using an aerial photograph of the year 1955 from Khoshraftar (2005), interpretation of aerial photographs of the years 1964 and 1982 derived from Kousari (1986) with modifications, and also 1991 and 2014 satellite images from Google Earth. This comparison allowed us to reconstruct not only sand spit formation and development of coastal lagoons, but also minor river avulsions and variations in the morphological features of the delta during the past 59 years.

3.2 GPR profiling

Recently, Ground Penetrating Radar (GPR) has been used for detailed subsurface imaging of deltaic deposits and most of these studies have focused on modern deltas associated with fluvial deposits (Jol and Smith, 1991; Pepola and Hickin, 2003; Roberts et

al., 2003). The objective of GPR in this study was to image the internal structure of sediments and consequently to find previous river channels of Sefidrud in order to study river avulsion.

In this technique a short pulse of high-frequency EM energy (10–1000 MHz) is transmitted into the ground. When the signal encounters a contrast in material properties, some of the energy is reflected back to the surface due to a change in the bulk electrical properties of different subsurface lithology. The interface between these two layers may be characterized by bedrock contact, organic-rich sediments, groundwater table, and changes in the sediment grain size and mineralogy (Davis and Annan, 1989). One significant limitation of the GPR system setup is penetration depth and resolution. Both of these attributes depend on the choice of the antennae. High-frequency antennae (500–1000 MHz) provide high resolution at the expense of relatively limited penetration. Antennae with frequency range of 12.5–50 MHz have poor resolution but allow for a maximum probable penetration of 45–65 m (Smith and Jol, 1995).

This method is a non-invasive, fast and relatively inexpensive technique. However, it has some limitation in fine-grained environments (silt and clay) and saline coastal environments, where GPR will generate poor to unusable results (Bristow, 2009; McCuaig and Ricketts, 2004), that are known as multiples. Multiples are produced when the transmitted signal is reflected back and forth between the surface and a reflecting horizon giving the impression of two or more reflections (Bristow, 2009). The presence of clay/silt sediments causes this problem. In fact fine sediments prevent the signal penetrate through the layers. Therefore, the only reflector (clay/silt layer) is repeated in the image (Fig. 3.1). Rapp and Hill (2006) states that a 100 MHz GPR can penetrate approximately 15 m of dry sandy sediment compared to as little as 1 m of wet clayey sediments. Also, the data collected through GPR methods are highly subject to the interpretation of the data, especially if interferences are not identified correctly (Beres and Haeni, 1991).

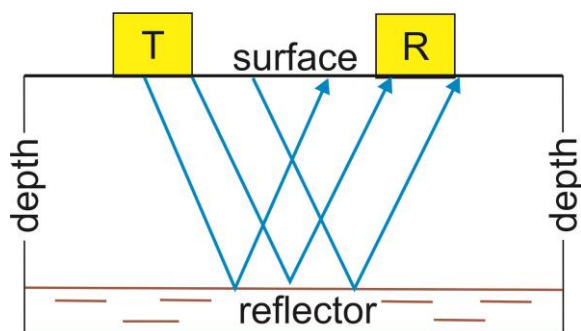


Fig. 3.1. Penetrating GPR signal in fine grain sediments. T: transformer, R: receiver.

A RAMAC/GPR system with a mean frequency of 50, 100 and 200 MHz was used in this study. The antenna separation distance was fixed at 1 m to obtain the antennae frequency of 100 MHz. This frequency allows a good penetration depth (10-20 m in ideal condition, e.g. low water table and low salinity), while still providing high-resolution images. The software Reflex W 2D/3D was used for processing the data. Different standard processing such as subtract DC shift, automatic static correction, gain function, band pass filtering and running average filter were used to provide a more realistic subsurface image. Lack of topographic mapping was a weak point of processing data. However, all the profiles were taken from flat or relatively surfaces with a dip of less than 10°.

3.3 Coring

Based on the location of study (e.g. coast, lagoon or marine), different coring systems were used to obtain the cores, including a gravity corer, a percussion corer (also known as vibra corer) and a Livingstone corer. A Garmin eTrex handheld GPS was used for locating all cores. A PVC pipe with an internal diameter of 5-7 cm was used as a core liner, and damp florist foams were placed both sides of the pipes in order to avoid both desiccation and sediment movement during transport to Brunel University London (UK). The PVC pipes for all the cores have the internal diameter of 5 cm, except offshore cores which have a PVC pipe with 7 cm internal diameter. The cores were stored in a cold room at 5°C, which provides darkness and coldness to prevent the oxidation of organic matter and re-equilibration under ambient conditions (such as modification of core length). All core sections were labelled and put in sealed plastic sleeves to avoid dehydration. A full identification number was used for labelling and as far as possible the core naming followed the following system: site, year of recovery, coring method, core number and section number. For example, “AL 11 L1-2” represents the second section of the core taken from location 1 using the Livingstone corer in 2011 from the Amirkola Lagoon. Subsequently, V (instead of L) in the identification number indicates that the core was taken by a percussion corer (vibra corer) and G by a gravity corer. Additionally, in some locations (using the percussion and the Livingstone corer), duplicated cores were obtained and in some situations three or four cores were taken from the same location. These parallel cores were used to cover gaps between the core sections; consequently, a continuous sequence (or a master sequence) was obtained. Therefore, in a sequence that was composed of several sections, an original depth was replaced by a composite depth which refers to the depth of a complete sequence. The other benefit of duplicated cores was to check the boundary between sedimentary facies and to increase the amount of samples for analysis. The identification numbers for duplicated cores contain A, B, C and D. For

example, ZL11L2A and ZL11L2B represent duplicated cores taken from location 2 by the Livingstone corer at 2011 from the Zibakenar Lagoon. Table 3.1 shows some examples of the identification numbers for the cores taken at different locations. In total, 113 m of sediments were retrieved during this study, and the list of the cores is presented in Appendix A.

Table 3.1. Examples of identification numbers for cores

Identification number	Site	Year of recovery	Coring method	Duplicated cores
KL11G1	Kiashahr Lagoon	2011	Gravity	
KL11P1	Kiashahr Lagoon	2011	Percussion	
ZL11G1	Zibakenar Lagoon	2011	Gravity	
ZL11L1D1	Zibakenar Lagoon	2011	Livingstone	*
105 13 V	GPR profile 105	2013	Percussion	
AAL13V	Astaneh water body	2013	Percussion	*
NSM14G1	Offshore in front of New Sefidrud	2014	Gravity	
LL13V	Langarud water body	2013	Percussion	*
AL11V	Outcrop near Amirkola	2011	Percussion	*

Following the field campaign, the cores were transported to Brunel University and stored in a dark cold room at 5°C, which provides darkness and coldness to prevent the oxidation of organic matter and re-equilibration under ambient conditions (such as modification of core length). Subsequently, each core was labelled in 2 cm intervals. After the core equilibrated to the ambient laboratory temperature (around 3 hours), the whole core was used for measuring magnetic susceptibility. Then, the cores were split lengthwise into working and archive halves. Both the working and archive halves were used for visual core description and photography. The samples were taken from the working half for sedimentology analysis, ¹⁴C dating, macro-fossil and pollen study, and the archived half was preserved and occasionally used for radionuclide dating. Finally, the core sections were wrapped in cling film and then in labelled water-proof plastic sleeves to prevent desiccation and transferred to the cold-storage space.

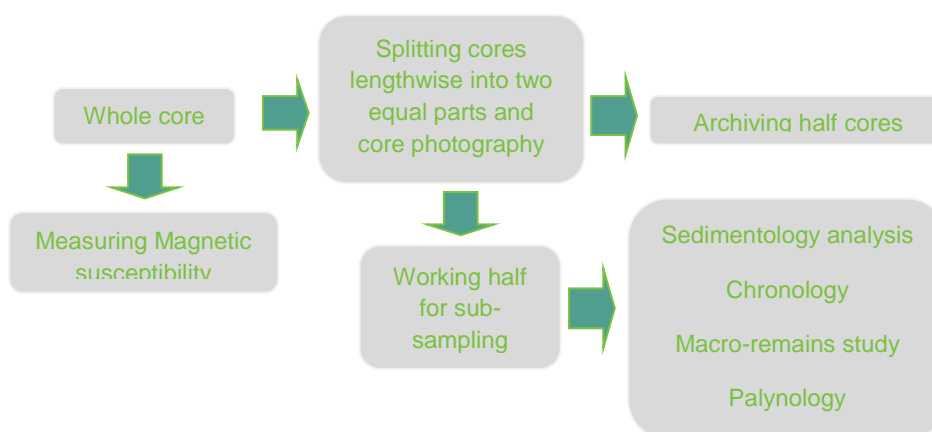


Fig. 3.2. Successive steps in core processing

Fourteen months after the second coring campaign, the accurate elevation of the coring locations of Langarud water body (LL13V), Astaneh water body (AAL13V) and AL13V sequence were surveyed by K. Kabiri (INIOAS) using a Leica Sprinter 150M Electronic Level in relation to bench marks in Langarud, Astaneh and Dastak towns.

3.3.1 Gravity corer

In this study, the gravity corer (KC small free fall corer, model 13.570) was used to obtain short cores (with a maximum length of one meter) from the modern lagoons using a fishing boat and two meter long cores from the marine part (onshore and offshore) using a ship. The corer body contained four lead weights and a corer tube with an internal diameter of 53 mm (Fig. 3.3). The weight of each lead weight was 2 kg and it was possible to increase the weight of the corer with a maximum of twenty four lead weights. The corer used its own mass to drive it through the sediments. Once the corer penetrated into the sediment, it was retrieved using an on-board winch installed on the cruise board. This means the depth of water for the marine survey was only limited by the length of cable on the winch. An orange peel closing system was placed inside of the corer tube to prevent the samples from exiting during the sample recovery. Using this type of small corer affords considerable saving in both time and effort (Glew, 1991); however, there was a limitation in the cores length, around 2 meters.

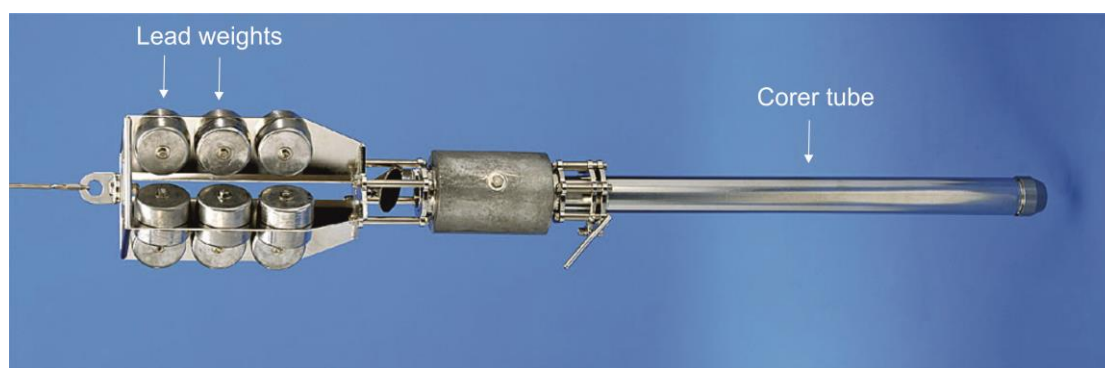


Fig. 3.3. KC small free fall corer (the gravity corer) photo: modified from the website: www.kc-denmark.dk

3.3.2 Percussion corer

The percussion corer (gasoline powered percussion hammer Cobra TT) (Fig. 3.4) was used in this study in order to take cores from land (inland water bodies, AL11V sequence and cores on GPR profiles). The percussion corer set contained a gasoline driven percussion hammer, a percussion gouge with an internal diameter of 55 mm, various extension rods and a mechanical rod puller. A PVC pipe was placed in the gouge and went into the ground using the power of gasoline percussion hammer (the left hand photo, Fig. 3.4). After the gouge was inserted into the ground, the extension rod was placed at the top

of gouge to assist in pulling it out. Subsequently, the mechanical rod puller was placed on top of this and the gouge was pulled out (the right hand photo, Fig. 3.4). Adding the extensions rods to this set made it possible to take core down to 12 meters; however, there was limitation in sandy sediments.



Fig. 3.4. Taking core from the land using the percussion corer (Photos: the Author). Left: going down. Right: extracting the core from the ground. Location: AAL13V, north of Astaneh Town.

3.3.3 Livingstone corer

The Livingstone-type drive rod piston corer (Livingstone, 1955) was used to collect cores from soft sediments of the modern lagoons. A drilling platform with a central working hole was required to take cores using the Livingstone corer. The purpose built platform was made from wood as a frame and polystyrene foam sheets as a body (Fig. 3.5), which provided a light weight. The platform was designed in three separate pieces, which made it portable and could be easily assembled in the field (Fig. 3.5). Sufficient positional stability during coring was obtained by anchoring the platform at its four corners.



Fig.3.5. Portable and light weight coring platform built to take cores in lagoons using the Livingstone corer. (Photos: the Author)

The Livingstone corer consists of a rod, a piston, a piston cable and a steel barrel. The piston is pulled into the barrel by the piston cable. When the bottom of the barrel reaches to the sediment surface, the piston cable is clamped, consequently, the piston is fixed in place, and the barrel is pushed down into the sediments by the rod (Fig. 3.6). Subsequently, the barrel is pulled out using the rod. A cling film is used to pack the sediments before keeping in a halved PVC pipe. The advantage of this corer is to take core sections from a required depth by fixing the piston cable; however, it requires calm weather to use the platform. Moreover, by using this corer, it is possible (but not necessarily) to continue at the same hole to take the second core section by fixing the piston cable.

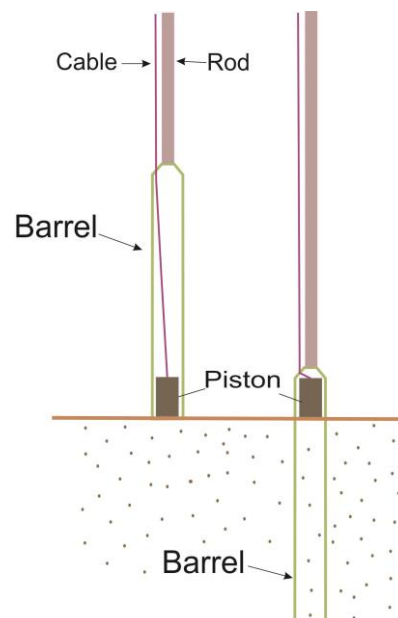


Fig.3.6. Schematic picture of the Livingstone corer, modified from Livingstone (1967).

3.4 Sedimentology

A multi-proxy approach combined with very carefully selected methods is essential in palaeo-environmental studies. It allows comparing different proxies to see the extent of their response to environmental changes, and provides a wider overview of the palaeo-

environmental conditions than could be obtained from a single proxy (Birks and Birks, 2006). Comparing different proxies allows exploiting the strengths and identifying the weaknesses of each proxy (Mann, 2002). In this study sedimentology analyses (including magnetic susceptibility, core photography, visual description, loss on ignition, and grain size analysis), chronology, macro-remains and palynological analyses were used to investigate the evolution of the Sefidrud delta through time. All the sedimentology analyses were performed in the sediment laboratory, Environmental Science, Brunel University London.

3.4.1 Magnetic susceptibility

In a very low inducing magnetic field, the magnetic susceptibility (MS) of a sample is given by the ratio of induced (temporary) magnetization and acquired magnetisation by the sample and therefore is a function of the concentration and composition of the material in a sample (Crick et al., 1997; Ellwood et al., 2000; Crick et al., 2001).

Five different kinds of magnetic behaviour have been recognised. The first group is ferromagnetism, which covers the most highly magnetic substances, like pure iron. These substances have a very high magnetic susceptibility, but will not normally be found in the environment. The most important category of magnetic behaviour in natural materials is ferrimagnetism. This second category includes magnetite and a few other Fe-bearing minerals with high MS values. Lower MS values are obtained for 'canted antiferromagnetic' such as haematite. All metals and minerals in these three magnetic groups are able to remain magnetised in the absence of a magnetic field. Similar or weaker MS values are obtained for a fourth group of minerals with the property of 'paramagnetism'. The minerals in this group are able to remain magnetised only in the presence of a magnetic field. Examples are biotite and pyrite. Finally, the last group is 'diamagnetism' which produce weak or even negative values of magnetic susceptibility. Materials which fall into this group include many minerals which do not contain iron, like quartz and calcium carbonate. Other non-mineral diamagnetic substances are organic matter and water. Therefore, the MS of an environmental material is the sum of all the magnetic susceptibilities of the ferrimagnetic, canted antiferromagnetic and paramagnetic minerals and diamagnetic components. Normally, the diamagnetic component is negative and very weak relative to the sum of the other three and can be ignored. Exceptions to this are where the sample is almost all water, quartz or organic matter (Dearing, 1999).

The main controlling factors on MS include weathering, erosion and sediment accumulation rate and biological productivity. These factors are tied to climate, tectonic and volcanic processes, availability of nutrients and sea level changes (Crick et al., 1997;

Ellwood et al., 2000; Crick et al., 2001). Secondary processes including diagenesis also can affect the MS amount in the sediments by sulphate reducing (Garcia-Alcalde et al., 2012). Therefore, MS can indicate palaeo-environmental changes in oceanic (Bloemendal, 1993; Robinson et al., 1995) and terrestrial settings (Heller et al., 1993; Maher et al., 1994; Hounslow and Maher, 1999). Also, peaks in MS can be corresponded to horizons with high heavy mineral concentrations (Thompson, 1986).

MS measurements have many uses in Quaternary studies and can be quickly and easily measured on the samples with a little expense. It is a non-destructive technique that leaves the core available for more proxy analysis (Thompson, 1986). The MS measurements reported in this study were performed using the Bartington MS2C core logging sensor (Fig. 3.7) at 2 cm intervals.



Fig.3.7. Bartington magnetometer MS2C core logging sensor (photo: www.bartington.com)

MS is an indicator of depositional environments and may vary considerably with particle size and sediment origin (Thompson and Morton, 1979; Yim et al., 2004). MS also can be used for correlation between individual cores where correlation between cores is unclear, because of the lack of distinct bedding (Thompson, 1986). MS in this study was used to propose an intra-lagoonal correlation between the cores and also as an indicator of depositional sedimentary environment.

3.4.2 Core photography

High quality photographs of cores can be used to image and archive sedimentological changes of the sequences, also to capture the sediments colour before oxidization of the sediment surface takes place. Consequently, after core splitting, the sediment surface was smoothed with a metal blade and photographs were taken immediately.

The core (the archive and the working halves), a ruler, an arrow showing the top direction and a colour chart were positioned on a black fabric under a high quality camera: Nikon D 7000, 16.2 effective megapixels, with 16-85 mm lens and high-speed image

processing. The cores were photographed a whole core at a time. Also, close-up photographs were taken every 25 centimetres. These images contain a Jessops colour chart; therefore, they may be manipulated to obtain the true colour of the sediments.

3.4.3 Visual description

Core descriptions immediately provide an impression of the sediment and help to understand depositional environment. Furthermore, core descriptions are an appropriate way for correlations and comparisons between equivalent sections from different locations (Tucker, 2003). A standard visual core description was performed on both the working and the archive halves immediately after photography. An ODP (Ocean Drilling Programme) standard barrel-sheet format using symbols (Mazzullo et al., 1988) was used to document visual description. The description contained graphic log, grain size, colour, fossil content, bioturbation, physical structures, type of contacts (e.g. sharp or gradual) and coring disturbance. Descriptive terms for bed and lamina was used based on terminology given by Tucker (2003) (Table 3.2). The grain size written in visual description was first based on the visual estimation. It is usually possible to distinguish between sand and finer sediments (silt and clay). For finer sediments, a tiny piece of the sediment was touched between fingers: silt material feels gritty between the fingers compared with clay, which feels smooth (Tucker, 2003). For accurate work, the visual grain size was then compared with the result of a grain size analyser and corrected as required. Sediment colour was determined by placing a Munsell Soil Colour Chart over the sediment and finding the best match.

Table 3.2. Terminology used to describe bed thickness from Tucker (2003).

1 m	very thickly bedded

0.3 m	thickly bedded

0.1 m	medium bedded

30 mm	thinly bedded

10 mm	very thinly bedded

3 mm	thickly laminated

	thinly laminated

3.4.4 Loss on ignition (LOI)

Available time and budget restrictions required a simple, cheap and reliable method to determine organic matter and carbonate contents. Loss on ignition (LOI) is a simple and widely used method for determination of organic matter (OM) and calcium carbonate (CaCO₃) (Dean, 1974, 1999; Korsman et al., 1999; Heiri et al., 2001; Beaudoin, 2003). One of the goals was to estimate the capacity of the environment to produce and store

carbon. The sampling spacing was 4 cm in clay and silt layers and 10 cm in sand layers. In case of any rapid change in colour and size, the sampling spacing was reduced and more samples were taken.

The process for LOI was as follows (Heiri et al., 2001) (Fig. 3.8):

(1) Dry the sample 12-24 h at 105°C. Calculate water content (LOI 105) as follows:

$$LOI_{105} = 100 (WS - DW_{105}) / WS$$

WS is the weight of the wet sample and DW_{105} is the dry weight of the sample heated at 105°C.

(2) Burn the sample at 550°C for 4 h. Calculate organic matter (LOI₅₅₀) as follows:

$$LOI_{550} = 100 (DW_{105} - DW_{550}) / DW_{105}$$

DW_{550} is the weight of the sample after heating at 550°C.

(3) Heat the sample at 950°C for 2 h. Calculate carbonate content (LOI₉₅₀) as follows:

$$LOI_{950} = 100 (DW_{550} - DW_{950}) / DW_{550}$$

DW_{950} is the weight of the sample after heating at 950°C.

The remaining sample after heating at 950°C is the residuum (LOI_{res}).

$$LOI_{550} + LOI_{950} + LOI_{res} = 100\%$$



Fig. 3.8. LOI process in order to measure water content, calcium carbonate and organic matter

Due to a time gap between the determination of the LOI and the sampling in the field, there is a risk of moisture loss. Therefore, water content of the sample at the time of measurement might be slightly different from the real water content at the time of sampling.

3.4.5 Grain size analysis

Grain size analysis provides important evidence of transport history and depositional environment (Folk and Ward, 1957; Tucker, 2003). Indeed, the particle size distribution of

sediment can provide indications of the energy condition and transport mechanism affecting the depositional environment. In fact, grain size analyses provide important evidence of depositional conditions (Folk and Ward, 1957) and together with MS reflect physical condition of depositional environment (Oldfield, 1991; Bloemendal et al., 1992). Therefore, particle size distribution is a valuable tool in the study of past depositional environments within delta settings, assisting in the identification of both long-term changes related to the evolution of the delta and in the identification of specific sub-environments (Dark and Allen, 2005).

The grain size was determined using a CILAS 1180 particle size analyser on homogenised and representative subsamples. The CILAS 1180 provides a measurement range from 0.04 to 2,500 μm . The cores were sub-sampled for grain size analyses and samples were chosen from different facies and in a different resolution along the sequence in order to cover the entire depositional environments and to obtain a representative grain size column. For some of the sequences, sub-sampling was performed every 1 cm in case of abrupt changes in grain size, while in the sandy sequences the samples were taken every 10 cm or more. A preparation was required before measuring the size. Initially, about 0.5 g of the sample was soaked in 10 ml of 10% tetra-sodium pyrophosphate solution and twenty seconds of ultrasound were used to prevent flocculation. If the samples contained plant materials and roots, the organic matter needs to be destroyed; therefore, the measured size represents the size of the sediment grains. The procedure suggested by Lewis and Mcconchie (1994) was used for organic matter oxidation. 5 cc (10 cc for each gram) peroxide hydrogen (H_2O_2) was added to the sample and left for 24 h. After 24 h, 1.5 cc (around 1/3 of the first time) H_2O_2 was added to the sample and left for 24 h. To make sure that the entire organic matter was destroyed, for the third time, 1.5 cc H_2O_2 was added to the sample and left for another 24 h. At this stage the samples were placed in 10% tetra-sodium pyrophosphate solution. Then, the samples were added to CILAS and grain size was measured using Size Expert software, offered by CILAS. Background measurements and rinsing were performed in between each sample measurement to keep the results consistent and reliable. Granulometric data were processed using the GRADISTAT program (Blott and Pye, 2001). The sand–silt–clay triangular diagram proposed by Folk (1974) was used for naming the textural group of the sediments (Fig. 3.9). In addition, the particle size results have been presented in a 3D plot using MATLAB software version 7.1 to highlight detailed changes over depth. The benefit of this plot is that it presents three variables on one graph: volume (%), grain size and depth.

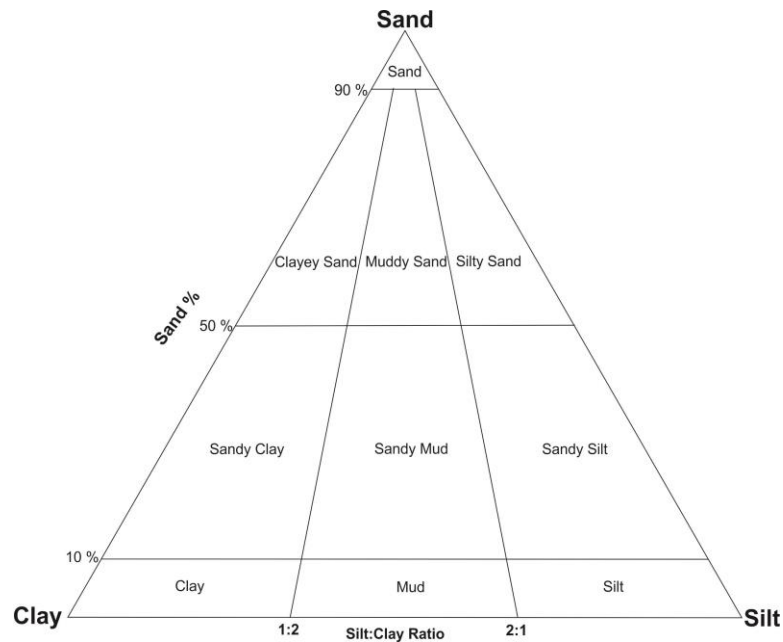


Fig. 3.9. Sand-silt-clay triangular diagram from Folk (1974) used for naming the textural group of the sediments.

The statistical parameters such as the mean (the average size), the sorting (the spread of the sizes around the average), the skewness (the symmetry or the preferential spread) and the kurtosis (the degree of concentration of the grains relative to the average) were calculated using the GRADISTAT programme based on a method suggested by Folk and Ward (1957). However, most of the analysed samples were polymodal and these terms are inappropriate since the distribution is not unimodal (Tucker, 2003). Indeed, grain size statistical parameters cannot be used as environmental indicators given that the grain size component in polymodal sediments reflects different transportation or depositional processes (Sun et al., 2002).

3.5 Chronology

A variety of direct and indirect tools have been used for dating samples. Radionuclide analyses were made on ZL11L2A sequence (Zibakenar Lagoon) and NSM14G3 (Offshore core) at the Environmental Change Research Centre, University College London, by Dr H. Yang and at laboratory of Modane in the French Alps, by Mr J. Reyss, respectively.

Moreover, radiocarbon dates were obtained on plant remains and shells from various sequences at the Chrono Centre, Queen's University of Belfast and Australian Nuclear Science and Technology Organisation (ANSTO). Radiocarbon ages younger than AD 1950 (modern ages) were calibrated using the CALIBomb programme (Reimer et al., 2004) with the Northern Hemisphere zone 2 calibration dataset (Hua et al., 2013). The date older than AD 1950 was calibrated using the CALIB programme version 7.1 (Stuiver and Reimer, 1993) with the IntCal13 and Marine13 calibration curve, for the wood and shell samples, respectively (Reimer et al., 2013).

As part of the indirect dating tools, spheroidal carbonaceous fly-ash particles (SCPs), unambiguous indicators of industrial fossil-fuel combustion, were performed at University College London on the ZL11L2A sequence (Zibakenar Lagoon) to identify recent sediments. The occurrences of plant (*Eucalyptus* and *Azolla filiculoides*) and bivalve (*Abra* cf. *segmentum*) species recently introduced by people were also exploited and used as indirect dating tools.

3.5.1 Radiocarbon dating

The Earth's atmosphere contains various isotopes of carbon, ^{12}C and ^{13}C which are stable and unstable isotope ^{14}C or radiocarbon. Through photosynthesis, plants absorb both forms from carbon dioxide in the atmosphere. When an organism dies, it contains the standard ratio of ^{14}C to ^{12}C , but as the ^{14}C decays with no possibility of replacement, the proportion of carbon 14 decreases at a known constant rate. The time taken for it to reduce by half is known as the half-life, which is 5730 years for ^{14}C . The measurement of the remaining proportion of ^{14}C in organic matter thus gives an estimate of its age (a raw radiocarbon age). However, over time, small fluctuations occur in the ratio of ^{14}C to ^{12}C in the atmosphere, fluctuations that have been noted in natural records of the past. The records require "calibration" of the raw radiocarbon age, to reach a more accurate estimate of the age, which is a calendar date of the material (Hua, 2009).

Radiocarbon samples which obtain their carbon from a different source (reservoir) than atmospheric carbon may yield too old apparent ages, which is caused both by the delay in exchange rates between atmospheric CO_2 and ocean bicarbonate, and the dilution effect caused by the mixing of surface waters with upwelled deep waters, which are very old (Mangerud, 1972). Therefore, a reservoir correction must be made to any conventional shell or plants that have obtained their C from water with old C, to account for this difference. However, various reservoir effects for the Caspian Sea may be found to correct radiocarbon dates, which range from 290 to 440 years with: 383 yr in Leroy et al. (2007), 290 yr in Kroonenberg et al. (2007), 390-440 yr in Kuzmin et al. (2007) and 345-384 yr in Karpychev (1993) (see Leroy et al., 2011). Because of these problems, finding terrestrial plant remains, like charcoal or wood sample, was essential; as they are believed to provide more accurate ages.

Atmospheric nuclear weapons testing doubled the amount of radiocarbon in the atmosphere in the late 1950 and early 1960 and can be used to provide age information (Reimer et al., 2004). Comparison of atmospheric $^{14}\text{CO}_2$ records indicates that the distribution of post-bomb ^{14}C was not nearly uniform as pre-bomb ^{14}C . In addition, CO_2 from fossil fuel is non-uniformly distributed and can be a substantial contribution of

carbon to a sample. In the tropics, ^{14}C -enriched CO_2 released from the terrestrial biosphere may result in slightly higher ^{14}C levels compared to mid-Northern Hemispheric in recent decades. Therefore, a regional, or even local, atmospheric ^{14}C data set is ideal for calibration of a post-bomb ^{14}C measurement (Reimer et al., 2004). The programme CaliBomb was used to calibrate the post-bomb dating results in the SCB area, which allows selecting calibration data set (Reimer et al., 2004).

3.5.2 Radionuclide dating

The implemented radionuclides include ^{210}Pb (half-life = 22.3 year), a naturally-produced radionuclide derived from atmospheric fallout (termed unsupported ^{210}Pb), ^{137}Cs (half-life = 30 years) and ^{241}Am (half-life = 432.2 years), artificially produced radionuclides introduced to the study area by atmospheric fallout from 1950s nuclear weapons testing.

The isotope ^{210}Pb (half-life of 22.3 years) is a naturally-produced radionuclide, decayed from radioactive gas radon (^{222}Rn). The ^{210}Pb dating is based on the escape of radon from the surface of soil to the atmosphere, returns to the surface soil or water reservoirs as solid fallout. Part of ^{210}Pb activity coming from the fallout and absorbed in the surface sediments is called excess. Because of the decay, the excess ^{210}Pb in each sediment layer declines with its age. Therefore, by studying the remaining lead as a function of the depth, the period since the lead was deposited can be determined and, thereby, the sediment accumulation rate (Olsson, 1986). If the erosive processes in the catchment are steady, and give rise to a constant rate of sediment accumulation, it is reasonable to suppose every sediment layer will have the same initial excess ^{210}Pb . Therefore, this model implies a constant sedimentation rate. But in many cases the rates of erosion and sedimentation vary during the time and ^{210}Pb profile will be non-linear. The constant rate of supply (CRS) model assumes that there is a constant fallout of ^{210}Pb from the atmosphere, resulting in a constant rate of supply of ^{210}Pb to the sediments irrespective of any variations which may have occurred in the sediment accumulation rate (Lubis, 2013). This model takes it into account that there is always a variable sedimentation, i.e. sedimentation rates vary with depth. Modelling by CRS requires a thorough knowledge of the bulk density variation with depth. The density of the wet sediment was measured using a 4 cm^3 capacity vial and a balance scale weight with 4 decimal places. The clean vial was weighed empty, then carefully filled with wet sediment. Any air bubbles were removed by tapping the base of the vial on a firm surface and the surface of the sediments was smoothed to be level with the edge of the vial. The vial was then re-weighed and the weight of the sediment divided by 4 to determine the density as gram per cm^3 :

$$\text{Bulk density} = \frac{(\text{the weight of vial+sample}) - (\text{the weight of vial})}{\text{ml fresh sample}} \text{ g/cm}^3$$

¹³⁷Cs and ²⁴¹Am are man-made radionuclides, introduced by atmospheric fallout from nuclear weapons testing and nuclear reactor accidents. They have been extensively used in the dating of recent sediments and the reliability of the ¹³⁷Cs method has been demonstrated in a large number of studies of lacustrine environments, whether sediment accumulation rates are uniform or non-uniform (Arnaud et al., 2006). ¹³⁷Cs has been detectable since 1945 and reached to its maximum in 1963. Therefore, it can be used for dating. ²⁴¹Am also been detected in recent sediments (Olsson, 1986).

3.5.3 Spheroidal carbonaceous fly-ash particles (SCPs)

Spheroidal carbonaceous fly-ash particles (SCPs) analyses were performed on core ZL11L2A (Zibakenar Lagoon) by Professor N. Rose at University College of London. SCPs were used as age-equivalent stratigraphic markers to compare with the result of radionuclide dating for core ZL11L2A. SCPs are a component of fly-ash and formed by the incomplete high-temperature burning of fossil fuels and are therefore indicators of atmospheric deposition from industrial sources including power generation (Griffin and Goldberg, 1983; Wik and Renberg, 1991; Rose, 1994; Rose et al. 1995).

Three marked features of SCP profiles are including:

- The start of the record (mid-nineteenth century)
- The start of the rapid increase in concentration following the Second World War (mid-twentieth century)
- The peak in SCP concentration (late-twentieth century) (Swindles, 2010)

Therefore, a rapid increase in SCPs accumulation rate at 1950 ± 5 years may also be used to compare with the radiometric chronology (Renberg and Wik, 1984, 1985; Rose et al., 1995, 2003). SCP extraction from sediments followed Rose (1994), while SCP identification used standard criteria (Rose, 2008).

3.6 Macro-remains analysis

The nature of the macrofossils and other macro-remains provides further evidence of the conditions under which the sediments have been deposited. Indeed, in a specific ecological place, only certain organisms live due to enhanced or reduced salinity. In this regard, macrofossils have been widely used by Quaternary scientists to reconstruct and understand past environments (Huntley et al., 1993). Macrofossils are proxies used to reconstruct a small local environment, as they are not transported far from where they grow (Cordova et al., 2009). However, macrofossil analysis has some weaknesses. For

example, sometimes the concentration of fossils might be too low for reliable statistics (Birks, 2001). Here we also counted plants, animals and minerals. Hence we used the term macro-remains. Macro-remain analyses were performed at Environmental Science, Brunel University London. Identification of bivalves and gastropods species was performed by Dr F. Wesselingh, Naturalis Biodiversity Centre, Netherlands.

Following Birks (2001), sub-samples with a weight of 15-20 g were taken at regular 4 cm intervals. The samples were soaked in 10% tetra-sodium pyrophosphate solution to prevent sediment flocculation. The samples were then washed through a column of sieves with a mesh diameter of 500, 125 and 53 μm . The finest fraction (e.g. 53 μm) was used to retrieve small foraminifera (Leroy et al., 2013b). The residue of each sieve was transferred to a plastic tube and soaked in water. The sample residues were distributed in a Petri dish in 2-3 mm depth of water and studied using a stereo-microscope, Olympus SZX12. All the samples were scanned, macrofossil and remains were identified and the percentages of each macro-remains were estimated for each sample. In the next step, some of the samples were selected and macrofossils and remains counted carefully. In most of the samples, all the materials were counted, but in some of the samples, where there were a large amount of materials, a portion of the sample was counted carefully and a total was estimated from it. The results were presented in percentage and concentration diagrams using Psimpoll software, version 4.27 (Bennett, 2007). Sum in percentages diagram represent the total number of counted objects and concentration/10 g shows the number of counted objects in 10 g. A zonation by CONISS after square root transformation of the percentages was applied.

The mineralogy of the minerals found in macro-remains was checked either by X-ray diffraction (XRD) or by dissolution in HCl. XRD analysis was carried out at the Experimental Techniques Centre (ETC), Brunel University London, using a Bruker D8 Advance equipped with a Lynx-eye position-sensitive detector.

3.7 Palynology

The palynological contents of the sediments are considered as a valuable approach for reconstructing past environments (Bennett and Willis, 2001). Palynology analyses were performed by Professor S. Leroy on the sequences ZL11L2, AL11V3, AAL3V and LL13V. Sections of palynology for these sequences are written by Professor Leroy. The samples were treated with 10% tetra-sodium pyrophosphate solution to prevent flocculation of the sediments. Then, the samples were treated with hydrochloric acid (first at 10% and then pure), hydrofluoric acid (32%), followed by a repeated hydrochloric acid treatment. In the next step, the samples were sieved through 120 and 10 μm meshes.

Finally, the residues were mounted on glass slides in glycerol. A light microscope at x400 magnification and at x1000 for special identification was used to count the palynomorphs. The addition of *Lycopodium* tablets allowed the estimation of concentrations (in number of palynomorphs per ml of wet sediment). The pollen atlas and reference collection at the Brunel University were used to identify the spores and pollen grains (Leroy et al., 2009; 2013a). The dinocysts were identified using the taxonomy developed by Marret et al. (2004). Percentages were calculated, and the diagrams were plotted using the psimpoll software, version 4.27 (Bennett, 2007). A zonation by cluster analysis (CONISS) after square root transformation of the percentage data was applied.

4 Results

4.1 Remotely sensed data

The earliest detailed outline and architecture of the New Sefidrud Delta prism was extracted from the aerial photograph of the year 1955 (Fig. 4.1 A). Kousari (1986) made the first classification that we largely follow here. However, an abandoned channel to the west of Sefidrud was considered as a sand spit by Kousari (1986). Moreover, we were unable to confirm the interpretation of a new sand barrier recognised by Kousari (1986) in front of the Ushmak River. Figures 4.1 B and C show the evolution of the delta in the years 1964 and 1982. We did not have access to the original photographs from these two years, but we modified some of Kousari's (1986) interpretations as follows. A feature in the Ushmak Lagoon was recognised by Kousari (1986) from aerial photographs of 1964 and 1982, and was classified as a sand barrier. However, based on the shape of this feature, the presence of sand spits on its two sides and present-day satellite photos, we consider it likely that this feature was a coastal lagoon at this time point. Moreover, this coastal lagoon is clearly recognisable at this site in the satellite image from the years 1991 and 2014 (Fig. 4.1 D and E). In Kazancı and Gulbabazadeh (2013) neither Zibakenar nor Ushmak Lagoons were plotted for the year 1964, and Zibakenar Lagoon does not appear on the map until 1982. Contrary to the situation for the Zibakenar Lagoon, all studies agree that the Kiashahr Lagoon started to form in 1955.

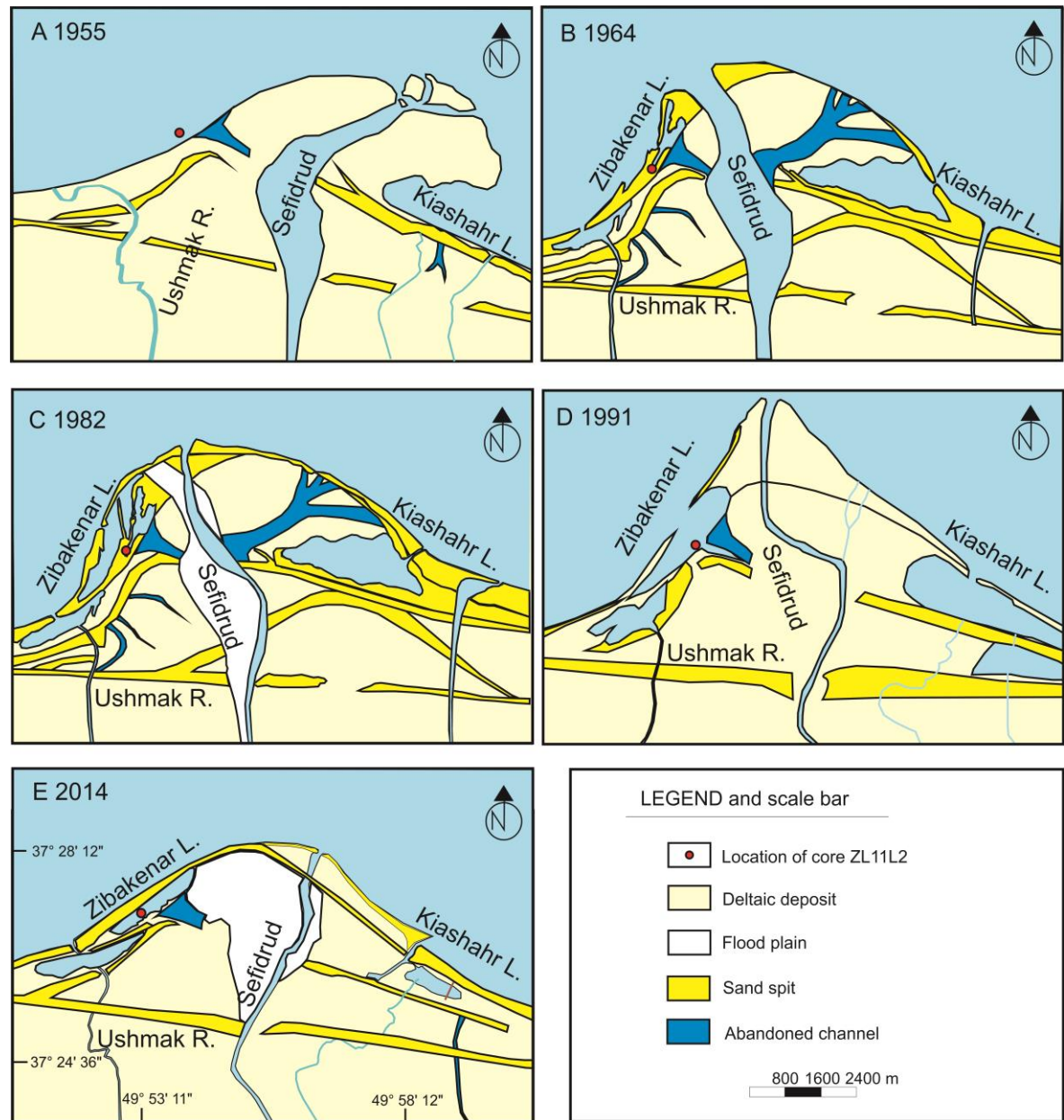


Fig. 4.1. Evolution of the new Sefidrud Delta since 1955, based on historical aerial photographs (A, B and C) and satellite images (D and E). Fig. 4.1 B and C after Kousari (1986) with modifications.

4.2 GPR profiles and sedimentary facies

Seven GPR profiles were taken from the coastal deposition of the Sefidrud delta in four locations (i.e. A, B, C and D in Fig. 4.2). The maximum penetration depth of the GPR signals varies in different profiles and generally is up to 4 m. In order to interpret depositional environments and to link the GPR results with sedimentological data, one core was collected along each radar profile (Fig. 4.2, Table 1, Appendix A). Visual description, grain size analysis and magnetic susceptibility were performed on the sequences.

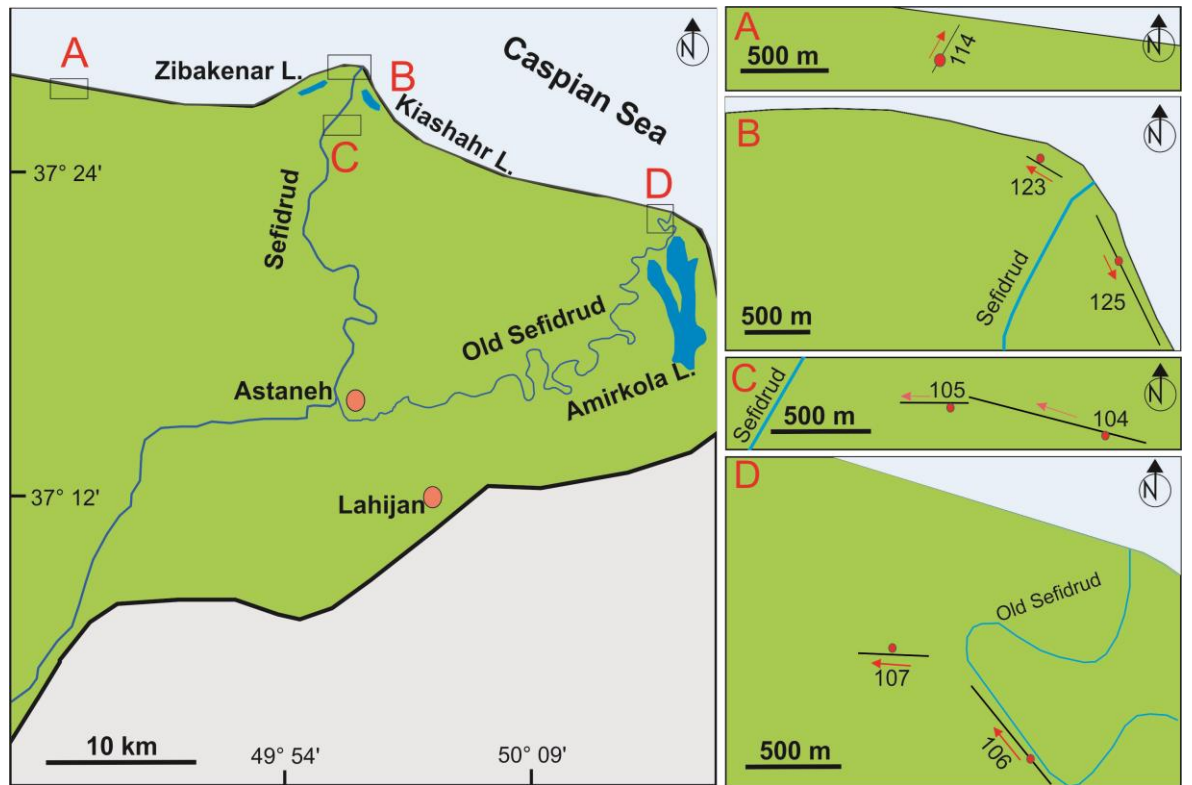


Fig. 4.2. The location of GPR profiles (black lines) and cores on the GPR profiles (red dots)

GPR profiles from Location A, B and C were taken from the saturated sand sediments. Vertical resolution of the profiles is considered to be one-quarter of the wave-length of the radar signal in the grounds (Reynolds, 1977). Wavelength is a function of both antenna frequency and the velocity of the radar signal through the ground (Bristow, 2009). The velocity of the radar signal for saturated sand is 0.06 m/ns. A 100 MHz transmitter has a pulse period of 10 ns and in saturated sand where velocity is 0.06 m/ns, the wavelength will be 0.6 m and the resolution will be one quarter on the wavelength or 0.15 m (i.e. $0.6 \text{ m} \times 0.25 = 0.15 \text{ m}$). GPR profiles from location D were taken from silt sediments. The velocity of radar signal for saturated silt is 0.07 m/ns and therefore the resolution will be 0.175 m (i.e. $0.7 \text{ m} \times 0.25 = 0.175 \text{ m}$). Vertical resolution has important implications for its sedimentological interpretation, because it will determine the scale of sedimentary structure that can be observed (Neal, 2004; Bristow, 2009). Therefore, in this study, the strata with a minimum thickness of 15 cm in sand and 17.5 cm in silt will be recognisable in the GPR profiles.

4.2.1 Location A

One GPR profile (profile 114) was taken from this location. The seaward profile 114 is presented in Fig. 4.2.

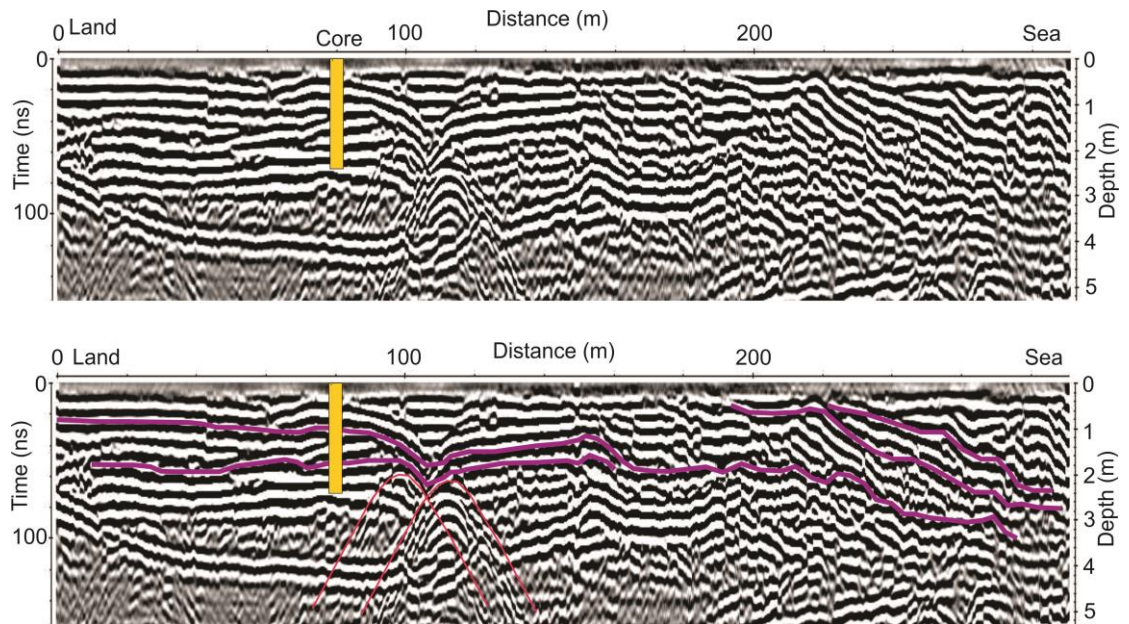


Fig. 4.3. GPR profile 114 from the east of Sefidrud Delta (location A in Fig. 4.2). The upper image is the original profile and the lower profile is the interpreted profile.

The penetration depth of the GPR signal is up to 3 m. Diffraction hyperbolae in this profile are due to presence of utility pole across the profile (red lines in Fig. 4.3). They can be used to calculate the velocity of radar waves using curve matching (Bristow et al., 2009). Based on this, the velocity of radar waves is 0.3 m/ns. Therefore, the wavelength and resolution will be 3 m and 0.75 m, respectively. As a result, only the strata with a minimum thickness of 75 cm can be recognised in this profile. The profile shows seaward dipping planar bedding with an angle of $\sim 25^\circ$ towards the sea, which is a diagnostic feature of beach-face sediments (Lindhorst et al., 2008).

A core was taken at 80 m distance from the starting point of the profile (Fig. 4.3). Fig. 4.4 shows sedimentary facies, grain size results and MS of core taken from profile 114. The sedimentology of the sequence from the bottom to the top is:

Sz1, 287-281 cm: black organic rich sediments with a sharp boundary with the following layer.

Sz2, 281-180 cm: dark yellowish brown silty sand with shell fragments, belonging to *C. glaucum* shells, and a layer of sand at 210-208 cm

Sz3, 180-11 cm: dark yellowish brown sand with gradual boundary with the lower and upper layers.

Sz4, 11-0 cm: dark brown silty sand with rootlets

From grain size results, it can be observed that the sequence is mostly dominated by sand, with maximum 30% silt and 1% of clay.

The magnetic susceptibility of the sequence shows a major variation along the core. The lower part (287-180 cm) stays constant, except one peak at 209 cm. However, the middle part contains several peaks with a maximum of 30 at 130 cm. The upper part also shows a constant value along the sequence (Fig. 4.4).

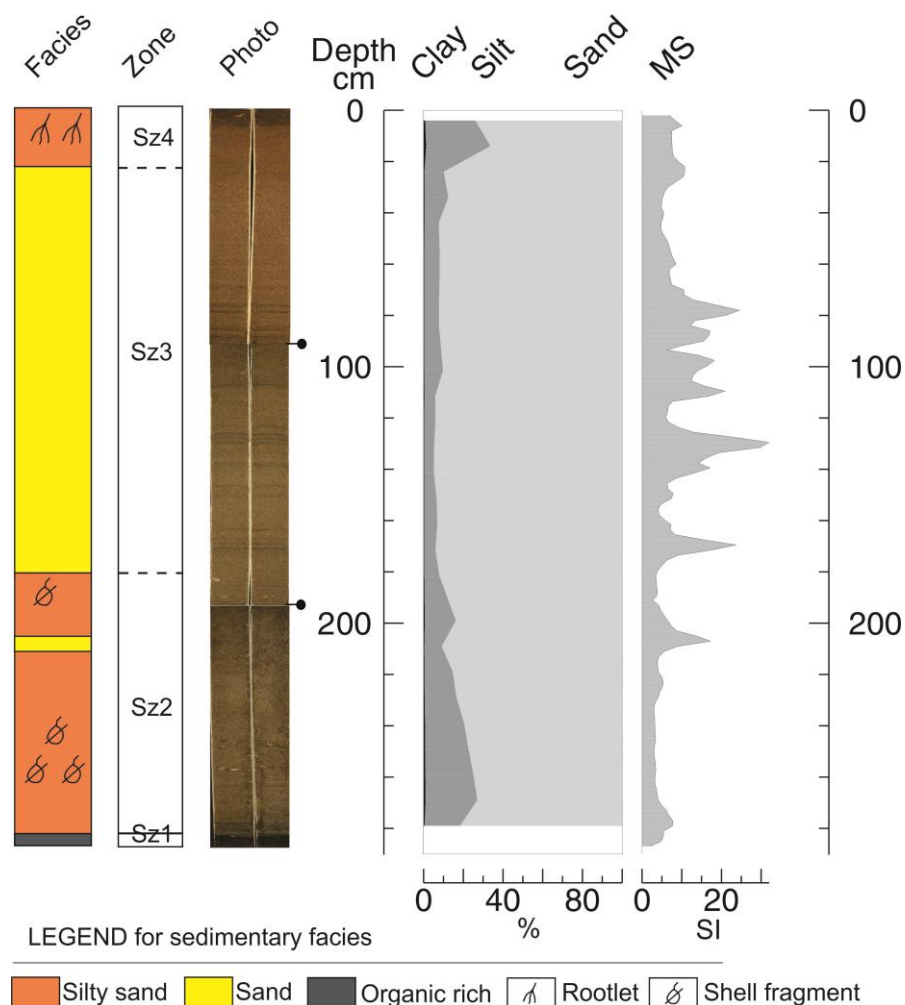


Fig. 4.4. Sedimentary log for the core 114, displaying sedimentary facies, sedimentary zones, core photo, grain size (clay, silt and sand) and magnetic susceptibility (MS). The black pin symbols show the core section limits.

4.2.2 Location B

Two GPR profiles including profile 123 and 125 were taken from this location. All these profiles are taken from coastal saturated sand. Profile 123 was retrieved from the west of Sefidrud and profile 125 from the east of the river (Fig. 4.2)

Profile 123

The penetration depth of the GPR signal in this profile is up to 4 m. This profile is characterized by gently dipping sigmoidal strata towards east, having a maximum dip angle of 10°. The sigmoidal shape of the internal pattern suggests a prograding deltaic system, building out into the Caspian Sea from the west to the east (Fig. 4.5).

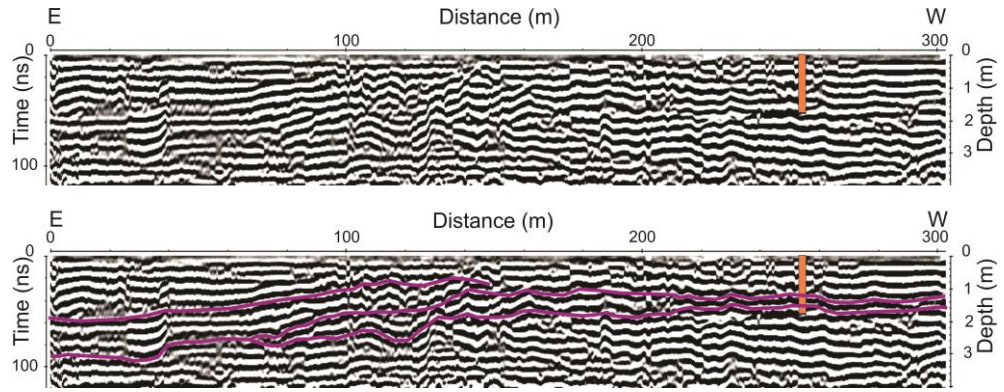


Fig. 4.5. GPR profile 123 from the west of Sefidrud Delta, next to Sefidrud River (location B in Fig. 4.2).

The upper image is the original profile and the lower profile is the interpreted profile.

A 171 cm long core was taken from the profile 123 (Fig. 4.5). Fig. 4.6 shows sedimentary facies, grain size results and MS of core taken from profile 114. The sedimentology of the sequence is very homogenous: brown silty sand consisting rootlets at the top 10 cm and a two cm thick layer of organic rich at the bottom. An obvious coarsening-upward trend was observed at the bottom of the sequence, at a depth of 140 cm. However, this trend is not recognisable in the clay, silt, sand diagram (Fig. 4.6). The grain size results shows that the sequence is mostly dominated by sand, with maximum 40% silt at the top and less than 1% of clay. Therefore, sand is split to very fine and fine sand, and medium sand. A coarsening-upward trend can be observed at the depth of 140 cm in this diagram (Fig. 4.6). The magnetic susceptibility of the sequence stays constant along the sequence with two major peaks in the middle of sequence with a value of 33 (Fig. 4.6).

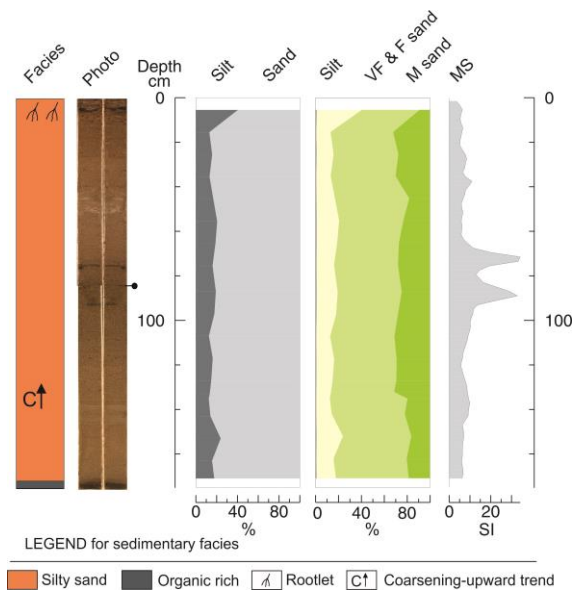


Fig. 4.6. Sedimentary log for the core 123, displaying sedimentary facies, core photo, grain size (silt and sand, VF: very fine, F: fine and M: medium) and magnetic susceptibility (MS). The black pin symbols show the core section limits.

Profile 125

The penetration depth of the GPR signal in this profile is up to 4 m. The sigmoidal shape feature is the only observed pattern in this profile which suggests a prograding deltaic system (Fig. 4.7).

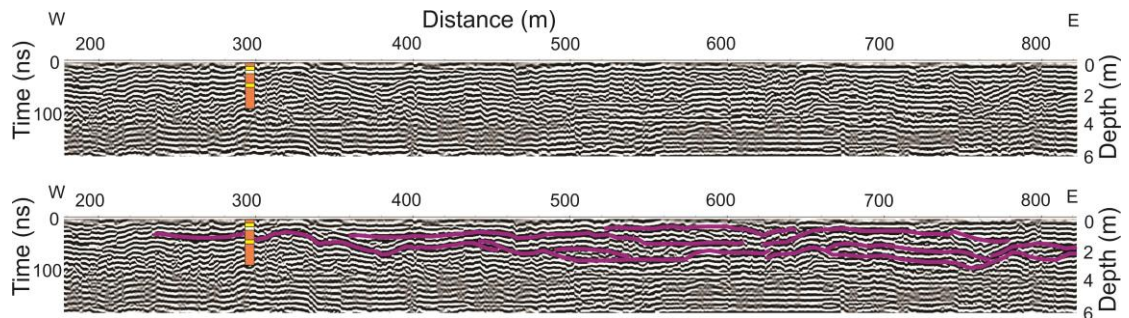


Fig. 4.7. GPR profile 125 from the East of Sefidrud Delta, next to Sefidrud River (location B in Fig. 4.2). the upper image is the original profile and the lower profile is the interpreted profile.

A 278 cm long core was taken from the profile 125 (Fig. 4.7). The sequence is very homogenous in terms of sedimentology: brown to very dark brown silty with a layer of yellowish brown silt at 60-51 cm. The grain size results shows that the sequence is mostly dominated by sand, with a peak of silt at 56 cm with up to 98% silt (Fig. 4.8). The MS indicates a background of 5 along the core with three major peaks at a depth of 128, 36 and 6 cm with a value of 45, 22 and 75, respectively (Fig. 4.8).

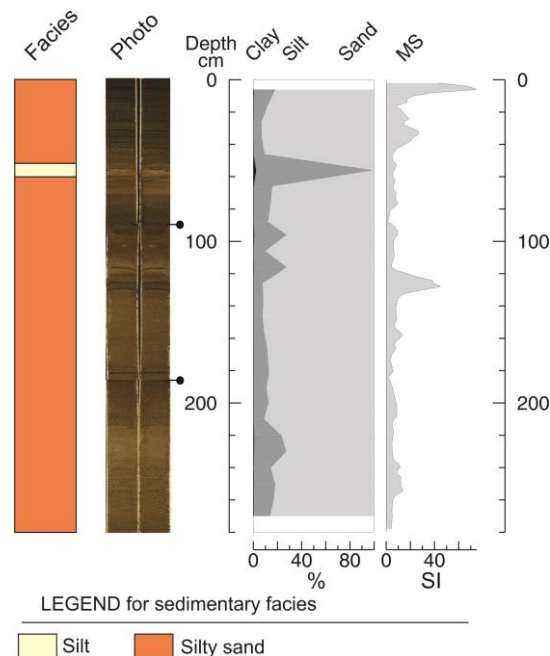


Fig. 4.8. Sedimentary log for the core 125, displaying sedimentary facies, core photo, grain size (clay, silt and sand) and magnetic susceptibility (MS). The black pin symbols show the core section limits.

4.2.3 Location C

Profiles 104 and 105 were collected from location C, near to Kiashahr Town, where the palaeo-beach is located.

Profile 104

The 920 m long profile was taken from east to west and the penetration depth of the GPR signal in this profile is up to 4 m. The clinoforms in this profile represents delta progrades from east to west (Fig. 4.9).

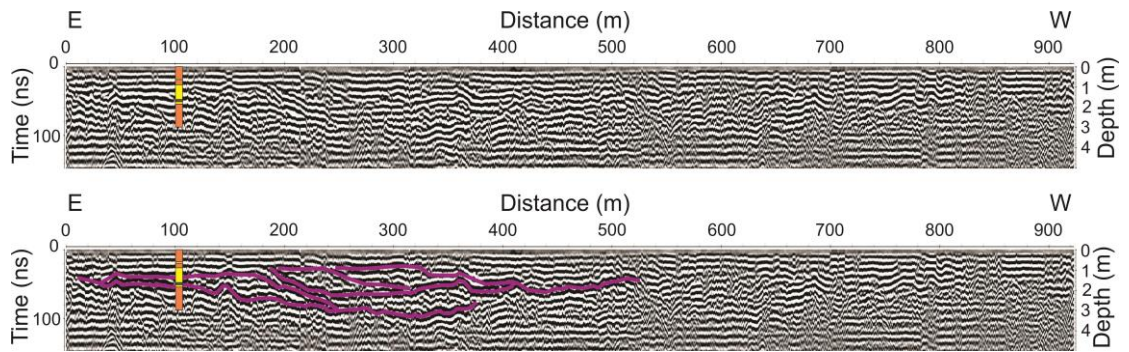


Fig. 4.9. GPR profile 104 from the east of Sefidrud, near to Kiashahr Town (location C in Fig. 4.2). the upper image is the original profile and the lower profile is the interpreted profile.

A core with 290 cm length was taken from the profile 104. Fig. 4.10 indicates sedimentary facies, grain size and MS of the core. The sedimentology of the sequence from the bottom to the top consists:

Sz1, 290-180 cm: brown silty sand with three bivalve shells (*C. glaucum*) at the depth of 270,234, 225 cm. Signs of coring disturbance was observed including uncompressed sediments and sediment movement in the PVC pipe.

Sz2, 180-83 cm: brown sand full of bivalve shell (*C. glaucum*) and a layer of organic rich at 168-160 cm. The shells were located horizontally within the sediments. This layer has a gradual contact with lower and upper zones.

Sz3, 83-0 cm: brown to dark brown silty sand with a thin layer of yellowish brown sand at a depth of 60 cm.

The grain size results shows that the sequence is mostly dominated by sand, with a maximum of 25% silt at 40 cm (Fig. 4.10). MS shows an increasing trend from the bottom to the top with a maximum value of 16 at a depth of 60 cm and a low point of 0 at a depth of 160 cm (Fig. 4.10).

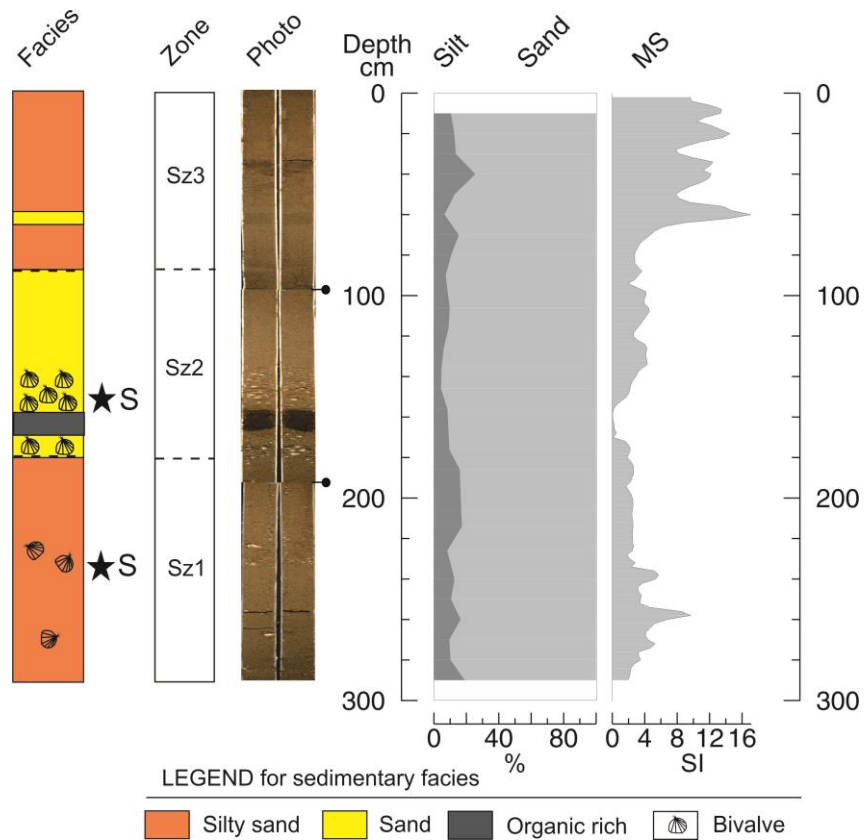


Fig. 4.10. Sedimentary log for the core 104, displaying sedimentary facies, sedimentary zone, core photo, grain size (clay, silt and sand) and magnetic susceptibility (MS). The black pin symbols show the core section limits. Black stars show the location of dated samples.

Additionally, two radiocarbon dates were obtained from two bivalve shells (*Cerastoderma glaucum*) at depths of 234 and 150 cm (Table 4.1 and Fig. 4.11).

Table 4.1. Radiocarbon dates from ANSTO, calibrated ages are reported for 2 σ range with highest probabilities shown in parentheses.

Laboratory number	Sample ID	Depth (cm)	Material Type	¹⁴ C Age (yr BP)	Calibration programme	Calibrated (2 σ range)	Median Probability
OZR390	KL11V1A 2-54	150	Shell (<i>C. glaucum</i>)	1190 \pm 25	CALIB 7.1 with Marine13	AD 1161-1284 (100%)	AD 1225
OZR391	KL11V1A 3-40	234	Shell (<i>C. glaucum</i>)	380 \pm 25	CALIB 7.1 with Marine13	0	-

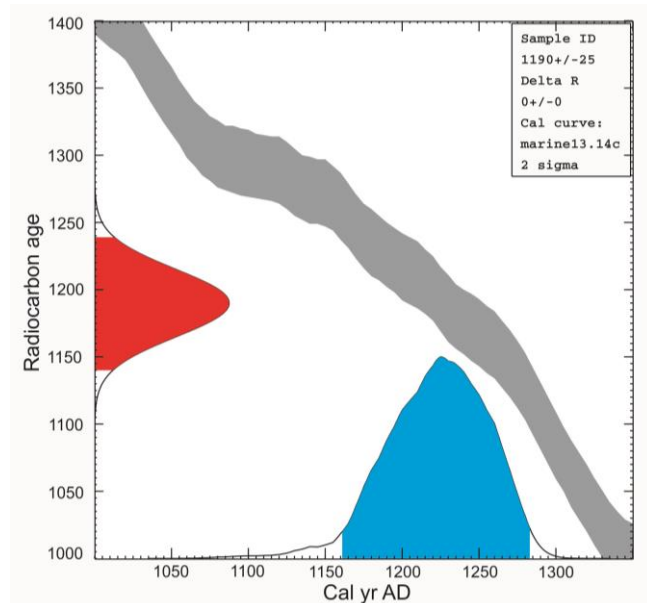


Fig. 4.11. The interception between the radiocarbon age (the red curve) and the calibrated age (the blue curve) with the calibration curve (the grey curve) from a shell sample at a depth of 150 cm core 104

Profile 105

The penetration depth of the GPR signal in this profile is up to 4 m and the length of profile is 320 m. The internal structure indicates a distinct sigmoidal pattern, suggesting delta prograding system (Fig. 4.12).

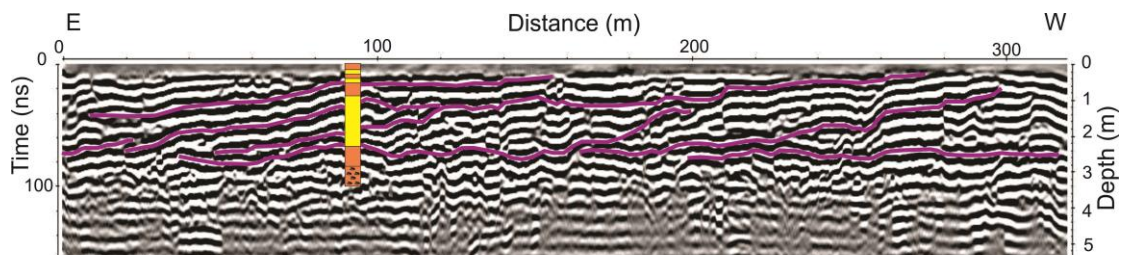


Fig. 4.12. GPR profile 105 from the east of Sefidrud Delta, near to Kiashahr Town (location C in Fig. 4.2). the upper image is the original profile and the lower profile is the interpreted profile.

A 269 cm long core was taken from the profile (Fig. 4.12). Fig. 4.13 shows sedimentary facies, grain size results and MS of the sequence. The sedimentology of the sequence from the bottom to the top is:

Sz1, 269-180 cm: brown silty sand with *C. glaucum* shells at the bottom

Sz2, 180-71 cm: dark brown sand with a gradual contact with the lower and upper facies.

Sz3, 71-0 cm: dark brown silty sand with two layer of dark brown sand at a depth of 40 and 20 cm.

From the grain size results, it can be observed that the sequence is mostly dominated by sand, with maximum 33% silt.

The magnetic susceptibility shows significant variations along the core. The graph shows an increasing trend from the bottom to the top, with a maximum value of 31% at a depth of 9 cm (Fig. 4.13).

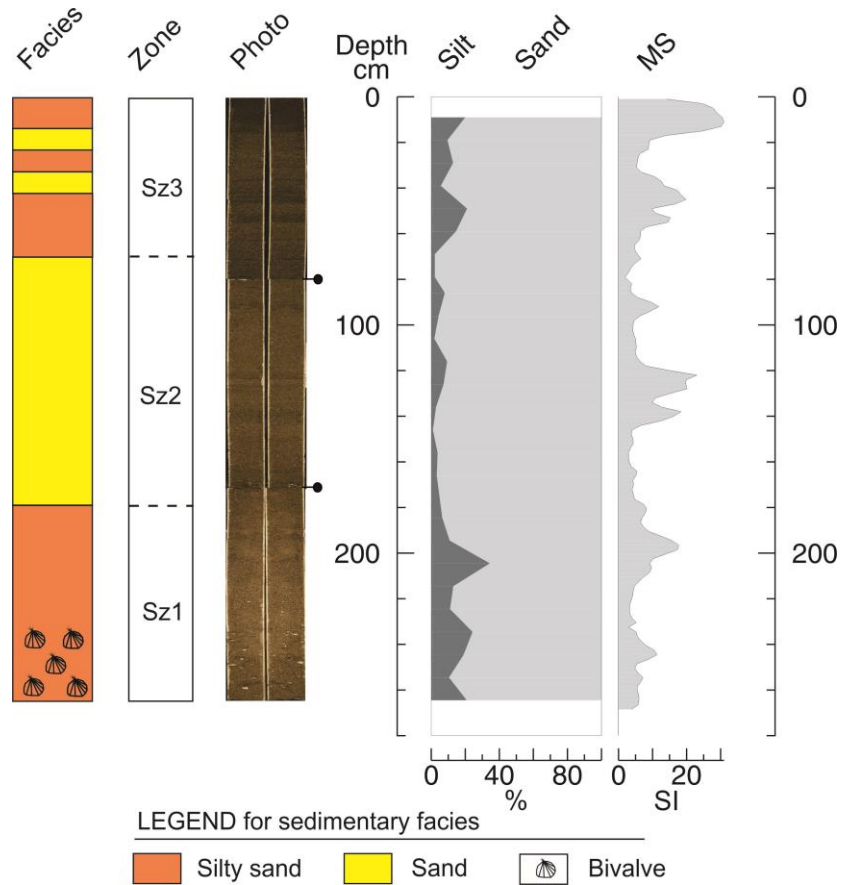


Fig. 4.13. Sedimentary log for the core 105, displaying sedimentary facies, sedimentary zone, core photo, grain size (clay, silt and sand) and magnetic susceptibility (MS). The black pin symbols show the core section limits.

4.2.4 Location D

Profiles 106 and 107 were taken from location D, near to Old Sefidrud River.

Profile 106

650 m long profile 106 was taken along Old Sefidrud River. The penetration depth of the GPR signal in this profile is very low (less than 2 m). The only observed feature in this profile is multiples (Fig. 3.1 and Fig. 4.14).

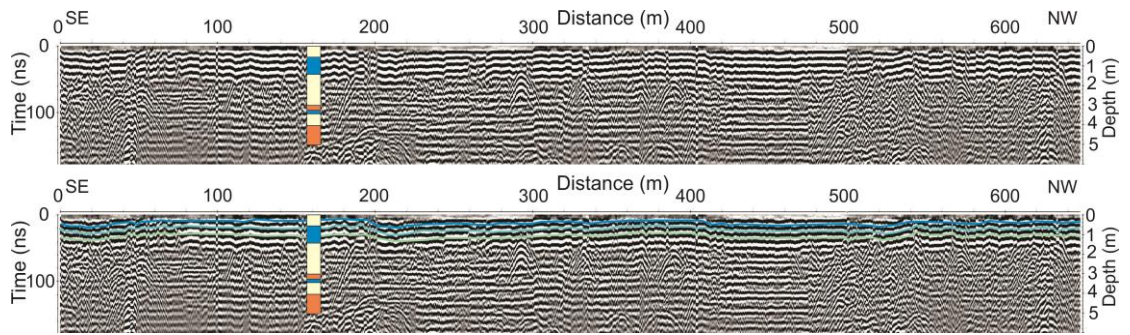


Fig. 4.14. GPR profile 106 along the Old Sefidrud River (location D in Fig. 4.2). The upper image is the original profile and the lower profile is the interpreted profile.

A 484 cm long core was taken from the profile (Fig. 4.14). The sedimentology of the sequence from the bottom to the top is:

Sz1, 484-388 cm: dark grey silty sand with a sharp contact with the following facies.

Sz2, 388-317 cm: alternation of weak red silt with plant remains at the bottom and dark grey sandy silt.

Sz3, 317-289 cm: reddish brown silty sand with sharp contacts with the lower and upper facies.

Sz4, 289-0 cm: alternation of reddish brown to strong brown silt and strong brown sandy silt.

Sedimentology analysis including grain size and LOI were performed on the sequence. From the data obtained by the CILAS Particle Size Analyser, it can be detected that the sequence is mostly dominated by silt (up to 98%), with up to 7% of clay and up to 76% sand. The top 289 cm is mainly silt, including sandy silt.

The magnetic susceptibility of this sequence shows a major variation along the core, with high MS in the two layers of silty sand (zone Sz1 and Sz3). The organic matter and carbonate content shows an ascending trend from the base with the maximum values of 4 and 5 % respectively (Fig. 4.15). High carbonate content in profile 106 (up to 5%) also contributes to signal attenuation (Smith and Jol, 1992).

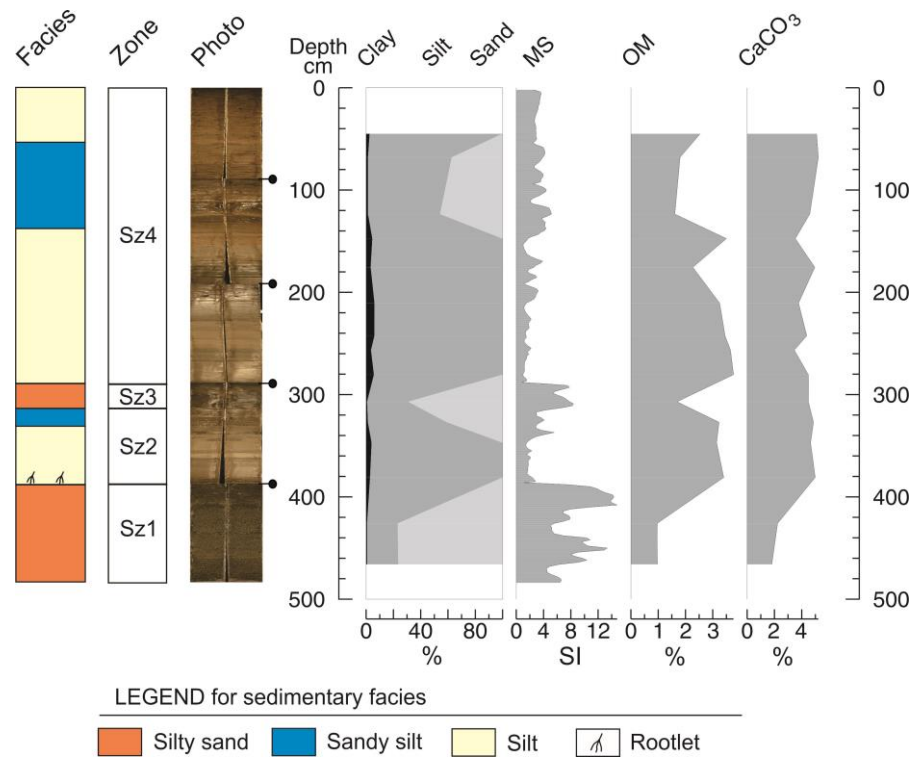


Fig. 4.15. Sedimentary log for the core 106, displaying sedimentary facies, sedimentary zone, core photo, grain size (clay, silt and sand) and magnetic susceptibility (MS), organic matter (OM) and calcium carbonate (CaCO₃). The black pin symbols show the core section limits.

Profile 107

Profile 107 with a length of 380 m was taken from flood plain of Old Sefidrud River. Similar to profile 106, the penetration depth of the GPR signal in this profile is very low (less than 2 m) and the only observed feature in this profile is ‘multiples’.

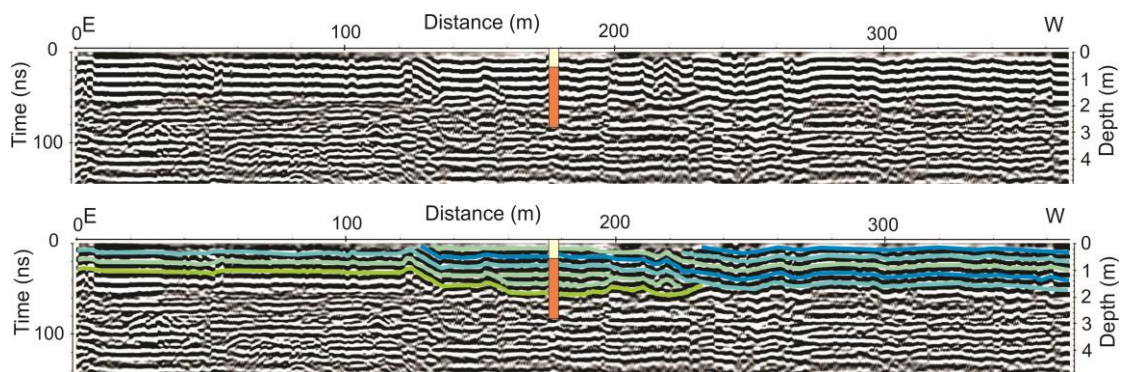


Fig. 4.16. GPR profile 107 (location D in Fig. 4.2), the upper image is the original profile and the lower profile is the interpreted profile.

The multiple horizons in profiles 106 and 107 have silt/clay up to 100%. Silt/clay sized particles within coarser sediments have been shown to cause signal attenuation (Jol and Smith, 1991; Jol et al., 1996).

A 289 cm long core was taken from the profile (Fig. 4.16). Fig. 4.17 shows sedimentary facies, grain size results and MS of the sequence. The sedimentology of the sequence from the bottom to the top is:

Sz1, 289-68 cm: dark brown silty sand with a sharp layer with the following facies.

Sz2, 68-0 cm: dark reddish brown to reddish brown silt

From the grain size results show that the sequence is mostly dominated by sand, with a maximum of 83%, at the bottom, however, the upper part is dominated by silt (up to 98%).

The magnetic susceptibility graph shows an increasing trend from the bottom to 100 cm, with a maximum value of 29 at a depth of 104 cm. The upper 100 cm, in general, show low values, with a low point of 1 at 61 cm (Fig. 4.17).

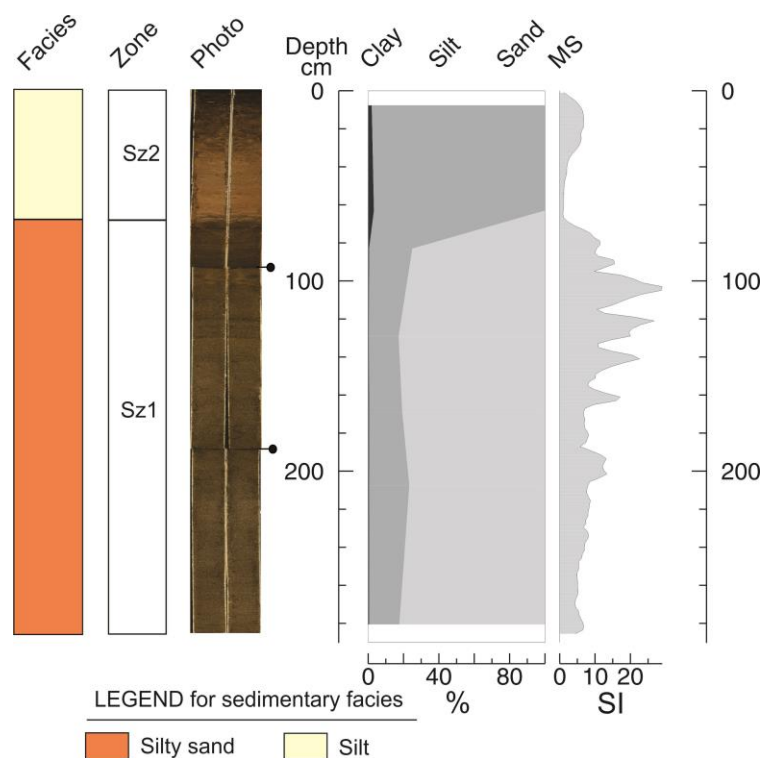


Fig. 4.17. Sedimentary log for the core 107, displaying core photo, sedimentary facies, grain size (clay, silt and sand) and magnetic susceptibility (MS). The black pin symbols show the core section limits.

4.3 Inland water bodies

4.3.1 Langarud

The name of Langarud is a compound name of two Persian words, Langar means harbour and Rud means river. Thus, it has been argued that Langarud was a harbour during the past, and was connected to the sea through a river. During Nader-Shah umpire (i.e. AD 1736-1747), Langarud became the centre of the Iranian Navy in the north of Iran and shipbuilding industry was developed in AD 1743 (Setudeh, 1970). In July 1744 a ship which had been built was ready, but the launching went wrong, due to a sudden sea level fall. This sudden sea level change between AD 1743 and 1744 was not documented in Naderi et al. (2013a). But it shows that sudden CSL changes may occur in short time periods and that they may have a large impact on industries and people.

Langarud town is now an agricultural and touristic area. Due to poor land management, the size of wetland has been reduced by dumping tons of waste every year. On the other hand, a part of the wetland is drained in order to create agricultural land.

4.3.1.1 Coring location

The coring location is situated at $37^{\circ} 11' 8.70''$ N and $50^{\circ} 8' 51.00''$ E (Fig. 4.18 and Table 2, Appendix A). Two parallel, but offset, 1 m long sections, cores LL13V A and B with a maximum composite depths of 665 and 578 cm were retrieved from the drained part of the Langarud wetland. The cores were taken using a percussion corer. These offset core sections were used to cover gaps between the sections; but due to good coverage of section A, section B was only used to check the boundary between sedimentary facies. The absolute elevation of the coring location equal to 21.44 m bsl was surveyed precisely. The data to calculate Absolute Sea Level for the year 2014 is extracted from USDA (2015). Based on this, the CSL in the year 2014 was -27.41 m (USDA, 2015).

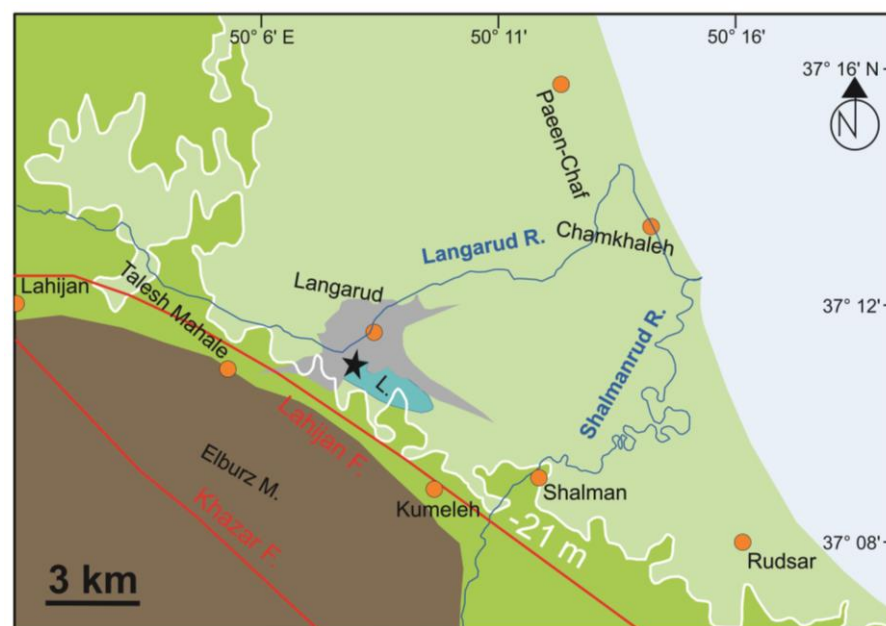


Fig. 4.18. Location map of Langarud with the contour line -21 m (from Haghani et al., in press). The data for -21 m is extracted from ASTER Global Digital Elevation Model (ASTER GDEM, 2015) with 30 m spatial resolution. L: Langarud wetland, F.: fault, M: Mountains, black star: location of coring, green area: agricultural fields, pale green area: areas under brackish water invasion, orange dots: towns, grey area: boundary of Langarud town.

Two small rivers flow into the CS near the Langarud wetland (Fig. 4.18). The first is the Langarud River with a length of ~54 km and catchment area of 260 km² located in the west of the Langarud wetland, which is only 700 m far away from the coring location used in this study. The second river is the Shalmanrud with a length of ~54 km and catchment area of 390 km² located ~6 km east of the wetland. However, at the present time, the wetland is not under direct influence of these rivers.

The origin of the depression for the Langarud wetland could be a sag pond created by collapse during the AD 958 earthquake or an oxbow lake created due to river avulsion caused by rapid sea level rise or earthquake (Berberian and Yeats, 1999; Naderi Beni et al., 2013b). The lithofacies map of Kazancı and Gulbabazadeh (2013) shows the Langarud wetland on a c. >25 km long coastal ridge with a NW and SE orientation. It is probably an old feature unrelated to the present orientation of the modern coastline.

4.3.1.2 Sedimentology

Generally, the Langarud sequence consists of silty sand (bottom), sandy silt and silt (top). These range in colour from frequently reddish brown to more rarely bluish grey (Table 4.2 and Fig. 4.19). From the bottom to top, the sequence is divided in nine sedimentological zones (Sz) based on visual description including colour, grain size, MS, OM and carbonate content that are detailed in Table 4.2 and represented in fig. 4.19 and 4.20.

Table 4.2. Sedimentological description, MS: magnetic susceptibility, red box: sedimentological zones of interest (from Haghani et al., in press).

Unit	Depth (cm)	Description	Bed boundaries
Sz9	0-90	Oxidised reddish brown silt with plant material at the top 40 cm and high MS at the surface.	Sharp
Sz8	90-149	Alternation of grey sandy silt and dark grey silty sand bedded with a black organic rich layer at the top, high MS.	
Sz7	149-242	Alternation of light reddish brown and pinkish grey silt, relatively low MS.	Sharp
Sz6	242-310	Light olive grey silt with an organic rich layer, very low MS.	Sharp
Sz5	310-340	Brown silt with rootlets and few nodules at a depth of 342 and 322 cm, medium MS	Gradational
Sz4	340-380	Bluish grey silt with very low MS	Gradational
Sz3	380-420	Light olive grey silt with very low MS	Gradational
Sz2	420-490	Light brownish grey to brown silt, abundant carbonate nodules, few rounded and sub-angular gravel (3-10 mm diameter) at a depth of 480 cm, low MS.	Gradational
Sz1	490-664.5	Dark grey silty sand with presence of rounded and sub-angular gravel (2.2-5.5 mm diameter), and high MS	Sharp

The carbonate content has a background of 2% with a slight decrease from the bottom to the top of the core with one large peak at 471 cm depth, and two small increases at 595 and 161 cm depth. The sharp peak of CaCO₃ can be roughly related to the presence of carbonate nodules (Fig.4.19).

The amount of OM content in the sequence is approximately 3%. In general, OM content shows a slight increase from the bottom of the sequence to the top with two peaks at 260 and 105 cm depth (Fig.4.19).

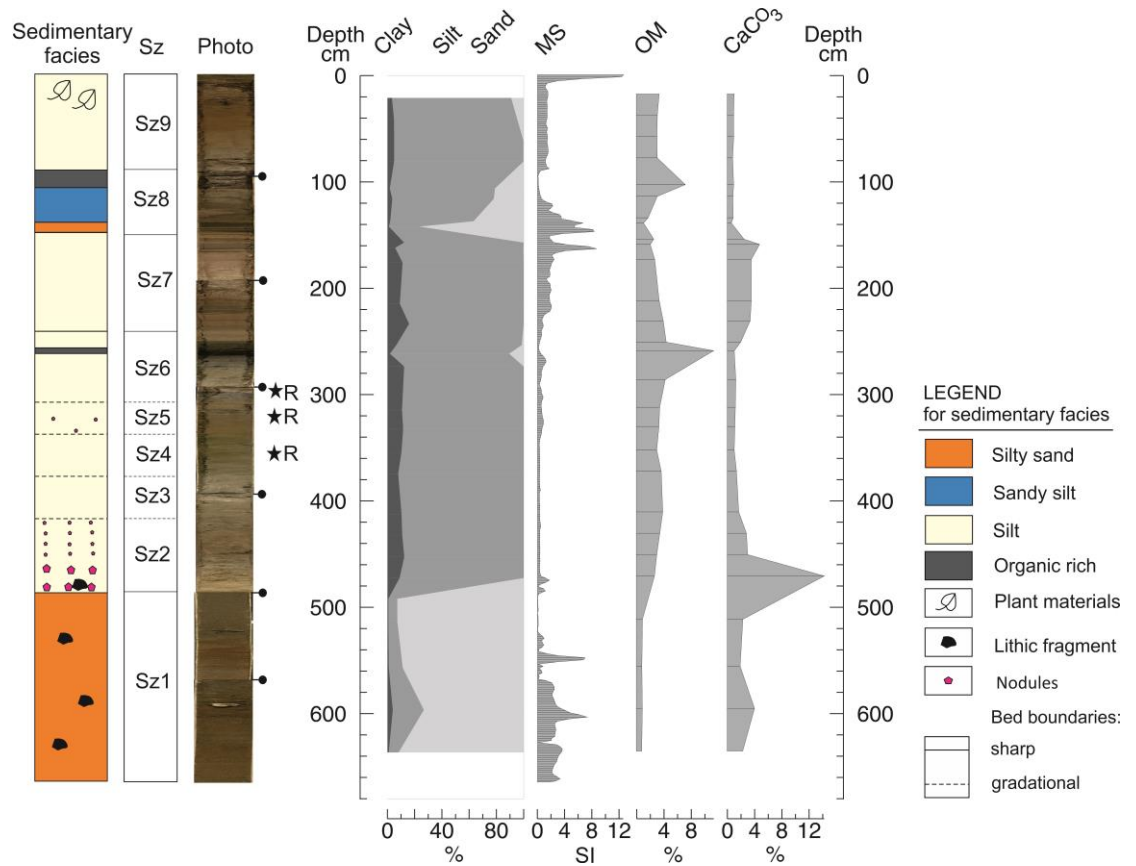


Fig. 4.19. Sedimentary log displaying sedimentology (Sz: sedimentological zone), core photo, grain size (clay, silt and sand), magnetic susceptibility (MS), organic matter (OM) and calcium carbonate (CaCO₃) content. The black stars refer to the depth of the radiocarbon date, R: rootlet (material dated), and the black pin symbols showing the core section limits (from Haghani et al., in press).

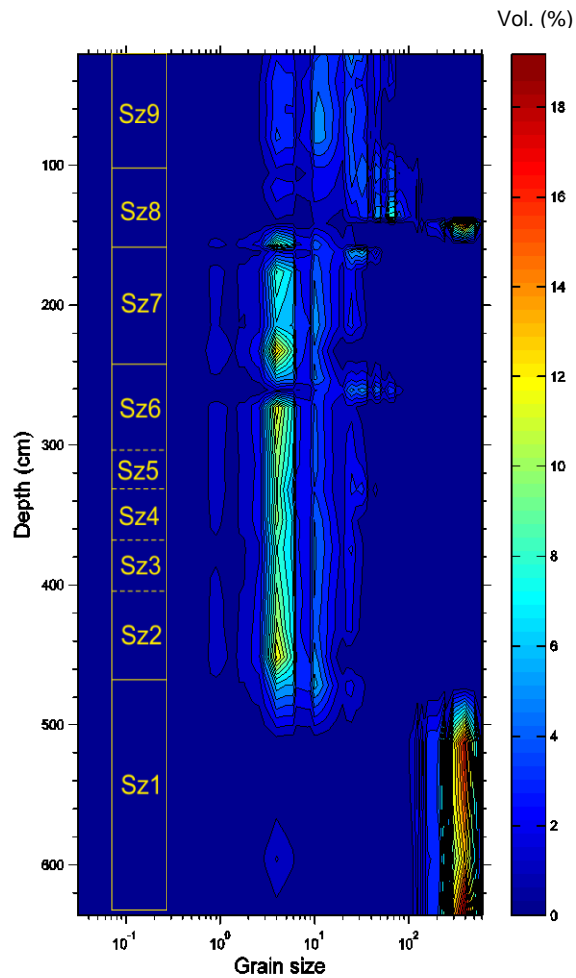


Fig. 4.20. 3D plot of grain size data in μm : the dark blue colour represents the lowest volume (%), while the red colour shows the highest volume (%). Sz represents sedimentological zone (from Haghani et al., in press).

4.3.1.3 Macro-remains

Twenty six samples from different facies were selected for macro-remains and fifteen different macro-remain types were identified. All the fractions were scanned; but due to the great scarcity of macrofossils in the smaller fractions, only the samples above 500 μm were counted and are presented in Fig. 4.21. Based on the results, the sequence was divided into four very distinct macro-remains zones (Mz).

Mz1, from the base to 500 cm

The first zone is characterized by abundant minerals including quartz and feldspar (up to 98%) and rounded and sub-angular lithic fragments (2.5%).

Mz2, 500-400 cm

CaCO₃ nodules are abundant in the second zone with percentages between 64 and 92%. Minerals (5-34%), plant material (0.2-11%) and charcoal (1.3-6.5%) were observed in this zone. Some rounded and sub-angular lithic fragments (3.2%) occur at a depth of 480 cm.

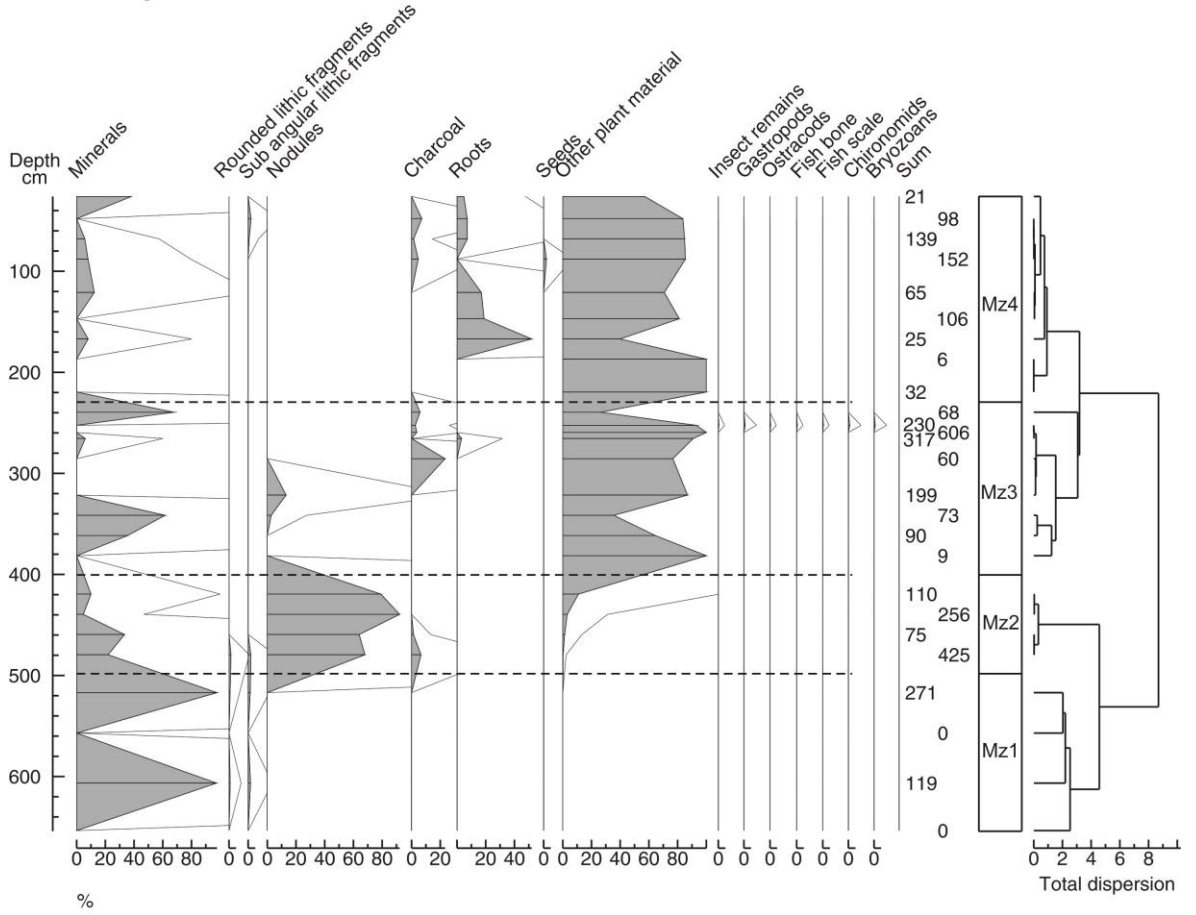
Mz3, 400-246 cm

The third zone is characterized by abundant plant material (35-100%) and some charcoal (2.5-23%), but also by minerals (6-62%). Other biological remains (insect remains, ostracods, gastropods, chironomid headcapsules, bryozoans, fish bones and fish scale) were recognised in a single sample at 253 cm depth. Two oogones of charophyte were observed in the fraction of 125 µm in the same sample.

Mz4, 246-0 cm

The last zone mainly contains organic material: the common type “other plant material” (40-100%), including especially here roots (4-52%) and seeds (2%). Charcoal (1.5-7%), minerals (6-68%) and sub-angular lithic fragments (0.7-2%) also occur in this zone.

Langarud, core LL13V, macro-remains in %



Langarud, core LL13V, concentration of macro-remains

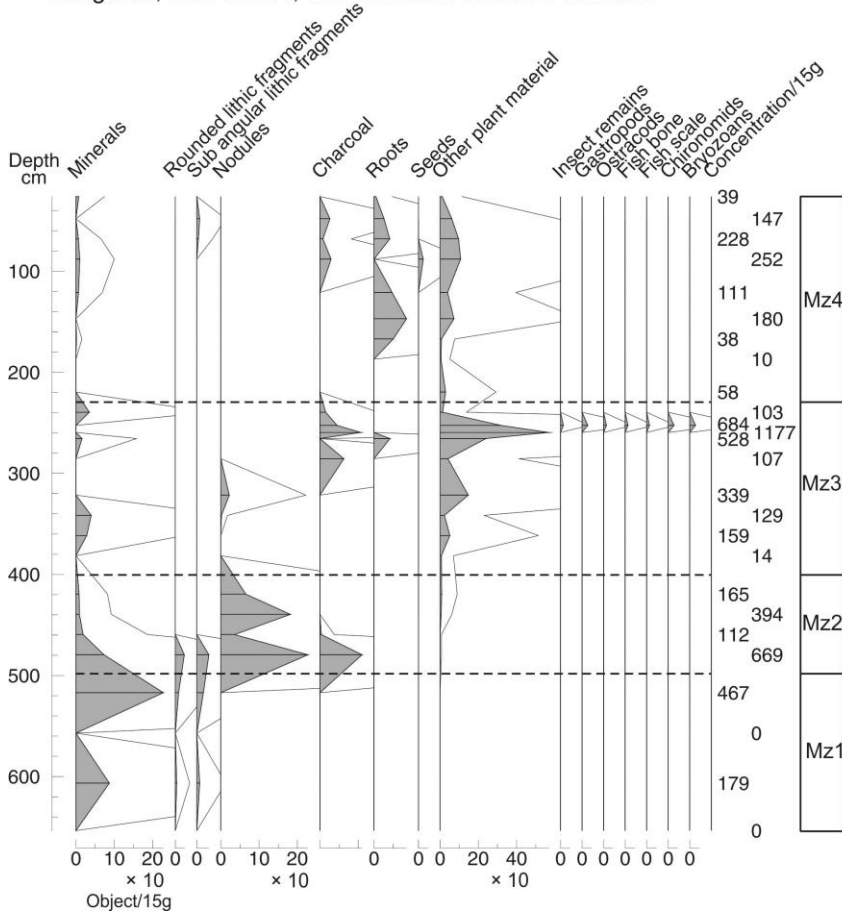


Fig. 4.21. Percentages of macro-remains above 500 μ m (the diagram at the top) and the concentrations (the diagram at the bottom) in LL13V sequence.

4.3.1.4 Palynology

Palynology analyses were performed by Professor S. Leroy on the sequence LL13V and the text was written by her. Seventeen samples from the sequence were chosen to study palynology. No sample was taken from the bottom sand, because of low preservation potential of pollen grains in coarse sediments. The concentrations are very varied with some samples with low concentration and some of them are very well preserved. Two barren samples were found at the bottom of the sequence (412 and 389 cm) (Pz0 in Fig. 4.22). Overall, the preservation is mediocre (often around 20 % indeterminable grains).

In general, the Arboreal Pollen (AP) is dominated by *Alnus* (Fig. 4.22). The next important tree pollen, with low values, belongs to the Hyrcanian forest. The lower part of the diagram is dominated by Cyperaceae, which are then replaced by Amaranthaceae, *Artemisia* and Poaceae. The aquatic plants are relatively diverse, mostly from plants rooted at the bottom of the wetland and dominated by *Typha-Sparganium*. Occasional fern spores are present; however various remains of the aquatic fern *Salvinia-Azolla* are observed (massulae and microspores) at times abundantly. Regarding the non-pollen palynomorphs (NPP), fungal spores of varied types are very abundant; the most remarkable findings are the presence of dinocysts (organic-walled dinoflagellate cysts) and one foraminifer inner organic lining.

The selected key palynomorphs, used in interpretation, are presented in Fig. 4.22. Three pollen zones have been defined by well-marked limits:

Pz1, 371-242 cm

Pz1 starts at 371 cm depth following the detection of two barren levels below this depth. The environment is rapidly changing throughout zone Pz1. It starts with a water body under marine influence, which is clearly shown by the presence of a range of dinocysts typical of the CS such as *Lingulodinium machaerophorum*, *Impagidinium caspiense* and *Spiniferites cruciformis*. Alder swamps are present in the distance. Then the alder swamps slightly regress to the expense of a vast area covered by sedges (top of Pz1).

Pz2, 242-146 cm

The land becomes drier. The alder forest has temporarily disappeared locally and regionally. The absence of dinocysts indicates that the area has become protected from the influence of the CS. Vegetation contains elements of salty/dry soils as seen in a peak of Amaranthaceae. This zone include the maxima of *Glomus*. This is a sign of strong soil erosion, and comes along human activity.

Pz3, 146 cm-top

The landscape is similar to that of the present: i.e. a mosaic of lowland forest, patches of *Alnus* swamps and fields. Large amounts of Poaceae reflect the development of rice paddies. This zone has the highest diversity of freshwater algae which are good indicators of very shallow waters. Massulae typical of the introduced aquatic fern, *Azolla filiculoides*, occur in the top two samples only. This fern is used as natural fertiliser in rice paddies. Fern spores become frequent, signalling water transport. Fungal spores are on the increase and become extremely abundant in the top sample. In brief, the water level of the wetland is very shallow and used intensively.

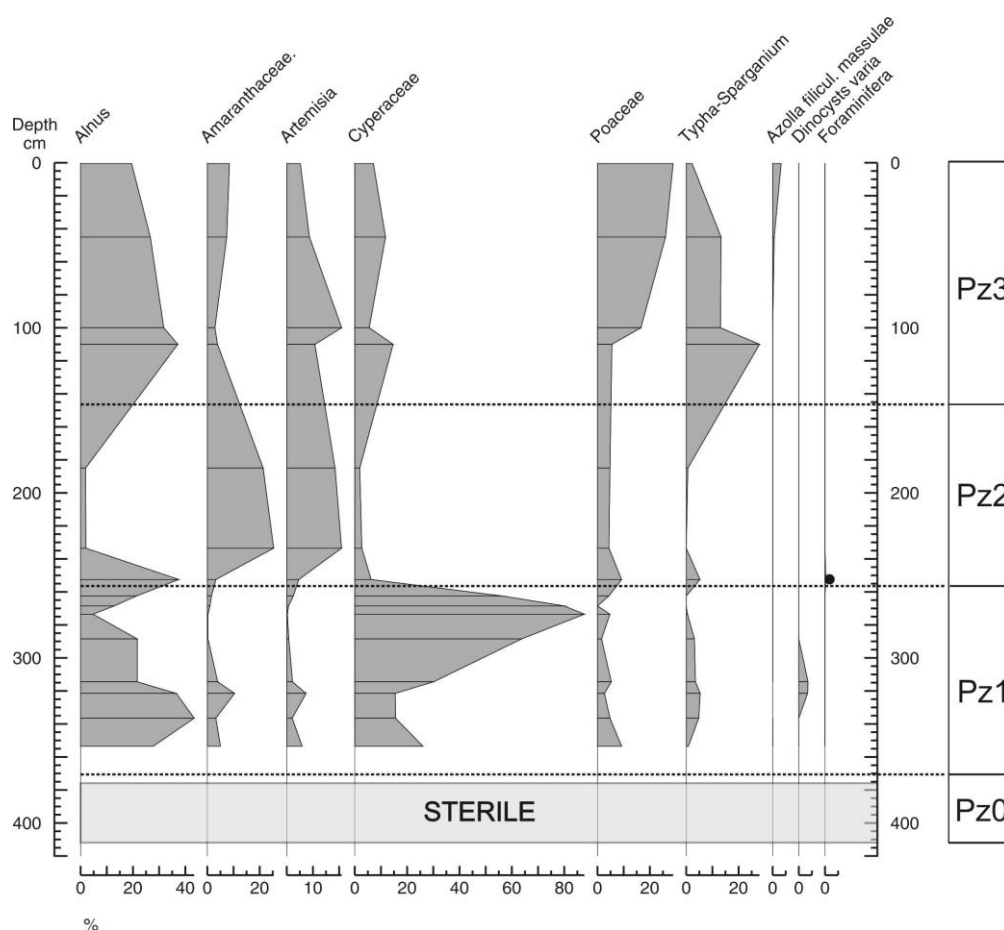


Fig 4.22. Palynological diagram of LL13V sequence, including the % of some significant palynomorph. Grey strip: barren samples. Adopted from Haghani et al., (in press).

4.3.1.5 Chronology

Three radiocarbon dates were obtained from plant remains at depths of 353.5 (Sz4), 321.5 (Sz5) and 298.5 cm (Sz6) (Table 4.3 and Fig. 4.23). No material suitable for radiocarbon dating was found at the bottom of the sequence (Sz1). With ample overlap and inversion, the three ages fall in the 14th century and very beginning of the 15th century.

Table 4.3. Radiocarbon dates from Queen’s University Belfast, calibrated ages are reported for 2σ range with highest probabilities shown in parentheses.

Laboratory number	Sample ID	Depth (cm)	Material Type	¹⁴ C Age (yr BP)	Calibrated age (yr AD) 2σ range	Median probability
UBA-22965	LL4-3	298.5	Rootlet	638 ± 25	1285-1326 (41.3%) 1343-1394 (58.7%)	1355
UBA-23788	LL4-27-29	321.5	Rootlet	535 ± 30	1318-1352 (25.1%) 1390-1438 (74.9%)	1408
UBA-27533	LL4-59	353.5	Rootlet	585 ± 49	1293-1423 (95.4%)	1352

Remains of *Azolla filiculoides* found from 44.5 cm depth upwards can be used as a time marker for the top of the core. According to its introduction to the study area in 1986, the core represents a time period up to at least 1986 and that, in context of the study, is effectively the present. Hence, the emersion of the coring location must have been extremely recent, in line with the current draining for fields and town expansion.

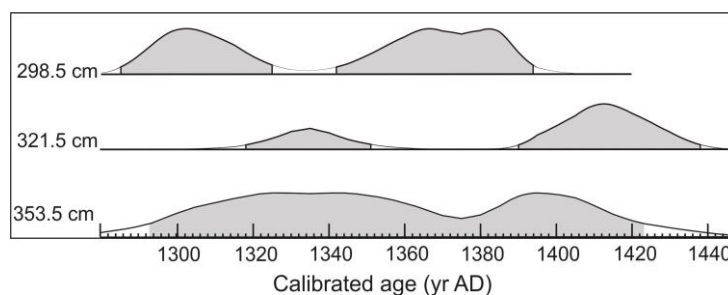


Fig. 4.23. Calibrated ages at two sigma for samples from different depths of Langarud sequence, using CALIB 7.0 with IntCal13.

4.3.2 Astaneh (AAL13V)

According to cores described in Kazancı and Gulbabazadeh (2013), deposition of fine sediments north of Astaneh Town was observed (Fig. 4 in Kazancı and Gulbabazadeh, 2013 and Fig. 4.24 A). Deposition of these fine sediments could be related to an old wetland environment. The other possibility is present-day deposition of silts and clays in overbank area of Sefidrud. To examine these hypotheses, two parallel long cores (1063 and 1026 cm) were taken nearby Astaneh Town in the north of Khazar Fault (Fig. 4.24 A, Table 2, Appendix A) using a percussion corer. The coring location was located at the edge of a wet area which was not used for agriculture (Fig. 4.24 B).

The coring location had higher elevation than the river surface and also the other side of the river. Therefore, the elevation was levelled precisely by INIOAS. The cross section of the channel (a-b in Fig. 4.24 B) with the accurately measured elevation made on March 2014 (i.e. 14 months after the coring campaign) is presented in Fig. 4.25. Based on the measurement the elevation of coring location is -11.38 m bsl which is -9.15 m higher than the current river surface (i.e. -20.53 m). The elevation of the other side of river was not

measured precisely. However, based on the elevation provided by Google Earth, ~ 4 m height difference was observed between the two sides of the river (Fig. 4.25). The profile a-b was also extracted from ASTER Global Digital Elevation Model (ASTER GDEM, 2015) with 30 m spatial resolution (Fig. 4.26). However, due to its low resolution, it did not correspond to our observations in the field; therefore, it was not used.

Two parallel cores (AAL13V A and B), with offset 1 m long sections, were retrieved in order to obtain a continuous sequence. These offset core sections were used to cover gaps between the sections; but due to good coverage of section A, section B was only used to check the boundary between facies. Sedimentology analysis (including grain size and LOI analysis), ¹⁴C dating, macrofossil analysis and pollen study were performed on section A which represent well the sequence AAL13V.

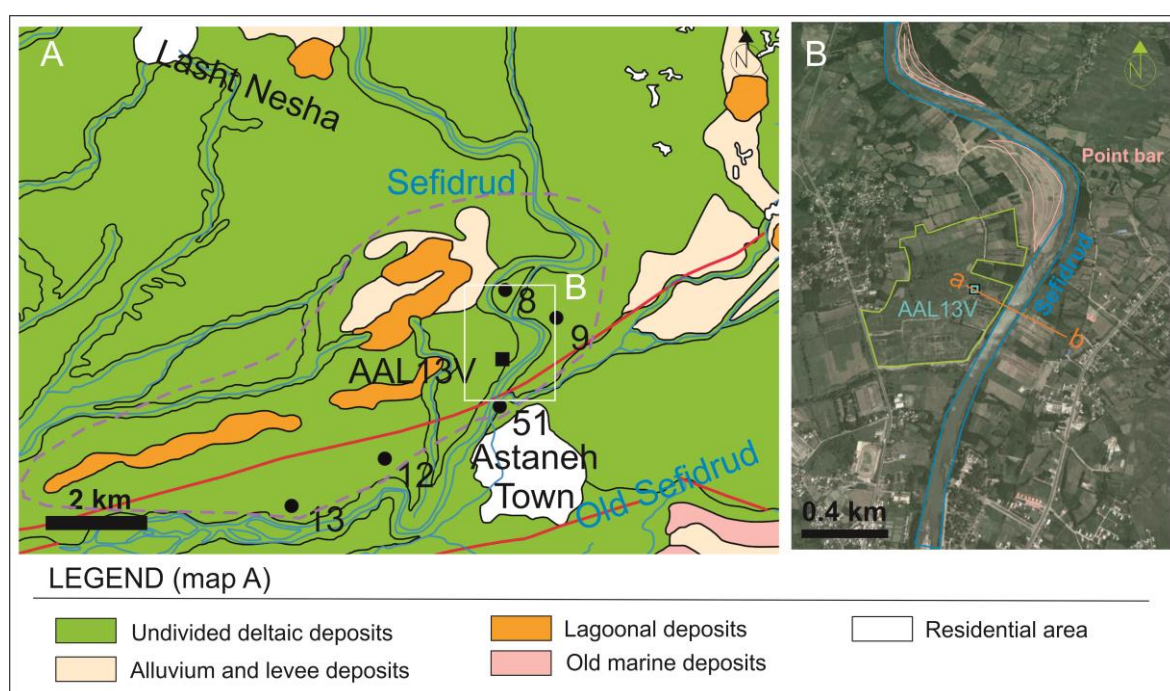


Fig. 4.24. A: Location of core AAL13V (black square). Fine sediment deposition near Astaneh (black circles) with core numbers from Kazancı and Gulbabazadeh (2013). Source of this geological map is from the Geological Survey of Iran 1/100 000 Rasht, series sheet 5964 compiled by Khabaznia and Sadeghi (2004). Purple dashed line represents the boundary of a probable wetland area. B: Location of AL13V in Google Earth Map. Pink crescent-shaped features represent present-day point bars and green line shows the boundary of marsh area.

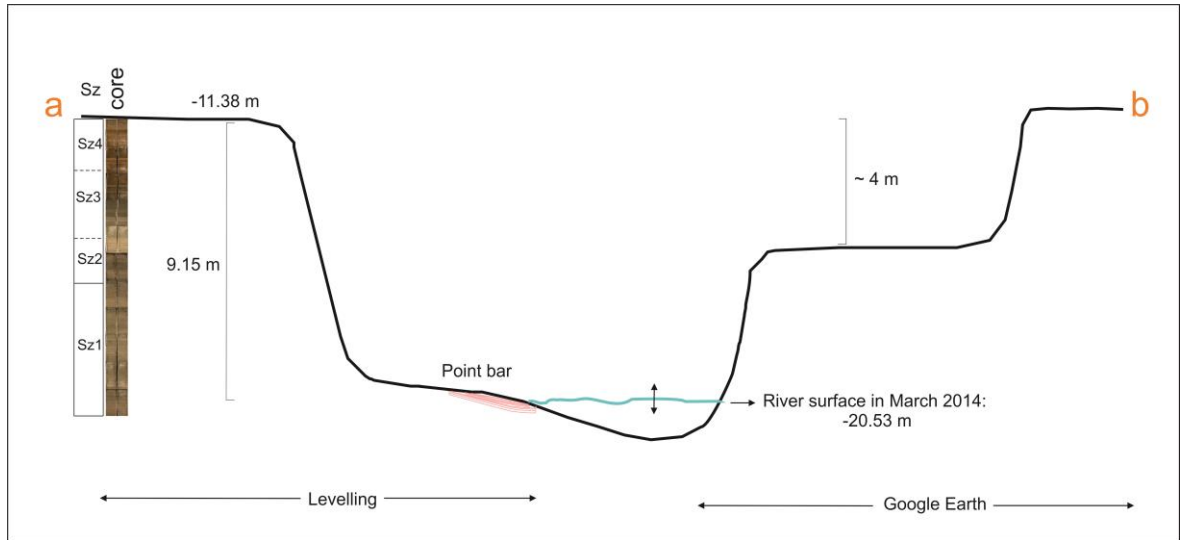


Fig. 4.25. Cross section of Sefidrud north of Astaneh Town area (Profile a-b in Fig. 4.24 B). The coring location and photos of core taken from the river bank are presented in the figure.

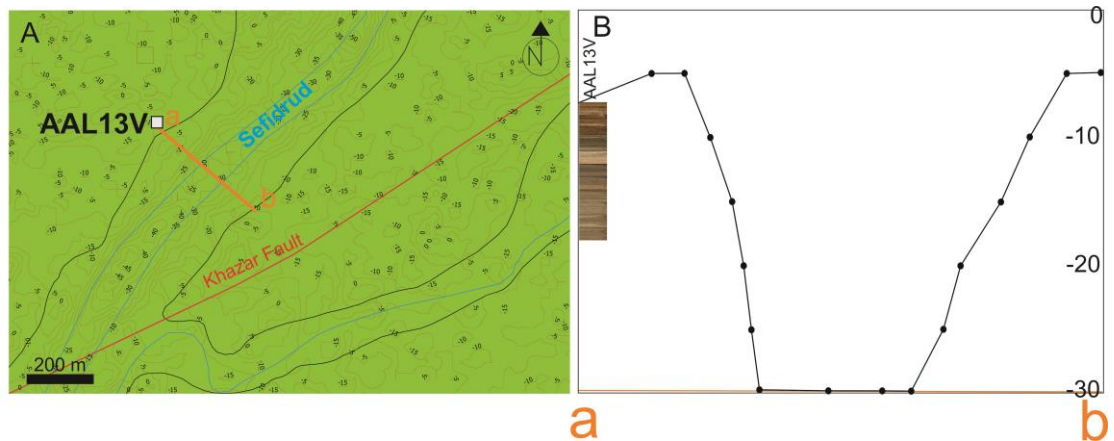


Fig. 4.26. A: Contour line extracted from ASTER Global Digital Elevation Model (ASTER GDEM, 2015) with 30 m spatial resolution. B: Profile a-b in figure 4.24 B based on ASTER GDEM (2015)

4.3.2.1 Sedimentology

The percentages of sand, silt and clay, also MS, OM % and CaCO_3 % are presented in Fig. 4.27. Based on visual description, grain size and sedimentological analyses the sequence can be divided into four main sedimentological zones including:

Sz1, 1063-590 cm: dark greyish brown to brown and reddish brown silt occurs with rootlets and bioturbation at ~900-800 cm. The contacts within the beddings are gradual, except the sharp contact with the sandy silt from the next zone. Tree roots (~2 cm long and 0.4 cm wide) also were observed at the top of this zone in section A. Moreover, a large root (20 cm long and ~ 1 cm wide) was observed in section B. Being vertically placed inside the core suggests that the roots are in situ. The magnetic susceptibility is low in this zone, only up to three. The content of organic matter shows a slight decreasing trend in this zone with a background of ~2%. The carbonate contents have a background of 5% and show a relatively high amount in this zone.

Sz2, 590-430 cm: medium bedded olive grey sandy silt followed by thickly bedded reddish brown to brown silt with rootlets contain a fine layer of organic rich silt in its middle. The contacts between organic matter layer and sandy silt are sharp, but it is gradual with the upper zone (Sz3). The content of organic matter shows a sudden increase at the base of this zone, reaching 5.21% at a 571 cm; this is followed by a slow decreasing trend upward. The calcium carbonate contents show abrupt fluctuations with two low points ~1% at the depths of 571 and 524 cm (Fig. 4.27).

Sz3, 430-184 cm: Alternation of grey to dark grey sandy silt, brown to grey silty sand, and brown silt are observed. The magnetic susceptibility clearly shows higher values in this zone, reaching even ~11 at 331 cm. The content of organic matter and carbonate are lower and remain relatively constant towards the top.

Sz4, 184-0 cm: Alternations of strong brown to brown silt with rootlets, and brown silty sand to sandy silt occur. The magnetic susceptibility is high and reached even ~18 at 135 cm. The content of organic matter and carbonate remain relatively constant towards the top.

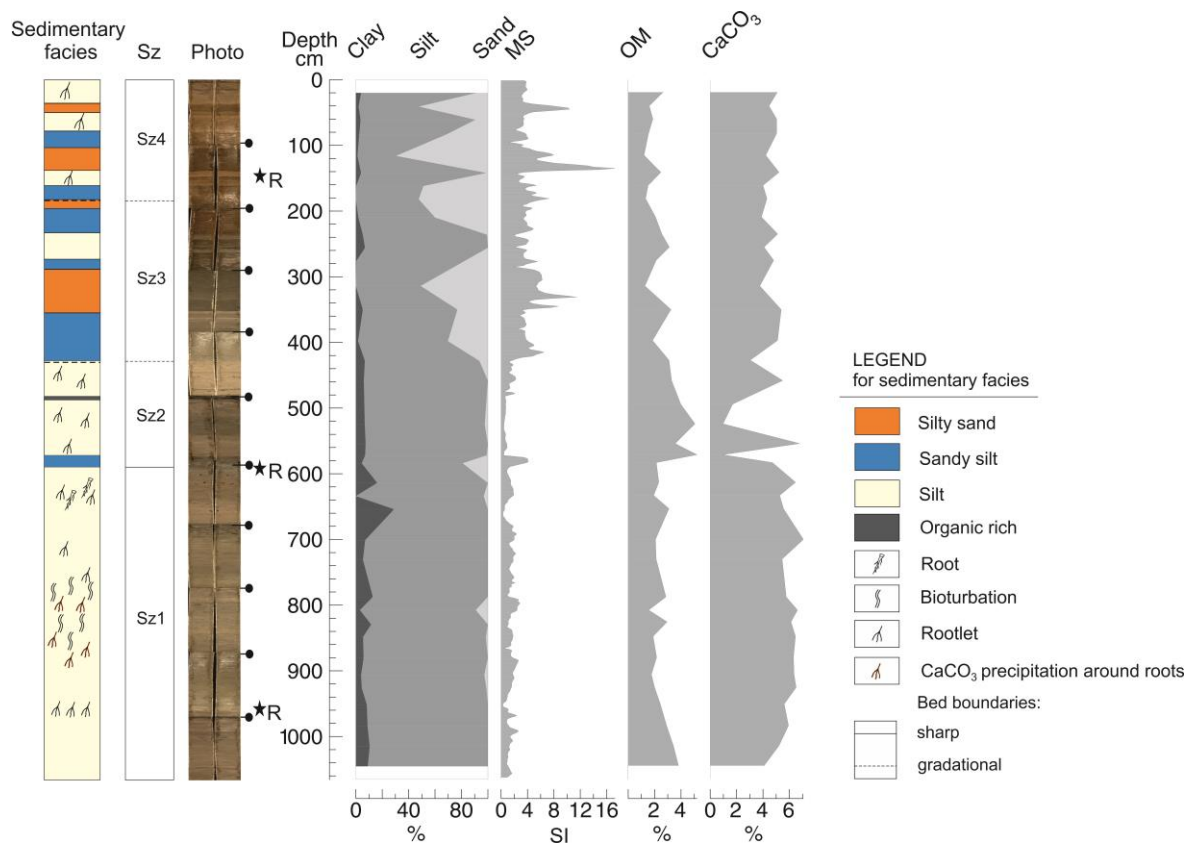


Fig. 4.27. Sedimentary sequence for Astaneh core AAL13V, displaying sedimentology, core photo, grain size (clay, silt and sand), magnetic susceptibility (MS), organic matter (OM) and calcium carbonate (CaCO_3) contents. The black stars refer to the depths of the radiocarbon dates, and R: rootlets and roots (material dated). The black pin symbols refer to core section limits.

The 3-D plot of the grain size suggest that the basal 633 cm is dominated mainly by silt and up to 30% clay; and the top 430 cm is more variable and dominated by silt and sand (Fig. 4.27 and 4.28).

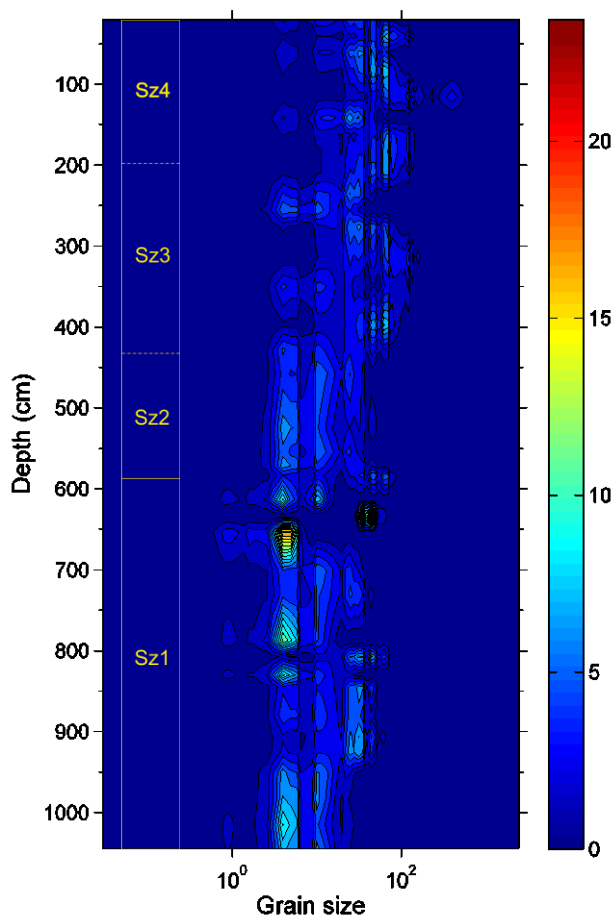


Fig.4.28. 3D plot of grain size data in μm for the sequence AAL13V: the dark blue colour represents the lowest volume (%), while the red colour shows the highest volume (%). Sz: sedimentological zone.

4.3.2.2 Macro-remains

Seventeen samples from the AAL13 sequence were chosen for a macrofossil study. Five different macro-remains have been identified in the fraction $>500 \mu\text{m}$. All the fractions were scanned; but due to lack of macro-remains which are indicator of environment (such as Foraminifera) and also similarity of assemblages of macro-remains in all the fractions, only the samples above $500 \mu\text{m}$ were counted. Macro-remain percentages and concentrations for the fraction $500 \mu\text{m}$ are presented in Fig. 4.29. Based on the results, the sequence is divided into three zones:

Mz1, 1057-653 cm (8 samples)

This zone is characterized by presence of CaCO_3 precipitation around the roots which reaches to 8.5% at a depth of 757 cm. Faecal pellets (up to 71%), clay flakes (up to 60%), plant material (up to 4.5%) and charcoal (2%) compose the rest of macro-remains.

Mz2, 653-401 cm (3 samples)

This zone is marked a maximal amount of plant material (95%) at 567 cm. Small amounts of clay flakes and faecal pellets were observed in this zone.

Mz3, 401-26 cm (6 samples)

This zone is marked by a maximal amount of clay flakes (up to 44%) and faecal pellets (71%). Furthermore, small amounts of plant materials and charcoal were also observed in this zone. This zone is similar to Mz1 but without the carbonate casts.

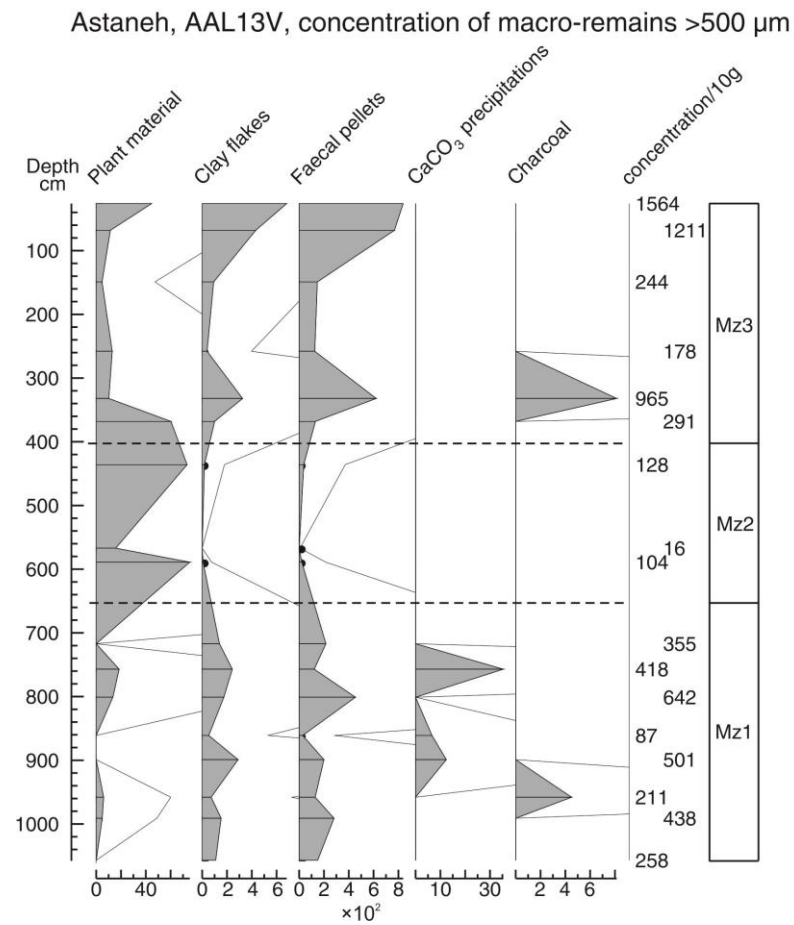
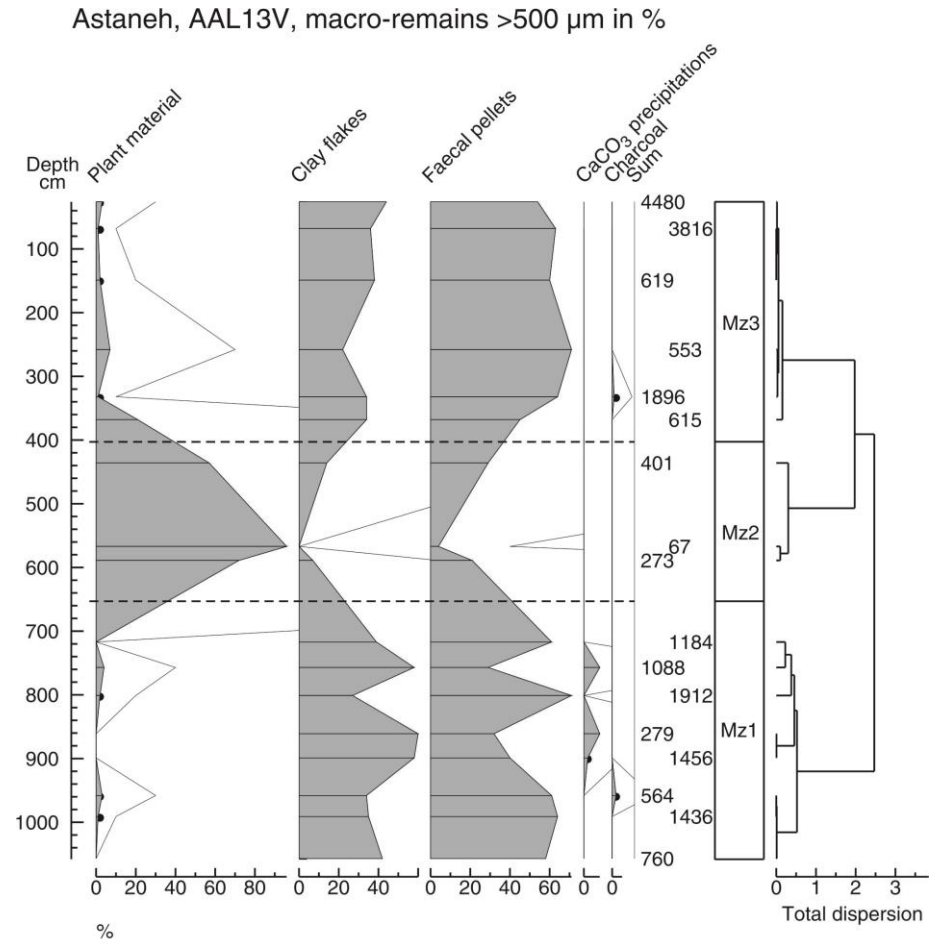


Fig. 4.29. Percentages of macro-remains above 500 μm (diagram at the top) and concentrations (diagram at the bottom) in the AAL13V sequence. Black dots represent very low concentration of macro-remains.

4.3.2.3 Palynology

Palynology analyses were performed by Professor S. Leroy on the sequence AAL13V and the text was written by her. Twelve samples from the sequence were chosen to study palynology (Fig. 4.30). Three samples were barren: one at 700 cm depth and two in the upper 150 cm. The concentrations of the other samples were rather low. Moreover, the palynomorphs were generally not well preserved. These two characteristics make this sequence not ideal for palynology. Extremely high values of fungal spores characterise the whole sequence. Hardly any aquatic algae spores, but some psilate fern spores were observed.

In the arboreal pollen (AP), *Alnus* is clearly dominant. The other frequent tree pollen are *Quercus* and *Pterocarya*. In the non-arboreal pollen (NAP), the diagram is dominated by Amaranthaceae, Asteraceae, Poaceae and Cyperaceae pollen grains.

No aquatic pollen occurs, except in two samples at 653 and 554 cm depth (across the two pollen zones): *Typha-Sparganium* (26 and 13 %, respectively) and *Salvinia*.

The sums of some key palynomorphs that are used in interpretation are presented in Fig. 4.30. Based on the results, the sequence is divided to three zones:

Pz1, from base to 690 cm

Alnus is dominant (around 20%) with c. 5 % of *Quercus* and of *Pterocarya*. *Pinus* and *Ephedra* are present. In the NAP, *Artemisia* and Amaranthaceae are dominant, with frequent Liguliflorae, Tubuliflorae and Poaceae.

Pz2, from 690 cm to 600

This zone is characterised by maximum aquatic pollen including: *Typha-Sparganium* (26 % at 653 cm) and *Salvinia*. Cyperaceae increase up to 63% at 650 cm.

Pz3, from 600 cm to 75 cm

The percentages in this zone are highly variable due to strong changes in *Alnus* (3 to 78%) corresponding to opposite changes in Amaranthaceae. All the other trees drop to very low values. A general drop of *Artemisia* is observed. Liguliflorae and Tubuliflorae remain stable, as well as Poaceae. Two samples at the top of this zone were too poor to be significant.

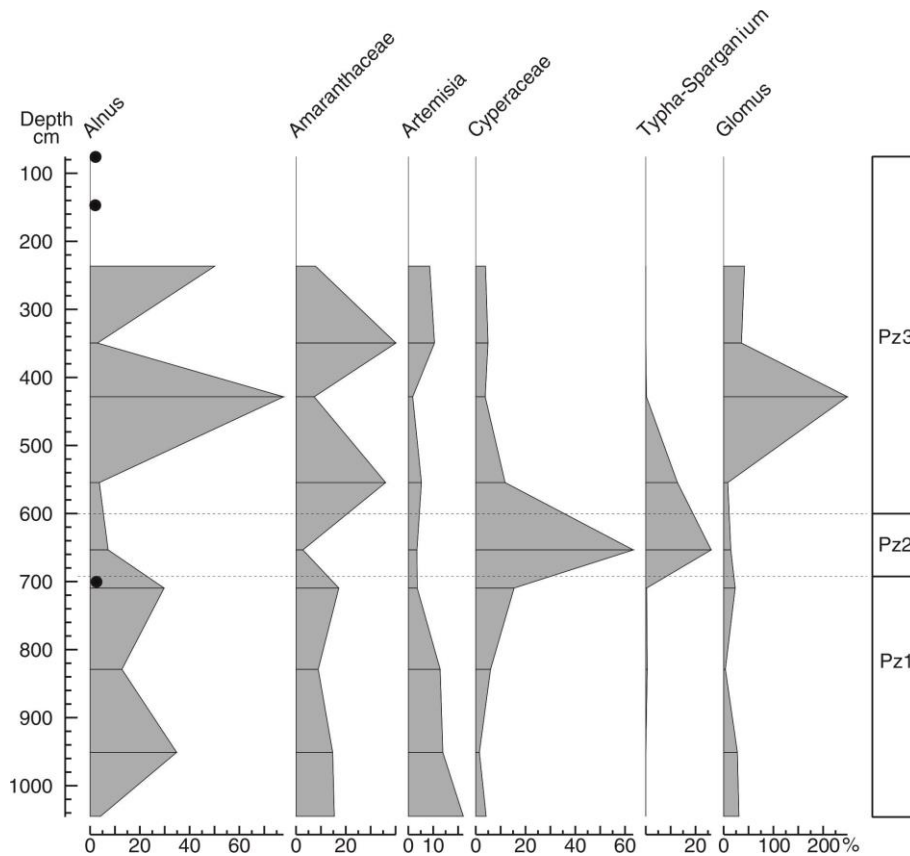


Fig 4.30. Palynological diagram of AAL13V sequence, including curves of some significant palynomorphs. Large black dots represent barren samples.

4.3.2.4 Chronology

Three radiocarbon dates were obtained from one root or branch and from two sets of rootlets at depths of 956, 589 and 142 cm along the sequence (Table 4.4).

Table 4.4. Radiocarbon dates of the samples from AAL13V. Calibrated ages are reported for 2σ range with highest probabilities shown in parentheses. Dates from ANSTO (OZR) and Queen's University Belfast (UBA).

Laboratory number	Sample ID	Depth (cm)	Material Type	^{14}C Age (yr BP)	$F^{14}\text{C}$	Calibrated yr AD (2σ range)	Median Probability
OZR388	AAL2-46-48	142	rootlets	modern	1.2584 ± 0.0100	1979-1983 (87.7 %)	-
OZR389	AAL7-15-17	589	rootlets	200 ± 40	-	1723-1816 (52.1%)	1769
UBA-22974	AAL10-90	956	Root/branch	1900 ± 30	0.7893 ± 0.0030	50-179 (93.1%)	103

The raw age for the root/branch sample at the depth of 956 cm is 1900 ± 30 BP. Its calibrated age at 95.4% probability (2 sigma) shows three possible ages: AD 50-179 (93.1% probability), AD 187-213 (5.1% probability) and AD 29-38 (1.8% probability) (Fig. 4.31 A). The raw age for the rootlets at the depth of 589 cm is 200 ± 40 BP and the calibrated age at 95.4% probability (2 sigma) shows four possible ages: AD 1723-1816 (52.1% probability), AD 1642-1697 (26.9% probability), AD 1916-1950 (16%) and AD

1834-1878 (4.9% probability) (Fig. 4.31 B). For the top sample, the post –bomb calibration at two sigma shows four possible ages: AD 1959 (1.7% probability), AD 1961-1962 (10.2 % probability), AD 1979-1983 (87.7 % probability) and AD 1984 (0.4 % probability) (Fig. 4.31 C).

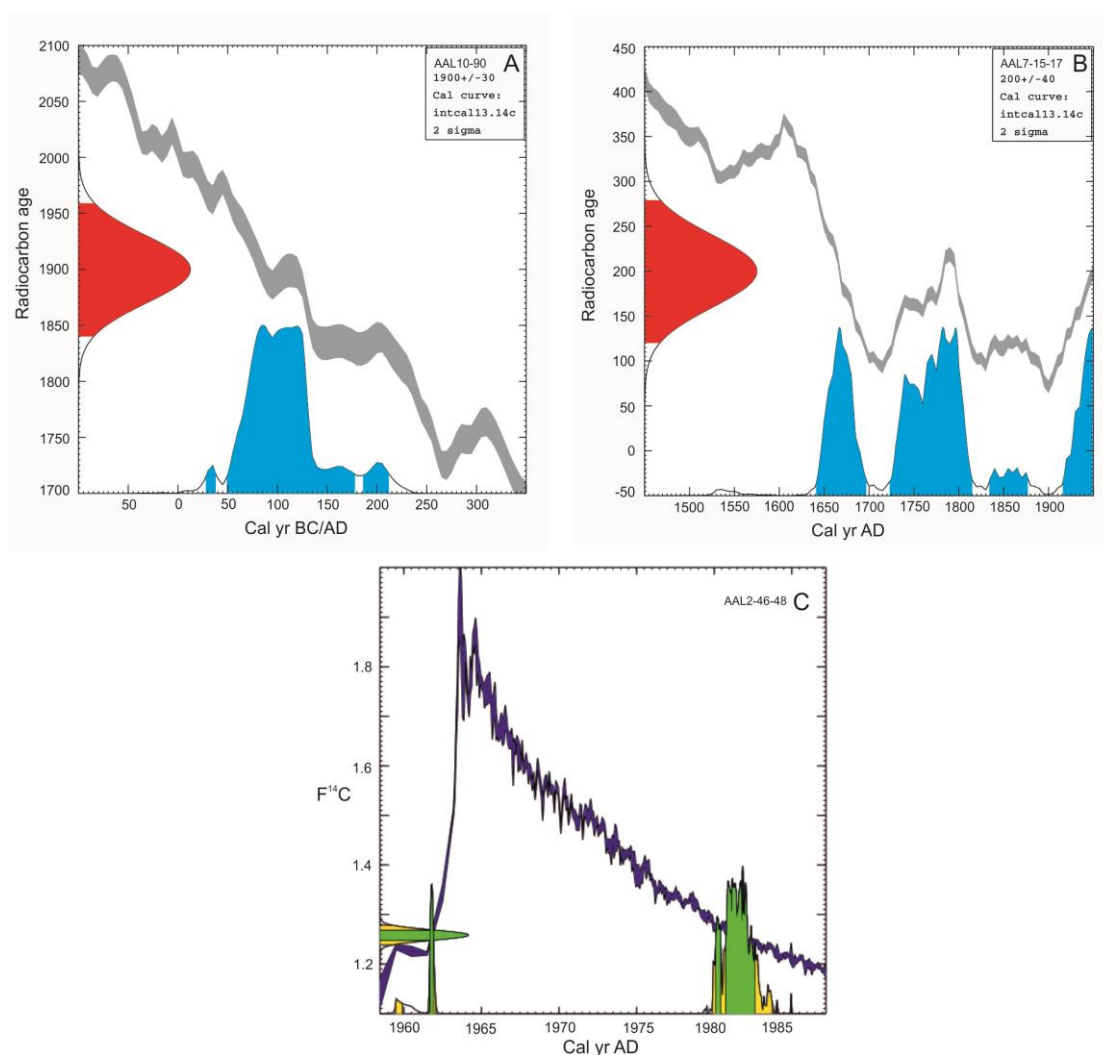


Fig. 4.31. Calibrated age for a root/branch at a depth of 956 cm (A), rootlets at 589 cm (B), and rootlets at 142 cm (C), AAL13V sequence.

4.4 Coastal lagoons

Coastal lagoons including the Zibakenar, the Kiashahr and the Amirkola Lagoons have been studied using a large number of cores (Tables 3-6, Appendix A).

4.4.1 Zibakenar Lagoon

Sediment cores with a maximum composite depth of 220 cm were taken using a gravity corer, a percussion corer and a Livingstone corer from Zibakenar (Fig. 4.32). Coring was made from a platform, as water depth around the middle of Zibakenar Lagoon (e.g. ZL11L1 and ZL11L2) is 185 cm.

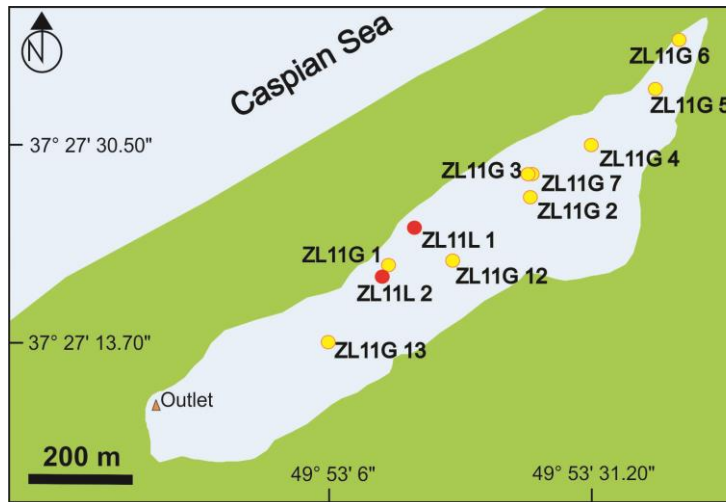


Fig. 4.32. Location of cores taken from Zibakenar Lagoon. Red dots represent location of core taken by Livingstone corer and yellow dots location of cores taken by gravity corer.

In Fig. 4.33 the core photos are shown from the west to the east of the lagoon. The horizontal axis shows the relative distance between the coring stations. However, when the distances between the locations that are very close to each other, they have been exaggerated (e.g. ZL11G3 and ZL11G7 or ZL11L2A and ZL11L2B). The vertical axis represents the composite depth of the cores.

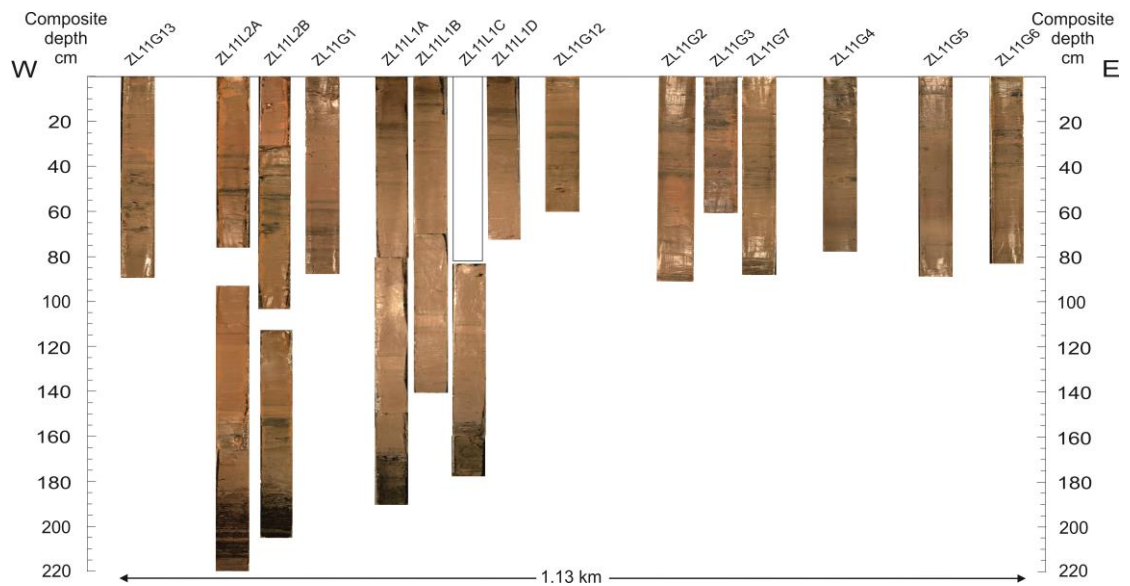


Fig. 4.33. Core photos are shown from the west (left) to the east (right) of the lagoon.

4.4.1.1 Sedimentology

MS measurements and standard core description were performed on all the cores. The MS results show a significant variation along the cores (Fig. 4.34). In general, the bottom of the long sequences (i.e. ZL11L2A, ZL11L1A and ZL11L1C, Fig. 4.34) contain high MS value (up to 32) followed by a significant sharp decrease (less than 4) upward. The MS values of the short cores are low and remain fairly constant.

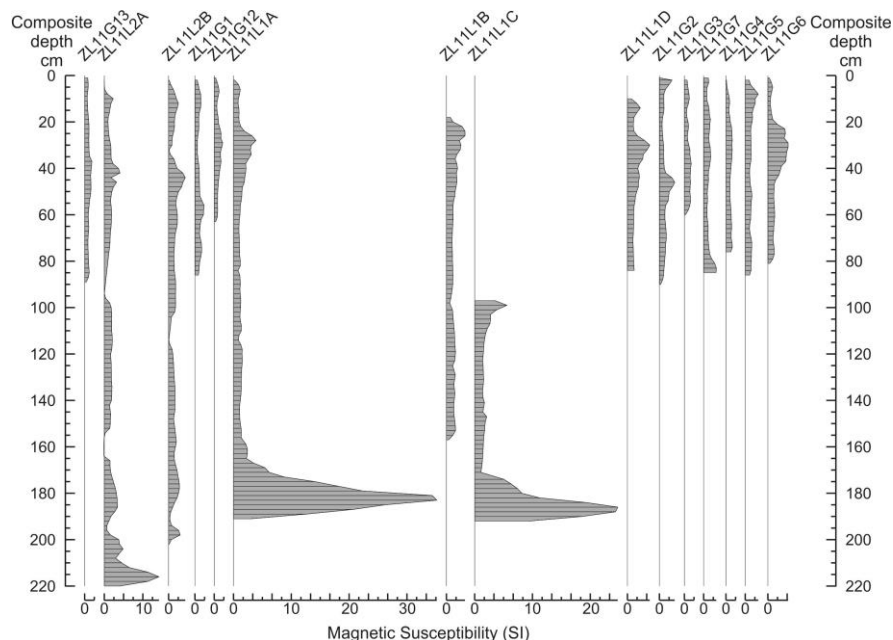


Fig. 4.34. MS values of the cores taken from the Zibakenar Lagoon. Diagrams are arranged from the west (right) to the east (left) of lagoon.

The Zibakenar Lagoon infill consists of different sediment layers (Fig. 4.35). From the bottom to the top, these layers contain: dark grey silty sand that appears only at the base of the long cores (ZL11L2A, ZL11L1A and ZL11L1C). Following this, a dark grey silty sand layer with plant remains appears. This layer continues by olive grey to olive silt with bivalve shells and rootlets. Subsequently, a thin red silt layer is followed by a thick layer of reddish brown to yellowish brown silt without any specific structure. The top horizon consists of bioturbated reddish brown to yellowish brown silt with horizons of dark greyish sandy silt and an organic rich layer (Fig. 4.35). In relatively shallower places (e.g. ZL11G1, G3, G4 and G6), a layer of very dark greyish silt occurs with abundant remains of emerged aquatic plants.

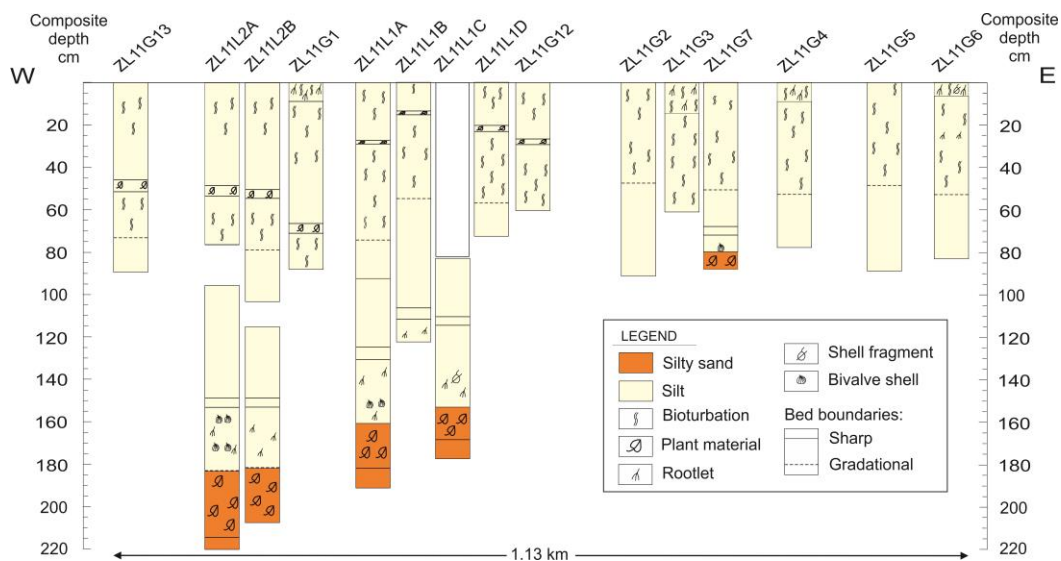


Fig. 4.35. Sedimentological logs of the cores from the Zibakenar Lagoon based on core description and grain size analysis. The logs are arranged from the west to the east of the lagoon.

In order to find out about the depositional environment of different sedimentary facies in this basin, the longest sequence (ZL11L2, A and B) has been selected for further study and it is described in more details. A composite depth has been prepared, made of the two parallel cores A and B. Indeed, section B has been used to fill the gap between the first and the second section of core A (i.e. 95-76 cm) and a complete sequence could then be constructed.

More specifically, the sedimentology of the core ZL11L2 from the bottom to the top is in composite depth:

Sz1, 220-182 cm: alternation of dark grey silty sand with plant remains. The boundary between this facies and the following facies is gradational.

Sz2, 182-151 cm: olive grey silt with a very well preserved pair of bivalves (*Cerastoderma glaucum*) at a depth of 171 cm (Fig. 4.36) and *Dreissena polymorpha* at a depth of 160 cm. this facies has a sharp boundary with the facies at the top.

Sz3, 151-76 cm: reddish brown silt, with a red layer of silt at the bottom with a sharp boundary (151-147 cm), which can be used as a key layer for correlation. There is a gradational boundary between this facies and the following facies.

Sz4, 76-0 cm: bioturbated reddish brown silt dark with rootlets and plant material.



Fig. 4.36. A well-preserved pair of bivalves shell, *C. glaucum*, at a composite depth of 171 cm, ZL11L2, Zibakenar Lagoon (Photo: by courtesy of F. Wesselingh)

Sedimentological analysis (including grain size and LOI analysis), ^{14}C dating, radionuclide dating, macrofossil analysis and palynological study were performed on this sequence (ZL11L2).

Granulometric data obtained from 67 samples show that the base of the core (220-182 cm) mostly consists of sand, with up to 41% silt. The top part of the sequence (182-0 cm) is mostly dominated by silt, with up to 12% of clay (Fig. 4.37 and 4.38). All the samples are poly-modal, showing three different modes.

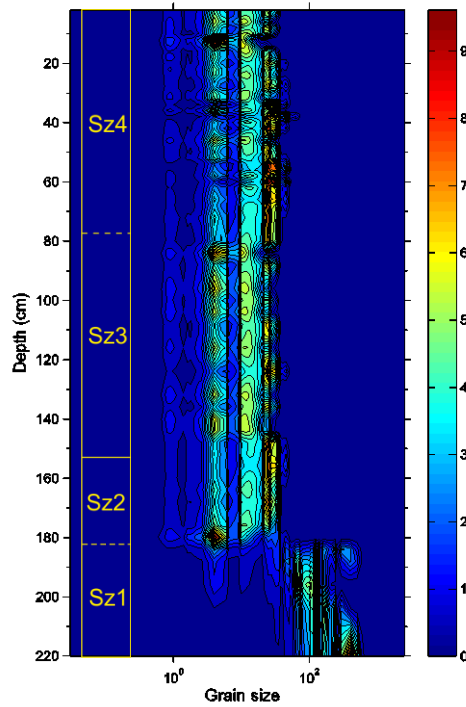


Fig.4.37. 3D plot of grain size data in μm for the sequence ZL11L2: the dark blue colour represents the lowest volume (%), while the red colour shows the highest volume (%). Sz: sedimentological zone.

The magnetic susceptibility of this sequence shows a significant variation along the core (fig. 4.38). The results indicate a substantial increase at the base of the core with a peak at a depth of 216 cm. Following this, the MS decreases and is relatively constant along the top 160 cm with two minor peaks at depths of 42 and 10 cm.

Overall, the content of organic matter shows a slight ascending trend from the base (Fig. 4.38). However, the basal 38 cm have two significant peaks of organic matter content at 209 and 197 cm depth with the amounts of 22 and 21 % respectively. The carbonate contents have a background of 4% and vary along the core with a gradual increase from the bottom upward (Fig. 4.38).

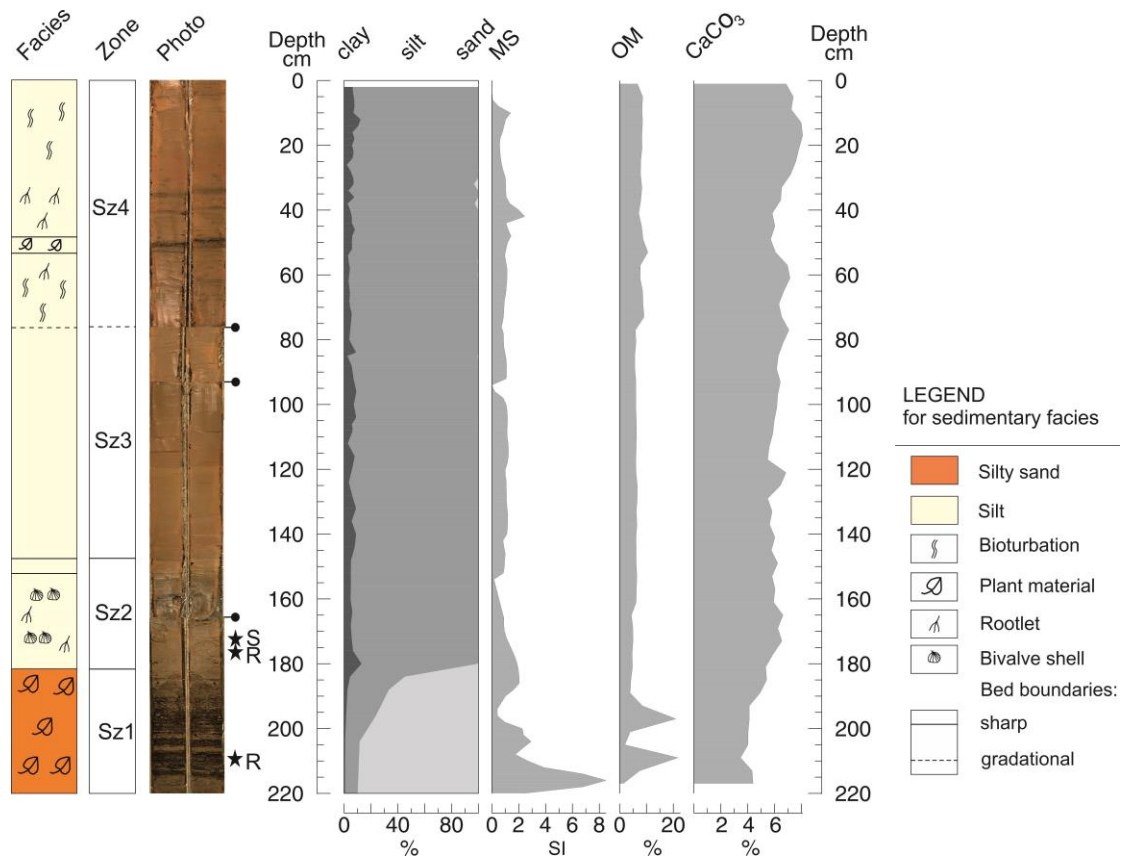


Fig. 4.38. Sedimentary log for the Zibakenar sequence (ZL11L2), displaying sedimentology (Sz: sedimentological zone), core photo, grain size (clay, silt and sand), magnetic susceptibility (MS), organic matter (OM) and calcium carbonate (CaCO_3). Black stars refer to the depth of the radiocarbon dated samples (R: rootlet, S: shell), and black pin symbols showing the core section limits.

4.4.1.2 Macro-remains

Thirteen samples from the ZL11L2 sequence were chosen to study macro-remains. Seven different macro-remain types have been identified in the fraction $>500 \mu\text{m}$ and eight macro-remain types in the fraction $>125 \mu\text{m}$. Identification of bivalve species was performed by Dr F. Wesselingh, Naturalis Biodiversity Centre, Netherlands. Macro-remain percentages and concentrations for the fraction 500 and 125 μm are presented in Fig. 4.39 and 4.40. The zonation was applied on percentages in the fraction 500 μm . In order to simplify the explanation, changes in macro-remains have been described based on the percentages of macro-remains in the 500 μm fraction. Meanwhile the main changes for the 125 μm fraction have been described. Overall the concentrations are very high at the base of the sequence and drop to nearly nothing at the top. Based on the results, the sequence is divided into four zones:

Mz1, from base to 184 cm (3 samples)

This zone is characterized by maximal values of plant material (up to 100%), with some bivalve shells (6.5%), minerals including quartz, plagioclase feldspar, calcite and muscovite (2.5%), faecal pellets (3%) and clay flakes (1.5%). In the fraction of 125 μm ,

the amounts of mineral and bivalve reach to up to 60% and 14%, respectively. Foraminifera tests (5%) and Ostracod valves (9%) appear in the fraction 125 µm. All the observed Foraminifera in Zibakenar Lagoon belong to *Ammonia beccarii* species. The bivalve shells in larval stage that contains species complexes are very difficult to distinguish (F. Wesselingh, pers. comm.). All the bivalve shells observed in the macro-remains samples are juvenile. These belong to Cardiidae and Semelidae family (Fig. 4.41 A and B). The largest shells either belong to *Monodacna edentula* or to *C. glaucum* (Cardiidae family). The further presence of adult shells of *C. glaucum* in the upper zone (i.e. Mz2 / Sz2) makes it more likely to consider them as *C. glaucum*. The bivalves in fig. 4.41 B belong to the invasive *Abra* cf. *segmentum* (Semelidae family). However, this is not absolutely certainty because of the complexity of distinguishing juvenile shells (F. Wesselingh, pers. comm.).

Mz2, from 184 to 154 cm (2 samples)

This zone is characterised by bivalve shells (*A. cf. segmentum* and *M. edentula* / *C. glaucum*) (1.5%), a sharp rise in faecal pellets (82%) and clay flakes (65%), and a drop in plant materials (9%). Furthermore, 10% minerals, 1% Foraminifera tests (*A. beccarii*) and 1% Ostracod valves have been observed in fraction of 125 µm. Adult bivalve shells including Dreissenidae and *C. glaucum* have been observed in this zone.

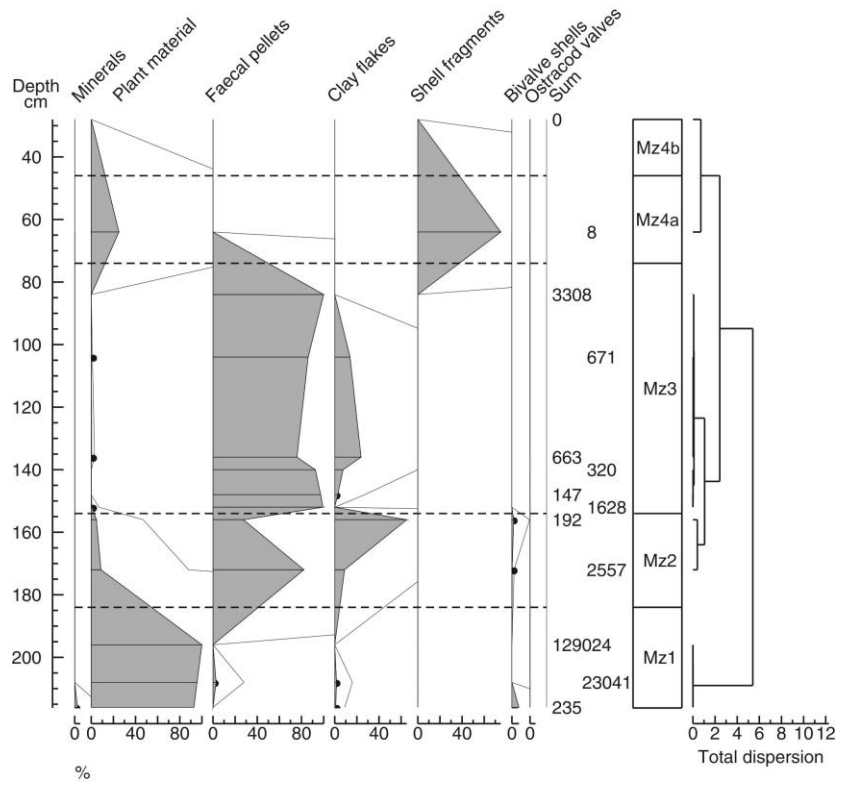
Mz3, from 154 to 75 cm (6 samples)

The third zone is marked by high values of faecal pellets especially at a depth of 85 cm, where it even reached 100%. Moreover, this zone contains clay flakes (0-24%) and only a small amount of plant materials (0.1-1%). In the fraction of 125 µm, this zone is characterised by up to 99% faecal pellet and 23% minerals.

Mz4 a and b, from 75 cm to the surface (2 samples)

This zone that is characterized by plant materials (25%) and shell fragments (75%) at a depth of 66-64 cm is very poor and at a depth of 30-28 cm no macro-remains have been observed. However, in the fraction 125 µm, 97% plant material and 3% mineral have been identified at a depth of 30-28 cm. Furthermore, 15% Foraminifera, 61% faecal pellets and 18% minerals have been identified at 66-64 cm.

Zibakenar, ZL11L2, macro-remains >500 µm in %



Zibakenar, ZL11L2, concentration of macro-remains >500 µm

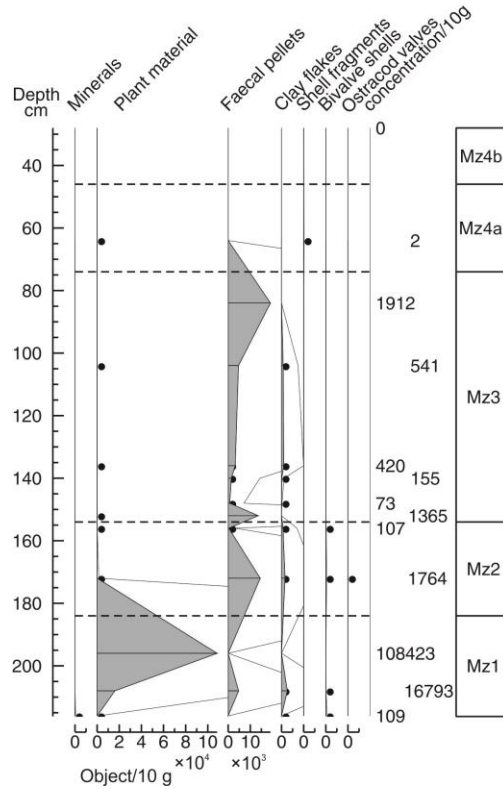
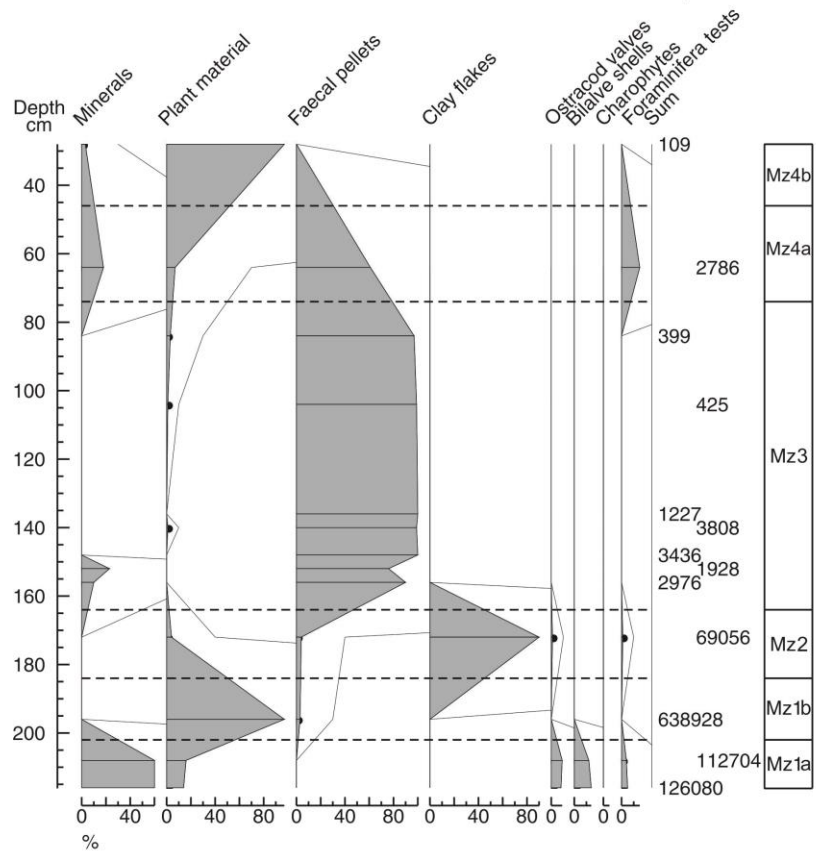


Fig. 4.39. Percentages of macro-remains above 500 µm (the diagram at the top) and concentrations (the diagram at the bottom) in the ZL11L2 sequence. Black dots represent very low concentrations of macro-remains.

Zibakenar, ZL11L2, macro-remains >125 µm in %



Zibakenar, ZL11L2, concentration of macro-remains >125 µm

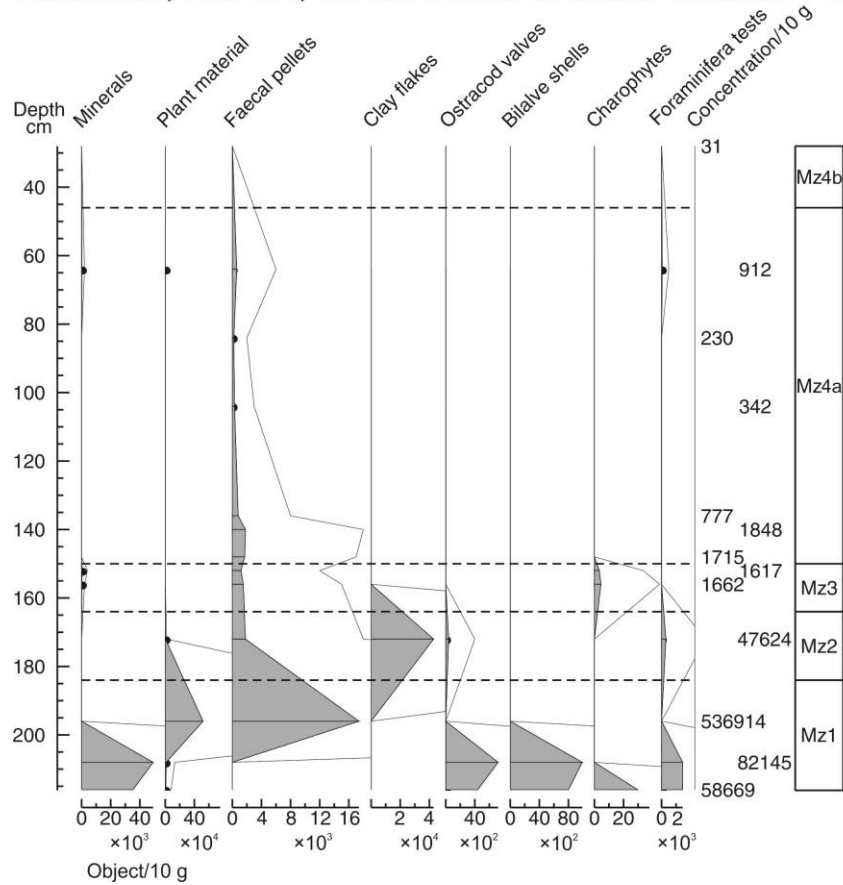


Fig. 4.40. Percentages of macro-remains above 125µm (the diagram at the top) and concentrations (the diagram at the bottom) in the ZL11L2 sequence. Black dots represent very low concentration of macro-remains.

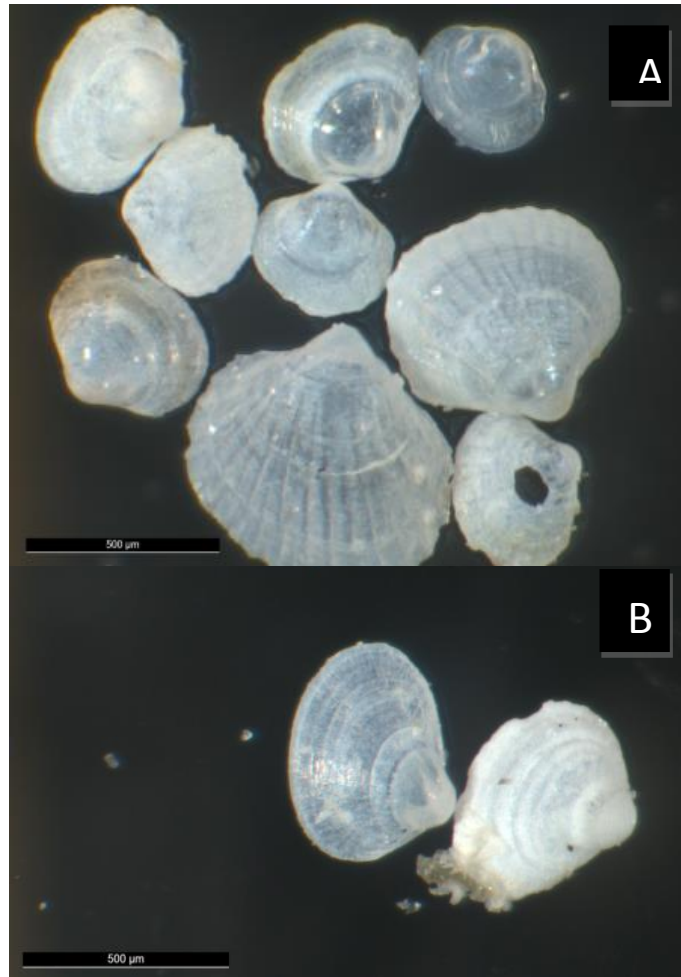


Fig. 4.41. Bivalve shells observed at a depth of 216-218 cm, ZL11L2A. A: Cardiidae Family, B: *Abra* cf. *segmentum* (Semelidae family) (Photo by courtesy of F. Wesselingh)

4.4.1.3 Palynology

Palynology analyses were performed by Professor S. Leroy on the ZL11L2 master sequence and the text was written by her. Sixteen samples from the master sequence were chosen to study palynology. Most samples came from core A, with only one from core B, i.e. at 86.5 cm depth. Three samples were barren between 114 and 94 cm.

In addition, two surface samples were taken at the same time (2011) along the Sefidrud in order to provide an idea of source of sediments in Zibakenar Lagoon and also the representation of the modern vegetation in the pollen assemblages. These two samples also turned out to be barren (Table 4, Appendix A).

In the core sequence, the preservation of the palynomorphs is generally good, with rare exceptions (e.g. at 134 cm depth). The concentrations are not high with usually around 5000 grains/ml, at the exception of the richer top sample (11,500 grains/ml). Three barren samples (114 to 94 cm) were also encountered.

The selected key palynomorphs, used in interpretation, are presented in Fig. 4.42. Three pollen zones have been defined by well-marked limits:

Pz1, from base to 189 cm

The AP are largely dominated by *Alnus* (up to 62 %). Dinocysts and Foraminifera linings are frequent. Fungal spores are abundant.

Pz2, from 189 to 138 cm

A sharp decrease of *Alnus* occur a cross this zone. From the base of this zone to its top, the values of dinocysts and Foraminifera drop. A minimum, which is nevertheless still of 50 to 90 % of the pollen sum, is reached for the fungal spores in the middle of this zone.

Pz3, from 138 cm to top

Alnus displays now the lowest values of the diagram, i.e. 3 to 21 % only. It is noteworthy to indicate that the first three samples of this zone, between 134 and 86 cm depth, are devoid of freshwater algae remains and of dinocysts. This depth range also contains the three barren samples (114 to 94 cm; grey strip on Fig. 4.42) and the maximum of fungal spores (i.e. 261% of the pollen sum).

From 66 cm depth upwards, the presence of some dinocysts and Foraminifera is again noted. Fungal spores are generally extremely abundant. The topmost sample (0.5 cm) contains a single peak of fresh water plants and fresh water NPPs, as well as a drop of the fungal spore values.

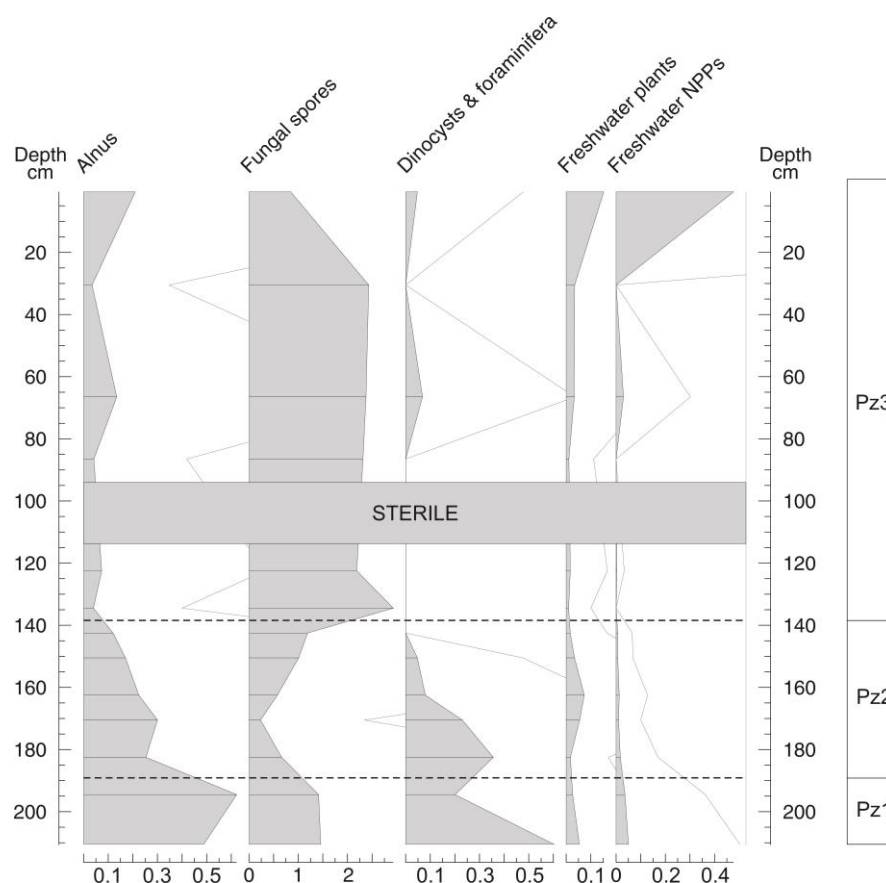


Fig 4.42. Diagram of ZL11L2 Sequence, including the sums of some significant palynomorph. Grey strip: barren samples.

4.4.1.4 Chronology

Radionuclide analyses were made on ZL11L2A sequence at the Environmental Change Research Centre, University College London, by Dr H. Yang and the text was written by him. ^{210}Pb activity measured on the top section of ZL11L2A1 appeared to reach equilibrium with the supported ^{210}Pb activity at a depth of about 74 cm (at the base of the top section). However, total ^{210}Pb and supported ^{210}Pb activities in the lower sediments (Fig. 4.43 A) suggest that the apparent equilibrium depth at c. 74 cm might have been due to dilution by fast sediment accumulation. Moreover, unsupported ^{210}Pb activities, calculated by subtracting supported ^{210}Pb activity from total ^{210}Pb activity, vary very irregularly with depth, and show little net decline between 2 and 72 cm (Fig. 4.43 B), suggesting an increasing trend in sediment accumulation. The ^{137}Cs activity versus depth profile has poorly resolved peaks between 35 and 67 cm. Detectable ^{241}Am at 58–59 cm (Fig. 4.43 C) suggests fallout from the atmospheric testing of nuclear weapons that peaked in 1963. Similar to the unsupported ^{210}Pb activities between 58 and 61 cm, the relatively low level of ^{137}Cs activities in the same section is likely to be a result of sediment dilution. High sediment accumulation may have occurred at the time when maximum deposition has removed the ^{137}Cs peak away from 56–63 cm. Deeper samples also showed ^{137}Cs concentrations, suggesting a post-1950 date. However, no further detection of ^{241}Am was possible in these levels. In the light of the results of both ^{210}Pb and ^{137}Cs , radionuclide chronologies can only provide a suggested chronology for post-1950 above 156 cm depth due to high and irregular accumulation rates in this sequence.

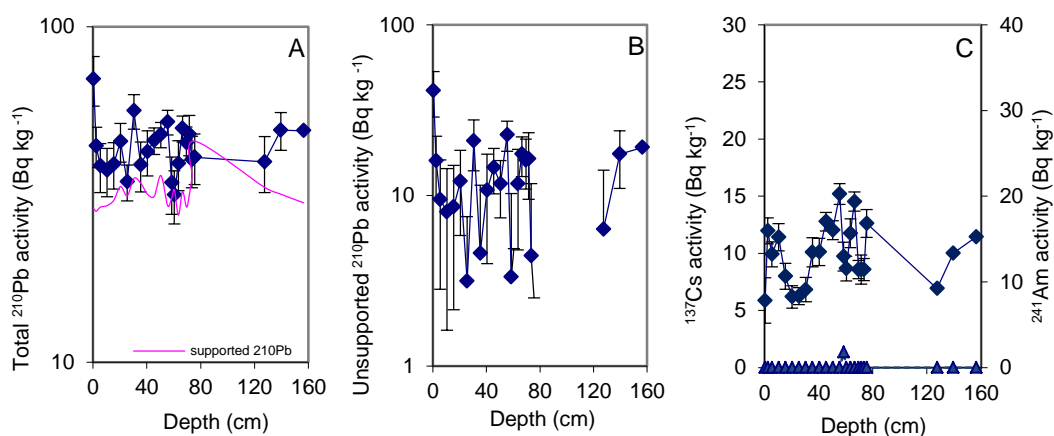


Fig. 4.43. Fallout radionuclide concentrations in core ZL11L2A taken from Zibakenar Lagoon, showing A: total ^{210}Pb , B: unsupported ^{210}Pb , and C: ^{137}Cs (diamond at the top) and ^{241}Am (triangle at the bottom) concentrations versus depth, (H. Yang, UCL).

From the third core section, three radiocarbon dates were obtained from two pieces of rootlets and one shell (*C. glaucum*) at depths of 209 (Sz2), 177 (Sz3) and 171 cm (Sz2), respectively (Table 4.5 and Fig. 4.38). CALIB Radiocarbon Calibration programme,

version 7.0 (CALIB 7.0) with Intcal13 (Reimer et al., 2013) were used to calibrate the obtained age from the first sample at 209 cm (Fig. 4.44). Radiocarbon dating places AD 30 at 209 cm, which is very different from the other dating results and has been rejected due to the possibility of reworking. Other indicators of sediment reworking in sequence Sz1 are discussed in chapter five. Samples located at 177 and 171 cm exhibited post-bomb radiocarbon activities. The sample at 177 cm was calibrated using CALIBomb programme (Reimer et al., 2004) with NHZ2 (Northern Hemisphere Zone) and Intcal13 (Reimer et al., 2013) (Fig. 4.44). However, CALIBomb is inappropriate for calibrating marine samples (e.g. shell sample at 171 cm). The ocean's uptake of bomb carbon was much slower and less dramatic than that of the atmosphere. At the moment there exists no agreed calibration curve for the oceans (R. Reimer, pers. comm.). Therefore, only the sample at 177 cm could be used in our interpretation.

Table 4.5. Radiocarbon dates from Queen's University Belfast, calibrated ages are reported for 2 σ range with highest probabilities shown in parentheses. *Median probabilities on the CALIBomb programme output are not available, because the ages obtained from CALIBomb are not sufficiently widely spaced (P. Reimer, pers. comm.).

Laboratory number	Sample ID	Depth (cm)	Material Type	¹⁴ C Age (yr BP)	F ¹⁴ C	Calibration programme	Calibrated (2 σ range)	Median Probability
UBA-22722	ZL2A3-7	171	Shell (<i>C. glaucum</i>)	modern	1.1174 ± 0.0031	-	-	*
UBA-25613	ZL11L2A3-12-14 cm	177	Root	modern	1.0326 ± 0.0056	CALIBomb with NHZ2	AD 1955-1956 (95.4%)	*
UBA-23787	ZL11L2A3-44-46cm	209	Root	1971±31	0.7824 ± 0.0030	CALIB 7.1 with Intcal13	BC 45- AD 85 (95.4%)	AD 30

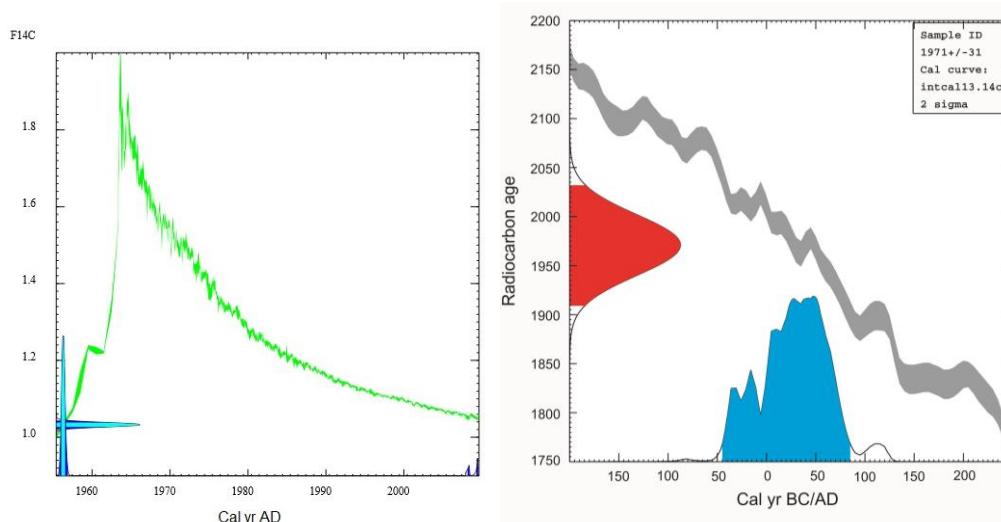


Fig. 4.44. Interception between F¹⁴C and the calibrated age with calibration curve from the rootlet sample at 177 cm (the left hand side), and interception between the radiocarbon age and the calibrated age with calibration curve from the rootlet sample at 209 cm (the right hand side).

Spheroidal carbonaceous fly-ash particles (SCPs) analyses were performed on master sequence ZL11L2A by Professor N. Rose at University College of London and text was written by him. SCPs are present in low but detectable concentrations in ZL11L2A1 above 65 cm depth (Fig. 4.45). Below 65 cm, no SCPs are observed. In lakes with high sediment accumulation rates, the start of the SCP record often occurs in c.1950, where an increase in contamination from high temperature fossil-fuel combustion increases SCP inputs from below to above the analytical limit of detection for the first time. This is seen at many sites across the world (Rose, 2015), and would suggest that in ZL11L2A1, 65 cm could be ascribed a 1950 date in agreement with the tentative radiometric chronology. SCP data cannot provide additional evidence for a recent date for the lower section of the core, but their absence could simply be due to a combination of low concentrations and high sediment accumulation rate diluting the signal.

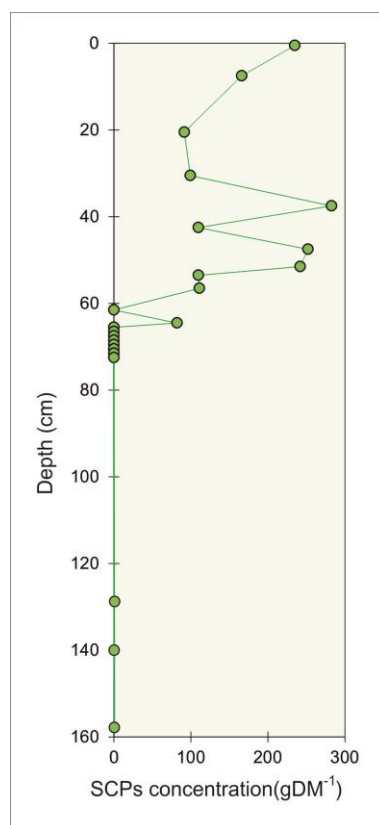


Fig.4.45. SCPs concentration versus depth in ZL11L2A1 (N. Rose, UCL)

4.4.2 Kiashahr Lagoon

Gravity and percussion cores from 14 locations with a maximum depth of 120 cm at KL11G5 were taken from the Kiashahr Lagoon (Fig. 4.46 and Table 5, Appendix A). Kishahr harbour is located at south west of the lagoon and cores KL11G1, KL11G2, KL11G10 and KL11G9 were taken from the channel that is connection between the harbour and the sea. Kiashahr Lagoon is surrounded by swampy area (pattern area in Fig.

4.46) and a Wooden Bridge on the swamp is used for access to the beach. Cores KL11G11, KL11G12 and KL11G13 were taken from the swamp (Fig. 4.46).

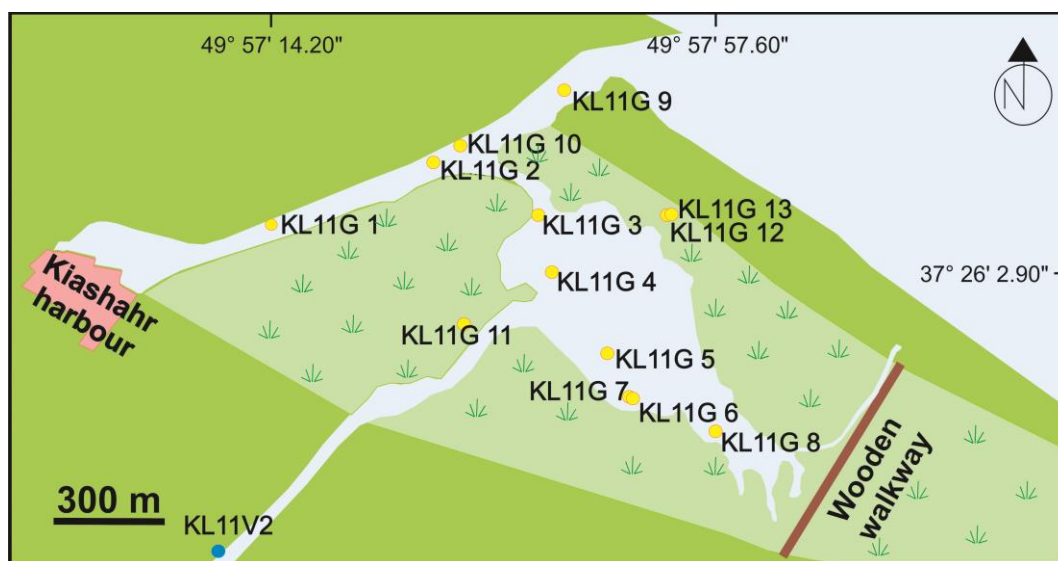


Fig. 4.46. The location of the gravity and percussion cores taken from Kiashahr Lagoon

Fig. 4.47 shows core photos from different part of lagoon.

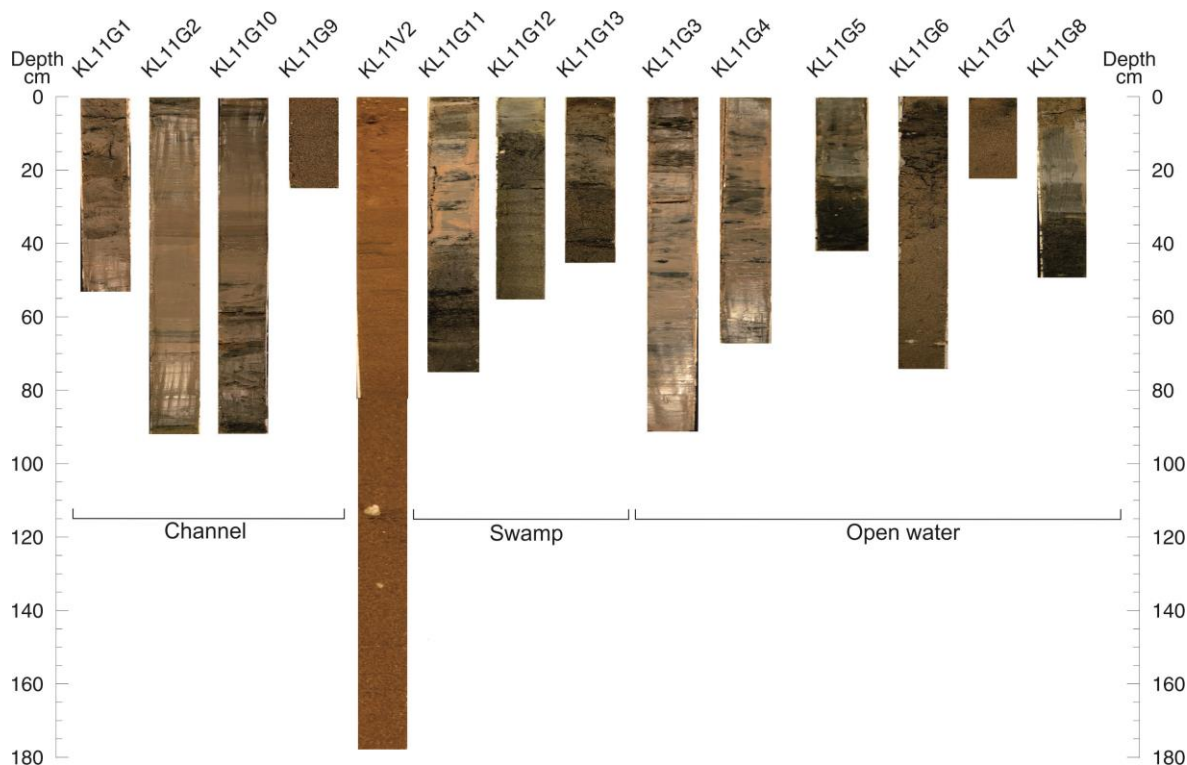


Fig. 4.47. Cores with a maximum depth of 178 cm taken by gravity and percussion corers from the channel, swampy area and intra lagoon of Kiashahr Lagoon.

4.4.2.1 Sedimentology

MS measurements and standard core description were performed on all the cores. The cores KL11V2, KL11G12 and KL11G13 in the overgrown lagoon (swamp) contain high

MS values (≥ 20 : Fig. 4.48). The MS values of the cores located in the margin of open water of the lagoon (KL11G3, KL11G6, KL11G7 and KL11G8) and channel (KL11G1, KL11G2, KL11G9 and KL11G10) (see Fig. 4.46 for locations) show medium MS values, up to five. The MS of the cores located in the open water of the lagoon have the lowest values (~ 1 : Fig. 4.48).

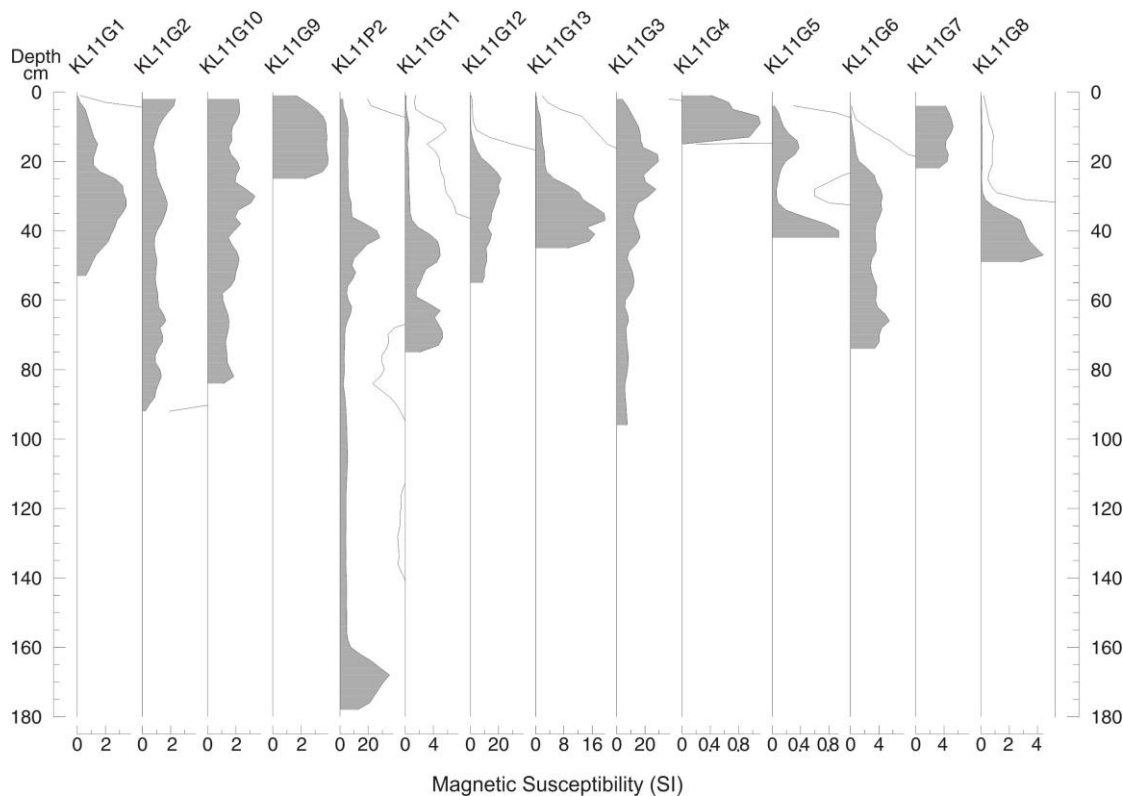


Fig. 4.48. The magnetic susceptibility values of the cores taken from the Kiashahr Lagoon.

The Kiashahr Lagoon consists of varied sediment layers (Fig. 4.49). In the open water cores, these layers contain brown silty sand with bivalve shells and rootlets, overlaid by greenish grey and reddish brown silt layers. The silt layer contains rootlets, bioturbation, bivalve and gastropod shells. More silt accumulation is observed in the north–west of the lagoon (e.g. KL11G3 and KL11G4), whereas more silty sand accumulation occurred in the south–east (e.g. KL11G5, KL11G6, KL11G7 and KL11G8).

The cores taken from swampy areas contain brown silty sand with rootlets, plant materials and gastropod shells. Furthermore, a bioturbated layer of reddish brown silt is observed between depths 40 and 9 cm, in the core KL11G11. The channel cores mainly contain bioturbated brown silt with rootlets and bivalve shells and thin layers of brown silty sand with bivalve shells and rootlets. Lack of sand in the channel is due to dredging operations associated with the change in its economical use from fishing to a commercial port in 2010 (Ramsar report 37, 2015). Core KL11G9 near the mouth of the channel contains homogenous brown silty sand brought by the CS (Fig. 4.49). The silty cores of the

open lagoon have similarity with the silty cores in the channel, such as silt without bioturbation, overlaid by silt with bioturbation. However, the silty layers in the channel are more brownish and the silty cores of open water contain greyish and brownish layers. It is also likely that the open water cores KL11G3 and KL11G4 consist of true lagoonal sediment whereas the silty cores of the channel may represent recent muds suspended after dredging.

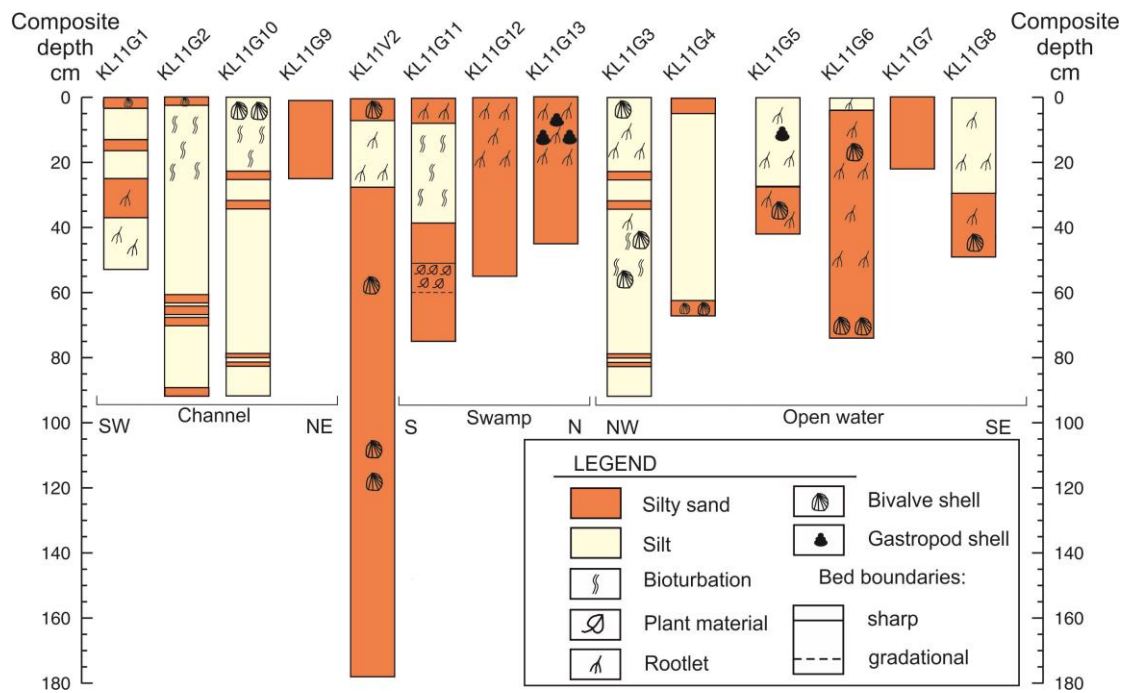


Fig. 4.49. Sedimentological logs of the cores from the Kiashahr Lagoon.

4.4.3 Amirkola Lagoon

Cores from 21 locations with a maximum composite depth of 119 cm were taken from the Amirkola Lagoon (Fig. 4.50, 4.51 and Table 6, Appendix A).

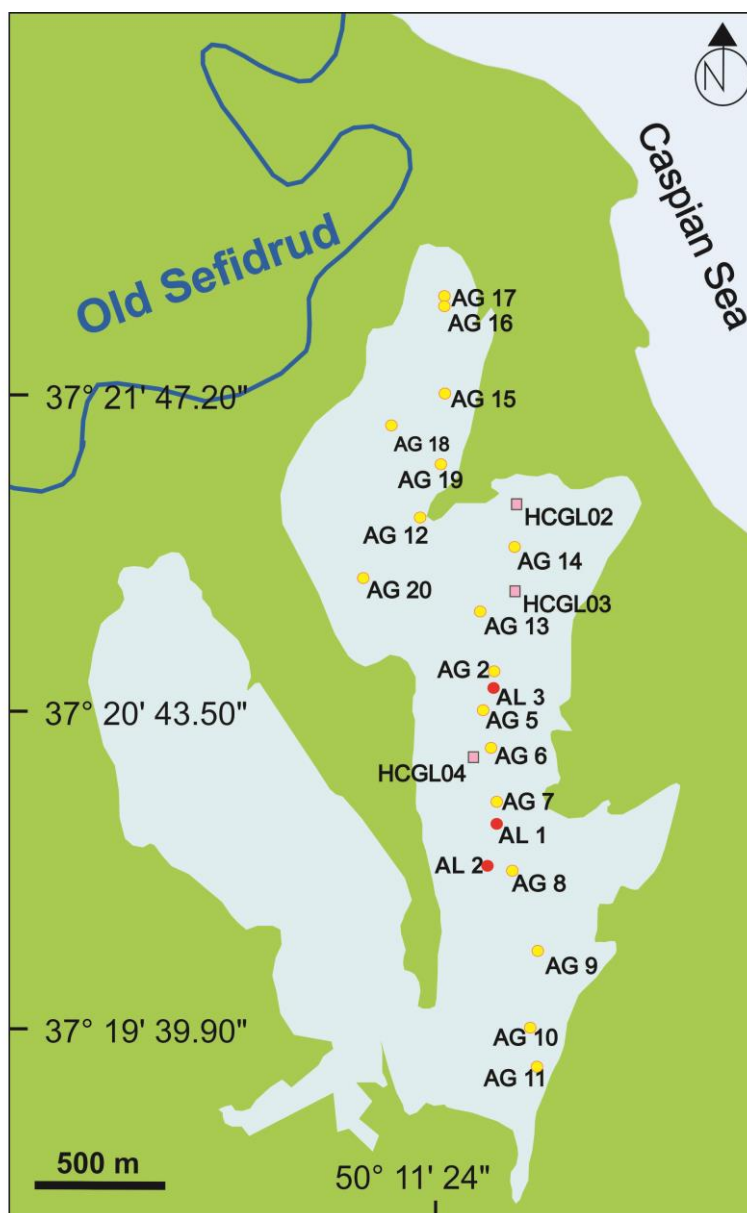


Fig. 4.50. Location of the cores taken from Amirkola Lagoon. Core identification has been simplified in this map, i.e.: AG17 full identification is AL11G17. Red dots represent the location of core taken by Livingstone corer and yellow dots the location of cores taken by gravity corer. Pink squares show location of cores in Leroy et al. (2011).

In Fig. 4.51 the cores are shown from the north to the south of the lagoon. The horizontal axis displays the relative distance between the coring and the vertical axis represents the composite depth of the cores.

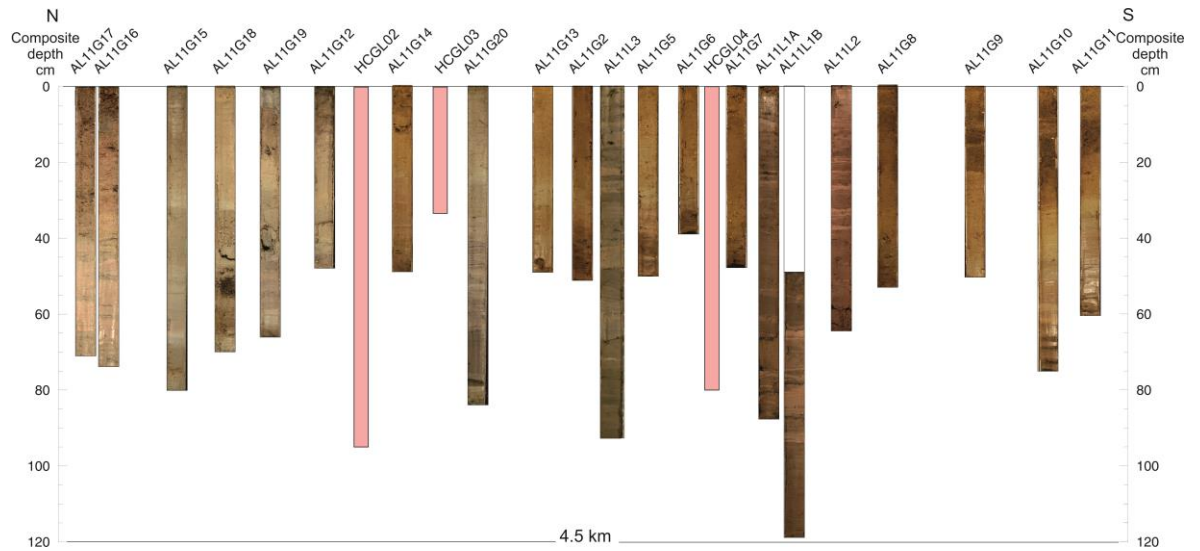


Fig. 4.51. Cores photos with a maximum depth of 119 cm taken by gravity and the Livingstone corers from the Amirkola Lagoon. Cores are shown from the North (left) to the South (right) of lagoon. Pink squares show location of cores in Leroy et al. (2011)

4.4.3.1 Sedimentology

MS measurements and standard core description were performed on all the cores. The MS results show a significant variation along the cores (Fig. 4.52). In general, the bottom of the sequences contains higher MS values followed by a significant sharp decrease upward. The MS values of the cores located in the middle of lagoon (AL11G2 to AL11G8) show higher MS values (up to 16) compared to the rest of the lagoon.

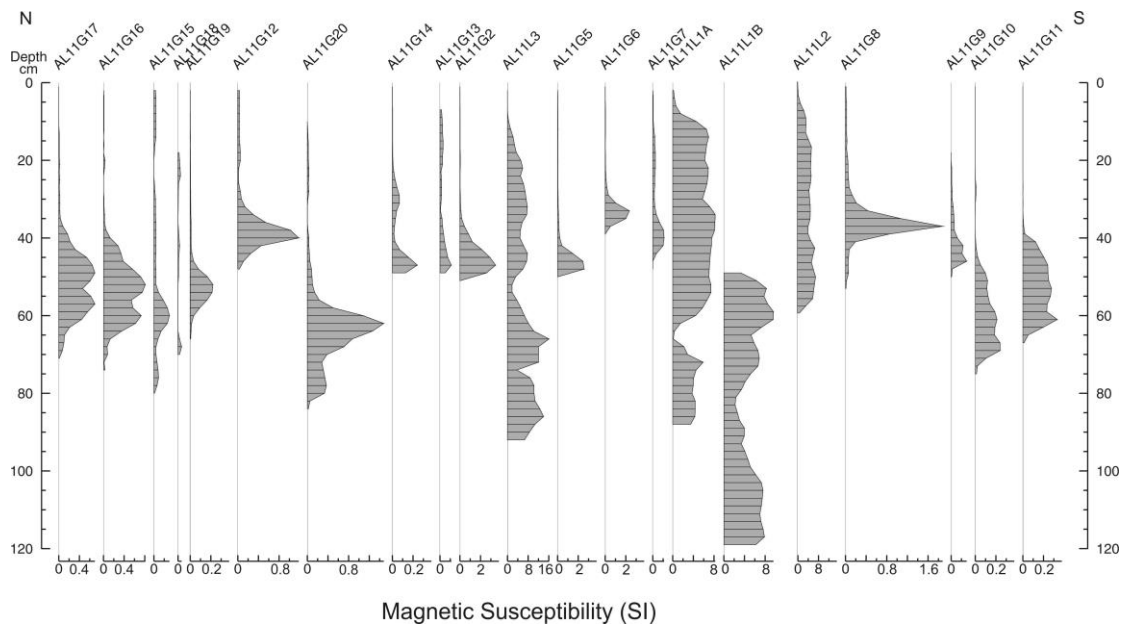


Fig. 4.52. Magnetic susceptibility values of cores taken from Amirkola Lagoon. Cores in the diagram are arranged from the north (left) to the south (right) of the lagoon

The Amirkola Lagoon infill consists of clearly distinct sediment layers. From the bottom to the top, these layers contain: brown silty sand that appears at the base of the long cores in the middle of the lagoon (e.g. AL11L3, AL11L1 and AL11L2). Following this, a

dark greyish brown sandy silt layer appears. This layer continues by olive grey and olive brown silt. Olive grey silt contains *Theodoxus pallasii* shells which have been observed in the cores: AL11G15 (at a depth of 22 cm), AL11G18 (36-48 cm), AL11G19 (17-26 cm), AL11G14 (22 cm), AL11G20 (34-37 cm), AL11G2 (19 and 30 cm), AL11G5 (31-26 cm), AL11G6 (20-23 cm) and AL11G7 (35-40 cm). Furthermore, *C. glaucum* has been observed in the sandy silt layer in the core AL11G8 and in the silty sand in the core AL11L1A. A very dark greyish brown silt layer has been observed at the top of the cores, which contains a considerable amount of plant material, rootlets and gastropods (Fig. 4.53).

The cores AL11G5 and AL11L2 have been selected for further study and are described in more details.

Sedimentology of the core AL11G5 from the bottom to the top is:

Sz1, 50-38 cm: dark greyish brown sandy silt with shell fragments (bivalve) and rootlets. This facies has a sharp boundary with the facies at the top.

Sz2, 38-31 cm: olive brown silt with shell fragments and rootlets

Sz3, 31-26 cm: olive grey silt with *T. pallasii*, shell fragments and rootlets, sandwiched between upper and lower layers with a gradual boundary.

Sz4, 26-14 cm: olive brown silt with shell fragments and rootlets. There is a gradual boundary between this facies and the following facies.

Sz5, 14-0 cm: very dark greyish brown silt with a considerable amount of plant material and rootlets, a *T. pallasii* at a depth of 11 cm and gastropod at a depth of 8 and 6 cm.

The sedimentology of the core AL11L2 from the bottom to the top is:

Sz1, 65-32 cm: brown silty sand without any specific structure

Sz2, 32-27 cm: dark greyish brown sandy silt without any specific structure, sandwiched between upper and lower facies with sharp boundaries.

Sz3, 27-12 cm: brown silty sand with shell fragments and rootlets. This facies has a sharp boundary with the upper facies.

Sz4, 12-0 cm: olive brown silt with shell fragments and rootlets

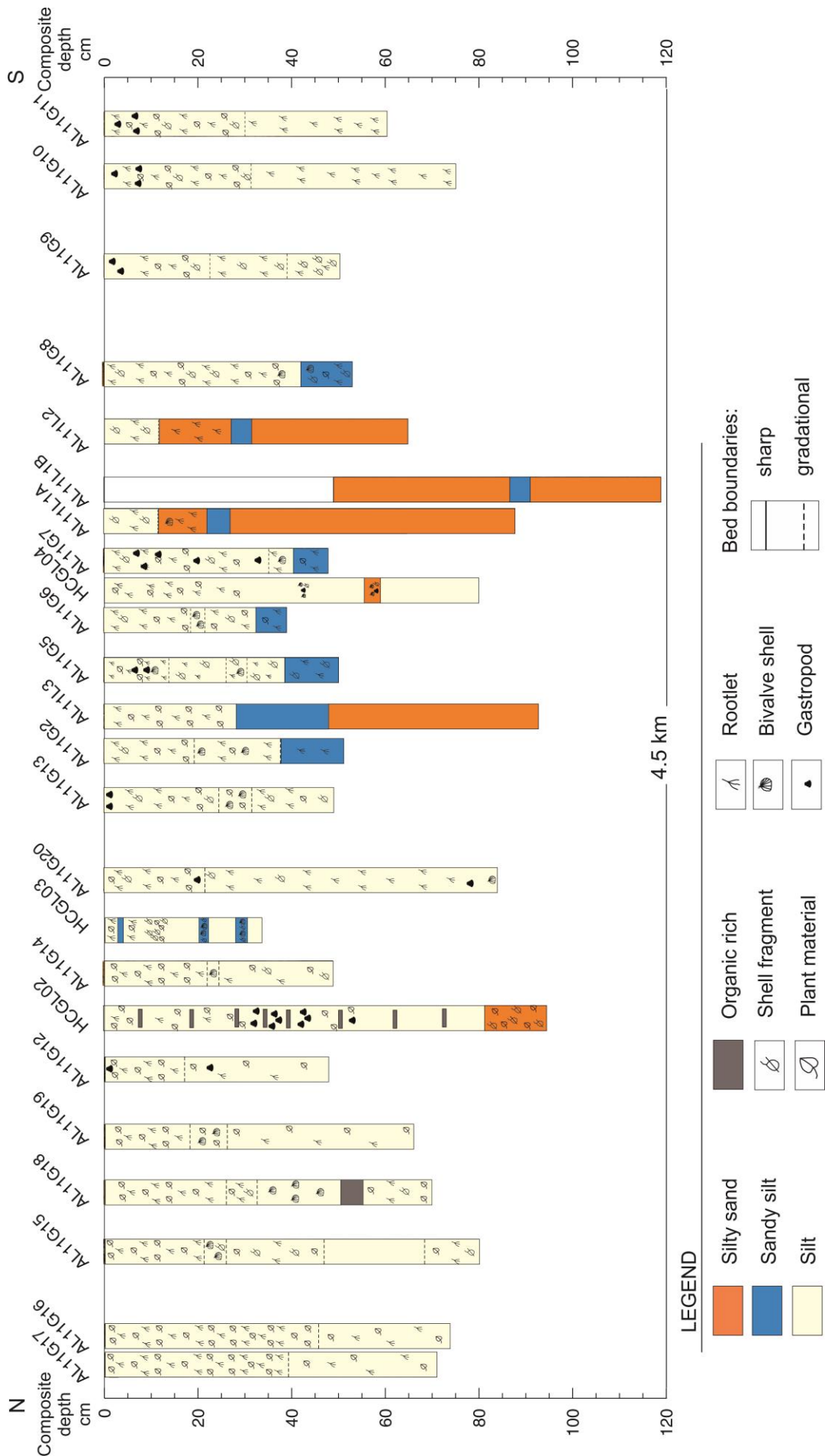


Fig. 4.53. Sedimentological logs of the cores from the Amirkola Lagoon. The logs have been arranged from the North to the South of the lagoon. Cores HCGL02, HCGL03 and HCGL04 from Leroy et al. (2011).

Sedimentological analyses, including grain size and LOI analysis, were performed on the sequences AL11G5 and AL11L2.

From grain size analyses it can be observed that AL11G5 mainly consists of silt and sandy silt. Magnetic susceptibility, OM% and CaCO₃ % for core AL11G5 has been presented in Fig. 4.54. The MS indicates substantial high values at the base of the core (Sz1) with a peak at 55 cm depth, followed by a sharp decrease in Sz2 onwards. The contents of organic matter and carbonate content show an ascending trend from the base of the core upward.

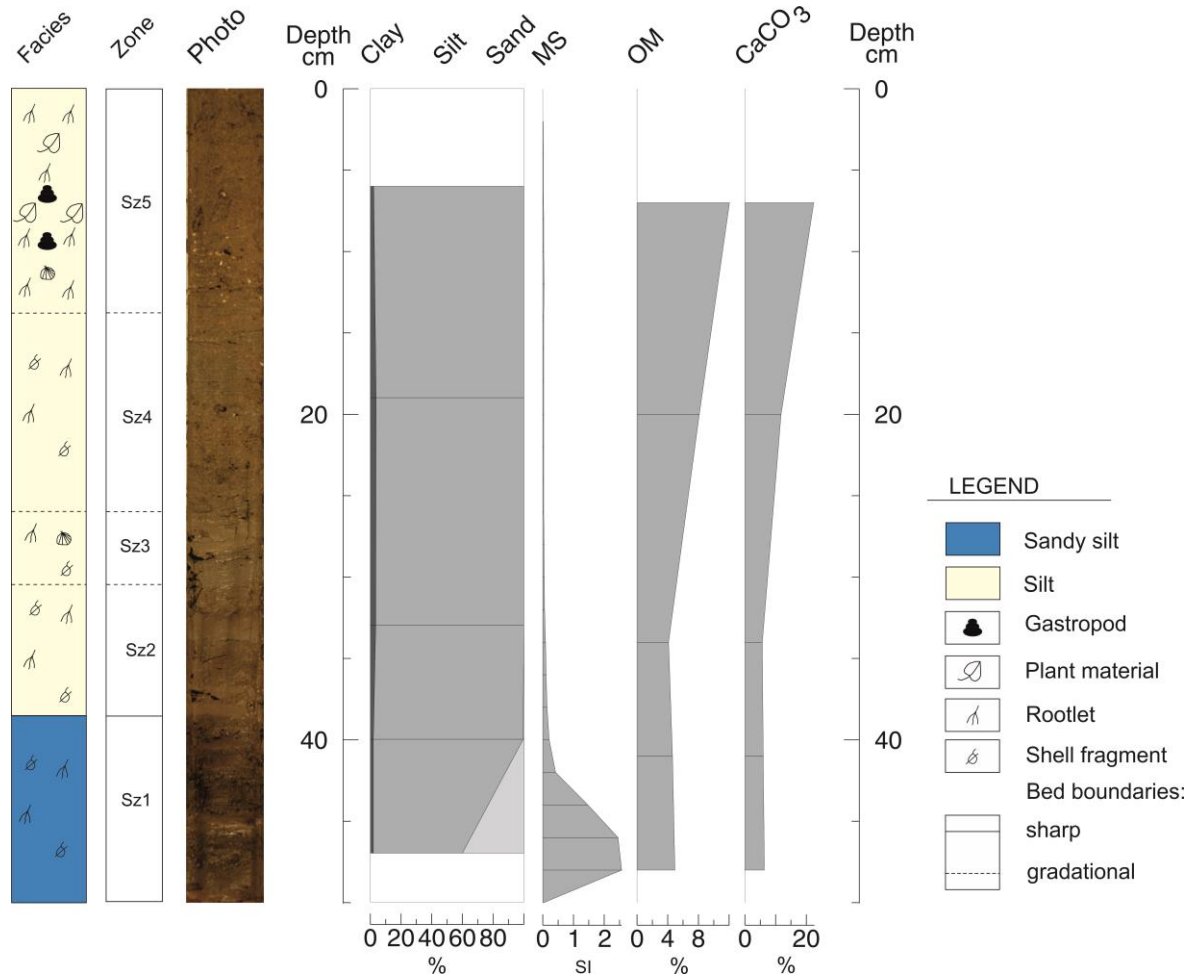


Fig. 4.54. Sedimentary log for core AL11G5, with sedimentary facies, sedimentary zone, core photo, grain size (clay, silt and sand), magnetic susceptibility (MS), organic matter (OM) and calcium carbonate (CaCO₃).

Fig. 4.55 represents the result of grain size, magnetic susceptibility and LOI analysis for core AL11L2. This core contains coarser grains, including silty sand, sandy silt and silt. The MS results indicate a slight decreasing trend towards the top of the sequence. The contents of organic matter show an upward rising trend. The amounts of CaCO₃ stay steady along the core, with a maximum value of 6.2% at a depth of 34 cm.

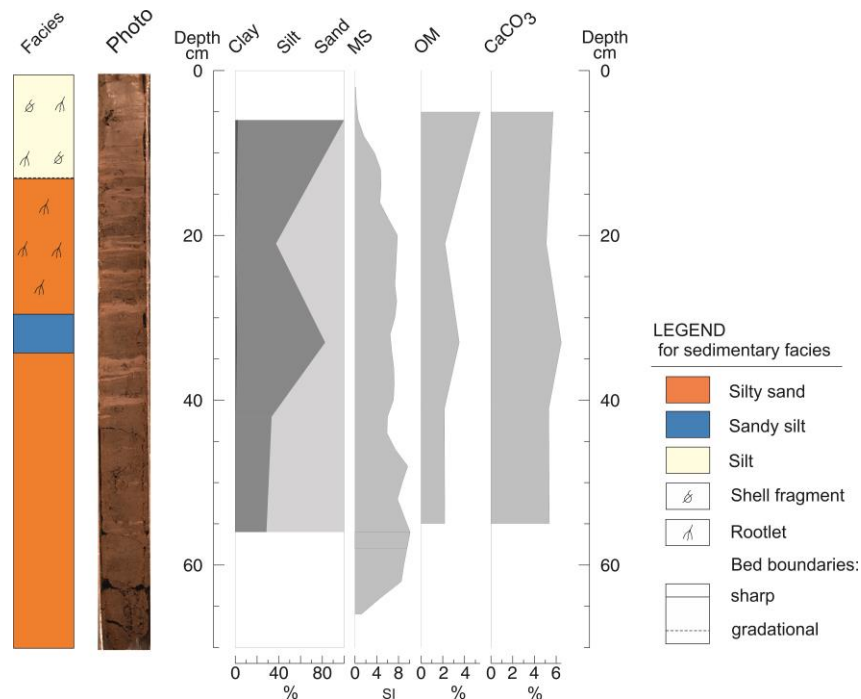


Fig. 4.55. Sedimentary log for core AL11L2, displaying sedimentology, core photo, grain size (clay, silt and sand), magnetic susceptibility (MS), organic matter (OM) and calcium carbonate (CaCO_3).

4.4.3.2 Macro-remains

Five samples from the AL11G5 sequence were chosen to study macro-remains. Nine different macro-remain types have been identified in the fraction $>500 \mu\text{m}$ and ten macro-remain types in the fraction $>125 \mu\text{m}$. Identification of bivalves and gastropods species was performed by Dr F. Wesselingh, Naturalis Biodiversity Centre, Netherlands. Macro-remain percentages and concentrations for the fraction 500 and 125 μm are presented in Fig. 4.56 and 4.57. In order to simplify the explanation, changes in macro-remains have been described based on the percentages of macro-remains in the 500 μm fraction. Meanwhile the main changes for the 125 μm fraction have been described following the 500 μm % zonation. Based on the results, the sequence is divided into two zones:

Mz1, 50-42 cm (2 samples)

This zone is characterized by maximal values of plant material (up to 100% at a depth of 42 cm), with charcoal (2%), gastropoda (*Ecrobia grimmeri* and *Lymnaea S.1.*) (0.2%) and *Theodoxus pallasi* (0.2%). Minerals, acari, bivalve shells and Foraminifera shells appear in the fraction of 125 μm .

Mz2, 42-8 cm (3 samples)

The second zone is categorised by high amount of plant materials (up to 96% at a depth of 21 cm), shell fragments (up to 9%), ostracod shells (up to 0.2%), gastropod shells (1.5%), charophytes (0.3%), *Theodoxus pallasi* (0.6%), other bivalve shells (1.75%), faecal

pellets (2%) and charcoal (0.78%). Furthermore, minerals, Foraminifera shells and acari have been observed in fraction of 125 μm .

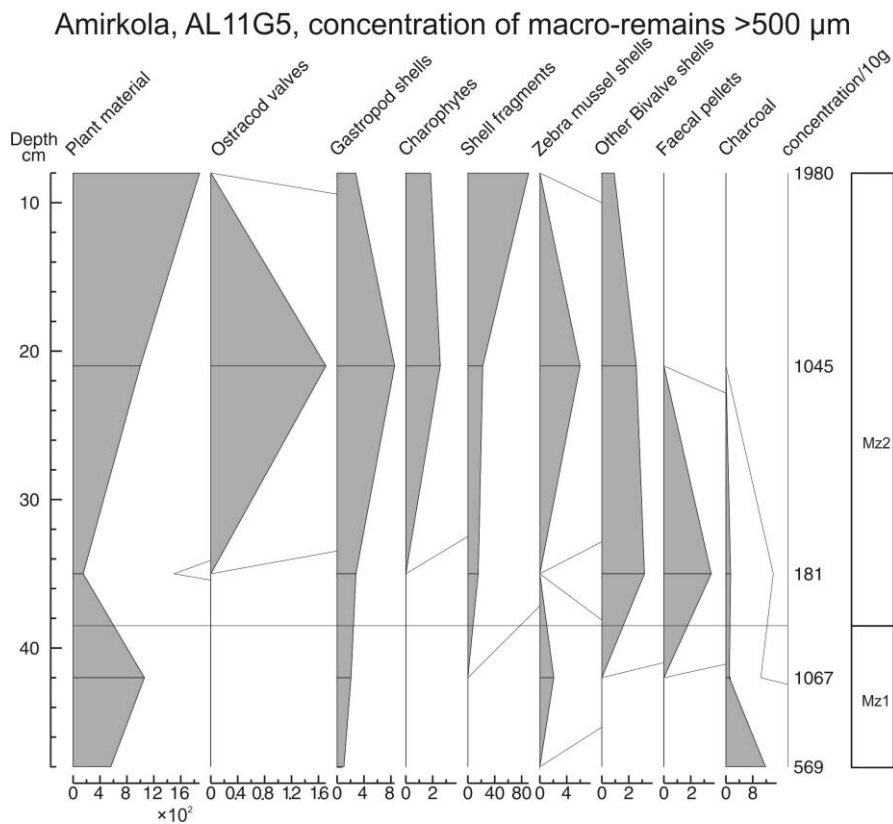
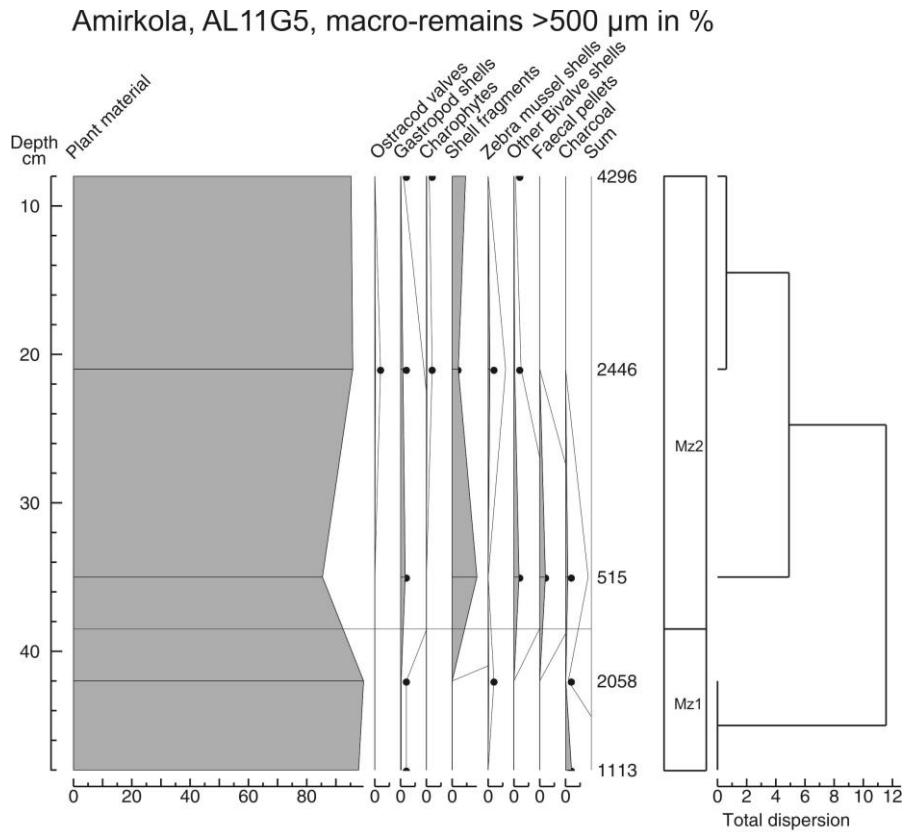
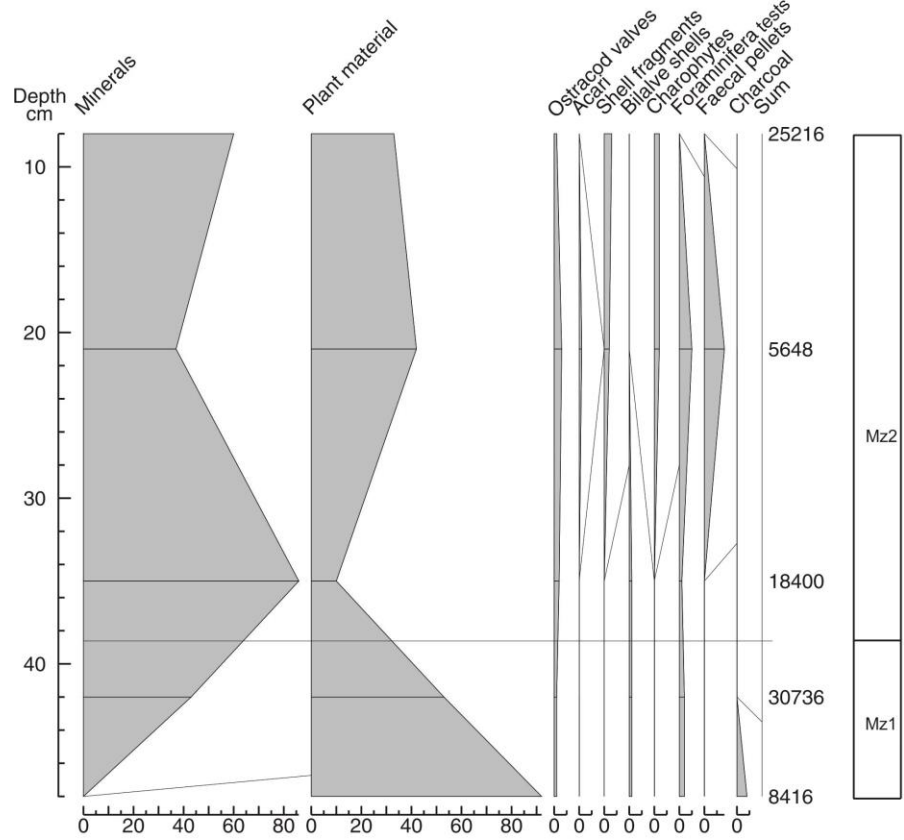


Fig. 4.56. Percentages of macro-remains above 500 μm (the green diagram on the left) and concentrations (the blue diagram on the right) in the AL11G5 sequence. Black dots represent very low percentages of macro-remains.

Amirkola, AL11G5, macro-remains >125 µm in %



Amirkola, AL11G5, concentration of macro-remains >125 µm

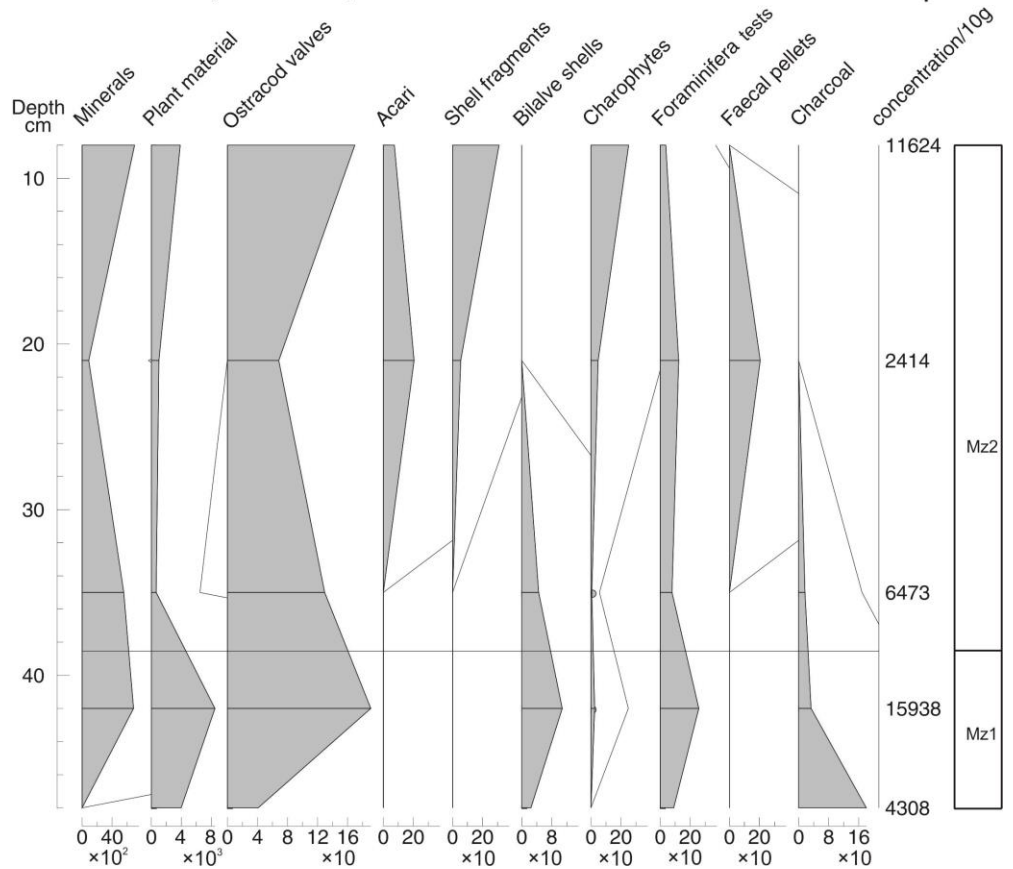


Fig. 4.57. Percentages of macro-remains above 125 µm (the green diagram at the top) and concentrations (the blue diagram at the bottom) in the AL11G5 sequence. Black dots represent very low concentration of macro-remains.

4.4.4 AL11V3 sequence

A sequence with a composite depth of 281 cm was cored from the top of an outcrop on a section where the coastline oriented west-east, west of Amirkola (Fig. 1.1 C and Fig. 4.58; Table 7, Appendix A). The accurate elevation of the outcrop was surveyed 29 months after the coring campaign. The outcrop had meanwhile eroded further inland, especially during storms. Therefore, a key layer was chosen to link the observations and sampling at these two different times: a red layer in the outcrop was considered as a key layer (marker) (dashed white line in Fig. 4.58 B). The elevation of the base of the red layer was -25.537 m. Taking into account the depth of red layer, which is 73 cm, the elevation of the top of the outcrop is -24.80 m (Fig. 4.58 B).

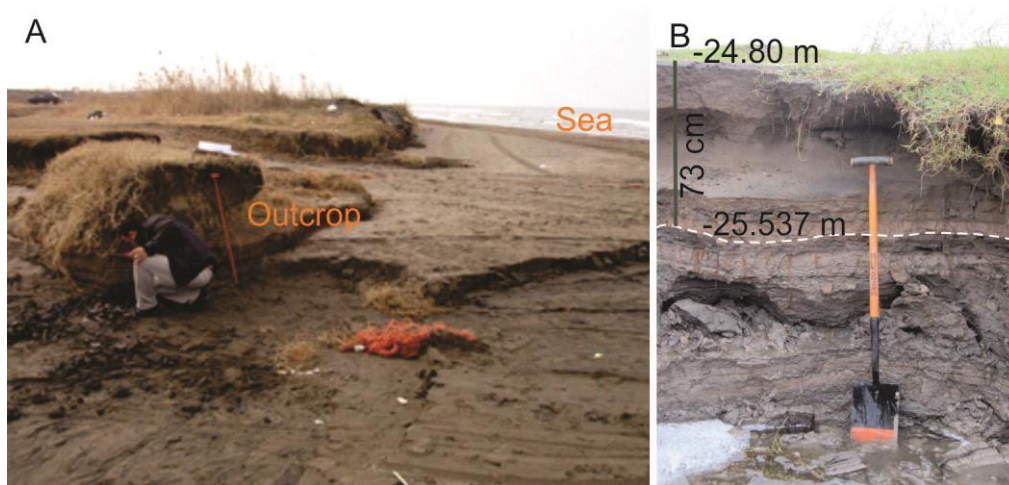


Fig. 4.58. A: Fine-grained sediments deposited at the coastline west of the Old Sefidrud mouth (Photo: by S. Leroy, taken in 2014), B: the outcrop with higher resolution. (Photo: by Author, taken in 2013)

4.4.4.1 Sedimentology

Based on the core description and grain size results, the sedimentology of this sequence is divided in six sedimentological zones that are from the bottom to the top (Fig. 4.59):

Sz1, 281-131 cm: very tickly bedded of dark brown sand with a thinly bedded organic rich layer (10 cm-thick) at depth of 170-160 cm. This layer has a sharp contact with upper layer.

Sz2, 131-119 cm: Alternation of olive sandy silt and olive-grey silt with a thinly laminated layer (1 mm-thick) of plant material at a depth of 129 cm and gastropod shells (*Theodoxus pallasi*) and bivalve shell fragments at a depth of 124 cm.

Sz3, 119-85 cm: Alternation of light brown silt and light reddish-brown silty sand with layers of plant material at 113 and 99 cm. The boundary between this zone and the following zone is sharp.

Sz4, 85-73 cm: Alternation of brown sandy silt and dark brown sandy silt with plant materials.

Sz5, 73-60 cm: Alternation of reddish-brown sandy silt and silt with thinly laminated layers (1 mm) of the plant material at 71.5 and 65 cm. This is the layer used for correlating the cored outcrop and the outcrop for which elevation was measured. This zone has a sharp boundary with its upper and lower zone.

Sz6, 60-0 cm: dark yellowish brown sand with plant remains and rootlets at the top 14 cm

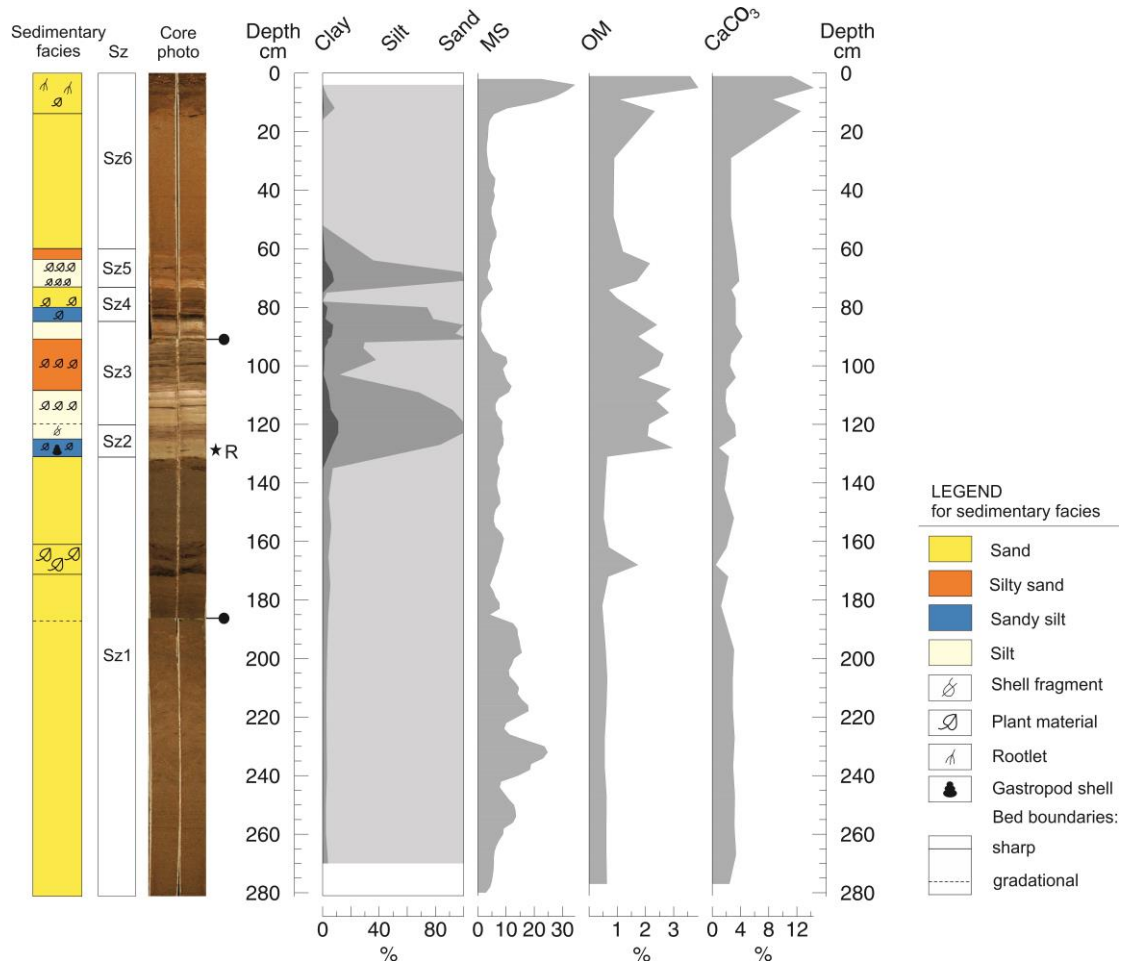


Fig. 4.59. Sedimentary log for the AL11V3 sequence, displaying sedimentology (Sz: sedimentological zone), core photo, grain size (clay, silt and sand), magnetic susceptibility (MS), organic matter (OM) and calcium carbonate (CaCO₃). Black star refers to the depth of the radiocarbon date, R: rootlets (material dated), and black pin symbols shows the core section limits.

The 3-D graph of the grain size from 39 samples shows that the top and bottom of the sequence are mostly dominated by sand, with a maximum of 8% silt. The middle of the core (131-60 cm) mostly consists of silt with three peaks of sand (Fig. 4.59 and 4.60).

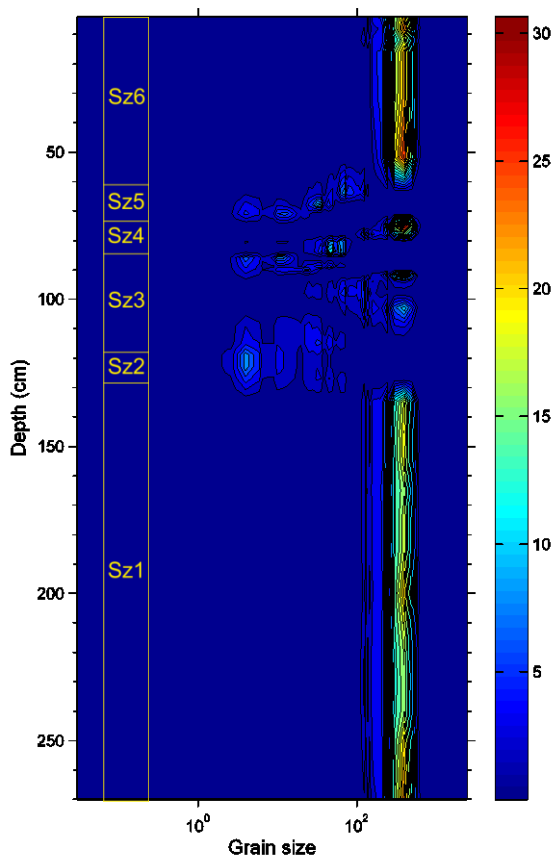


Fig.4.60. 3D plot of grain size data in μm for the sequence AL11V3: the dark blue colour represents the lowest volume (%), while the red colour shows the highest volume (%). Sz: sedimentological zone.

The MS results show significant changes along the sequence. Overall, the bottom 98 cm of the sequence has relatively high values compare to the upper part. A peak of MS occurs at the top of sequence. From the base to 131 cm, the organic matter values are less than 1% with a small peak at a depth of 165 cm, followed by a sharp increase at a depth of 131 cm. From 131 to 60 cm, the OM is 2-3 % and shows a continuous slight decrease upwards, with some fluctuations. Then it remained quasi constant from 60 to 14 cm, followed by a sharp increase in the top 14 cm. Overall, the carbonate content stayed constant along the sequence with two low points at the depths of 165 and 131 cm (corresponding to two peaks of OM), followed by a suddenly increase in the top 14 cm (Fig. 4.59).

4.4.4.2 Macro-remains

Twelve samples from the AL11V3 core were selected to study macro-remains. Ten different macro-remain types were identified in the fraction $>500 \mu\text{m}$ and nine in the fraction $>125 \mu\text{m}$. Macro-remain percentages and concentrations for the fraction 500 and

125 µm are presented in the Fig. 4.61 and 4.62. Changes in macro-remains have been described based on the percentages of macro-remains at fraction 500 µm and meanwhile the main changes for the fraction of 125 µm (percentage and concentration) have been included in the above description. Based on the results, the sequence is divided into six zones suggested by the % of the 500 µm fraction:

Mz1, 204-123 cm (3 samples)

This zone is characterized by maximal values of minerals (92 to 100%) and <1 to 7% plant materials. Also, a small amount of Charophytes (0.7%), charcoal (0.3%) and ostracod shells (0.1%) has been recognised at a depth of 128 cm. In the fraction of 125 µm, 98-100% minerals and 0-2% plant materials have been observed.

Mz2, 123-97 cm (2 samples)

This zone is dominated by the faecal pellets (78 to 88%) and plant materials (6 to 20%). Furthermore, 1-2% shell fragments, 1% Dressenidae (*Dreissena polymorpha*), <1% other bivalve species (larval shells), ~ 1% ostracod shells, ~ 1% gastropods (*Ecrobia grimmeri* and *T. pallasii*), 1% charcoal and <1% Charophyte have been recognised in this zone. Furthermore, 8% to 80% minerals, 11 to 12% plant materials and 5 to 80% faecal pellets have been observed in 125 µm fraction. Moreover, 3% Foraminifera (mainly *Ammonia beccarii* and some *Elphidiella brotzkajae*), <1% bivalve shells (in larval stage), 1% ostracod shells, <1% gastropod shells (broken *T. pallasii*) and <0.1% acari have been seen at a depth of 120 cm.

Mz3, 97-76 cm (2 samples)

The third zone is marked by a peak of the faecal pellets (up to 82%), minerals (up to 17%) and plant materials (18 to 83%). Additionally, this zone contains a small amount of bivalve shells (larval shells) and charcoal (<1%). In the fraction of 125 µm, this zone is dominated by up to 97% minerals, up to 80% faecal pellets and 3 to 20% plant materials. Furthermore, <0.1% charcoal, 1% ostracods, <0.1% bivalve shells (larval) and <0.1% Foraminifera (*A. beccarii* and *E. brotzkajae*) have been observed at a depth of 96 cm.

Mz4, 76-66 cm (2 samples)

The fourth zone is characterized by plant materials (<1 to 55%) and minerals (45 to 99%). The fraction 125 µm shows the same trend that includes 2 to 90% plant materials and 10 to 98 minerals.

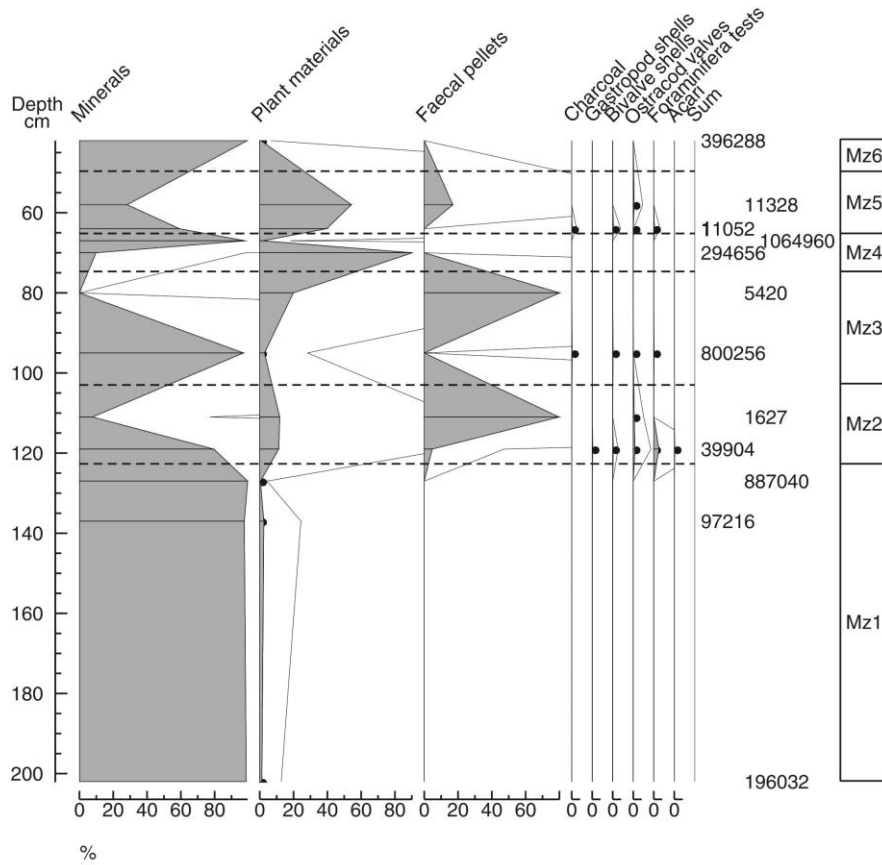
Mz5, 66-51 cm (2 samples)

This zone is characterised by plant material (47- 97%), faecal pellets (2 to 53%) and charcoal (<1%). The fraction of 125 µm is marked by minerals (28 to 59%), plant materials (40-54%) and faecal pellets (17%). Furthermore, less than 1% of charcoal, ostracod shells, bivalve shells (larval) and Foraminifera (*A. beccarii* and *E. brotzkajae*) have been observed in this fraction.

Mz6, 51-42 cm (1 sample)

The sixth zone is distinct by 100% of minerals. In the fraction >125 µm, 1% plant materials and 99% minerals has been recognised at a depth of 43 cm.

Outcrop, AL11V3, macro-remains >125 µm in %



Outcrop, AL11V3, concentration of macro-remains >125 µm

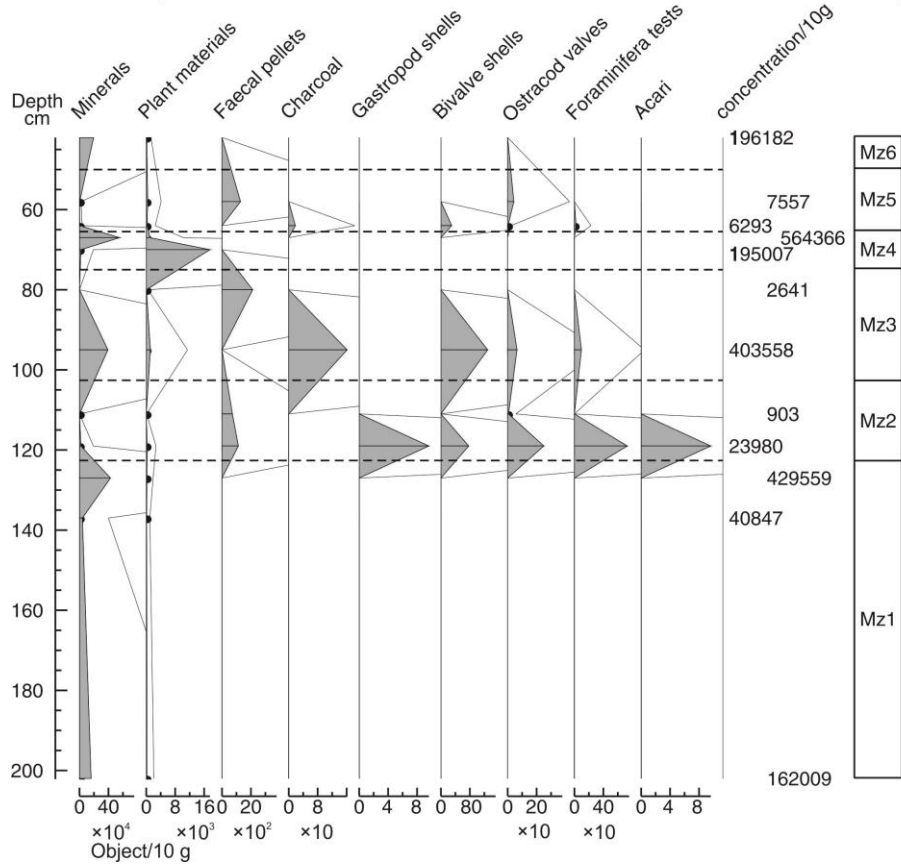


Fig. 4.62. Percentages of macro-remains above 125 µm (the diagram at the top) and concentrations (the diagram at the bottom) in the sequence AL11V3. Black dots represent very low concentration of macro-remains.

4.4.4.3 Palynology

Palynology analyses were performed by Professor S. Leroy on the sequence AL11V3 and the text was written by her. The palynomorphs are moderately well preserved as seen in the relatively high amounts of indeterminate and reworked pollen grains, besides three very good samples at the base (129 to 121 cm). This is also reflected in concentrations that fluctuate around 5000 grains/ml, but that reach c. 30,000 grains/ml in the two lowermost samples (129 and 126 cm).

The curves of some selected palynomorphs, used in interpretation, are presented in Fig. 4.63. Based on terrestrial pollen grains mainly including *Alnus* (wooded swamp), *Artemisia* (steppe and/or ruderal), Amaranthaceae (mostly salt marsh) and Poaceae (indicator of open landscape or marshes), three pollen zones have been identified including:

Pz1, 130 to 117 cm

This zone contains a peak of *Alnus* (up to 59 %) and of *Carpinus* (16 %). The Cyperaceae are very high in the first sample (129 cm): 29 %. *Botryococcus* is relatively abundant. Amaranthaceae increase slightly across this zone. The preservation and concentration are optimal for this sequence, although the concentrations sharply drop before the zone ends. Proportionally low fungal spores and *Glomus* occur. A mixture of freshwater algae and marine organisms (dinocyst and Foraminifera) is observed.

Pz2, 117 to 68 cm

This zone is still dominated by *Alnus*, albeit with much lower values (approx. 10 %), and it starts with a small peak of *Pterocarya* and finishes with a small peak of *Vitis*. A maximum of *Artemisia* occurs first (24 %), which is followed by a maximum of Amaranthaceae (34 %). While Poaceae are still stable, Cerealia-t. appears but is present in this zone only.

A sharp increase of indeterminate palynomorphs, reworked palynomorphs, fungal spores, and *Glomus* is observed. Fungal spores reach a maximum at the end of this zone at 70 cm depth. Dinocysts and Foraminifera are less abundant in this zone, except at 83 cm where the dinocyst *Impagidinium caspiense* increases slightly and briefly.

Pz3, 68 to 66 cm

This zone is made of only one sample at 66 cm. It is only distinguished from the zone below by significant percentages of *Parrotia persica*, *Pterocarya* and Urticaceae-Moraceae and *Gloeotrichia*, a slight drop of Poaceae and a clear maximum of Caspian Sea waters indicators (13%).

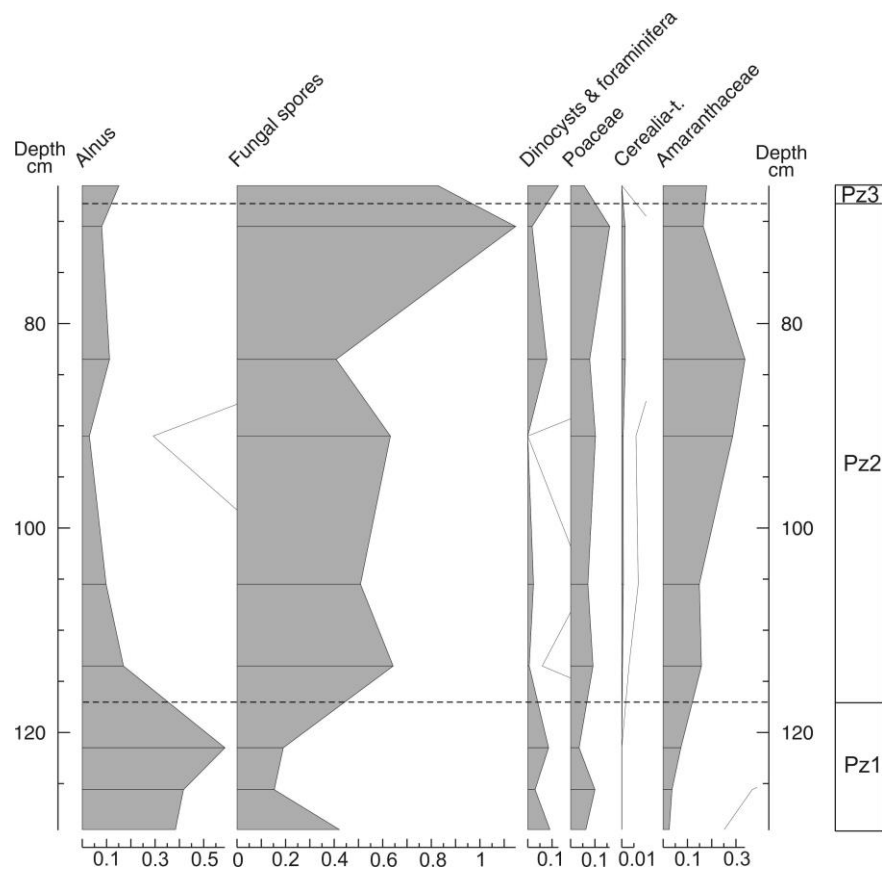


Fig. 4.63. Diagram of AL11V3 sequence, including the sums of some significant palynomorphs.

4.4.4.4 Chronology

A rootlet sample from the facies Sz2 at 128 cm was taken for radiocarbon dating (Table 4.6). Its median probability is AD 1847; however two periods are possible: AD1810-1922 (74%) and 1691-1729 (26%). This is especially visible on fig. 4.64.

Table 4.6. Radiocarbon dates from AL11V3. Calibrated ages are reported for 2σ range with highest probabilities shown in parentheses. Dates from Queen's University Belfast.

Laboratory number	Sample ID	Depth (cm)	Material Type	^{14}C Age (yr BP)	Calibrated age (yr AD) (2σ range)	Median probability
UBA-22991	AL11V3-2-41	128	rootlet	82 ± 27	1810-1922 (74.1%) 1691-1729 (25.9%)	1847

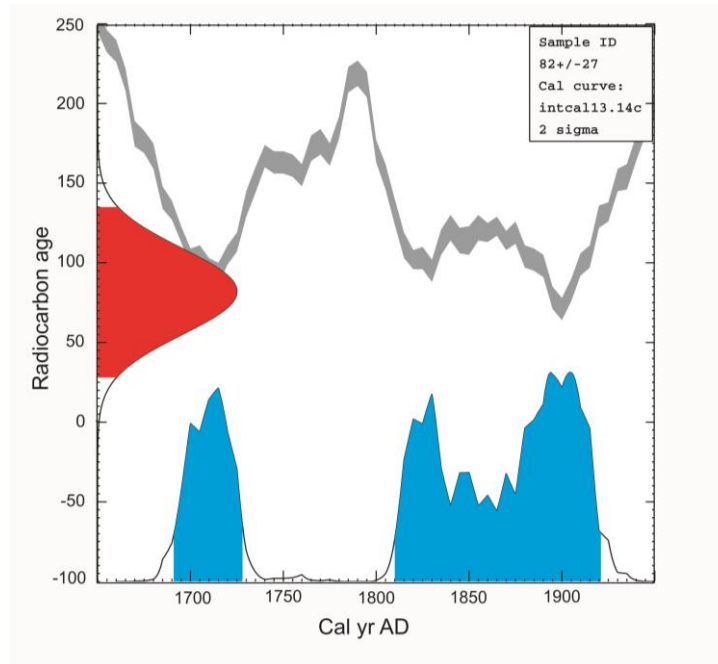


Fig. 4.64. AL11V3 dating result: interception between radiocarbon age (red curve) and calibrated age (blue curve) with calibration curve (grey curve).

4.5 Marine deposits

Five cores with a maximum length of 157 cm were retrieved using a gravity corer from the CS at the water depths of 17, 105, 301, 431 and 470 m (Fig. 4.65 A and Table 8, Appendix A). The cores were taken in front of the current main distributary of Sefidrud (see Fig. 4.65 B and C). Additionally, seven seismic profiles were taken from this area by the Geological Survey of Iran for other purposes but were made available to us (Fig. 4.65 B). Furthermore, surface samples were taken by INIOAS using a grab sampler in order to document the modern plume of the main distributary (Fig. 4.65 C). The water depths varied between 15 to 20 m (Table 9, Appendix A).

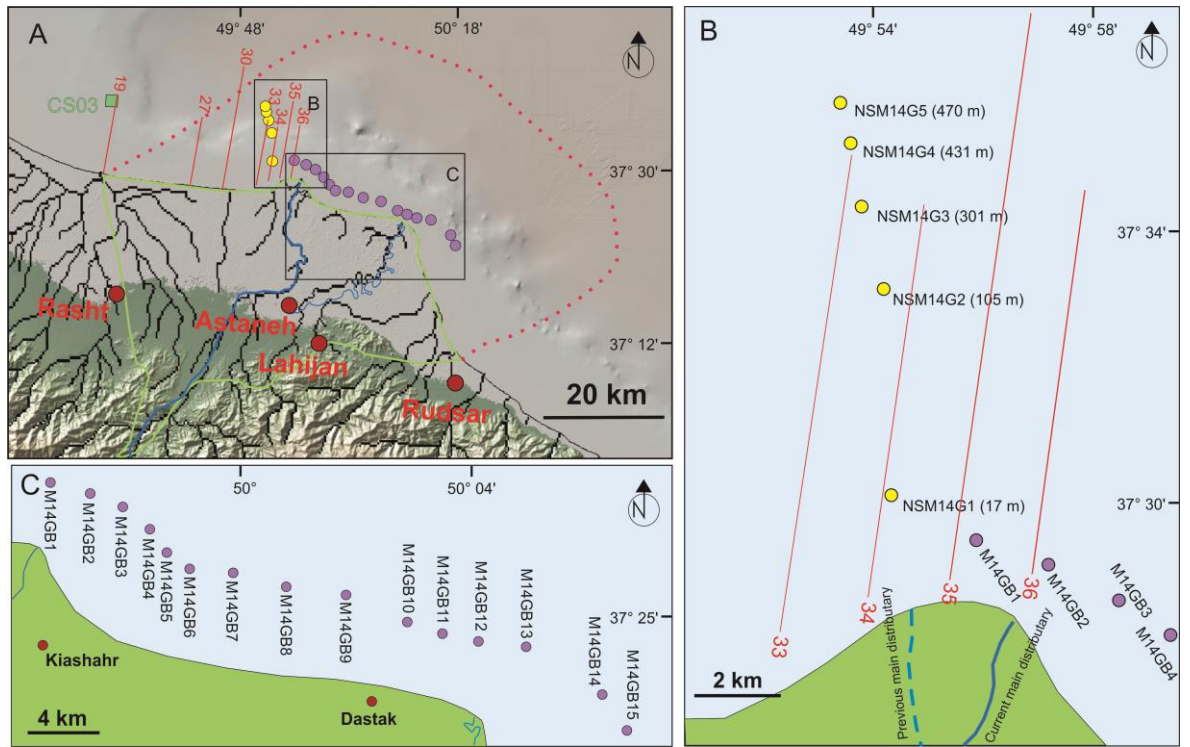


Fig. 4.65. A: Location map of cores taken from the Caspian Sea (yellow dots) and surface samples (purple dots), red lines represent the location of seismic profiles with the name of the profiles in red, green line represents subaerial delta limit and red dashed line represents subaqueous delta limit from Kazancı and Gulbabazadeh (2013); red dots represent the location of main towns; green square: Location of CS03 (Leroy et al., 2013 b). Default base-map from Ryan et al. (2009) (<http://www.geomapp.org>). B: Location of cores taken from offshore by gravity corer, numbers in parentheses show water depth. Red lines: seismic profile, blue dashed line: the main distributary between 1964 and 1991. C: Location of surface samples taken by grab sampler.

In order to have an idea about how steep is the slope of the CS in the Sefidrud Delta, the seismic profiles are simplified and the topographic profile of the sub-aqueous part of the delta is presented in figure 4.66.

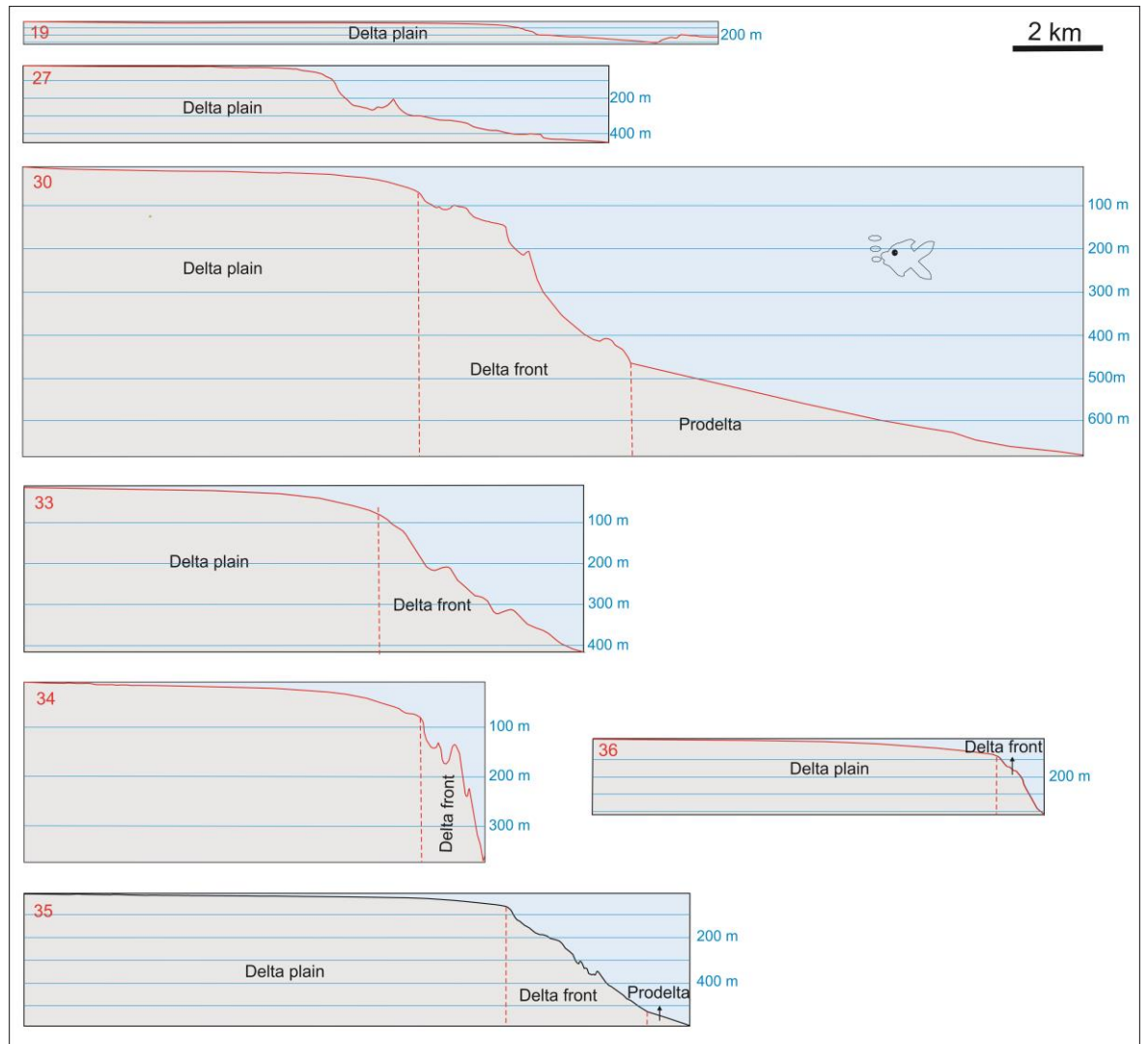


Fig.4.66. Topographic profiles of the sub-aqueous part of Sefidrud Delta based on seismic profiles. For the location of seismic profiles, see Figure 4.65 A and B.

4.5.1 Sedimentology

Grain size analyses performed on surface samples show a variation from silt to sandy silt and silty sand (Fig.4.67 and Table 9, Appendix A). Silty sand appears in the east (in front of Old Sefidrud); however, silt and sandy silt are dominant towards the west (Fig. 4.67). The core NSM14G1 at 17 m water depth is silty and this fits well with the westernmost grab samples which are also silty.

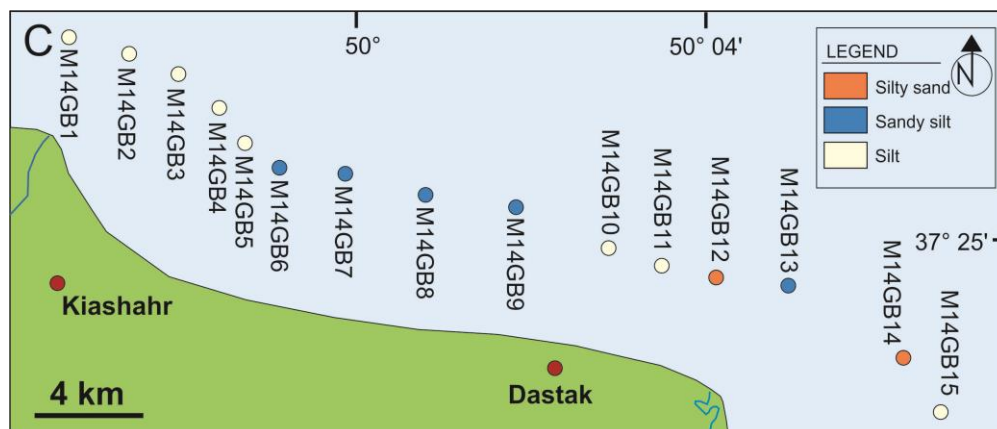


Fig. 4.67. Distribution of silt, sandy silt and silty sand in surface samples from offshore.

MS measurements, standard visual core description, grain size, macro-remains and LOI analyses were performed on all the cores. Furthermore, chronology was performed on the NSM14G3 sequence. The results show the sequences mainly consist of silt (Fig. 4.68). However, core NSM14G3 contains one sandy silt interruption (Fig. 4.68 and 4.69).

The MS values of the five cores are extremely low and the fluctuations are hardly worth discussing, probably within the error bars. The most proximal core NSM14G1 has the highest values, reaching 1.5

The sediment of core NSM14G1 (17 m) is dark grey silt with up to 97% silt. This core contains two layers of shell fragment and bivalve shells at depths of 75 and 71 cm. The organic matter stays constant along the core with a background of 4%. The carbonate content shows an increasing trend upward, which reaches to 9% at the top of the core (Fig. 4.68).

Core NSM14G2 (105 m) is mainly dominated by dark grey silt with 97% silt. This sequence is marked by dark laminations, which quickly disappear under oxidising condition. The organic matter has a background of 6.5%, which increases to 7.5% at the top of the core with two low points of 5% at a depth of 132 and 114 cm. The amounts of carbonate with a background of 6% show an increasing trend, reaching up to 7% at the top of the sequence (Fig.4.68).

The sediment of core NSM14G3 (301 m) is comprised of bioturbated dark grey silt with a layer of sandy silt with sharp contact at a depth of 78 cm which contain 27% sand. The amount of organic matter has a background of 6% and reaches to 7% at the bottom of the core. The amount of carbonate is relatively constant and reaches 8% at a depth of 65 cm (Fig.4.68). Fig. 4.69 shows the 3D plot results from the CILAS on nine samples. The sharp change in grain size at 78 cm is very clear in this plot.

The sediment of core NSM14G4 (431 m) consists of dark greyish brown silt with up to 96% silt. The mean amounts of organic matter and carbonates are stable along the core, with a maximum value of 7.5 and 7%, respectively (Fig.4.68).

The sediment of core NSM14G5 (470 m) contains of dark greyish brown silt with up to 96% silt. The amounts of organic matter and carbonates remain stable, with a maximum value of 8 and 7%, respectively (Fig.4.68).

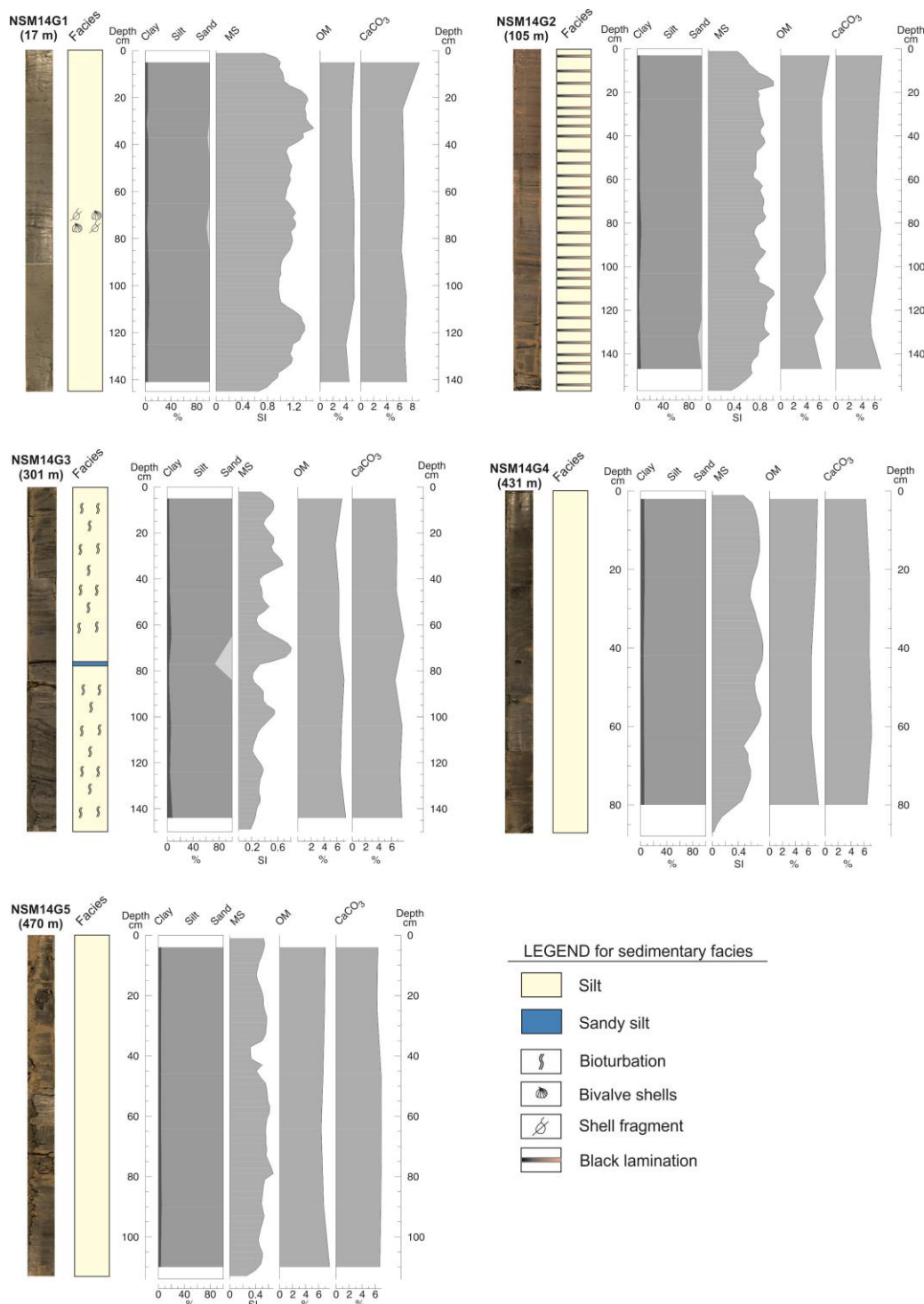


Fig. 4.68. Sedimentary log for the marine sequence, displaying core photo and water depth in parentheses, sedimentary facies, grain size (clay, silt and sand), magnetic susceptibility (MS), organic matter (OM) and calcium carbonate (CaCO₃).

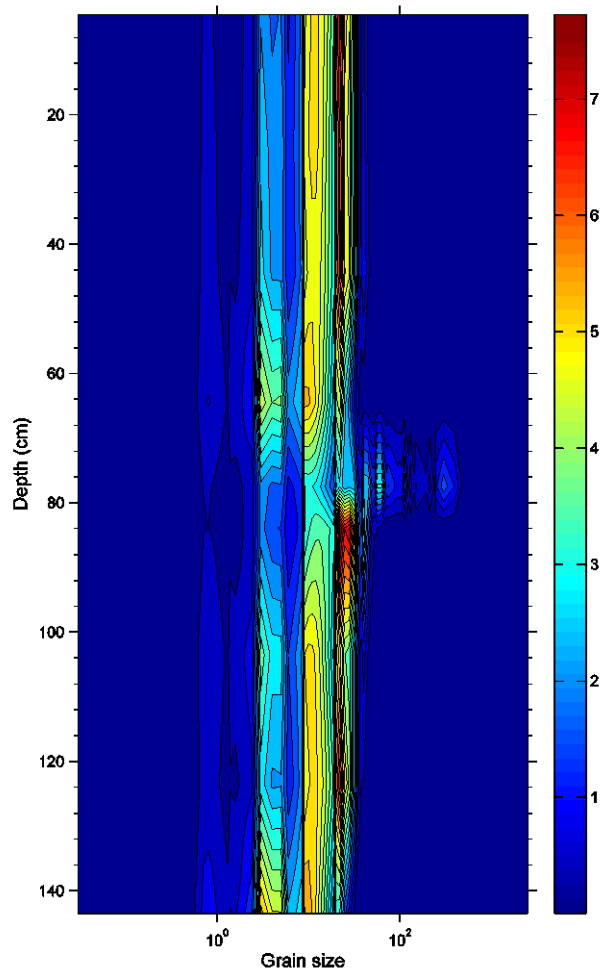


Fig. 4.69. 3D plot of grain size data in μm for the sequence NSM14G3, the dark blue shows the lowest volume (%), while the red colour shows the highest volume (%).

4.5.2 Macro-remains

Eight samples from the longest sequence (e.g. NSM14G3 sequence) were chosen to survey the vertical changes in macro-remains. Furthermore, in order to investigate the horizontal changes in the macro-remains with the distance from the coast line to the deeper part, three samples were selected in each sequence, i.e. NSM14G1, NSM14G2, NSM14G4 and NSM14G5. Due to great scarcity of macro-remains in the fraction $>500 \mu\text{m}$, changes in macro-remains is described based on the percentages in the $125 \mu\text{m}$ fraction (Fig. 4.70).

NSM14G1

This sequence is dominated by faecal pellets (up to 62%), plant materials (up to 29%), foraminifers (up to 27) and bivalve shells (up to 46%). Moreover, shell fragments (11%), ostracod shells (up to 8%), charcoal (up to 2%) and gastropod shells (up to 0.3%) have been found in this sequence.

NSM14G2

Six various macro-remains have been observed in this sequence, including faecal pellets (up to 97%), plant materials (up to 20%), ostracod shells (up to 21%), charcoal (up to 7%), Bivalvia shells (up to 2%) and Foraminifera (up to 3).

NSM14G3

This sequence is characterized by plant material (36%), charcoal (32%), faecal pellet (61%), clay flakes (33%), gastropod shells (up to 0.1%), bivalve shells (12%), ostracod shells (6%) and foraminifers (18%).

NSM14G4

Based on the results up to 97% faecal pellets, 2% clay flakes, 0.9% charcoal, 32% plant material, 0.9% ostracod shells, 6% bivalve shells, 3% foraminifers and 0.8% shell fragments have been observed in this sequence.

NSM14G5

Seven different macro-remains have been observed in this sequence including clay flakes (up to 0.3%), faecal pellets (up to 84%), charcoal (up to 5%), plant materials (up to 44%), ostracod shells (up to 0.3%), bivalve shells (up to 1.2%) and foraminifers (up to 1).

The highest absolute abundance (or concentration) of macro-remains occurs in core NSM14G1 at 65 cm where the number of bivalve shells reach up to 10,000/g. The second highest peak belongs to core NSM14G5 at 4 cm where the number of faecal pellets reach to ~ 14,000 (concentration diagram in Fig. 4.70). The highest amount of Foraminifera tests observed in core NSM14G1 and ~ 2800 foraminifers were observed at 65 cm.

4.5.3 Chronology

Radionuclide analyses were made on core NSM14G3 at laboratory of Modane in the French Alps, by Mr J. Reyss and the text was written by him. The radionuclide results of core NSM14G3 show that ^{210}Pb values reach nearly to a back ground at 24 cm depth. The sedimentation rate for the top 9.5 cm is 1.65 mm/yr and between 13 and 24 cm the sedimentation rate of 1.8 mm/yr (Fig. 4.71 A). Between 9.5 and 13 cm, sedimentation rate decreases to 1.2 mm/yr. The record of artificial fallout ^{137}Cs also exhibits a roughly linear decreasing activity for the top 9.5 cm, followed by an increase between 9.5 and 13 cm and a decreasing activity for the samples between 13 and 24 cm (Fig. 4.71 B).

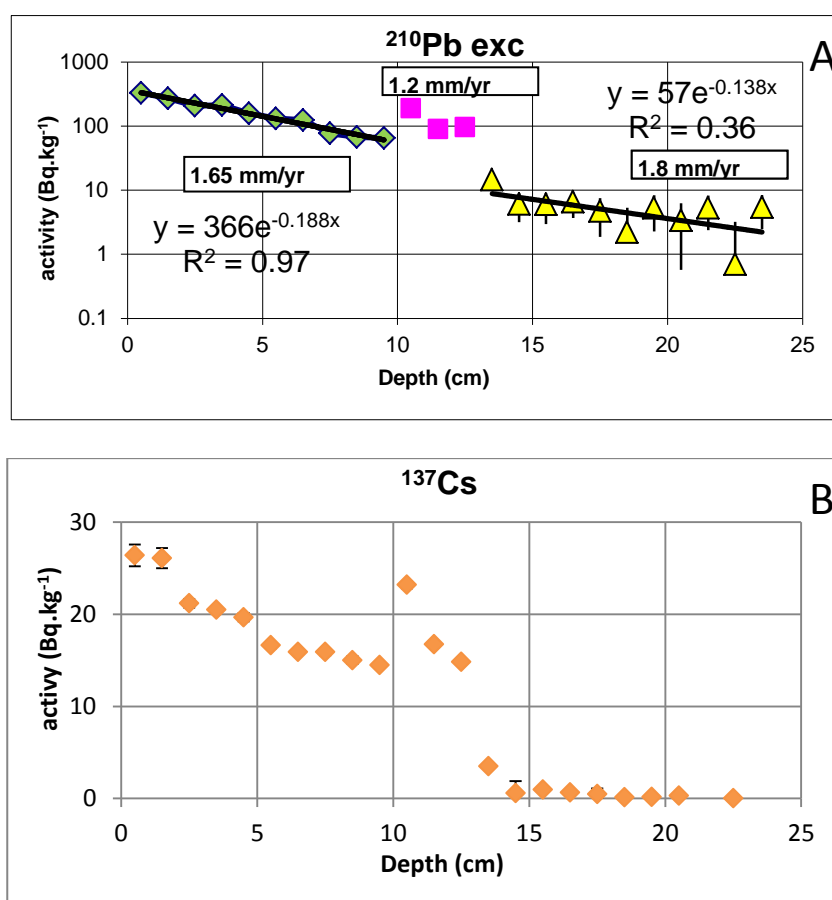


Fig. 4.71. Radionuclide dating of core NSM14G3, based on CRS (constant rate of supply) model. (A): Profiles of $^{210}\text{Pb}_{\text{exc}}$ activities (Bq kg^{-1} , dry weight) with depth in cm. The regression line corresponds to an average sedimentation rate of 1.67 mm/yr. (B): Profiles of ^{137}Cs activities (fallout from nuclear weapon testing) with depth in cm.

If sedimentation rate is considered to be constant, a sedimentation rate of 1.67 mm/yr is obtained for the top 28 cm of sediment (Fig. 4.72). The base of the core is therefore estimated to be at around AD 1120 and the sequence covers the last 900 years.

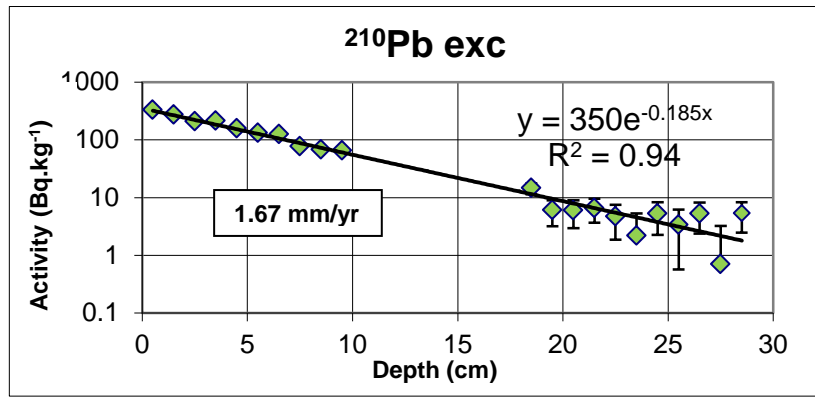


Fig. 4.72. Radionuclide dating of core NSM14G3, based on constant sedimentation rate, Profiles of $^{210}\text{Pb exc}$ activities (Bq kg⁻¹, dry weight) with depth in cm

5 Interpretation and Discussion

This chapter presents the discussion of the main results for three introduced sections site by site, following the evolution of the delta, contribution of this study to CSL curve, and sediment accumulation within the delta. Figure 5.1 shows the location of areas subjected to study in this research.

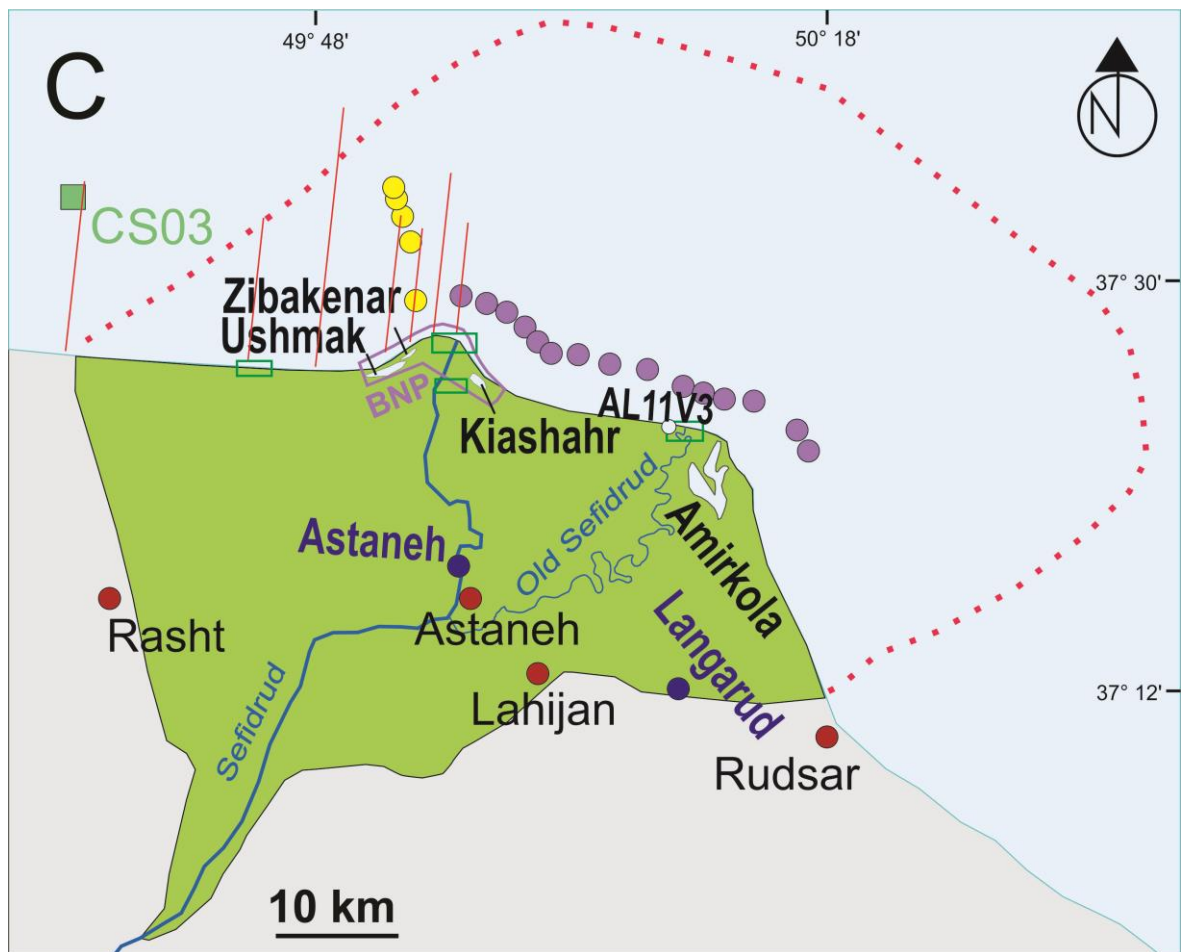


Fig. 5.1. The location of coastal lagoons: Zibakenar, Ushmak, Kiashahr and Amirkola (light blue bodies) and inland water bodies: Langarud and Astaneh (dark blue dots), yellow dots: location of offshore cores, purple dots: location of surface samples, light blue dot: location of AL11V3 sequence, red lines location of seismic profiles, green boxes: location of GPR profiles, red dashed line represents submarine delta limit from Kazancı and Gulbabazadeh (2013) and purple line: Boujagh National Park (BNP) boundary from Naqinezhad (2012), red dots: the location of main towns.

5.1 The development of the coastal lagoons using remotely sensed data

Based on aerial photograph from 1955 (Fig. 4.1 A), the Sefidrud Delta prograded into the CS with a north–east trend. High sediment supply resulted in an eagle head shaped

delta and even the formation of islands in the Sefidrud mouth. The sand barrier that in a later stage determined the formation of the Kiashahr Lagoon had already started to form.

Between 1955 and 1964 (Fig. 4.1 A and B), a minor avulsion occurred and the Sefidrud direction changed westwards. Further sand barriers were formed and as a result two lagoons came into existence on the west side of the Sefidrud: Zibakenar and Ushmak. The latter was formed at the mouth of the Ushmak River. This small avulsion from east to west had a strong impact on the formation of Ushmak and Zibakenar Lagoons by providing more sediment to the western half of the delta, which resulted in the formation of the sand spits.

During the years from 1964 to 1982 (Fig. 4.1 B and C), Zibakenar and Ushmak Lagoons developed further. The natural inlet from the CS to the enclosing Kiashahr lagoon became narrower and migrated to the south as the spit grew. The Sefidrud direction changed from north–west to north and the active channel belt became narrower. This reflects the impact of reducing Sefidrud sediment supply as a result of the construction of the Manjil Dam in 1962 (Table 2.2). Despite this, the delta progradation remained constant due to continuous sea level fall that ended only in 1977 (Fig. 2.2).

From 1977 until 1995, sea level in the CS rose rapidly (Fig. 4.1). During the years from 1982 to 1991 (Fig. 4.1 C and D), the Sefidrud Delta progradation rate was higher than in the previous period, as a result of the Manjil Dam flushing operations from the early 1980s, with a peak in 1984–1985 (Table 2.2), which resulted in an arrow–like shaped delta. Therefore, despite continuous sea level rise from 1977 to 1995, the delta continued to prograde. At the same time, erosion in the Kura delta increased and coastlines retreated 10–15 m (Kaplin and Selivanov, 1995). In 1991, a minor tributary of the Sefidrud started to form in the east, between Kiashahr lagoon and the main tributary of the Sefidrud (Fig. 4.1 D).

Between 1991 and 2014 (Fig. 4.1 D and E), a minor river avulsion happened and the Sefidrud changed its course from N to NE. Indeed, the minor tributary of the Sefidrud (Fig. 4.1 D) became the main tributary in 2014. Erosion increased in the western part of the Sefidrud Delta. By 2014, the navigable connection with the CS had ceased to exist and the Zibakenar lagoon became choked and completely isolated (Fig. 4.1 E). If a ‘natural’ evolution had continued (see below), the water body would have become progressively infilled by land–derived sediments, introduced mainly by the Sefidrud. At the same time, a rapid infill by sediment and *Phragmites* and *Typha australis* plants occurred in the Kiashahr Lagoon (Fig. 4.1 E; Naqinezhad, 2012; Ramsar report 37, 2015).

5.2 Radar profiles and sedimentary facies

The limited depth of penetration of the GPR signal, ~ 2-4 m, was expected in the study area. The relatively low penetration depth in this area is partially due to the high water table (Naderi Beni et al., 2013). High amount of silt/clay in some area (location D, Fig. 4.2) and high carbonate content (in profile 106, location D, Fig. 4.2) also contribute to signal attenuation (Jol and Smith, 1991; Smith and Jol, 1992; Jol et al., 1996) and cause problem in GPR study in some locations as it was clearly explained in chapter four. Naderi Beni et al. (2013) conducted GPR survey to study the development of lagoons in the south Caspian Sea and some parts are interpreted as lagoonal deposits. However, it seems that the GPR signal does not penetrate through fine sediments and therefore the lagoon deposits cannot be recorded in GPR profiles (see location D, Fig. 4.2). GPR imaging of coastal deposits in sandy sediments is moderately successful in this study and despite the limited depth of penetration, GPR provides useful data on stratigraphy of coastal area. The strongly progradating system in the current shoreline (location B, Fig. 4.2) and palaeo-shoreline (location C, Fig. 4.2) indicates a high sedimentation supply relative to accommodation. Direction of sigmoidal records of progradation, also indicates movement of the deltaic system along the coastline.

Two radio-carbon datings were performed on a core taken from profile 104 at 234 and 150 cm depths (Table 4.1). The deepest sample (at 234 cm) showed a very young age and the sample at 150 cm shows an age of AD1225. The possibility of sediments fallen from the wall during coring and the fact that the shells in the third section are not parallel, makes us to reject the second dating (at 234 cm). In fact, the shells in the third section (234 cm) are not eligible for radiocarbon dating as they are likely reworked from upper parts.

In brief, the GPR profiles 104 and 105 and radiocarbon dating show that sediment supply was high enough either in time of deposition of palaeo-beach (i.e. AD 1225) or in recent shoreline to continue progradation over the coastline.

5.3 Inland water bodies

5.3.1 Langarud

5.3.1.1 Sedimentary depositional environment

Different zonations including Sz, Mz and Pz based on different proxies (sedimentology, macro-remain and palynology, respectively) are combined and presented in Fig. 5.2, showing a good agreement in general. The dissimilarity is mostly due to difference in sampling resolution. Finally, the combination of the different proxies allows us to reveal five main depositional environments, which are from the bottom to the top:

I: Fluvial deposits from 664.5 to 490 cm

Coarse grains (sand) occur with angular and sub-angular lithic fragments and high MS values, which imply a high-energy environment (i.e. river) (Fig. 4.19) and a terrestrial source for the sediment. Also, no marine fauna has been found at these depths. We interpret it as fluvial deposit. These sands may have accumulated in a small incised river. The down-cutting is prior to the onset of the Little Ice Age, and hence it is hypothesised here to be linked to the Medieval Climate Anomaly low-stand in the absence of dating.

II: Soil formation under water table fluctuation from 490 to 380 cm

After the deposition of the sand, due to river avulsion sand deposition stopped and a soil developed. The presence of CaCO₃ nodules may suggest the formation in a dry environment, as the precipitation of calcium carbonate and formation of nodules is common in soils from dry environments (Durand et al., 2010; Cerling, 1984). However, the climate of the Little Ice Age in the south Caspian Sea area is rather humid (Kroonenberg et al., 2007; Djamali et al., 2009; Leroy et al., 2011). Another situation when nodules may form is in a leached soil. This is when a previously lower water table rises into the leached soil and precipitates CaCO₃ at the new interface as a result of CO₂ escape (Magaritz et al., 1981). Such situations are widespread in areas of drastic climatic changes or near a shore where transgressions and regressions affect the uppermost soil layers. We suggest it is a water table fluctuation driven by sea level rise. At the base of this facies, when the water table fluctuated frequently, large nodules were formed. Gradually, the soil was more continuously saturated and this led to less fluctuations, hence the formation of smaller nodules (Bouzigues et al., 1997).

III: A wetland influenced by sea and river from 380 to 242 cm

The low-energy sediment (silt) formed in the depression of wetland. At this stage, a transgression happened at a larger scale and sediments being deposited became influenced by CS water. This sedimentary facies contains typical CS dinocysts, indicative of a brackish water invasion to the wetland. It is suggested that this invasion happened under quiet conditions overland.

Based on the results of radiocarbon dating, this invasion can be dated to the 14th century and beginning of the 15th century. The brief re-occurrence of CaCO₃ nodules could be due to temporary river transport to the wetland, as a strong erosion is indicated by palynology.

IV: Wetland surrounded by very open, dry and erosive environment from 242 to 149 cm

Following maximal high-stand, the water level started to fall and the connection between the sea and the wetland was severed. The presence of dry soil elements in the pollen assemblages indicate an open landscape which was probably very degraded due to the brackish water invasion, soil salinization and subject to strong erosion.

V: Shallow freshwater wetland and intensive human activities from 149 cm to the top

This zone is interpreted as a very shallow freshwater wetland with a strong soil component. No connection with the CS is noted. The wetland area where the core was taken is now drained. Hence a soil has developed which is now under intensive agriculture.

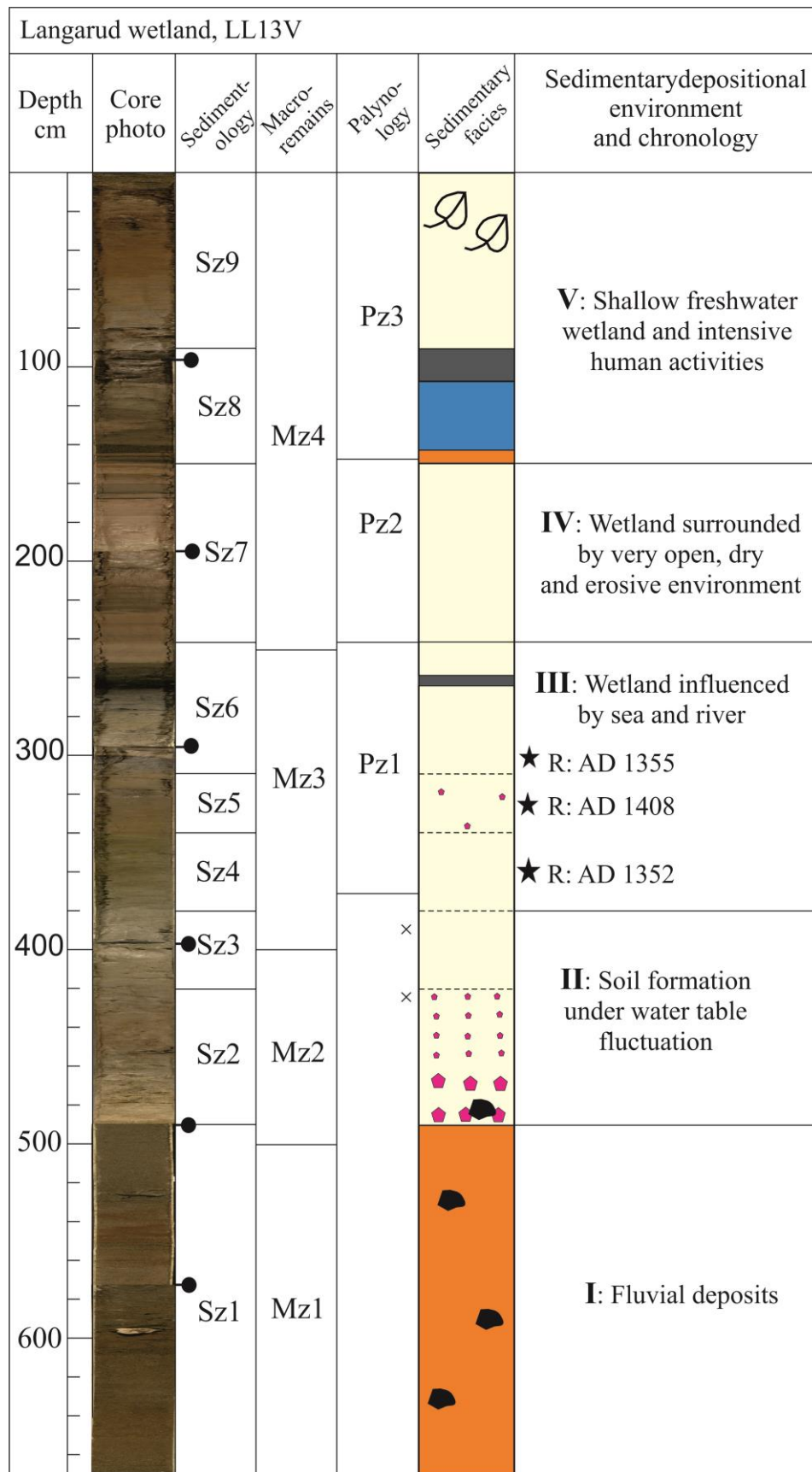


Fig. 5.2. Comparison of different zones, including sedimentology (Sz), macro-remains (Mz) and palynology (Pz), and depositional environments in Langarud sequence LL13V. Black pin symbols show the core section limits. × in palynology column display the location of barren samples. Black stars refer to the depth of the radiocarbon date, R: rootlet (material dated) with median calibrated age (For legend see Fig. 4.19). From Haghani et al. (in press) with modifications.

5.3.1.2 Terrestrial cover: comparison to other sequences and economical/historical impact

The diagrams from the Amirkola lagoon (a core and several surface samples) serve as a good comparison point in order to reconstruct the proximity of the alder forest (Leroy et al., 2011). Values in the order of 30% of pollen zones Pz1 and Pz3 of Langarud have been found in or close to narrow strips of alder forest along the Amirkola lagoon and also in rice paddies nearby, but never in the alder swamp itself (surface samples near Amirkola lagoon) where the percentages climb very quickly to high values (Leroy et al., 2011). Hence, the Langarud wetland was never in the alder forest itself.

After the brackish water invasion the alder swamp, that is very sensitive to salt, became extensively damaged and the soils were salinized making them unsuitable for agriculture, and prone to erosion. Even the Hyrcanian forest would have been affected. Important agricultural activities on the narrow coastal zone, relevant not only to the economy of the Guilan coast but also for the rest of Persia, were damaged. This massive brackish water invasion has taken place as Tamerlane went through Persia to Azerbaijan from AD 1383 onwards (Encyclopedia Britannica, 2015). Armies reached the then-impoverished Caspian coastal plain that at the time would have borne more resemblance to the steppe where the Turko-Mongol army came from than the Hyrcanian jungle.

5.3.1.3 Brackish water invasion: impacts, causes and comparison to other studies

The main hypothesis of this study was that the Langarud wetland might have been flooded by CSL rise during the LIA high-stand, and this was found to be the case. Moreover, the Langarud wetland itself was under closer influence of the river than today. However, only the microfossil data are informative here, as the macro-remains did not deliver any of the expected data on marine macrofossils, such as foraminifer tests.

Regarding the signs of the CSL rise and brackish water invasion in the Langarud wetland, similar assemblages of dinocysts have been found in coastal lagoons such as Anzali Lagoon at present and in the past, as well as in Amirkola Lagoon in the LIA and in the open sea (Leroy et al., 2011; 2013a,b). The presence of these dinocysts clearly indicates an intermittent marine influence to the water body. However, no objective observations allow suggesting that Langarud has ever been a coastal lagoon. Under normal circumstances, its current elevation, which is clearly above the highest high water, prevented the Langarud wetland from being considered as a coastal lagoon. Indeed, the informal use of the term of lagoon for any water body has posed problem for the correct interpretation of this kind of wetland that never acted as a coastal lagoon (Bao et al., 2007). Due to CSL rise and an overland connection between the sea and the water body, the

Langarud depression was under CS indirect influence during the early LIA and in a distal position during the brackish invasion. Taking into account the elevation of this distal wetland, it is proposed that the CSL reached up to -21.44 m: at least 6 m higher than the present level of the CS (-27.41 m in 2014).

In addition, the results of the present study can be correlated with a high-stand reported in historical documents and geological evidence in the region. Mostowfi (1999) discussed how the city and port of Abeskun was flooded by the CS in AD 1304. It was hypothesized that the location of Abeskun is consistent with the current location of Gomishan (Fig. 1.1), which lies at approximately -23.5 m and currently is 7 km from the present coast line. A survey of the literature (Kroonenberg et al., 2007; Kakroodi et al. 2012, 2014 and 2015; Leroy et al., 2013a,b; Naderi Beni et al., 2013a) clearly indicates that the Langarud sequence has recorded the brackish invasion the furthest inland and at the highest altitude. Our results support the information provided by Brückner (1890) who stated higher levels in AD 1306 carrying on until AD 1400 at -21.4 m because it was reported that water reached a mosque in Baku (Azerbaijan). These latter values in a compilation by Naderi Beni et al. (2013a) were regarded as too high because of other contradictory evidence. Also Brückner himself expressed a slight doubt about this high stand at AD1400. However this can now be clearly dismissed (Fig. 5.3).

Different causes have been accounted for the high stand. Kroonenberg et al. (2007) interpreted these higher water levels as being the results of the increased precipitation, and decreased evaporation over the CS, which they correlated with a lower solar activity. However, Naderi Beni et al. (2013a) proposed that the beginning of the water level rise during thirteenth century was linked to a man-made diversion of Amu-Darya River into the CS. Indeed, the town of Guganj and its great dam on the Amu-Darya River was destroyed by Genghis Khan's army in AD 1219 (Mostowfi, 1999) following the Mongol invasion of Chorasmia (Khwarezm). The Amu-Darya then flowed into the Caspian Sea for an unknown period of time.

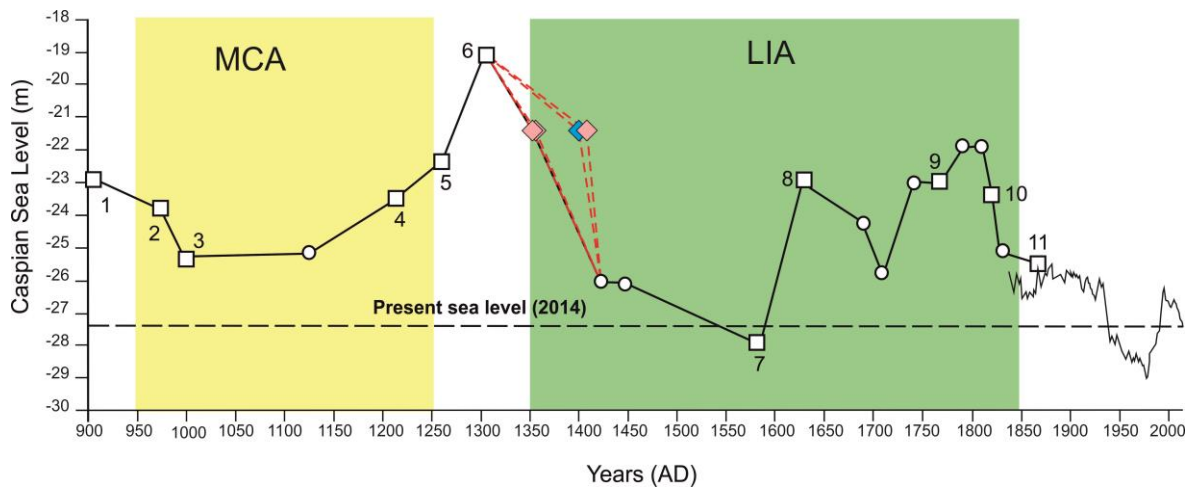


Fig. 5.3. Caspian Sea Level curve for the last millennium, after Naderi Beni et al. (2013a). Three pink diamonds are based on the results of this study and blue diamond is based on the study of Brückner (1890). Red dashed lines present the possible sea level curve. Data from 1900 to 1992 from Lepeshevkov et al. (1981); from 1992-2014 from USDA (2015). From Haghani et al. (in press).

5.3.2 Astaneh (AAL13V)

5.3.2.1 Sedimentary depositional environment

Astaneh sequence is subdivided into three main depositional environments based on different proxies (sedimentology, macro-remains and palynology) presented in Fig. 5.4. Based on chronological data, the deposits record three stages of development and provide evidence for significant changes in sediment deposition.

I: Shallow water body (1063-430 cm)

The lower deposits consist of horizontally bedded dark greyish brown to reddish brown silt with in situ tree roots, rootlets and bioturbation. The low magnetic susceptibility and relatively high amount of clay and also maximum aquatic pollen at the Pz2 zone suggest a shallow water body environment surrounded by alder trees. These fine grain sediments contain precipitation of CaCO_3 around rootlets, which suggests that the water body was temporary. Wieder and Yaalon (1982) discussed that carbonate precipitation is related to the metabolism of roots. High pressure of CO_2 as a result of root respiration contributes to a relatively rapid crystallisation of dissolved calcium. The top section of this zone is characterised by a maximal amount of plant material (Mz2 in macro-remain diagram and Sz2 with the peak of OM) and absence of CaCO_3 precipitation and therefore a decrease in CaCO_3 , corresponding to Pz2 aquatic vegetation.

Based on radiocarbon dating at 956 cm, most of these sediments were deposited before the Sefidrud avulsion, most likely as a part of a larger wetland (Purple dashed line in Fig. 4.24). Based on chronological data (at 956 and 589 cm), without considering any hiatus, the sedimentation rate for this part of sequence would be low, i.e. 2.2 mm/yr. However, the

presence of long woody tree roots below the sample at 589 cm caused the concern that the rootlet was penetrating a little deeper, along with the main tree root. Therefore, the date may show an age slightly younger than that of the sediment. This is the ‘Astaneh Wetland’ in the sense we defined on the cores of Kazancı and Gulbabazadeh (2013) (see Fig. 6 in Kazancı and Gulbabazadeh, 2013).

II: Fluvial environment (430-184 cm)

The deposits consist of alternation of reddish brown sandy silt and dark grey to olive brown silt. The sudden increase of MS and grain size shows an obvious change in depositional environment. Presence of reworked pollen grains and fungal spores indicate strong erosion and suggest river transport. High MS in this zone indicates a transport of minerals from igneous and metamorphic rock with an Elburz Mountains origin. Indeed, after Sefidrud avulsion, it is suggested that the temporary body water was flooded by Sefidrud and fluvial deposits were deposited. The timing of avulsion could be considered after AD 1769 based on the radiocarbon dating at 322 cm (Fig. 5.4 and Table 4.3). These fluvial deposits consist of river terrace (silty sand and sandy silt) and point bar (silt) were deposited in form of incised valley during rapid sea level fall happening after AD 1805. Indeed, incised valleys occur where rivers have eroded delta plain as a result of sea level fall (Reading, 2009). If the carbon dating at 589 cm is accepted, the average sedimentation rate has increased to 21 mm/yr in this zone.

III: Marsh under river influence (184 cm to surface)

The upper sediments consist of alternation of strong brown to brown silt with rootlets, and brown silty sand to sandy silt. As the topmost date is very young, it indicates a sedimentation that has carried on until the last years. This is perhaps linked to the progressive reduction of some contemporary marshes, still visible a less than a km west of the coring location (the green line in Fig. 4.24 B and Fig. 3.4). High MS in the silty sand deposits suggests that the coarser fragments are deposited by river. This river is a distributary of Sefidrud that flows to lagoonal deposits (see Fig. 4.24 A). Considering the radiocarbon dating at 142 cm, the sedimentation rate has increased to 43 mm/yr for the top sediments. During stages II and III, the Sefidrud has cut into its flood plain and now it is > 9 m lower than the surface of the current wetland.

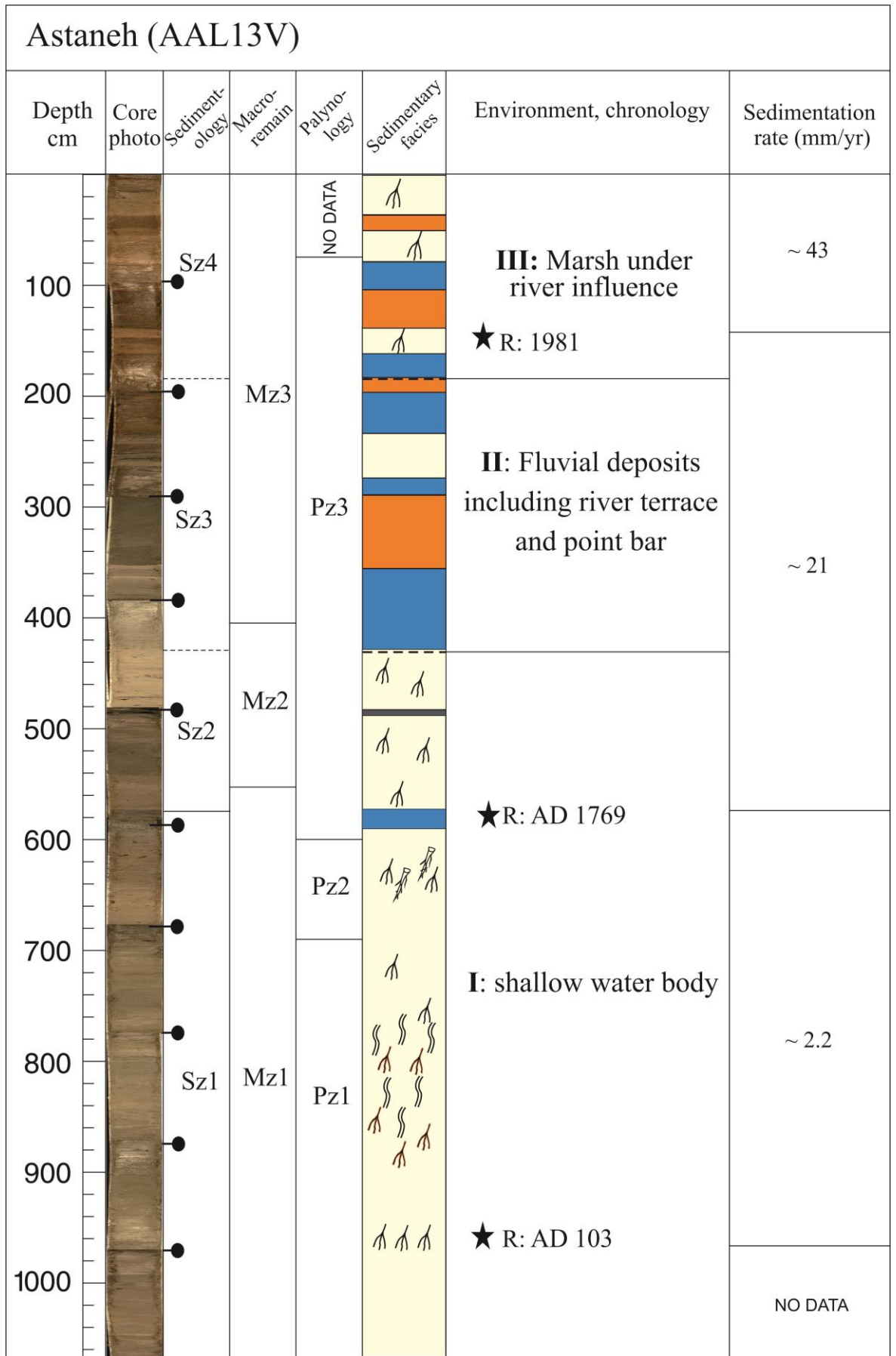


Fig. 5.4. Interpretation of facies based on sedimentology, macro-remains and palynology of the sequence of AAL13V. Black stars: radiocarbon dates. Coring took place in 2013.

5.4 Coastal lagoons

5.4.1 Zibakenar Lagoon

5.4.1.1 Age validation and sedimentation rates in Zibakenar Lagoon

A multiple dating approach including radionuclide dating and radiocarbon dating, indirect biotic dating (based on known arrival dates for immigrant species) and evidence from SCPs and remote sensing was applied on core ZL11L2 and Zibakenar Lagoon. The radionuclide chronology shows that sediments shallower than 156 cm are more recent than 1950. Radiocarbon age estimates were 1955–1956 at 177 cm (Fig. 5.5). These data are corroborated by biological time–marker elements. One pollen grain of *Eucalyptus* (a tree introduced from the southern hemisphere) was found at 66.5 cm depth. *Eucalyptus* trees were introduced not earlier than 1952 in the Hyrcanian forests, and only became abundant after 1970 (Akhani et al., 2010; Sagheb–Talabi, 2004). The other time marker that can be used to validate the dating is the occurrence of the invasive bivalve *A. segmentum*. This bivalve was brought from the Azov–Black Sea into the Caspian in 1939–1940 and by the end of 1959 it populated the western part of the middle and southern CS (Grigorovich et al., 2003). The presence of juvenile *A. segmentum* (earlier this species was reported as *A. ovata*) at 217 cm depth confirms that the whole sequence was probably formed after 1959. Only larval shells of *A. segmentum* were found, which eliminate any concern about burrowing. Remote sensing also confirms that the Zibakenar Lagoon was formed between 1955 and 1964 (Fig. 4.1 A and B).

To sum up, these time markers, together with remote sensing results, are in agreement with the results of radiocarbon dating (1955 at 177 cm), which provides an approximate sedimentation rate of 31 mm/yr. Therefore, this lagoon is younger than what has been suggested by previous research in the area (i.e. after 1880 in Naderi Beni et al., 2013b and the last four centuries in Lahijani et al., 2009), and older than what has been suggested by Kazancı and Gulbabazadeh (2013) i.e. 1982. Other lagoons in the southern CS have shown relatively low sedimentation rates (Table 5.1).

Table 5.1. Sedimentation rates in lagoons of the southern Caspian Sea

Site name	Sedimentation rate (mm/yr)	References
Gorgan Bay	0.2-5.4	Amini et al., 2012
Anzali	1-6	Leroy et al. 2011
Amirkola	3.1	Leroy et al. 2011
Karabogaz Gol	4.6	Leroy et al., 2006

5.4.1.2 20th century depositional sedimentary environments of Zibakenar Lagoon

Different zonations based on sedimentology, macro–remains and palynology proxies (Sz, Mz and Pz) are combined and presented in Fig. 5.5. The proxy zonations are in close agreement. Small discrepancies are mostly due to differences in sampling resolution. The combination of the different proxies allows to recognition of four main depositional environments, from bottom to top:

I: Estuary phase (220–182 cm)

Estuarine facies are found in the deepest part of the sequence ZL11L2 (A and B), ZL11L1 (A and C), ZL11G2 and ZL11G7 and has high MS values, indicating a terrestrial source for the sediments. Nevertheless, it is also characterised by the presence of typical Caspian fauna including bivalves such as *A. segmentum*, *C. glaucum* / *M. edentula* and foraminifers such as *A. beccarii*, a typical inhabitant of silty–sandy grounds of the CS (Latypov, 2004). Dinocysts and foraminifers are abundant. Hence, CS and fluvial sediment sources contributed to the formation of this facies. The presence of charophytic oogonia, the reproductive body of a multicellular green algae encrusted by limestone, does not contradict the interpretation of a marginal marine environment. Charophytes tolerate a wide range of salinities, from fresh to hypersaline, though they do not occur in normal marine environments (García et al., 2002).

The plant material encountered may have been transported by river, possibly explaining the ‘old’ radiocarbon age on a wood sample at 209 cm depth. Also, high concentrations of *Alnus* pollen were found in this unit; the site is probably not in the alder swamp itself, but under its strong influence as the trees would have vanished if they were under the direct influence of saline waters. In brief, this environment may correspond to an estuary of a minor distributary of the Sefidrud.

II: Open lagoon phase (182 – 147 cm)

Deposition of lagoonal sediment containing both charophytes and typical CS bivalves (such as *A. segmentum* and *M. edentula* / *C. glaucum*), and Foraminifera (*A. beccarii*) is indicative of the beginning of the separation from the open CS through formation of a sand barrier. This facies is found in cores ZL11L2 (A and B), ZL11L1 (A, B and C). A clear change in sediment colour at the top of this facies (at 151 cm depth) suggests a transitional zone between the open lagoon the successive closed lagoon. This transitional zone contains a small amount of dinocysts, but Foraminifera are absent. The alder swamp is nearby in phase I, but its progressive disappearance occurs in phase II. Based on the results of radiocarbon dating, the formation of a coastal lagoon under brackish water invasion can be

dated to 1955–1956. However, as *A. segmentum* was already found in the preceding phase, this environment dates from 1959.

III: Closed lagoon phase (147–76 cm)

The replacement of typical CS molluscs by fossil-poor, fine-grained deposits reflects a decrease in brackish water influence and the build-up of a continuous sand barrier protecting the lagoon from the sea. Part of this silty sequence is even devoid of palynomorphs and has an orange shine from 118 to 90 cm depth, probably caused by oxidation and/or strong soil influx. As the two surface samples from the Sefidrud were devoid of pollen, it is not unlikely that the river was the source for lagoonal deposits. Therefore, sediment may have been transported through flushing operations at Manjil Dam since 1980 and most likely in the peak years 1984 and 1985 (Table 2.2). This would have instantaneously transported large amounts of fine-grained sediment downstream, killing fish and modifying phytoplankton communities (Morris and Fan, 1998; Pourafrahyabi and Ramezani, 2014). In this environment (environment III) and also the final phase (IV), pollen grains of Alder can be used as a taphonomical indicator of long-distance transport. Pollen analysis shows the occurrence of rice paddies and wetlands in the drainage.

IV: Closed lagoon in-filling phase (76–0 cm)

The fourth and last phase corresponds to terrestrial deposition that includes fine sediments. A brief brackish water incursion is indicated by considerable amounts of Foraminifera (*A. beccarii*), dinocysts and also broken bivalve shells at a depth of 66 cm, which could be related to maximum sea level rise at 1995. The increased abundance of aquatic vegetation spores and pollen and decrease of fungal spores and *Glomus* in the top sample may represent re-vegetation as a result of increased protection offered by the Nature Park status acquired in 2001.

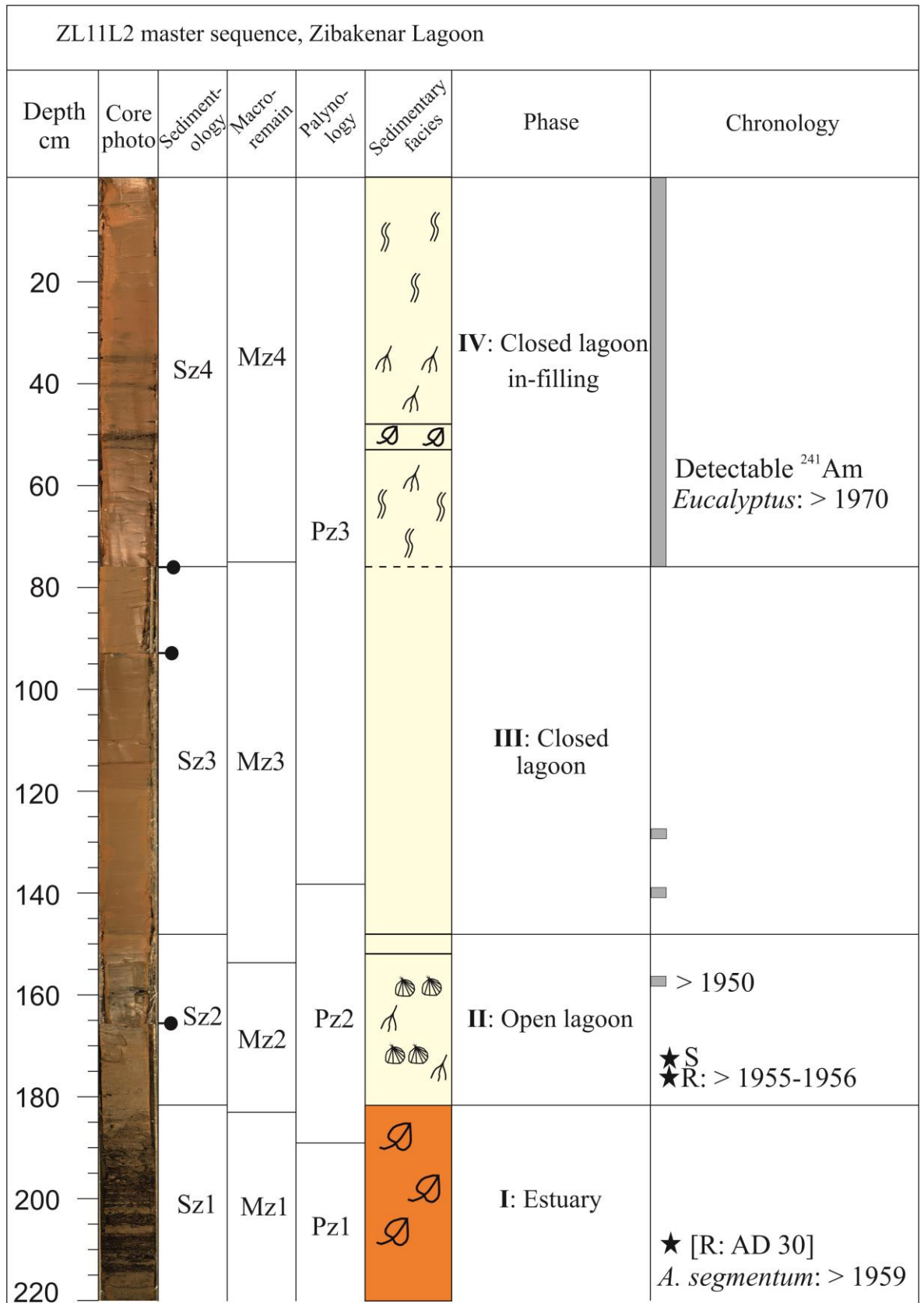


Fig. 5.5. Comparison of different zones, including sedimentology (Sz), macro-remains (Mz) and palynology (Pz), and depositional environments in ZL11L2A master sequence. Grey strip and rectangles: radionuclide dating. Black stars: ¹⁴C, R: rootlet and S: shell (material dated). The radiocarbon age of AD 30 at 209 cm is rejected. (For legend of sedimentary facies see Fig. 4.38).

5.4.1.3 Evolution of the Zibakenar lagoon through time and related sea levels

Based on the four phases and key layers such as sterile and transitional zones in the third phase, discussed in the previous section, the cores were correlated and an internal sediment distribution pattern in the Zibakenar Lagoon obtained (Fig. 5.6).

The Zibakenar infill has the typical form of a lagoon (Bungenstock and Schafer, 2009; Costas et al., 2009) in which the fine sediment accumulation is larger in its centre (e.g. cores ZL11L1 (A and B) and ZL11L2 (A–C)), sandy at the bottom (e.g. cores ZL11L1, ZL11L2 and ZL11G7) and organic rich at the margins (gravity cores ZL11G1, ZL11G3, ZL11G4 and ZL11G6). Oertel et al. (1992) showed that lagoons that have developed along tide-dominated coasts typically have floors that are irregular, reflecting the antecedent bottom topography. By contrast, lagoons developed along wave-dominated coasts tend to have a simple floor-topography.

Fine sediment thicknesses reach up to 182 cm. The boundary between phases I and II (Fig. 5.6) represent the time of lagoon formation. The ZL11L2 sequence illustrates the progressive decline of the alder swamp and the opening of the landscape in a strongly erosive catchment, with a peak of erosion at 134 to 86 cm, perhaps due to peak flushing operation of the Manjil Dam in 1984–1985 (Table 2.2). The decline of the CS influence is due to the delta progradation and minor changes in the Sefidrud distributary.

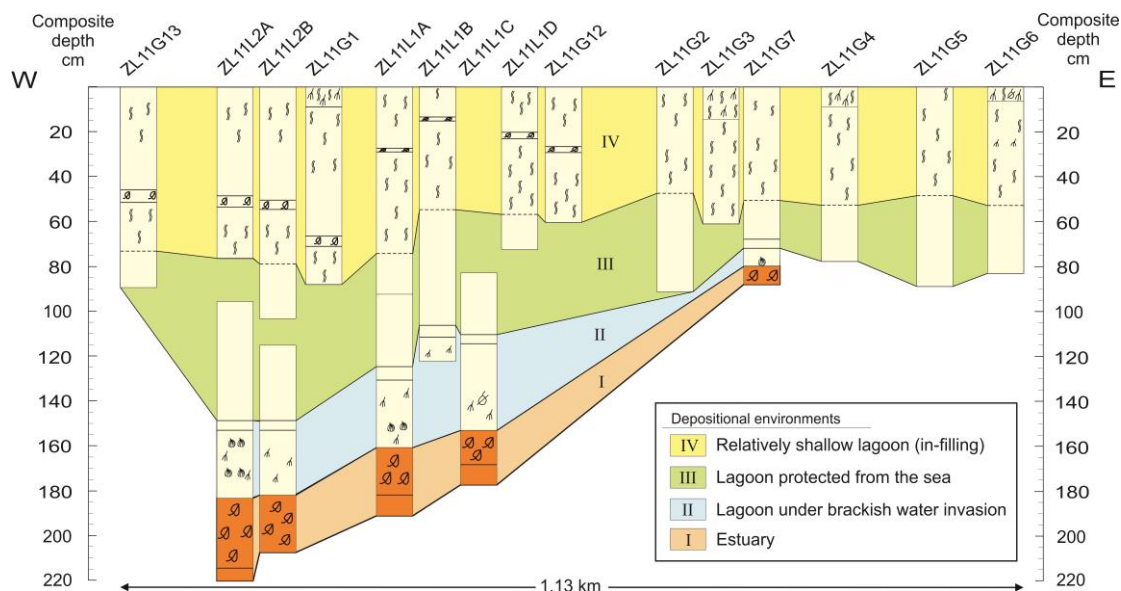


Fig. 5.6. Correlation of cores in Zibakenar Lagoon based on four sedimentary facies (For legend of sequences see Fig. 4.38).

The evolution of Zibakenar Lagoon can be divided into three stages based on whether the area was transgressive, regressive, or almost stationary relative to sea-level. The lagoon originated between 1955 and 1964 as a result of Sefidrud Delta progradation into the CS in a period when sea level was relatively stable. During that period, long-shore currents formed a sand spit and Zibakenar Lagoon came into existence. The lagoon had inlets to the CS as shown by the presence of CS bivalves, Foraminifera and dinocysts. In the next stage, the coastal embayment became enclosed by wave-built barriers. Along this wave-dominated stretch of coastline, the wave induced long-shore sediment transport resulted in formation and growth of a spit. The same process can lead to a progressive choking of the lagoon, decreasing its equilibrium volume (Duck and da Silva, 2012). The response to sea-level fluctuation of a lagoon is a function of sedimentation rate and sea level rise (Nichols and Boon, 1994; Kirk and Lauder, 2000). As increasing sedimentation rate while the rate of sea level rise is low yields a surplus lagoon where the lagoon is infilling and short-lived. In contrast, when sea level rise exceeds sedimentation rate it yields a deficit lagoon where the lagoon is gaining volume (Nichols and Boon, 1994; Kirk and Lauder, 2000). Between 1977 and 1995, sea level rose and Zibakenar was flooded by the CS. The maximum CSL rise of 1995 is recognisable by the presence of CS indicators (Fig. 4.40, 4.42). The connection of Zibakenar Lagoon with the CS is also visible in remote sensing data (Fig. 4.1 D). Since 1995, the CS has been falling and sediment supply from the Sefirud restricted due to the lack of flushing operations since 1998 (Table 2.2; Yamani et al., 2013).

5.4.1.4 Future of the coastal lagoons

The most common scenario of lagoon evolution is the so-called diverging model (Oertel et al., 1992), which describes coastal lagoonal evolution as being driven by sediment infill and therefore coastal lagoons have been considered to be natural sediment sinks (Boyd et al., 1992; Nichols and Boon, 1994). The Kiashahr, Zibakenar and Ushmak Lagoons are located in the active growing Sefidrud Delta with high sedimentation rates and can be categorised as surplus lagoons. The present study demonstrated their very recent appearance between 1955 and 1964. It can also be reasonably predicted that the lagoons will be filled relatively soon because of the high sedimentation rates in the Zibakenar Lagoon (c. 31 mm/yr). If this rate is used, the middle of the lagoon, that is now under 185 cm of water, will be filled in 59 years. The total longevity of the Zibakenar Lagoon would then only be c. 115 years. Such a duration is not unusual for coastal lagoons (Oertel et al., 1992; Martin and Dominguez, 1994; Kirk and Lauder, 2000; Duck and da Silva, 2012).

The CS is a special case as sea level rises and falls are much faster than the global ocean and hence lagoons may appear and disappear much faster (Ignatov et al., 1993; Kaplin et

al., 2010). This provides additional constraints on conservation of lagoons around the CS not seen in marine coastlines elsewhere. The CS has a coastline of the order of 7000 km long, which is punctuated by many lagoons (Ignatov et al., 1993). Many have known similar history to that of Zibakenar, for example the Caspijsk Lagoon in Dagestan. Conservation often is aiming at preserving steady-stable environments while the Sefidrud Delta and its lagoons are extremely dynamic. Future plans by the Ramsar Convention for the adequate protection of the Boujagh National Park (and many other lagoons around the CS) should take this in consideration if they want to maintain its high biodiversity and shelter role for regionally rare species and migrating birds. The condensed evolution history of the CS lagoons should be considered when evaluating changes happening to coastlines around the world threatened by flooding due to the current sea level rise.

5.4.2 Amirkola Lagoon

5.4.2.1 Source of the sediments

Previous studies have suggested that the Amirkola Lagoon was formed by littoral drift of sediments supplied by the Old Sefidrud during a high stand in the LIA (around AD 1600) (Kroonenberg et al., 2000; Lahijani et al., 2009; Leroy et al., 2011; Naderi Beni et al., 2013b). Based on the radiocarbon dating on core HCGL02 (Leroy et al., 2011), the age of Amirkola Lagoon at 63 cm depth was estimated at AD1750 and as a result sedimentation rate for this core was estimated at ~ 3.1 mm/yr. However, this dating was performed on a sample in the middle of the lagoonal deposits (e.g. 63 cm depth in Fig 5.6), and not at the base of the lagoonal deposits (e.g. 80 cm in Fig. 5.7). Considering the estimated sedimentation rate, the age of lagoon initiation is not older than AD 1700. Two sources for the sediments were distinguished which includes the river supply of the Old Sefidrud and littoral drift. The results of this study, confirming previous studies, indicate that the sandy layer (sandy silt and silty sand) at the bottom of the cores belongs to a sand barrier deposition. High MS in these sediments is a result of transporting heavy minerals by the Old Sefidrud and re-deposition of the sediments by littoral drift and finally formation of barrier. Moreover, these sediments contain *C. glaucum* shells that are a sign of deposition of sediments from marine environment. Also, the presence of bivalve shell fragments in this layer shows the role of wave action in deposition of the barrier. The same layer of silty sand with marine shells was recognised at the bottom of core HCGL02 (see figure 5 and 6 Leroy et al. (2011) and figure 4.51 for the location). This core (HCGL02) shows the same increasing upward of OM and CaCO₃ as the core AL11G5 (Fig. 4.54). However, the OM in HCGL02 reaches up to 40%, while in this study and Lahijani et al. (2009) amount of OM is up to 10%. The present study shows the horizontal extension of the basal silty sand layer from the north to the west (Fig. 5.7). The top silt layer contains

Ecrobia grimmeri, *Lymnaea S.l.*, *Theodoxus pallasi* and charophyte which shows that the upper part belongs to a lagoonal environment. The presence of brackish bivalves (*C. glaucum*) in the lagoonal sediments is due to its connection to the sea in the past (Leroy et al., 2011).

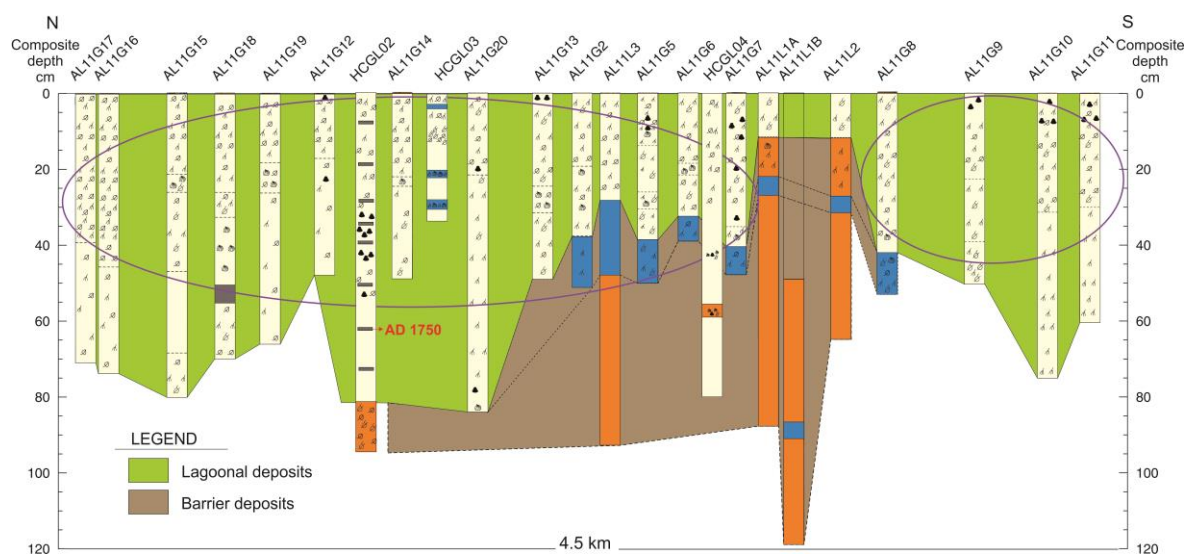


Fig. 5.7. Correlation of cores in Amirkola Lagoon (For legend of sequences see Fig. 4.53 and for the core locations see Fig. 4.50). Core HCGL02, HCGL03 and HCGL04 from Leroy et al. (2011).

The results also show that the lagoonal sediments are thinner in the centre of lagoon and becoming thicker towards the north and the south (Fig. 5.7). It may suggest that the present-day Amirkola Lagoon is consisting of two separated smaller lagoons which are now connected together.

5.4.3 AL11V3 sequence

5.4.3.1 Depositional sedimentary environment

Different zonations, including Sz, Mz and Pz based on different proxies (sedimentology, macro-remain and palynology, respectively), have been presented in Fig. 5.8. Different types of sedimentary environments can be distinguished, reflecting terrestrial, fresh water and marine conditions. These sub-environments from the bottom to the top include:

Facies I: Floodplain (281-131 cm)

The first facies contains dark brown sand that infers a high-energy environment. This facies has a high MS value (up to 30), indicating indicates a terrestrial source for the sediments. The presence of plant material in the middle part (170-160 cm) indicates a terrestrial origin. Also, due to the lack of marine biota in this facies, these deposits are interpreted as fluvial sediments, deposited by Old Sefidrud. This facies is probably not

directly deposited in the river channel itself, but under a strong river influence, such as in a floodplain environment.

Facies II: Lagoon under frequent brackish water influence (131-119 cm)

The second sedimentary unit consists of olive to olive-grey fine silts and fine sandy sediments, rich in organic matter (up to 3%) with a rich fossil component consisting of numerous gastropod shells (*T. pallasi* and *E. grimmi*), bivalves (*D. polymorpha* and larval shells), charophytes, Foraminifera (mainly *A. beccarii* and some *E. brotzkajae*) and dinocysts. This unit is interpreted as a lagoon environment that is under frequent brackish water influence. Indeed, the presence of charophytes and gastropod shells confirm that these facies was deposited in an environment of mixed influences. Presence of Foraminifera and dinocysts is an evidence of brackish water invasion from the CS. This lagoon has not be subjected to study previously and thanks to Professor Klaus Arpe who discovered the outcrop in 2011, we decided to name the lagoon Klaus Lagoon.

Facies III: Lagoon protected from the sea (119-73 cm)

Above the lagoonal and brackish deposits (facies II), the third unit consists of fine silt and fine sandy sediments, rich in organic matter, with considerable amounts of fungal spores and terrestrial plants. This unit is interpreted as mostly a closed lagoonal environment with in its middle part (109-93 cm) a minor marine invasion (presence of dinocysts and Foraminifera).

Facies IV: Lagoon under strong brackish water influence (73-60 cm)

Fine brown silty sediments, rich in OM, is considered as deposited in a lagoonal environment. This facies is indicated by a considerable amount of Foraminifera (*A. beccarii* and *E. brotzkajae*), bivalve shells and dinocysts.

Facies V: Sand dune and modern soil (60-0 cm)

The fifth facies consists of dark yellowish brown sand deposits with relatively high MS (up to 28). This facies is interpreted as sand dune, covered by soil at the top.

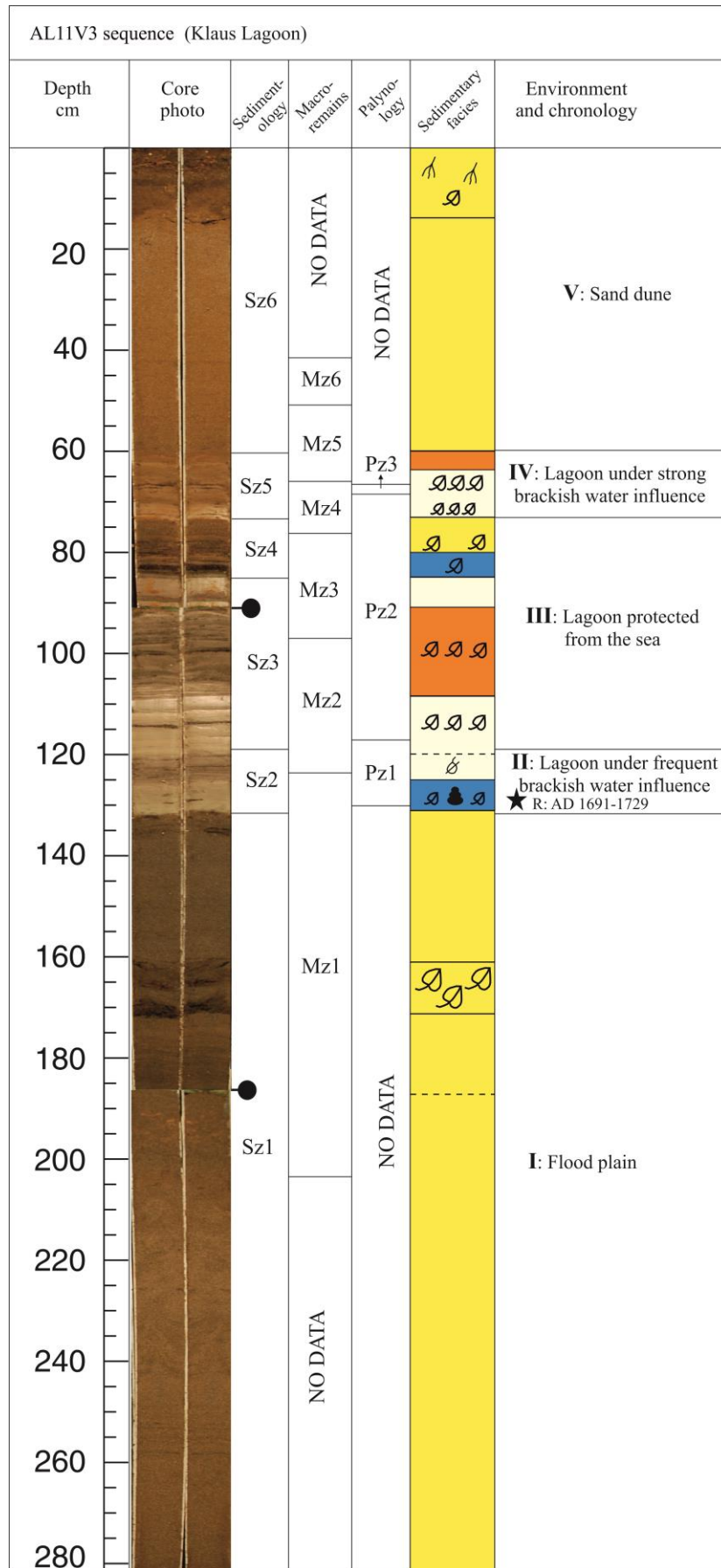


Fig. 5.8. Comparison of different zones, including sedimentology, macro-remains and palynology, and depositional environments in sequence AL11V3, the outcrop near Amirkola. (For legend see Fig. 4.59), black star: location of radiocarbon date, R: rootlet (material dated).

5.4.3.2 Age validation of Klaus Lagoon

Dating performed on the bottommost part of facies II provides two possible ages: AD 1810-1922 with 74% probability and AD 1691-1729 with 26% probability (Table 4.6). During the period of AD 1810 to 1922 the sea level was relatively constant with minor fluctuations less than one meter. Therefore, the second probability (i.e. AD 1691-1729) and more likely after AD 1715 (start of sea-level rise) is used for the interpretation of the sequence. At the same period, Amirkola Lagoon was formed in AD 1750 (Leroy et al., 2011) under rapid sea level rise (Fig. 5.10). Formation of sand barriers and lagoons behind them along the western Caspian coast in Dagestan are discussed in Kroonenberg et al. (2007). In Klaus Lagoon, the formation of lagoon happened at the same time of Amirkola Lagoon formation and slightly after the Turali Lagoon formation in Dagestan (i.e. AD 1628). The Klaus Lagoon was under the brackish water invasion (facies II in Fig. 5.8) and became protected from the sea through time (facies III in Fig. 5.8). Taking into account the elevation of coring location at -24.80 m, this suggests that CSL reached up to -24.80 m: at least 2.61 m higher than the present level of the CS in time of formation of Klaus Lagoon (Fig. 5.9).

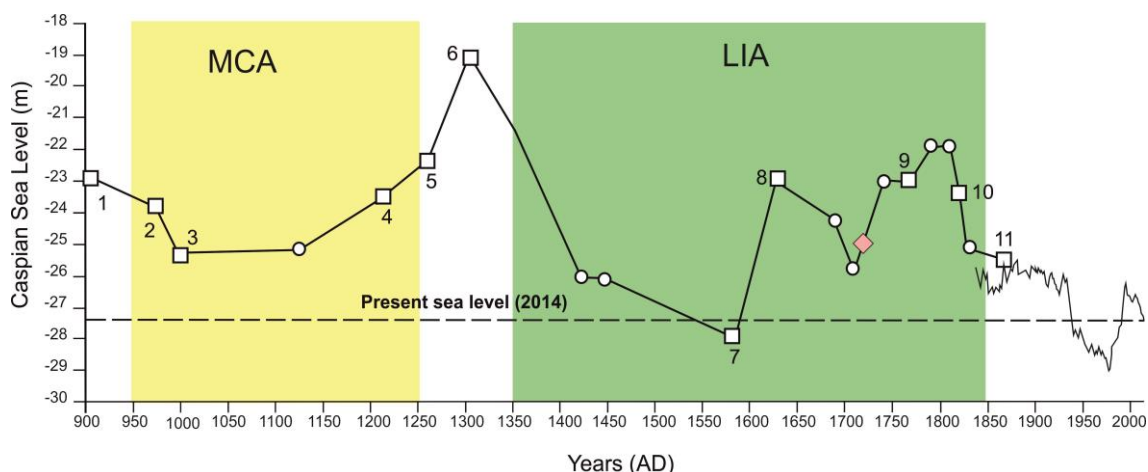


Fig. 5.9. Caspian Sea Level curve for the last millennium, after Naderi Beni et al. (2013a). Pink diamond is based on the results of this study. Data from 1900 to 1992 from Lepeshevkov et al. (1981); from 1992-2014 from USDA (2015)

5.4.3.3 Evolution of the Klaus coastal lagoon through time and related sea levels

In the first stage, between AD 1715 and AD 1805, CSL rose up to -23.8 m (the sea level rise between AD 1715-1805 (Brückner, 1890; Leroy et al., 2011; Naderi Beni et al., 2013) and Klaus Lagoon formed under a sand barrier (stage B in Fig. 5.10). At this stage, a connection with the CS still existed or the salinity in the lagoon is not lowered by run-off or ground water input (Yanina et al., 2005). Therefore, the lagoon formed a suitable environment for brackish water species.

The rapid sea level fall between AD 1805 and 1875 when the CSL reached -25 m in AD 1875 caused a seaward shift (stage B in Fig. 5.10). Meanwhile, the area was subjected to intensive erosion as a result of abrupt reduction of sediment supply from the Old Sefidrud due to river avulsion since ~ AD 1600. Since the avulsion happened, the Old Sefidrud is not the main tributary flowing into the sea in this area and sediment output and water discharge have decreased considerably. Therefore, more erosion processes are happening along the coast in this area rather than deposition and progradation. Recent evidence of erosion suggests that landward shift of the coast is happening in this area since AD 1978 in response to rapid sea level rise (Kakroodi et al., 2012). According to Kakroodi et al. (2012), the rate of regression during 1978 to 2000 in this area was 181 m/yr. Regressions with rate of 60-100 and 150-200 m/yr were also recorded in the north-eastern and north-western of CS, during the rapid sea level fall (Ignatov et al., 1993; Kaplin and Selivanov, 1995). However, wind still remains a source of sediment deposition in this area and sand dunes can develop along the coast (stage C in Fig. 5.10). Lahinjani et al. (2009) and Kazancı et al. (2004) have discussed possibility of coastal sand deposition in form of sand dune in the Sefidrud Delta. Sand dune formation has also observed during field observations along the coastal line in the area between Anzali and Zibakenar Lagoons (Location A in Fig. 4.2).

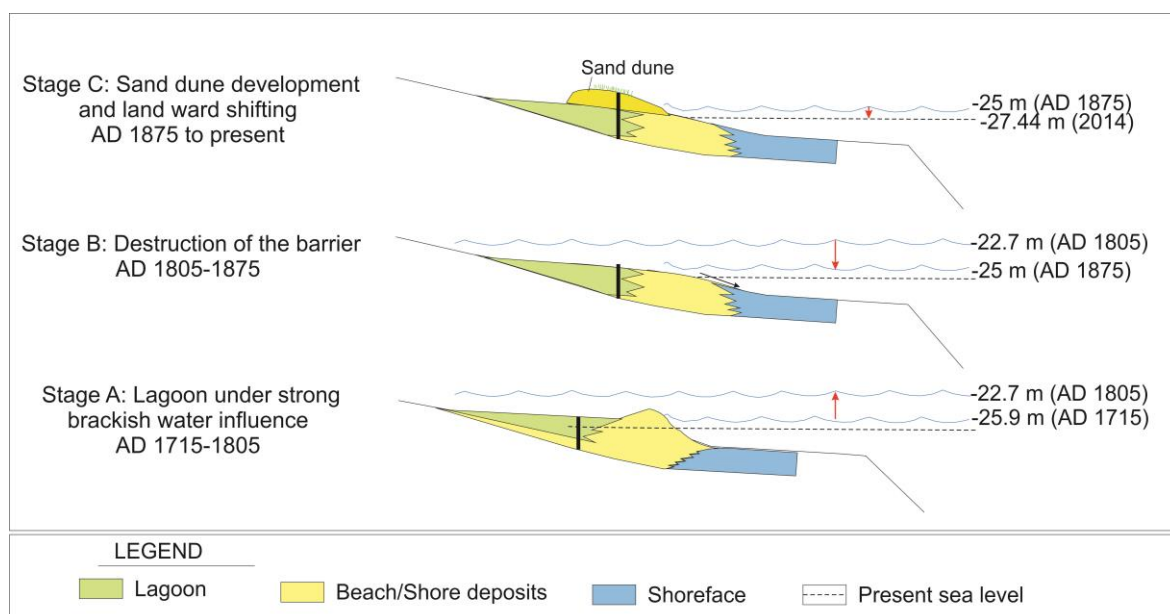


Fig. 5.10. Evolution of Klaus Lagoon through time and related sea levels (dates from the sea level curve of Naderi Beni et al., 2013)

5.5 Marine deposits

The near shore and offshore deposits of Sefidrud Delta in front of previous main tributary (1964-1991) mainly consist of dark grey and greyish brown silt. At 105 m water

depth, the sediments show dark lamination which disappear very fast under oxidising condition. These dark laminations were observed also in other offshore sequences of the CS (Haghani, 2009; Leroy et al., 2013). Jelinowska et al. (1999) discussed the presence of these black and grey laminations. They indicate an anoxic condition at the bottom of the basin and formation of authigenic iron sulphide (greigite). Magnetic susceptibility shows extremely low values (less than 1) compare to other sequences offshore Sefidrud Delta, and offshore Southern CS (Haghani, 2009; Leroy et al., 2013b) where magnetic susceptibility reaches to 60 offshore Babolsar and 24 offshore Anzali (Fig. 4 in Leroy et al., 2013b). It should also be considered that the diameter of core for the offshore cores from this study (7 cm diameter) is even larger than the diameter of cores from other studies (5 cm diameter). Numbers of foraminifers remain considerably high in the cores NSM14G3 and G4 where the water depth is 301 and 431 cm, respectively (~ 450 and 300 foraminifers in NSM14G3 and G4, respectively. See concentration diagram in Fig. 4.70). However, all the species of CS Foraminifera are benthic and live above 50 m water depth (Boomer et al., 2005).

5.5.1 Steep slope setting

Profile 35 is the longest profile in front of the Sefidrud which shows the characteristic three-partite structure of a delta. The area from the coastline to 11 km distance from the coastline belongs to delta plain (topset) where the gradient is up to 8°. At this stage, the main depositional structure is parallel bedding (Fig. 5.11 A and B). The next stage which is known as delta front (foreset) is marked by an abrupt change in slope where the gradient reaches to 60° (between 11 and 13 km). At this stage the slope is mostly too steep for sediment accumulation and acts as a by-pass margin. At this stage, fine-grained sediments tend to be unstable on the slope and slumping of the sediments may occur which results in re-deposition in deeper parts of basin. At the third stage (from 13 to 14 km), the gradient is reduced to 20° where deposition of sediments occurs in a prodelta setting, also known as bottomset. Therefore, the Sefidrud Delta is categorised as a Gilbert-type delta where a distinctive pattern of steeply-dipping delta plain beds sandwiched between horizontal delta plain and prodelta strata is observed (Nichols, 2009).

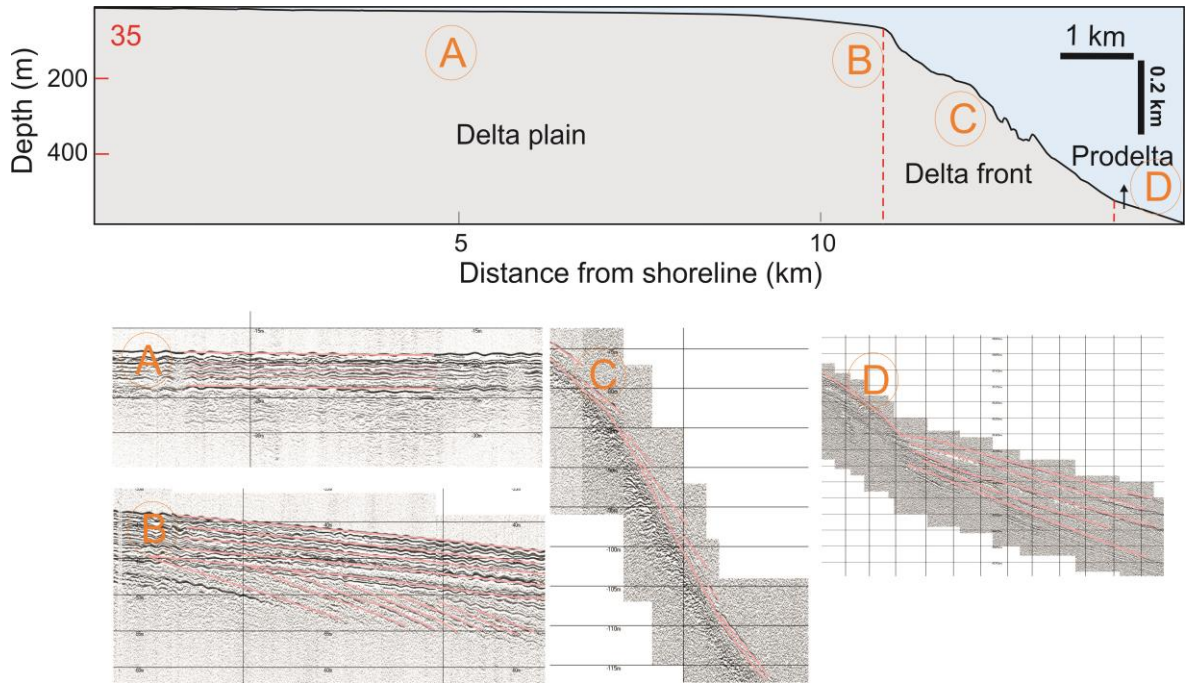


Fig. 5.11. Seismic profile 35 displaying delta plain (A and B), delta front (C) and prodelta (D).

Figure 5.12 presents a 3D model of the slope setting of Sefidrud Delta based on seven seismic profiles (Fig. 4.65 and 4.66). The slope is very steep near to the main channel (profiles 36 to 34 in Fig. 4.66 and 5.12) and has a low gradient towards the east (profiles 33 and 30 in Fig. 4.66 and 5.12) and becomes flat towards Anzali (profiles 27 and 19 in Fig. 4.66 and 5.12). The core locations are also presented on this diagram to have a rough idea of the location of cores on the offshore delta.

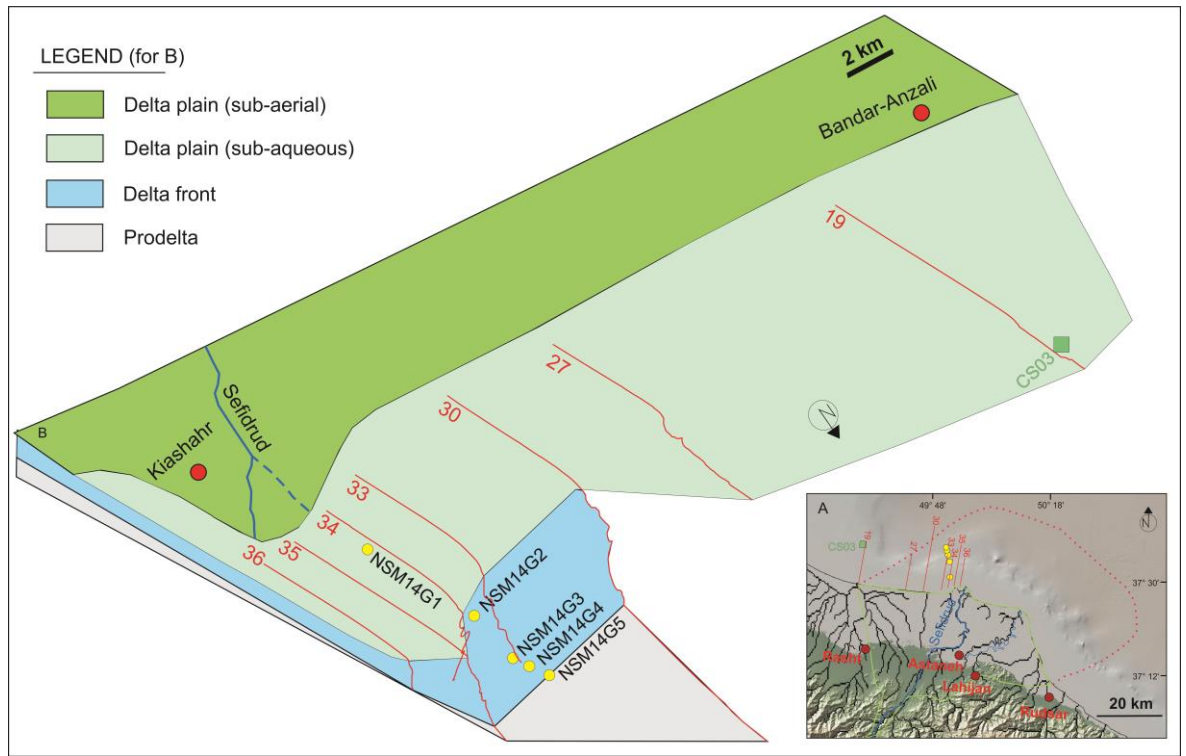


Fig. 5.12. A: Location map of seismic profiles (red lines) and cores (yellow dots) taken from the Caspian Sea, green line represents subaerial delta limit and red dashed line represents subaqueous delta limit from Kazancı and Gulbabazadeh (2013); red dots: location of main towns; green square: location of CS03 (Leroy et al., 2013 b). Default base-map from Ryan et al. (2009) (<http://www.geomapapp.org>). Block diagram of the slope of the Sefidrud Delta in the study area. Red lines: seismic profiles, yellow dots: location of cores from this study and green square: location of core CS03 (Leroy et al., 2013 b)

5.5.2 Sedimentation rate and sediment delivery to the basin

The sedimentation rate of core NSM14G3 where the water depth is ~300 m is 1.67 mm/yr. Based on the CRS model, the sedimentation rate for the top 24 cm of the core shows three sedimentation rates (1.65 mm/yr for the top 9.5 cm, 1.2 mm/yr for 9.5 to 13 cm and 1.8 mm/yr for 13 to 24 cm). Although, the CRS model is more accepted for calculating sedimentation rate, but here the constant sedimentation rate is used to make a comparison with other sequences in the SCB. Based on this, the sedimentation rate for the top 24 cm is 1.67 mm/yr. However, the sedimentation rate in the middle part could be more reliable and the higher sedimentation rate at the top and bottom of that section could be a result of mass-wasting movement/turbidities. Higher concentration of Foraminifera in the core NSM14G3 in comparison with the shallower cores (NSM14G1 and NSM14G2) is a sign of mass wasting and slumping of the sediments. Nevertheless, this rate of sedimentation is around 12 times lower than sedimentation rate in an offshore sequence near to the boundary of Sefidrud Delta (31 mm/yr in CS03, 250 m water depth, in Fig. 5.12 and Leroy et al., 2013b). However, this sedimentation rate is similar to the sedimentation rate in an offshore sequence in the middle of SCB (i.e. 2 mm/yr in core US02, 315 m water

depth, in Leroy et al. (2013 b)) (Fig. 1.1 for location of the core, Table 5.2). The huge difference between sedimentation rates in CS03 and NSM14G3 can be explained by the very steep continental shelf in the study area. Indeed, due to the steep slope of the shelf, core NSM14G3 location acts as a bypassing zone and plumes continue carrying the sediments far from the river mouth until the plume loses momentum and the sediments accumulate into the basin as bottom set beds (Fig. 5.12). However, in core CS03 that was taken from the area with gentle slope more sedimentation occurred (Fig. 5.12). The sedimentation rate in the basin can be compared with the sedimentation rates in the lagoonal area (Table 5.1). Leroy et al. (2013) discussed that the sedimentation rates in the lagoons are higher than the sedimentation of those in the open sea. However, it should be taken in consideration in which part of the basin the cores are taken. Also, sediment loss during the core penetration, where there is a possibility of losing top core sediments up to 1 m (See Fig. 8 in Leroy et al., 2013c). Absence of a clear peak of ^{137}CS in radionuclide results could mean that some loss occurred during core penetration. This should be considered when calculating sedimentation rates.

Table 5.2. Sedimentation rates in the southern Caspian Sea. See figure 1.1 for the location of the cores

Core name	Setting	Water depth (m)	Sedimentation rate (mm/yr)	References
NSM14G3	Offshore Sefidrud	301	1.67	This study
GS05	Middle south basin	518	0.1 – 0.3	Leroy et al., 2013c
US02	Middle south basin	315	2	Leroy et al. 2013b
CS03	Offshore Anzali	250	20	Leroy et al. 2013b
CP14	Middle south basin	330	0.2	Leroy et al., 2013c Leroy et al., 2007

5.6 Evolution of Sefidrud delta during the last millennium

Delta evolution depends upon three main factors including basinal factors (wave, tide and sea level fluctuation), tectonic setting and sediment supply. In tide-free CS, delta evolution depends on sediment supply by river and longshore current under rapid CSL fluctuation and tectonic setting at the point of entry to the basin. Between the main deltas spread around the CS, Kura Delta due to similar slope (Fig. 2.4) and similar sediment supply, received from Kura River and longshore currents (Table 2.1) could be the best delta around the CS to compare their evolutions. Comparison of Sefidrud Delta with other deltas around the CS could be even a non-sense comparison, because of different slope and sediment supply. For the Sefidrud Delta, major Sefidrud avulsion is a major key in evolution of the Sefidrud delta during the last millennium. Tectonic setting at the point of entry to the basin is similar between Amirkola and Kiashahr locations. The sediment sources in both places (Amirkola and Kiashahr) are invariant before and after avulsion and are supplied from Sefidrud drainage basin and longshore currents. CSL fluctuation therefore is the main variable factor and the evolution of the Sefidrud Delta during the last millennium is best explained based on CSL fluctuations in four steps. Time scale of major events in relation with CSL fluctuation are presented in figure 5.13.

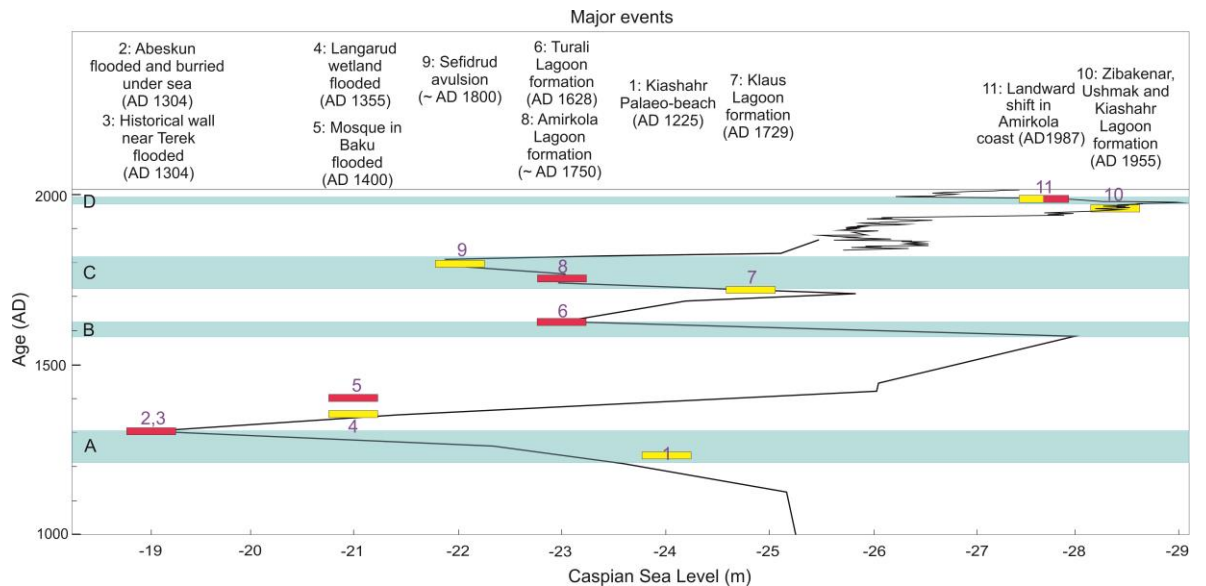


Fig. 5.13. Time scale of important events within Sefidrud Delta and along western CS coast, black curve: CSL, data from 1000 to 1900 from Naderi Beni et al. (2013a), from 1900 to 1992 from Lepeshevskov et al. (1981), from 1992-2014 from USDA (2015), red squares: data from other studies, yellow squares: data from this study, blue strips: major sea level rise.

Stage A: Between AD 1208 and 1304 CSL rose up -19 m (blue strip A in Fig. 5.13 and Fig. 2.3) and reached its highest datum level during the last millennium (Fig. 5.13). At this period Kiashahr was a linear coastline which is known as ‘palaeo-beach’ at present day. Old Sefidrud Delta progradation in the area of Kiashahr palaeo-beach into the CS basin (GPR profiles 104 and 105: Fig. 4.9 and 4.10) is dated to AD 1225 (Table 4.1). Therefore, the Kiashahr palaeo-beach was a ‘deltaic’ linear coastline and a part of the Old Sefidrud Delta. At this period sedimentation rate in Astaneh water body was very low (~ 2.2 mm/yr, see Fig. 5.4). As a result of CSL rise at this period, the coastal town of Abeskun (SE corner of the SCB) was flooded and buried under the CS (Gümilev, 1980; Mostowfi, 1999; Kakroodi et al., 2012; Naderi Beni et al., 2013a) and a historical wall near the Terek River was flooded by the CS (Gümilev, 1980). This huge sea level rise caused invasion further inland where the ‘newly formed’ Langarud wetland was under CS invasion and a mosque in Baku (Azerbaijan) was flooded by the CS (Brückner, 1890). The other impact of CSL fluctuation on inland places was water table fluctuation and formation of CaCO₃ nodules in Langarud before AD 1350 (Fig. 5.2).

Stage B: The next rapid CSL rise happened between AD 1587 and 1628 (blue strip B in Fig. 5.13) and had two major impacts on the CS coast: coastal lagoon formation (Kroonenberg et al., 2000; Storms et al., 2002; Kroonenberg et al., 2007; Leroy et al., 2011; Naderi Beni et al., 2013b), and river avulsion (Hoogendoorn et al., 2005; Krasnozhan et al., 1999). Turali Lagoon was formed ~ 1628 AD in response to sea level rise when CS reached to -23 m (Kroonenberg et al., 2007). At the same time, the Kura

(Hoogendoorn et al., 2005) and Gorgan (Barthold, 1984) rivers also experienced avulsion in response to the rapid CSL rise at AD 1600 (Hoogendoorn et al., 2005; Naderi Beni et al., 2013a). A historical fort wall in Derbent was also flooded as a result of this CSL rise (Brückner, 1890) and CS reached -21.3 m in AD 1638. However, there is no other geological evidence that CS rose up to ~ -21 at ~AD 1600.

Stage C: The third rapid CSL rise happened between AD 1715 and 1816 CSL (blue strip C in Fig. 5.13). Klaus Lagoon in ~ AD 1729 (Fig. 5.8 and 5.10) and Amirkola Lagoon in ~ AD 1750 (Fig. 5 in Leroy et al., 2011) were formed when when the CS rose up to -24.8 and -23 m respectively (Fig. 5.10; Leroy et al., 2011; Naderi Beni et al., 2013b). The results of this study suggest that major avulsion of Sefidrud from Old Sefidrud to the New Sefidrud happened after AD 1769 (Fig. 5.4) which correspond to a period of rapid CSL rise (Fig. 2.3).

Stage D: The last rapid CSL rise happened between AD 1977 and 1995 (blue strip D in Fig. 5.13) and in absence of river sediment supply in Amirkola caused landward shift of the coast, since AD 1987 (Kakroodi et al., 2012). Sand barrier of Klaus Lagoon was destroyed as a result of the landward shift of the coast. At the same time, erosion in the Kura delta increased as a result of abrupt reduction of sediments due to dam construction on Kura River and CSL rise (Ignatov et al., 1993; Kaplin and Selivanov, 1995). However, in the vicinity of Kiashahr where the Sefidrud flows into the CS the sediment supply from the river was sufficient to form recent coastal lagoons of Kiashahr, Zibakenar and Ushmak between 1955 and 1964 during a period of stable sea-level where CSL fluctuated between -28.45 to -28.18 m (Fig. 2.2). The long shore current in this part of the basin had a major role in formation of these lagoons by forming the sand barriers which were supplied by Sefidrud and longshore currents from western coast. Beside this, the minor Sefidrud avulsion (Fig. 4.1 A and B) had a strong impact on the formation of Ushmak and Zibakenar Lagoons by providing more sediment to the western half of the delta, which resulted in the formation of the sand spits. At this period and despite continues CSL rise the New Sefidrud Delta continued to prograde even with a higher rate than in the previous period (Fig. 4.1), as a result of the Manjil Dam flushing operations from the early 1980s, with a peak in 1984–1985 (Table 2.2). Since 1995 the CS has been falling and a minor river avulsion happened (Fig. 4.1 D and E), and sediment supply from the Sefidrud became restricted due to the lack of flushing operations since 1998 (Table 2.2; Yamani et al., 2013).

5.7 Contribution to CSL curve construction

The result of this study confirming the CSL curve constructed by Naderi Beni et al. (2013a), suggest the following two additional points for the CSL curve (Fig. 5.14). The first point which is based on brackish water invasion in Langarud Lagoon suggests that the CSL reached up to -21.44 m during the fourteen century. This finding supports the research by Brückner (1890) who reported CSL at -21.4 m in AD 1400. The second point based on brackish water invasion in Klaus Lagoon suggests that the CSL reached up to -24.80 m in eighteen century.

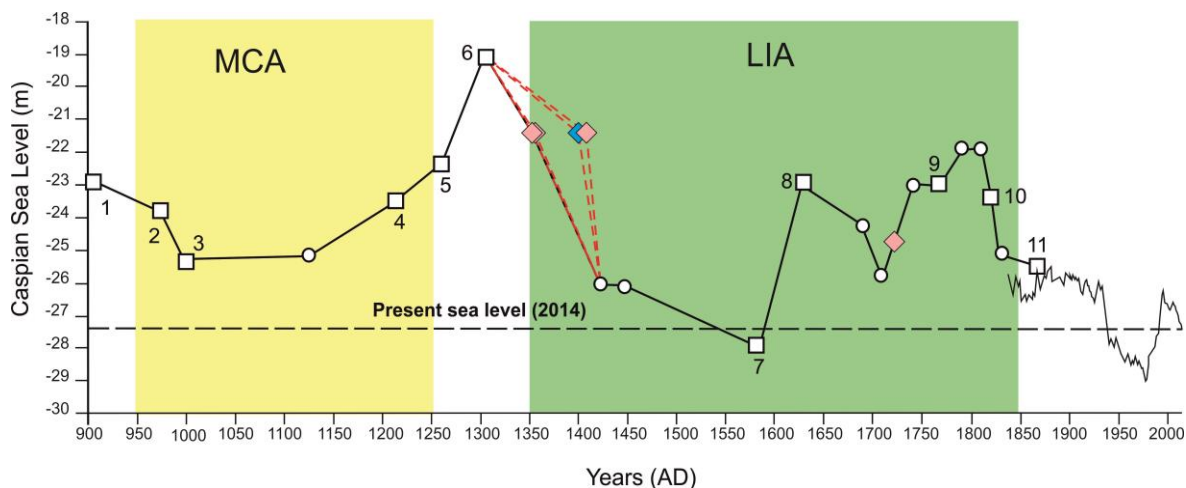


Fig. 5.14. Caspian Sea Level curve for the last millennium, after Naderi Beni et al. (2013a). Four pink diamonds are based on the results of this study and blue diamond is based on the study of Brückner (1890). Red dashed lines present the possible sea level curve. Data from 1900 to 1992 from Lepeshevkov et al. (1981); from 1992-2014 from USDA (2015). From Haghani et al. (in press).

5.8 Sediment accumulations within the Sefidrud Delta

The goal of this research was to understand where sediment accumulation happens in the Sefidrud Delta, the mechanism behind this and sedimentation rates. The concept of division of the delta into three sections was followed: inland wetlands, coastal lagoons and marine (offshore) deposits (Fig. 5.15).

In the Langarud site, fluvial and wetland sediments were deposited. However, radionuclide dating was not possible in this sequence owing to the changing nature of the sediment, but extrapolating the radiocarbon dating at 298 cm, sedimentation rate for the wetland deposits can be estimated at least 5 mm/yr (Fig. 5.2). In Astaneh, the deposition of wetland and fluvial deposits occurred. After the Sefidrud avulsion and deposition of fluvial sediments in this part of the delta, sedimentation rate increased considerably and continued until recent years (Fig. 5.4).

In recent coastal lagoons that developed in relation to the New Sefidrud (Zibakenar, Kiashahr and Ushmak), sedimentation is very high (~ 30 mm/yr) (Fig. 5.5). These lagoons were formed at a time when the CSL was stable. Therefore, their development was not as a response to rapid CSL rise, as it was proposed by Naderi Beni, et al. (2013b). Sefidrud and longshore currents from the western coast were responsible for the formation of sand barriers and the development of lagoons behind them. The older coastal lagoons (Amirkola and Klaus) developed in relation with the Old Sefidrud in response to rapid CSL rise around AD 1750. Continuation of rapid CSL rise caused river avulsion ~ AD 1800 and the main source of sediments in these lagoons are wind and formation of sand dune. This is taking place until recent years (Fig. 5.8). As a result, sedimentation rate remains low (~ 3 mm/yr) in the Amirkola Lagoon (Table. 5.1).

In the submerged part of the delta, sedimentation occurs mostly in delta plain and prodelta. The sedimentation rate is very high in this part of the delta (~ 20 mm/yr in CS03, Fig. 5.12), while it is low in delta front (~ 1.67 mm/yr in NSM14G3, Fig. 5.12). Sand deposition occurs mainly in the fluvial system (channel and flood plain) and along the coast (section 4.2). Onshore, the sand deposition takes place mainly in front of the Old Sefidrud (Fig. 4.67) and only a thin layer of sand (1 cm thick) was observed offshore on a core at 301 m water depth (Fig. 4.68). Organic production within the delta is very low, in general, with a maximum of 20% of organic matter content in Zibakenar Lagoon (Fig. 4.38). MS is higher in coarse sediments.



Fig. 5.15. Schematic figure of different environments studied in this project.

6 Conclusions

6.1 Synopsis of key findings

Key findings are presented here in relation with the original aims of the dissertation.

During the thirteenth century, Kiashahr was not the point of Sefidrud entry to the CS and Kiashahr town was located on a linear coastline. A strongly progradation system in palaeo-shoreline (~AD 1225) indicates a high sedimentation supply relative to accommodation and the fact that Kiashahr was a part of an active delta. A CSL rise in the thirteenth century caused distal brackish water flooding in Langarud wetland (Fig. 6.1 A).

During the eighteenth century, a rapid sea level rise happened. In the early eighteenth century Klaus Lagoon and then Amirkola Lagoon came into existence on the two sides of the Sefidrud (the current Old Sefidrud). Continuous sea level rise caused Sefidrud avulsion in the late eighteenth century (Fig. 6.1 B).

When avulsion occurred Sefidrud started to form a new prism into the CS (Fig. 6.1 C). Therefore, the new delta prism is ~ 200 years old (deposited after avulsion in AD 1800). Sefidrud Delta progradation into the CS in the new prism (Profiles 123 and 125 in Fig. 4.2) indicates a high sedimentation supply relative to accommodation. During the twentieth century, Zibakenar, Ushmak and Kiashahr Lagoons came into existence on the two sides of the Sefidrud during a period of stable CSL (Fig. 6.1 C). Rapid sea-level rise (between 1977 and 1995) and Manjil Dam flushing (from 1980 to 1998) provoked rapid sedimentation in the lagoons. High sedimentation rate (~ 30 mm/yr) was observed within New Sefidrud Delta in the coastal lagoon and in offshore area in delta plain (~ 20 mm/yr). However, the coastal line in the previous entry point of the Old Sefidrud is subjected to erosion due to reduction of sediment supply caused by river avulsion and landward shift especially happened during the recent rapid CSL rise (between 1977 and 1995).

The results of this study confirm that the rapid CSL rise had two major impacts: river avulsion and lagoon formation. However, the formation of coastal lagoons is not only a result of rapid CSL rise, but also due to the human impacts during a period when the CSL was relatively stable.

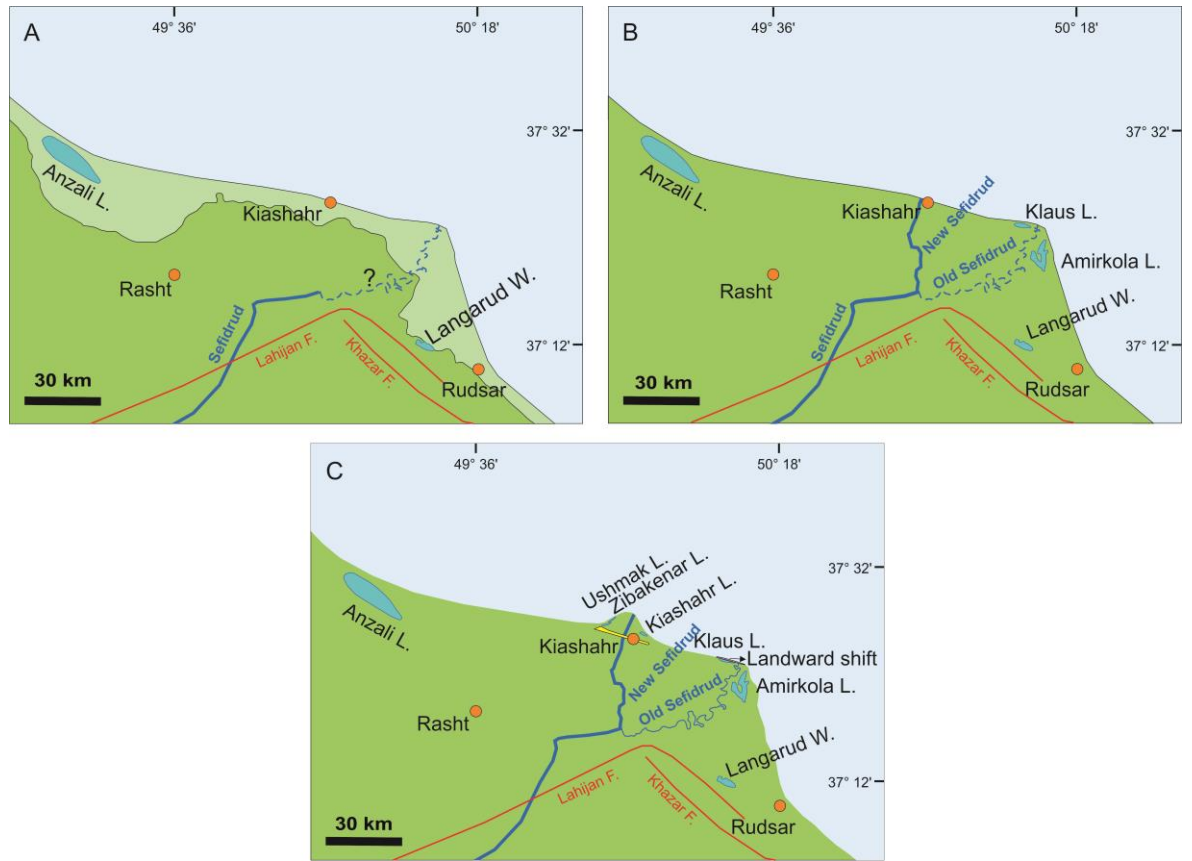


Fig. 6.1. Conclusion of Sefidrud Delta evolution based on river avulsion and lagoon formation during the last millennium, showing A: before avulsion in 13th century, B: after avulsion in 18th century, C: new delta prism formation in 20th century.

The results of this study also confirm the steep slope setting of the CS in the Sefidrud Delta, probably due to the subduction zone in the SCB. This study also constructed a high stand during the early LIA.

In addition, the results of this study show that the evolution of the coastal lagoons on new prism will depend on the relative interactions of CSL change, sediment supply, river avulsion and human activity. The situation in the CS is quite unique in the very dynamic character of the various processes that drive lagoonal evolution and consequently make conservation of Caspian lagoons challenging. As a final point, a revision by Ramsar Convention Secretariat is required to incorporate the need to remain flexible as lagoons may appear and disappear relatively fast. This would be essential to maintain the future quality of a Ramsar site in the south coast of the CS. Meanwhile, because of the very rapid changes in the CSL, the CS can be used to predict changes along coastlines around the world.

6.2 Potential areas for further study

A radiocarbon dating on Astaneh sequence at 430 cm will provide a more precise age for river avulsion.

The results of radionuclide dating show that the offshore core NSM14G3 covers the last 900 years. Therefore, an additional radiocarbon dating at the bottom of the sequence will confirm the age of sequence. However, the lack of sufficient plant material at the base of this core made it impossible to date plant material. Therefore, we decide to date foraminifers. In that case, reservoir effect should be considered in term of calibration.

Performing μ -XRF analyses on the offshore core NSM14G3 not only provide an idea of the effect of river avulsion on offshore sediments, but also may provide evidence of sea level fall during MCA by deposition of minerals which are a sign of sea level fall. If low-stand becomes distinguishable in this sequence, it might be possible to date the low-stand of CSL during MCA, which is problematic at the moment as very poorly documented. Therefore, postponing radiocarbon dating after the result of XRF can be a better idea, to date the horizon of low-stand, if distinguishable.

A radiocarbon dating on AL11V3 sequence at 135 cm (just below Klaus lagoonal deposits) will provide a more precise age for Klaus Lagoon formation and confirm the choice made of using the second most probable date.

A rapid CSL rise happened around AD 1600. This rapid CSL rise could result in coastal lagoon formation and river avulsion. In this study, we were not able to detect any evidence on river avulsion during the sixteenth century. Further investigation in the area would be required to examine Sefidrud Delta evolution during the sixteenth century.

References

- Abrams, M.A., Narimanov, A.A., 1997. Geochemical evaluation of hydrocarbons and their potential sources the western South Caspian depression, Republic of Azerbaijan. *Marine Petroleum Geology* 14, 451–468.
- Aghanabati, A. 2004. *Geology of Iran*. Geological Survey of Iran, Tehran.
- Akhani, H., Djamali, M., Ghorbanalizadeh, A., Ramezani, E., 2010. Plant biodiversity of Hyrcanian relict forests, N Iran: an overview of the flora, vegetation, palaeoecology and conservation. *Pakistan Journal of Botany* 42, 231–258.
- Anders, F.J., Byrnes, M.R., 1991. Accuracy of shoreline change rates as determined from maps and aerial photographs. *Shore and Beach* 59, 17–26.
- Annotated Ramsar List, 2011. http://ramsar.rgis.ch/cda/en/ramsar-documents-list-anno-iran/main/ramsar/1-31-218%5E16557_4000_0__ (Last accessed 13 March 2015).
- Appleby, P. G., Richardson, N., Nolan, P.J., 1992. Self-absorption corrections for well-type germanium detectors. *Nuclear Instruments and Methods B* 71, 228–233.
- Appleby, P.G., Nolan, P.J., Gifford, D.W., Godfrey, M.J., Oldfield, F., Anderson, N.J., Battarbee, R.W., 1986. ^{210}Pb dating by low background gamma counting. *Hydrobiologia* 141, 21–27.
- Arnaud, F., Magand, O., Chapron, E., Bertrand, S., Boës, X., Charlet, F., Mélières, M. A. 2006. Radionuclide dating (^{210}Pb , ^{137}Cs , ^{241}Am) of recent lake sediments in a highly active geodynamic setting (Lakes Puyehue and Icalma—Chilean Lake District). *Science of the Total Environment* 366 (2), 837–850.
- Arpe, K., Bengtsson, L., Golitsyn, G.S., Mokhov, I.I., Semenov, V.A., Sporyshev, P.V., 2000. Connection between Caspian Sea level variability and ENSO. *Geophysical Research Letters* 27, 2693–2696.
- Arpe, K., Leroy, S.A.G., Lahijani, H., Khan, V., 2012. Impact of the European Russia drought in 2010 on the Caspian Sea level. *Hydrology and Earth System Sciences* 16, 19–27.
- Arpe, K., Leroy S.A.G., Mikolajewicz U., 2011. A comparison of climate simulations for the last glacial maximum with three different versions of the ECHAM model and implications for summer-green tree refugia. *Climate of the Past* 7, 91–114.
- Arpe, K., Leroy, S., Wetterhall, F., Khan, V., Hagemann, S., Lahijani, H., 2014. Prediction of the Caspian Sea level using ECMWF seasonal forecasts and reanalysis. *Theoretical and Applied Climatology* 117, 41–60.
- Aslan, A. and Autin, W.J., 1999. Evolution of the Holocene Mississippi River floodplain, Ferriday, Louisiana: insights on the origin of fine-grained floodplains. *Journal of Sedimentary Research* 69 (4), 800–815.
- Aslan, A., Autin, W.J. and Blum, M.D., 2005. Causes of river avulsion: insights from the late Holocene avulsion history of the Mississippi River, USA. *Journal of Sedimentary Research* 75 (4), 650–664.
- ASTER GDEM, 2015. www.jspacesystems.or.jp/ersdac/GDEM/E/4.htm (last accessed 02 February 2015).
- Bao, R., Alonso, A., Delgado, C., Pages, J. L., 2007. Identification of the main driving mechanisms in the evolution of a small coastal wetland (Traba, Galicia, NW Spain) since its origin 5700 cal yr BP. *Palaeogeography, Palaeoclimatology, Palaeoecology*, 247 (3), 296–312.
- Barthold, V. V., 1984. *An historical geography of Iran*. Princeton University Press, Princeton.
- Beaudoin, A., 2003. A comparison of two methods for estimating the organic content of sediments. *Journal of Paleolimnology* 29 (3), 387–390.
- Bennett, K., 2007. Psimpoll and Pscomb Programs for Plotting and Analysis. Version 4.27. www.chrono.qub.ac.uk/psimpoll/psimpoll.html (Last accessed 16 January 15).

- Bennett, K., Willis, K., 2001. Terrestrial, Algal and siliceous indicators: Pollen. In: Smol, J. P., Birks, H. J. B., Last, W. M. (Eds.). *Tracking environmental change using lake sediments*. Springer, Netherlands, pp. 5-32.
- Berberian, M., King, G., 1981. Towards a paleogeography and tectonic evolution of Iran. *Canadian Journal of Earth Sciences* 18, 210–265.
- Berberian, M., Yeats, R. S. 1999. Patterns of historical earthquake rupture in the Iranian Plateau. *Bulletin of the Seismological Society of America* 89 (1), 120-139.
- Beres, M., Haeni, F. P., 1991. Application of Ground-Penetrating-Radar Methods in Hydrogeology Studies. *Groundwater* 29, 375-386.
- Birks, H. H., Birks, H. J. B., 2006. Multi-proxy studies in palaeolimnology. *Vegetation history and Archaeobotany* 15, 235-251.
- Birks, H.H., 2001. Plant macrofossils. In: Smol, J.P., Birks, H.J.B. and Last, W.M. (Eds.), *Tracking environmental change using lake sediments*. Springer, Netherlands pp. 49–74.
- Bloemendal, J., King, J. W., Hunt, A., Demenocal, P. B., Hayashida, A., 1993. Origin of the sedimentary magnetic record at Ocean Drilling Program sites on the Owen Ridge, western Arabian Sea. *Journal of Geophysical Research: Solid Earth* 98, 4199-4219.
- Bloemendal, J., King, J. W., Hall, F. R., Doh, S. J., 1992. Rock magnetism of Late Neogene and Pleistocene deep sea sediments: Relationship to sediment source, diagenetic processes, and sediment lithology. *Journal of Geophysical Research: Solid Earth* 97, 4361-4375.
- Blott, S.J., Pye, K., 2001. GRADISTAT: a grain size distribution and statistics package for the analysis of unconsolidated sediments. *Earth surface processes and Landforms* 26 (11), 1237–1248.
- Boomer, I., von Grafenstein, U., Guichard, F., Bieda, S., 2005. Modern and Holocene sublittoral ostracod assemblages (Crustacea) from the Caspian Sea: a unique brackish, deep-water environment. *Palaeogeography, Palaeoclimatology, Palaeoecology* 225 (1), 173-186.
- Bouzigues, R., Ribolzi, O., Favrot, J. C., Valles, V., 1997. Carbonate redistribution and hydrogeochemical processes in two calcareous soils with groundwater in a Mediterranean environment. *European Journal of soil science* 48 (2), 201-211.
- Boyd, R., Dalrymple, R. and Zaitlin, B., 1992. Classification of clastic coastal depositional environments. *Sedimentary Geology* 80 (3), 139–150.
- Bristow, C. S., 2009. Ground penetrating radar in aeolian dune sands. In: Jol, H., (Eds.), *Ground Penetrating Radar: Theory and Applications*. Amsterdam: The Netherlands, 273-297.
- Brunet, M. F., Korotaev, M. V., Ershov, A. V., Nikishin, A. M., 2003. The South Caspian Basin: a review of its evolution from subsidence modelling. *Sedimentary Geology* 156, 119-148.
- Brückner, E., 1890. *Klima-Schwankungen Seit 1700: Nebst Bemerkungen Über Die Klimaschwankungen Der Diluvialzeit*. E. Hölzel.
- Bungenstock, F., Schäfer, A., 2009. The Holocene relative sea-level curve for the tidal basin of the barrier island Langeoog, German Bight, Southern North Sea. *Global and Planetary Change* 66 (1), 34–51.
- Cerling, T.E., 1984. The stable isotopic composition of modern soil carbonate and its relationship to climate. *Earth and Planetary Science Letters* 71, 229-240.
- Cordova, C. E., Harrison, S. P., Mudie, P. J., Riehl, S., Leroy, S. A., Ortiz, N., 2009. Pollen, plant macrofossil and charcoal records for palaeovegetation reconstruction in the Mediterranean-Black Sea Corridor since the Last Glacial Maximum. *Quaternary International* 197 (1), 12-26.
- Costas, S., Sobrino, C. M., Alejo, I., Pérez-Arlucea, M., 2009. Holocene evolution of a rock-bounded barrier lagoon system, Cíes Islands, northwest Iberia. *Earth Surface Processes and Landforms* 34 (11), 1575–1586.
- Crick, R.E., Ellwood, B.B. El Hassani, A., Hladil, J., Hroudá, F., Chlupac, I., 2001. Magnetostratigraphy susceptibility of the Pridoli-Lochkovian (Silurian-Devonian) GSSP (Klonk, Czech Republic) and a coeval sequence in Anti-atlas Morocco. *Palaeogeography, Palaeoclimatology, Palaeoecology* 167, 73-100.

- Crick, R.E., Ellwood, B.B., El. Hassani, A., Feist, R., Hladil, J., 1997. Magnetosusceptibility Event and Cyclostratigraphy (MSEC) of the Eifelian-Givetian GSSP and associated boundary sequences in north Africa and Europe. *Episodes* 20 (3), 167-175.
- Dark, P., Allen, J. R. L., 2005. Seasonal deposition of Holocene banded sediments in the Severn Estuary Levels (southwest Britain): palynological and sedimentological evidence. *Quaternary Science Reviews* 24 (1), 11-33.
- Davis, J.L. and Annan, A.P., 1989. Ground penetrating radar for high resolution mapping of soil and rock stratigraphy. *Geophysical prospecting* 37, 531–551.
- Dean, W. E., 1999. The carbon cycle and biogeochemical dynamics in lake sediments. *Journal of paleolimnology* 21 (4), 375-393.
- Dean, W. E. Jr., 1974. Determination of carbonate and organic matter in calcareous sediments and sedimentary rocks by loss on ignition: Comparison with other methods. *Journal of Sedimentary Petrology* 44, 242–248.
- Dearing, J., 1994. Environmental magnetic susceptibility. Using the Bartington MS2 system. Kenilworth, Chi Publ. www.bartington.com (Last accessed 30 June 2015).
- Di Stefano, A., De Pietro, R., Monaco, C., Zanini, A., 2013. Anthropogenic influence on coastal evolution: A case history from the Catania Gulf shoreline (eastern Sicily, Italy). *Ocean and Coastal Management* 80, 133-148.
- Djamali, M., de Beaulieu, J.-L., Miller, N., Andrieu-Ponel, V., Berberian, M., Gandouin, E., Lahijani, H., Ponel, P., Salimian, M., Guiter, F., 2009. A late Holocene pollen record from Lake Almalou in NWIran: evidence for changing land-use in relation to some historical events during the last 3700 years. *Journal of Archaeological Science* 36, 1364–1375.
- Djamour, Y., Vernant, P., Bayer, R., Nankali, H. R., Ritz, J. F., Hinderer, J., Hatam, Y., Luck, B., Le Moigne, N., Sedighi, M., 2010. GPS and gravity constraints on continental deformation in the Alborz mountain range, Iran. *Geophysical Journal International* 183, 1287–1301.
- Dolan, R., Hayden, B., Heywood, J. (1978). A new photogrammetric method for determining shoreline erosion. *Coastal Engineering*, 2, 21-39.
- Dolotov, Y. and Kaplin, P., 2005. Black and Caspian Seas, Coastal Ecology and Geomorphology. In: *Encyclopedia of Coastal Science*. Springer, pp. 194–203.
- Dolukhanov, P. M., Chepalyga, A. L., and Lavrentiev, N. V., 2010. The Khvalynian transgressions and early human settlement in the Caspian basin. *Quaternary International* 225, 152–159.
- Doriniana, T.A., Myakokin, V. S., 1972. Sediment transport along the western Caspian Coast, according to their mineralogical analysis. *Comprehensive study of the Caspian Sea* 3, 147-154 (in Russian).
- Duck, R.W. and da Silva, J.F., 2012. Coastal lagoons and their evolution: A hydromorphological perspective. *Estuarine, Coastal and Shelf Science* 110, 2–14.
- Dumont, H.J., 1998. The Caspian Lake: history, biota, structure, and function. *Limnology and Oceanography* 43, 44–52.
- Durand, N., Monger, H.C., Canti, M.G., 2010. Calcium carbonate features. Interpretation of micromorphological features of soils and regoliths. Elsevier, Amsterdam, 149-194.
- Eia Report, 2013. Overview of oil and natural gas in the Caspian Sea region. U.S. Energy Information Administration, 25 pp. (<http://www.eia.gov/beta/international/regions-topics.cfm?RegionTopicID=CSR>, (Last accessed 24 Jun. 2015).
- Ellwood, B.B., Crick, R.E., El Hassani, A., Benoist, S.L.R.H., Young, R.H., 2000. The magnetosusceptibility event and cyclostratigraphy (MSEC) method applied to marine rocks: detrital input versus carbonate productivity. *Geology* 28, 1134-1138.
- Emberger, L., Sabeti, H., 1962. Forêts denses intertropicales et forêts Caspiennes humides. *Nat. Monspel., Série Bot.* 14, 55– 61.
- Encyclopedia Britannica, 2015. Tamerlane . www.britannica.com (last accessed 16 January 2015).
- ETOPO1, 2015. www.ngdc.noaa.gov/mgg/global/global.html (last accessed 02 February 2015).

- Farley Nicholls, J., Toumi, R., 2014. On the lake effects of the Caspian Sea. *Quarterly Journal of the Royal Meteorological Society*, 140 (681), 1399-1408.
- Folk, R.L., 1974. *Petrology of Sedimentary Rocks*. Hemphill, Texas.
- Folk, R. L., Ward, W. C., 1957. Brazos River bar: a study in the significance of grain size parameters. *Journal of Sedimentary Research* 27 (1), 3-26.
- García, A., Jones, B. G., Chenhalland, B. E., Murray–Wallace, C. V., 2002. The charophyte *Lamprothamnium succinctum* as an environmental indicator: a Holocene example from Tom Thumbs Lagoon, eastern Australia. *Alcheringa* 26 (4), 507–518.
- García-Alcalde, J. L., Ellwood, B. B., Soto, F., Truyóls-Massoni, M., Tomkin, J. H., 2012. Precise timing of the Upper Taghanic Biocrisis, Geneseo Bioevent, in the Middle–Upper Givetian (Middle Devonian) boundary in Northern Spain using biostratigraphic and magnetic susceptibility data sets. *Palaeogeography, Palaeoclimatology, Palaeoecology* 313, 26-40.
- Ghamgosar, M., Haghyghy, M., Mehrdoust, F., Arshad, N., 2011. Multicriteria Decision Making Based on Analytical Hierarchy Process (AHP) in GIS for Tourism. *Middle-East Journal of Scientific Research* 4, 501-507.
- Glew, J. R., 1991. Miniature gravity corer for recovering short sediment cores. *Journal of Paleolimnology* 5, 285-287.
- Griffin, J. J., Goldberg, E. D., 1983. Impact of fossil fuel combustion on sediments of Lake Michigan: a reprise. *Environmental science and technology* 17 (4), 244-245.
- Grigorovich, I.A., Therriault, T.W. and MacIsaac, H.J., 2003. History of aquatic invertebrate invasions in the Caspian Sea. *Biological Invasions* 5, 103–115.
- Gümilev, N., 1980. History of the Caspian sea level changes during the last 2000 years, In: Adrianov, B. V., Zorin, L. B., and Nikolaeva, R. V. (Eds.) *Humidity change in Aral-Caspian region during the Holocene*. USSR, Academy of Science, Institute of water problem, NAUKA, Moscow.
- Haghani, 2009. *Sedimentology of South-West Caspian Sea offshore deposits and processes responsible for their deposition*. MSc thesis, 142 pp. (in Persian).
- Haghani, S., Leroy, S., Khdir, S., Kabiri, K., Naderi Beni, M., Lahijani, H.A.K., in press (accepted 26 May 2015). An early Little Ice Age brackish water invasion along the south coast of the Caspian Sea (sediment of Langarud wetland) and its wider impacts on environment and people. *The Holocene*.
- Hashemloian, B.D., Azimi, A.A., 2009. Alien and exotic *Azolla* in northern Iran. *African Journal of Biotechnology* 8, 187-190.
- Heiri, O., Lotter, A.F. and Lemcke, G., 2001. Loss on ignition as a method for estimating organic and carbonate content in sediments: reproducibility and comparability of results. *Journal of Paleolimnology* 25 (1), 101–110.
- Heller, F., Shen, C. D., Beer, J., Liu, X. M., Liu, T. S., Bronger, A., Bonani, G., 1993. Quantitative estimates of pedogenic ferromagnetic mineral formation in Chinese loess and palaeoclimatic implications. *Earth and Planetary Science Letters* 114 (2), 385-390.
- Heyvaert, V.M.A. and Baeteman, C., 2008. A Middle to Late Holocene avulsion history of the Euphrates river: a case study from Tell ed–Dēr, Iraq, Lower Mesopotamia. *Quaternary Science Reviews* 27 (25), 2401–2410.
- Hoogendoorn, R.M., Boels, J.F., Kroonenberg, S.B., Simmons, M.D., Aliyeva, E., Babazadeh, A.D., Huseynov, D., 2005. Development of the Kura delta, Azerbaijan; a record of Holocene Caspian sea-level changes. *Marine Geology* 222, 359–380.
- Hounslow, M. W., Maher, B. A., 1999. Source of the climate signal recorded by magnetic susceptibility variations in Indian Ocean sediments. *Journal of geophysical research* 104, 5047-5061.
- Hua, Q., Barbetti, M., Rakowski, A. Z., 2013. Atmospheric radiocarbon for the period 1950–2010. *Radiocarbon* 55 (4), 2059–2072.
- Huntley, B., Spicer, R. A., Chaloner, W. G., Jarzembowski, E. A., 1993. The use of climate response surfaces to reconstruct palaeoclimate from Quaternary pollen and plant macrofossil data [and discussion]. *Philosophical Transactions of the Royal Society B: Biological Sciences* 341, 215-224.

- Ignatov, Y. I., Kaplin, P. A., Lukyanova, S. A., Solovieva, G. D., 1993. Evolution of the Caspian Sea coasts under conditions of sea-level rise: model for coastal change under increasing "greenhouse effect". *Journal of Coastal Research*, 104-111.
- Jackson, J., Priestley, K., Allen, M., and Berberian, M., 2002. Active tectonics of the South Caspian Basin, *Geophysical Journal International* 148, 214–245.
- Jelinowska, A., Tucholka, P., Badaut-Trauth, D., 1999. Magnetic Mineral variation of south Caspian Sea sediments at laminate scale. *Physics and Chemistry of the Earth* 24 (9), 823-828.
- Johnson Ibach, L.E., 1982. Relationship between sedimentation rate and total organic carbon content in ancient marine sediments. *Association Petroleum Geology Bulletin* 61, 170–188.
- Jol, H. M., Smith, D. G., Meyers, R. A., 1996. Digital Ground Penetrating Radar (GPR): A new geophysical tool for coastal barrier research (examples from the Atlantic, Gulf and Pacific coasts, USA). *Journal of Coastal Research* 12 (4), 960-968.
- Jol, H.M., Smith, D.G., 1991. Ground penetrating radar of northern Lacustrine deltas. *Journal of Earth Sciences* 28, 1939–1947.
- Jones, L.S. and Schumm, S.A., 2009. Causes of avulsion: an overview. In: Smith, N.D. and Rogers, J. (Eds.), *Fluvial Sedimentology VI: Oxford, UK. Blackwell Publishing Ltd.*, pp. 171–178.
- Jones, R.W., Simmons, M.D., 1996, A review of the stratigraphy of Eastern Paratethys (Oligocene–Holocene). *London, Natural History Museum Bulletin, Geology* 52, 25-49.
- Kakroodi, A.A., Leroy, S.A.G., Kroonenberg, S.B., Lahijani, H.A.K., Alimohammadian, H., Boomer, I., Goorabi, A., 2015. Late Pleistocene and Holocene sea-level change and coastal palaeoenvironment evolution along the Iranian Caspian shore. *Marine Geology*, In Press. Available online 8 January 2015.
- Kakroodi, A.A., Kroonenberg, S.B., Goorabi, A., Yamani, M., 2014. Shoreline Response to Rapid 20th Century Sea-Level Change along the Iranian Caspian Coast. *Journal of Coastal Research* 30, 1243–1250.
- Kakroodi, A.A., Kroonenberg, S.B., Hoogendoorn, R.M., Mohammad Khani, H., Yamani, M., Ghassemi, M.R., Lahijani, H.A.K., 2012. Rapid Holocene sea-level changes along the Iranian Caspian coast. *Quaternary International* 263, 93-103.
- Kaplin, P., Selivanov, A., Lukyanova, S., 2010. Azerbaijan. In: Bird, E. (Ed.), *Encyclopedia of the world's coastal landforms*. Springer Science and Business Media, pp. 885-888.
- Kaplin, P.A. and Selivanov, A.O., 1995. Recent coastal evolution of the Caspian Sea as a natural model for coastal responses to the possible acceleration of global sea–level rise. *Marine Geology* 124 (1), 161–175.
- Karpychev, Y. A., 2001. Variations in the Caspian Sea level in the historic epoch. *Water Resources* 28 (1), 1-14.
- Kazancı, N. and Gulbabazadeh, T., 2013. Sefidrud delta and quaternary evolution of the southern Caspian Lowland, Iran. *Marine and Petroleum Geology* 44, 120–139.
- Kazancı, N., Gulbabazadeh, T., Leroy, S.A.G., Ileri, O., 2004. Sedimentary and environmental characteristics of the Gilan-Mazenderan plain, northern Iran: influence of long- and short-term Caspian water level fluctuations on geomorphology. *Journal of Marine Systems* 46, 145-168.
- Khabbaz-nia, A.R., Sadeghi, A., 2004. *Geological Map of Rasht at 1/100 000 Scale. Sheet No. 5964*. Published by Geological Survey of Iran. Tehran.
- Khoshraftar, R., 2005. Geomorphological evolution Kiashahr lagoon using aerial photographs and satellite images and GPS. *Proceedings of the 9th International Conference on Environmental Science and Technology*. Rhodes Island, Greece, pp. 381–387.
- Khosronejad, A., 2009. Optimization of the Sefid–Roud Dam desiltation process using a sophisticated one–dimensional numerical model. *International Journal of Sediment Research* 24 (2), 189–200.
- Kirk, R.M. and Lauder, G., 2000. Significant coastal lagoon systems in the South Island, New Zealand: coastal processes and lagoon mouth closure. *Science for Conservation* 146. Department of Conservation, Wellington, New Zealand.
- Kjerfve, B., 1994. *Coastal lagoons*. Elsevier oceanography series 60, 1-8.

- Korsman, T., M. B. Nilsson, K. Landgren I., 1999. Spatial variability in surface sediment composition characterised by near-infrared (NIR) reflectance spectroscopy. *Journal of Paleolimnology* 21, 61–71.
- Kosarev, A.N., 2005. Physico–geographical conditions of the Caspian Sea. In: Kostianoy, A., Kosarev, A. (Eds.), *The Caspian Sea Environment*. Springer Science and Business Media, pp. 5–31.
- Kousari, S., 1986. Evolution of Sefidrud Delta, Development in Geological Education 1, 31–41 (in Persian).
- Krasnozhon, G.F., Lahijani, H., Voropayev, G.V., 1999. Evolution of the delta of the Sefidrud River, Iranian Caspian Sea coast, from space imagery. *Mapping Science and Remote Sensing* 36, 256–264.
- Kroonenberg, S.B., Abdurakhmanov, G.M., Badyukova, E.N., Borg, K.V.D., Kalashnikov, A., Kasimov, N.S., Rychagov, G.I., Svitoch, A.A., Vonhof, H.B. and Wesselingh, F.P., 2007. Solar–forced 2600 BP and Little Ice Age highstands of the Caspian Sea. *Quaternary International* 173, 137–143.
- Kroonenberg, S., Badyukova, E., Storms, J., Ignatov, E. and Kasimov, N., 2000. A full sea–level cycle in 65years: barrier dynamics along Caspian shores. *Sedimentary Geology* 134 (3), 257–274.
- Kroonenberg, S.B., Boels, J.F., Hoogendoorn, R.M., Overeem, I., Aliyeva, E., Huseynov, D., Badyukova, E.M., Svitoch, A.A., Hinds, D., Simmons, M.D., 2004. Sandstone deposition in lacustrine environments: Implications for exploration and reservoir development. AAPG Conference, Baku, Azerbaijan.
- Kroonenberg, S. B., Rusakov, G. V., Svitoch, A. A., 1997. The wandering of the Volga delta: a response to rapid Caspian sea-level change. *Sedimentary Geology* 107 (3), 189–209.
- Kroonenberg, S. B., Simmons, M. D., Alekseevski, N. I., Aliyeva, E., Allen, M. B., Aybulator, D. N., Baba-Zadeh, A., Badyukova, E. N., Davies, C., Hinds, D. J., Hoogendoorn, R. M., Huseynov, D., Ibrahimov, B., Mamedov, P., Overeem, I., Rusakov, G. V., Suleymanova, S., Svitoch, A. A., Vincent, S. J., 2005. Two deltas, two basins, one river, one sea. The modern Volga Delta as an analogue of the Neogene Productive Series, South Caspian Basin. In: *Special Publications of the Society of Economic Paleontologists and Mineralogists. River Deltas-concepts, models and examples* (83). Society of Economic Paleontologists and Mineralogists, Tulsa, pp. 231–256.
- Kuzmin, Y.V., Nevesskaya, L.A., Krivonogov, S.K., Burr, G.S., 2007. Apparent ¹⁴C ages of the ‘pre-bomb’ shells and correction values (R, ΔR) for Caspian and Aral Seas (Central Asia). *Nuclear Instruments and Methods in Physics Research* 259, 463–466.
- Lahijani, H.A.K., Rahimpour–Bonab, H., Tavakoli, V. and Hosseindoost, M., 2009. Evidence for late Holocene highstands in central Guilan–East Mazanderan, south Caspian coast, Iran. *Quaternary International* 197 (1), 55–71.
- Lahijani, H., Tavakoli, V., 2012. Identifying provenance of South Caspian coastal sediments using mineral distribution pattern. *Quaternary International* 261, 128–137.
- Lahijani, H.A.K., Tavakoli, V., Amini, A.H., 2008. South Caspian river mouth configuration under human impact and sea level fluctuations. *Environmental Sciences* 5, 65–86.
- Latypov, Y.Y., 2004. Succession in the *Abra ovata* community on soft grounds of a newly flooded area of the Caspian Sea. *Russian Journal of Ecology* 35 (4), 267–273.
- Leatherman, S.P., 1983. Shoreline mapping: A comparison of techniques. *Shore and Beach* 51, 28–33.
- Lepeshevkov, I.N., Buynevich, D.V., Buynevich, N.A., Sedel’nikov, G.S., 1981. Perspectives of use of Salt Resources of Kara-Bogaz-Gol. *Academia Nauka, Moscow*, p. 273 (in Russian).
- Lefor, M.W., Kennard, W. C., 1977. *Inland Wetland Definitions*. Special Reports, 27 pp.
- Leroy S.A.G., 2010. Palaeoenvironmental and palaeoclimatic changes in the Caspian Sea region since the Lateglacial from palynological analyses of marine sediment cores. *Geography, Environment, Sustainability, Faculty of Geography of Lomonosov Moscow State University and by the Institute of Geography of RAS*. 2, 32–41. <http://www.geogr.msu.ru/GESJournal/> (Last accessed 30 June 2015).
- Leroy, S.A.G., Arpe K., 2007. Glacial refugia for summer-green trees in Europe and S-W Asia as proposed by ECHAM3 time-slice atmospheric model simulations. *Journal of Biogeography* 34, 2115–2128.
- Leroy, S.A.G., Kakroodi, A.A., Kroonenberg, S.B., Lahijani, H.A.K., Alimohammadian, H., Nigarov, A., 2013a. Holocene vegetation history and sea level changes in the SE corner of the Caspian Sea: relevance to SW Asia climate. *Quaternary Science Reviews* 70, 28–47.

- Leroy, S., Lahijani, H., Reyss, J., Chalié, F., Haghani, S., Shah–Hosseini, M., Shahkarami, S., Tudryn, A., Arpe, K., Habibi, P., 2013b. A two–step expansion of the dinocyst *Lingulodinium machaerophorum* in the Caspian Sea: the role of changing environment. *Quaternary Science Reviews* 77, 31–45.
- Leroy, S., Marret, F., Giralt, S. and Bulatov, S., 2006. Natural and anthropogenic rapid changes in the Kara–Bogaz Gol over the last two centuries reconstructed from palynological analyses and a comparison to instrumental records. *Quaternary International* 150 (1), 52–70.
- Leroy, S. A. G., Marret, F., Gibert, E., Chalié, F., Reyss, J. L., Arpe, K., 2007. River inflow and salinity changes in the Caspian Sea during the last 5500 years. *Quaternary Science Review* 26, 3359–3383.
- Leroy, S. A., Tudryn, A., Chalié, F., López-Merino, L., Gasse, F., 2013c. From the Allerød to the mid-Holocene: palynological evidence from the south basin of the Caspian Sea. *Quaternary Science Reviews* 78, 77-97.
- Leroy, S.A.G., Tavakoli, V., Habibi, P., Naderi Beni, M., Lahijani, H.A.K., Djamali, M., Naqinezhad, A., Moghadam, M.V., Arpe, K., Shah–Hosseini, M., Hosseindoust, M. and Miller, C.S., 2011. Late Little Ice Age palaeoenvironmental records from the Anzali and Amirkola Lagoons (south Caspian Sea): Vegetation and sea level changes. *Palaeogeography, Palaeoclimatology, Palaeoecology* 302 (3), 415–434.
- Leroy, S.A.G., Warny, S., Lahijani, H.A.K., Piovano, E.L., Fanetti, D. and Berger, A.R., 2010. The role of geosciences in the mitigation of natural disasters: five case studies. In: Beer, T. (Ed.), *Geophysical Hazards*. Springer, pp. 115–147.
- Lewis, D. W., McConchie, D., 1994. *Analytical sedimentology*. Springer Science and Business Media.
- Lindhorst, S., Betzler, C., Hass, H. C. 2008. The sedimentary architecture of a Holocene barrier spit (Sylt, German Bight): Swash-bar accretion and storm erosion. *Sedimentary Geology* 206 (1), 1-16.
- Livingstone, D. A., 1955. A lightweight piston sampler for lake deposits. *Ecology*, 137-139.
- Lubis, A. A., 2013. Constant rate of supply (CRS) model for determining the sediment accumulation rates in the coastal area using 210Pb. *Journal of Coastal Development* 10 (1), 9-18.
- Maher, B. A., 1998. Magnetic properties of modern soils and Quaternary loessic paleosols: paleoclimatic implications. *Palaeogeography, Palaeoclimatology, Palaeoecology* 137 (1), 25-54.
- Makaske, B., 2001. Anastomosing rivers: a review of their classification, origin and sedimentary products. *Earth–Science Reviews* 53 (3), 149–196.
- Mangerud, J., 1972. Radiocarbon dating of marine shells, including a discussion of apparent age of recent shells from Norway. *Boreas* 1 (2), 143-172.
- Mann, M.E., Zhang, Z., Rutherford, S., Bradley, R.S., Hughes, M.K., Shindell, D., Ammann, C., Faluvegi, G., Ni, F., 2009. Global Signatures and Dynamical Origins of the Little Ice Age and Medieval Climate Anomaly. *Science* 326, 1256-1260.
- Mann, M. E., 2002. The Value of Multiple Proxies. *Science* 297, 1481-1482.
- Magaritz, M., Kaufman, A., Yaalon, D.H., 1981. Calcium carbonate nodules in soils: $^{13}\text{O}/^{16}\text{O}$ and $^{13}\text{C}/^{12}\text{C}$ ratios and ^{14}C contents. *Geoderma* 25, 157-172.
- Marret, F., Leroy, S.A.G., Chalié, F. and Gasse, F., 2004. New organic–walled dinoflagellate cysts from recent sediments of Central Asian seas. *Review of Palaeobotany and Palynology* 129 (1), 1–20.
- Martin, L., Dominguez, J. M. L., 1994. Geological history of coastal lagoons. *Elsevier Oceanography Series* 60, 41–68.
- Mazzullo, J.M., Meyer, A., and Kidd, R., 1988. New sediment classification scheme for the Ocean Drilling Program. In: Mazzullo, J.M. and Graham, A.G. (Eds.), *Handbook for shipboard sedimentologists*. ODP Technical Notes 8, 45–67.
- McBride, R. A., Hiland, M. W., Penland, S., Williams, S. J., Byrnes, M. R., Westphal, K. A., Sallenger, A. H., 1991. Mapping barrier island changes in Louisiana: techniques, accuracy, and results. *Coastal Sediments*, 1011-1026.
- McCuaig, S. J., Ricketts, M. J., 2004. Ground-Penetrating Radar: A tool for delineating aggregate-resource deposits. *Geological Survey of Newfoundland and Labrador–Current Research* 04-1, 107-115.

- Molavi–Arabshahi M., Arpe K., Leroy S.A.G., June 2015. Precipitation and temperature of the Southwest Caspian Sea during the last 56 years, their trends and teleconnections with large–scale atmospheric phenomena. *International Journal of Climatology*, accepted with minor changes.
- Morris, G.L. and Fan, J., 1998. *Reservoir sedimentation handbook: design and management of dams, reservoirs, and watersheds for sustainable use*. McGraw Hill Professional, New York.
- Mostowfi, H., 1999. *Noz'hat Al-Gholub*. Taha Publication, Qazvin.
- Naderi Beni, A., Lahijani, H.A.K., Harami, R.M., Arpe, K., Leroy, S.A.G., Marriner, N., Berberian, M., Andrieu–Ponel, V., Djamali, M. and Mahboubi, A., 2013a. Caspian Sea level changes during the last millennium: historical and geological evidences from the south Caspian Sea. *Climate of the Past* 9, 1645–1665.
- Naderi Beni, A., Lahijani, H., Harami, R.M., Leroy, S.A.G., Shah–Hosseini, M., Kabiri, K. and Tavakoli, V., 2013b. Development of spit–lagoon complexes in response to Little Ice Age rapid sea–level changes in the central Guilan coast, South Caspian Sea, Iran. *Geomorphology* 187, 11–26.
- Nadirov, R. S., Bagirov, E., Tagiyev, M., Lerche, I., 1997. Flexural plate subsidence, sedimentation rates, and structural development of the super-deep South Caspian Basin. *Marine and Petroleum Geology* 14, 383–400.
- Naqinezhad, A., 2012. A Physiognomic–Ecological Vegetation Mapping of Boujagh National Park, the first Marine–land National Park in Iran. *Advances in Bioresearch* 3, 37–42.
- Naqinezhad, A., Saeidi M.S., Noroozi, M., and Faridi, M., 2006. Contribution of the vascular and bryophyte flora as well as habitat diversity of Boujagh National Park, N. Iran. *Rostaniha* 7, 83–105.
- Nazari, H., Omrani, J., 2004. *Geological Map of Bandar-e-anzali at 1/100 000 Scale*. Sheet No. 5864. Published by Geological Survey of Iran. Tehran.
- Neal, A., 2004. Ground-penetrating radar and its use in sedimentology: principles, problems and progress. *Earth-science reviews* 66 (3), 261–330.
- Nichols, G., 2009. *Sedimentology and stratigraphy*. John Wiley and Sons.
- Nichols, M.M. and Boon, J.D., 1994. Sediment transport processes in coastal lagoons. *Elsevier Oceanography Series* 60, 157–219.
- Oertel, G.F., Kraft, J.C., Kearney, M.S., Woo, H.J., 1992. A rational theory for barrier lagoon development. In: Fletcher, C.H., Wehmiller, J.F. (Eds.), *Quaternary Coasts of the United States* 48, SEPM, pp. 77–87.
- Oldfield, F., 1991. Environmental magnetism—a personal perspective. *Quaternary Science Reviews* 10 (1), 73–85.
- Ollivier, V., Fontugne, M., Lyonnet, B., Chataigner, C., 2015. Base level changes, river avulsions and Holocene human settlement dynamics in the Caspian Sea area (middle Kura valley, South Caucasus). *Quaternary International*. In Press, Corrected Proof, Available online 3 April 2015.
- Olsson, I. U., 1986. Radiometric dating. In: Berglund, B.E. (Eds.), *Handbook of Holocene palaeoecology and palaeohydrology*, pp. 273–296.
- Overeem, I., Kroonenberg, S., Veldkamp, A., Groenesteijn, K., Rusakov, G. and Svitoch, A., 2003. Small–scale stratigraphy in a large ramp delta: recent and Holocene sedimentation in the Volga delta, Caspian Sea. *Sedimentary Geology* 159 (3), 133–157.
- Ozyavas, A., Khan, S. D., Casey, J. F., 2010. A possible connection of Caspian Sea level fluctuations with meteorological factors and seismicity. *Earth and Planetary Science Letters* 299 (1), 150–158.
- Pepola, C.P., Hickin, E.J., 2003. Long-term bed load transport rate based on aerial-photo and ground penetrating radar surveys of fan-delta growth, Coast Mountains, British Columbia. *Geomorphology* 57, 169–181.
- Pourafrahyabi, M. and Ramezani, Z., 2014. Phytoplankton as bio–indicator of water quality in Sefid Rud River, Iran (South of Caspian Sea). *Caspian Journal of Environmental Sciences* 12 (1), 31–40.
- Rahmati Iikhchi, M., Mosavi, E., Bahreman, M., 2004. *Geological Map of Langarud at 1/100 000 Scale*. Sheet No. 6064. Published by Geological Survey of Iran. Tehran.
- Ramsar Report 37, 2015. www.ramsar.org/sites/default/files/documents/library/ram37e_iran.pdf (Last accessed 16 April 2015).

- Rapp, G. R., Hill, C. L., 2006. *Geoarchaeology: the earth-science approach to archaeological interpretation*. Yale University Press.
- Reading, H. G., 2009. *Sedimentary environments: processes, facies and stratigraphy*. John Wiley and Sons.
- Reimer, P.J., Bard, E., Bayliss, A., Beck, J.W., Blackwell, P.G., Ramsey, C.B., Buck, C.E., Cheng, H., Edwards, R.L., Friedrich, M., Grootes, P.M., Guilderson, T.P., Haflidason, H., Hajdas, I., Hatté, C., Heaton, T.J., Hoffmann, D.L., Hogg, A.G., Hughen, K.A., Kaiser, K.A., Kromer, B., Manning, S.W., Niu, M., Reimer, R.W., Richards, D.A., Scott, E.M., Southon, J.R., Staff, R.A., Turney, C.S.M. and Plicht, J.V.D., 2013. IntCal13 and Marine13 radiocarbon age calibration curves 0–50,000 years cal BP. *Radiocarbon* 55 (4), 1869–1887.
- Reimer, P.J., Brown, T.A. and Reimer, R.W., 2004. Discussion: reporting and calibration of post-bomb ^{14}C data. *Radiocarbon* 46 (3), 1299–1304.
- Reynolds, J.M., 1997, *An Introduction to Applied and Environmental Geophysics*, John Wiley and Sons, Chichester.
- Renberg, I., and M. Wik., 1984. Dating recent lake sediments by soot particle counting. *Verhandlungen des Internationalen Verein Limnologie* 22, 712–718.
- Renberg, I., and M. Wik., 1985. Soot particle counting in recent lake sediments: An indirect dating method. *Ecology Bulletin* 37, 53–57.
- Ritz, J. F., Nazari, H., Ghassemi, A., Salamati, R., Shafei, A., Solaymani, S., Vernant, P., 2006. Active transtension inside central Alborz: A new insight into northern Iran–southern Caspian geodynamics. *Geology* 34, 477–480.
- Roberts, M. C. Niller, H.P., Helmstetter, N., 2003. *Sedimentary architecture and radar facies of a fan delta, Cypress Creek, West Vancouver, British Columbia*. Geological Society, London, Special Publications 211, 111–126.
- Robinson, S. G., Maslin, M. A., McCave, I. N., 1995. Magnetic susceptibility variations in Upper Pleistocene deep-sea sediments of the NE Atlantic: Implications for ice rafting and paleocirculation at the last glacial maximum. *Paleoceanography* 10 (2), 221–250.
- Rose, N.L., 2015 in press. Spheroidal carbonaceous fly-ash particles provide a globally synchronous stratigraphic marker for the Anthropocene. *Environmental Science and Technology* <http://dx.doi.org/10.1021/acs.est.5b00543>, (Last accessed 20 June 2015).
- Rose, N.L., 2008. Quality control in the analysis of lake sediments for spheroidal carbonaceous particles. *Limnology and Oceanography: Methods* 6, 172–179.
- Rose, N., Flower, R. and Appleby, P., 2003. Spheroidal carbonaceous particles (SCPs) as indicators of atmospherically deposited pollutants in North African wetlands of conservation importance. *Atmospheric Environment* 37 (12), 1655–1663.
- Rose, N., Harlock, S., Appleby, P. and Battarbee, R., 1995. Dating of recent lake sediments in the United Kingdom and Ireland using spheroidal carbonaceous particle (SCP) concentration profiles. *The Holocene* 5 (3), 328–335.
- Rose, N.L., 1994. A note on further refinements to a procedure for the extraction of carbonaceous fly-ash particles from sediments. *Journal of Paleolimnology* 11, 201–204.
- Rucevska, I., Herberlin, C., Rekecewicz, P., Skaalvik, J.F., Baker, E., Novikov, V., Radvany, J., Demartino, L., 2006. *Vital Caspian Graphics: Challenges beyond Caviar*. UNEP/GRID, Arendal.
- Ruddiman, W. F., 2008. *Earth Climate, Past and Future*, W. H. Freeman and Company, New York.
- Ryan, W.B.F., Carbotte, S.M., Coplan, J.O., O'Hara, S., Melkonian, A., Arko, R., Weissel, R.A., Ferrini, V., Goodwillie, A., Nitsche, F., Bonczkowski, J., Zemsky, R., 2009. Global Multi-Resolution Topography synthesis, *Geochem. Geophys. Geosyst.*, 10, Q03014, doi:10.1029/2008GC002332.
- Rychagov, G. I., 1997. Holocene oscillations of the Caspian Sea and forecasts based on paleogeographical reconstructions. *Quaternary International* 41, 167–172.
- Sagheb-Talebi, K., 2004. Rehabilitation of temperate forests in Iran (Chapter 26). In: Stanturf, J.A., Madsen, P. (Eds.), *Restoration of Boreal and Temperate Forests*. CRC Press, New York, pp. 397–407.
- Seighali, N., Ghomi, M., Zaker, S., Ramezanighara, M., Karimi, P., 2011. Medicinal plants diversity in the flora of Langaroud of Iran. *Advances in Environmental Biology* 5, 413–417.

- Selley, R. C., 1996. Ancient sedimentary environments and their sub-surface diagnosis. Chapman and Hall, London.
- Setudeh, M., 1970. Historical geography of Langarud, in Anonymous From Astara to Astarabad. Community of cultural figures, Tehran, pp. 220-259, (In Persian).
- Smith, D.G., Jol, H.M., 1995. Ground penetrating radar: Antennae frequencies and maximum probable depths of penetration in Quaternary sediments. *Journal of Applied Geophysics* 33, 93–100.
- Smith, D. G., Jol, H. M. 1992. Ground-penetrating radar investigation of a Lake Bonneville delta, Provo level, Brigham City, Utah. *Geology* 20 (12), 1083-1086.
- Smith-Rouch, L.S., 2006. Oligocene–Miocene Maykop/Diatom Total Petroleum System of the South Caspian Basin Province, Azerbaijan, Iran, and Turkmenistan. *U.S. Geological Survey Bulletin* 2201-I, 27 pp.
- Storms, J. E. A., Kroonenberg, S. B., 2007. The impact of rapid sea level changes on recent Azerbaijan ridges, *Journal of Coastal Research* 23, 521–527.
- Stuiver, M., Reimer, P.J., 1993. Extended ^{14}C database and revised Calib 3.0 ^{14}C age calibration program. *Radiocarbon* 35, 215–230.
- Sun, D., Bloemendal, J., Rea, D. K., Vandenberghe, J., Jiang, F., An, Z., Su, R., 2002. Grain-size distribution function of polymodal sediments in hydraulic and aeolian environments, and numerical partitioning of the sedimentary components. *Sedimentary Geology* 152 (3), 263-277.
- Swindles, G. T., 2010. Dating recent peat profiles using spheroidal carbonaceous particles (SCPs). *Mires and Peat* 7 (03), 1-5.
- Thompson, R., 1986. Modelling magnetization data using SIMPLEX. *Physics of the Earth and Planetary Interiors* 42, 113-127.
- Thompson, R., Morton, D. J., 1979. Magnetic susceptibility and particle-size distribution in recent sediments of the Loch Lomond drainage basin, Scotland. *Journal of Sedimentary Research* 49 (3), 801-812.
- Törnqvist, T.E., 1993. Holocene alternation of meandering and anastomosing fluvial systems in the Rhine–Meuse delta (central Netherlands) controlled by sea–level rise and subsoil erodibility. *Journal of Sedimentary Petrology* 63, 683–693.
- Törnqvist, T.E., Snijders, Els MA, Storms, J.E., van Dam, R.L. and Wiemannt, M.C., 1996. A revised chronology for Mississippi River subdeltas. *Science* 273, 1693–1696.
- Tucker, M. E., 2003. *Sedimentary rocks in the field*. John Wiley and Sons.
- UNEP, 2006. Stolberg, F., Borysova, O., Mitrofanov, I., Barannik, V., Eghtesadi, P. *Caspian Sea, GIWA Regional assessment 23*. University of Kalmar, Kalmar, Sweden.
- USDA, 2015. www.pecad.fas.usda.gov/cropexplorer/global_reservoir (last accessed 10 February 2015)
- Varushchenko, S., Varushchenko, A., Klige, R., 1987. Changes in the regime of the Caspian Sea and closed basins in time. Nauka, Moscow. (In Russian).
- Vernant, P., Nilforoushan, F., Chery, J., Bayer, R., Djamour, Y., Masson, F., Tavakoli, F., 2004. Deciphering oblique shortening of central Alborz in Iran using geodetic data. *Earth and Planetary Science Letters* 223, 177-185.
- Voropaev, G. V., Krasnozhan, G. F., and Lahijani, H., 1998. Caspian river deltas, *Caspia Bulletin*, 1, 23–27.
- Yamani, M., Moghimi, E., Motamed, A., Jafarbeglo, M. and Lorestani, G., 2013. Fast shoreline changes in Sefidrud Delta using transects analyses method. *Physical Geography Research Quarterly* 84 (2), 1–20 (in Persian).
- Yanina, T.A., Svitoch, A.A., Wesselingh, F., 2005. Mollusc assemblages from Holocene Turali reference section of Caspian, Daghestan. *Bulletin of Moscow Naturalists Association, Geological Series* 80 (1), 56–65 (in Russian).
- Yim, W. S., Huang, G., Chan, L. S., 2004. Magnetic susceptibility study of Late Quaternary inner continental shelf sediments in the Hong Kong SAR, China. *Quaternary International* 117 (1), 41-54.
- Yousefi, A., Bahmanpour, H., Mafi, A., 2012. Survey of microhabitats use by birds in national parks (Case Study: Wetland Boujagh National Park, Southwest Caspian Sea, Iran). *Annals of Biological Research* 3 (6), 2938–2946.

Wik, M., Renberg, I., 1991. Spheroidal carbonaceous particles as a marker for recent sediment distribution. *Hydrobiologia* 214 (1), 85-90.

Zohary, M., 1973. *Geobotanical Foundations of the Middle East*. G. Fischer Verlag, Stuttgart.

APPENDIX A

Length and location of the cores

Table 1: Length and location of cores taken on GPR profiles

Core Number	Location		length (cm)
	Longitude	Latitude	
105 13 V	37°25'37.40"N	49°55'30.90"E	269
106 13 V	37°22'34.30"N	50°10'36.00"E	486
107 13 V	37°22'52.60"N	50°10'5.00"E	286
114 13 V	37°27'6.30"N	49°42'7.00"E	286
123 13 V	37°28'8.80"N	49°56'19.20"E	173
125 13 V	37°27'47.20"N	49°56'46.70"E	280
104 13 V (KL 11 V1)	37°25'33.20"N	49°56'2.60"E	284

Table 2: Length and location of cores from inland water bodies

Core Number	Location		length (cm)
	Longitude	Latitude	
LL13VA	37° 11' 8.70" N	50° 8' 51.00" E	665
LL13VB	37° 11' 8.70" N	50° 8' 51.00" E	578
AAL13VA	37°17'27.60"N	49°56'15.50"E	1063
AAL13VB	37°17'27.60"N	49°56'15.50"E	1026

Table 3: Length and location of Zibakenar Lagoon cores

Core Number	Location		length (cm)
	Longitude	Latitude	
ZL 11 G1	37°27'20.10"N	49°53'11.70"E	86.5
ZL 11 G 2	37°27'26.10"N	49°53'25.40"E	90
ZL 11G 3	37°27'27.90"N	49°53'25.10"E	59.5
ZL 11G 4	37°27'30.50"N	49°53'31.20"E	76
ZL 11G 5	37°27'35.20"N	49°53'37.30"E	86.5
ZL 11G 6	37°27'39.20"N	49°53'39.30"E	82
ZL 11G 7	37°27'27.90"N	49°53'25.40"E	87
ZL 11G 8	37°27'11.90"N	49°53'23.00"E	13
ZL 11G 9	37°27'19.70"N	49°53'4.70"E	67.5
ZL 11G 10	37°27'36.90"N	49°53'30.10"E	94.5
ZL 11G 11	37°28'9.60"N	49°54'22.20"E	52.5
ZL 11G 12	37°27'20.70"N	49°53'18.00"E	63
ZL 11G 13	37°27'13.70"N	49°53'6.00"E	88.5
ZL 11L 1A	37°27'23.10"N	49°53'14.00"E	191
ZL 11L1B	37°27'23.10"N	49°53'14.00"E	157
ZL 11L 1C	37°27'23.10"N	49°53'14.00"E	192
ZL 11L 1D	37°27'23.10"N	49°53'14.00"E	85
ZL 11L 2A	37°27'19.10"N	49°53'11.10"E	220
ZL 11L 2B	37°27'19.10"N	49°53'11.10"E	202

Table 4: Description of the surface pollen samples near Zibakenar Lagoon

Site name	Location		Description of location
	Longitude	Latitude	
Sefidrud SS1	37°25'06.5"N	49°54'44.8"E	fine sediment along Sefidrud: sterile
Sefidrud tip	37°27'56.4"N	49°56'17.5"E	rive side mud, a few tens of m from tip of delta, clayey layer at base of plants: sterile

Table 5: Length and location of Kiashahr Lagoon cores

Core Number	Location		length (cm)
	Longitude	Latitude	
KL 11 G 1	37°26'9.90"N	49°57'14.20"E	55
KL 11 G 2	37°26'14.90"N	49°57'32.00"E	95.5
KL 11 G 3	37°26'8.80"N	49°57'43.10"E	98
KL 11 G 4	37°26'2.90"N	49°57'44.20"E	79
KL 11 G 5	37°25'55.40"N	49°57'48.90"E	42
KL 11 G 6	37°25'51.50"N	49°57'50.80"E	74.5
KL 11 G 7	37°25'51.70"N	49°57'50.50"E	23.5
KL 11 G 8	37°25'48.90"N	49°57'57.60"E	50
KL 11 G 9	37°26'23.90"N	49°57'46.50"E	26
KL 11 G 10	37°26'18.60"N	49°57'33.20"E	85.5
KL 11 G 11	37°25'58.20"N	49°57'35.70"E	75.5
KL 11 G 12	37°26'8.40"N	49°57'56.20"E	57
KL 11 G 13	37°26'8.50"N	49°57'56.70"E	46
KL 11 V 1	37°25'33.20"N	49°56'2.60"E	284
KL 11 V2	37°25'41.60"N	49°57'16.90"E	178.5
KL 11 V 3	37°25'24.70"N	49°58'34.90"E	97
KL 11 V 4	37°25'43.44"N	49°58'35.20"E	54.5

Table 6: Length and location of Amirkola Lagoon cores

Core Number	Location		length (cm)
	Longitude	Latitude	
AL 11 G 1	37°20'51.00"N	50°11'40.30"E	41.5
AL 11 G 2	37°20'51.40"N	50°11'36.70"E	48.5
AL 11 G 3	37°20'48.20"N	50°11'26.90"E	49
AL 11 G 4	37°20'49.10"N	50°11'42.70"E	39
AL 11 G 5	37°20'43.50"N	50°11'33.80"E	49
AL 11 G 6	37°20'36.00"N	50°11'35.90"E	39
AL 11 G 7	37°20'25.40"N	50°11'37.30"E	44.5
AL 11 G 8	37°20'11.60"N	50°11'41.50"E	47.5
AL 11 G 9	37°19'55.70"N	50°11'48.20"E	46
AL 11 G 10	37°19'39.90"N	50°11'46.60"E	75
AL 11 G 11	37°19'32.30"N	50°11'48.40"E	67
AL 11 G 12	37°21'22.30"N	50°11'17.10"E	46.5
AL 11 G 13	37°21'3.50"N	50°11'32.30"E	47.5
AL 11 G 14	37°21'16.60"N	50°11'41.10"E	48.5
AL 11 G 15	37°21'47.20"N	50°11'22.80"E	81.5
AL 11 G 16	37°22'4.90"N	50°11'22.40"E	74
AL 11 G 17	37°22'6.90"N	50°11'22.10"E	72.5
AL 11 G 18	37°21'40.60"N	50°11'9.30"E	70.5
AL 11 G 19	37°21'32.90"N	50°11'22.10"E	65
AL 11 G 20	37°21'9.90"N	50°11'2.60"E	86
AL 11 G 21	37°21'40.30"N	50°10'51.10"E	90.5
AL 11 L1 A	37°20'20.40"N	50°11'36.90"E	87
AL 11 L1 B	37°20'20.40"N	50°11'36.90"E	72
AL 11 L2	37°20'12.50"N	50°11'36.10"E	66
AL 11 L3	37°20'48.10"N	50°11'35.50"E	93

Table 7: Length and location of core taken from AL11V3 sequence

Core Number	Location		length (cm)
	Longitude	Latitude	
AL11V3	37°23'22.7"N	50°09'55.5"E	281

Table 8: Length and location of cores from onshore and offshore locations

Core Number	Location		Water depth	Distance from the coast	length
	Longitude	Latitude	m	km	(cm)
NSM14G1	37°29'59.87"N	49°54'15.79"E	17	3	145
NSM14G2	37°32'47.82"N	49°54'6.07"E	105	8.2	157
NSM14G3	37°33'59.53"N	49°53'41.831"E	301	10.5	150
NSM14G4	37°34'46.36"N	49°53'29.23"E	431	12	87
NSM14G5	37°35'19.06"N	49°53'18.474"E	470	13	113

Table 9: Location of surface samples offshore

Sample Number	Location		Water depth	Grain size characterisation
	Longitude	Latitude	m	
M14GB1	37°30'07.50"N	49°56'57.24"E	16	Silt
M14GB2	37°29'42.50"N	49°58'26.80"E	18.9	Silt
M14GB3	37°29'15.00"N	49°59'39.8"E	19	Silt
M14GB4	37°28'30.80"N	50°00'41.00"E	16	Silt
M14GB5	37°27'47.00"N	50° 01'18.58"E	15	Silt
M14GB6	37°27'14.01"N	50° 2'07.77"E	15	Sandy silt
M14GB7	37°27'04.90"N	50° 3'41.81"E	19.5	Sandy silt
M14GB8	37°26'35.00"N	50° 5'35.48"E	18	Sandy silt
M14GB9	37°26'15.40"N	50° 7'43.49"E	18.2	Sandy silt
M14GB10	37°25'22.33"N	50° 9'49.80"E	18	Silt
M14GB11	37°24'59.71"N	50° 11'03.11"E	17	Silt
M14GB12	37°24'42.72"N	50°12'17.90"E	17	Silty sand
M14GB13	37°24'30.50"N	50°13'57.65"E	20	Sandy silt
M14GB14	37°23'03.08"N	50°16'22.90"E	20.1	Silty sand
M14GB15	37°22'02.90"N	50°17'02.81"E	19.5	Silt

APPENDIX B

Publications

Published (Appendix C):

Haghani, S., Leroy, S., Khdir, S., Kabiri, K., Naderi Beni, M., Lahijani, H.A.K., in press (accepted 26 May 2015). An early Little Ice Age brackish water invasion along the south coast of the Caspian Sea (sediment of Langarud wetland) and its wider impacts on environment and people. *The Holocene*.

Submitted (Appendix D):

Haghani, S., Leroy, S., Wesselingh, F., Rose, N., 23 Jun. 2015. Rapid evolution of a Ramsar site in response to human interference under rapid sea level change: a south Caspian Sea case study. *Marine Geology*.

Under preparation:

Haghani, S., Leroy, S., Wesselingh, F., Sep. 2015. Coastal erosion in South West of Caspian Sea in response to rapid Sea Level change and abrupt reduction of sediment supply. To be submitted to *Quaternary International*.

Haghani, S., Leroy, S., Bristow, R., Nazari, H., Ensani, R., Oct. 2015. Progradation of the unique Sefidrud Delta into the unique Caspian Sea Basin: high sedimentation rate and steep slope setting. To be submitted to *Marine Geology*.

Haghani, S., Leroy, S., Nov. 2015. Evolution of the Sefidrud Delta (South West Caspian Sea) during the last millennium. To be submitted to *Marine and Petroleum Geology*.

Haghani, S., Leroy, S., Unkel, I., J.-L. Reyss, Nov. 2015. Sefidrud major avulsion during the Late Little Ice Age in response to rapid sea level change, South West Caspian Sea. To be submitted to *Marine Geology*.

APPENDIX C

Paper accepted

An early Little Ice Age brackish water invasion along the south coast of the Caspian Sea (sediment of Langarud wetland) and its wider impacts on environment and people

Safiyeh Haghani¹, Suzanne A.G. Leroy¹, Sarkar Khdir^{1,2}, Keivan Kabiri³, Abdolmajid Naderi Beni³, Hamid A.K. Lahijani³

¹Institute for the Environment, Brunel University London, UB8 3PH, London, UK

²Geography Department, University of Raparin, Rania, Iraq

³Iranian National Institute for Oceanography and Atmospheric Science (INIOAS), Tehran, Iran

Abstract

Caspian Sea level has undergone significant changes through time with major impacts not only on the surrounding coasts, but also offshore. This study reports a brackish water invasion on the southern coast of the Caspian Sea constructed from a multi-proxy analysis of sediment retrieved from the Langarud wetland. The ground surface level of wetland is >6 m higher than the current Caspian Sea level (at -27.41 m in 2014) and located >11 km far from the coast. A sequence covering the last millennium was dated by three radiocarbon dates. The results from this new study suggest that Caspian Sea level rose up to at least -21.44 m (i.e. >6 m above the present water level) during the early Little Ice Age. Although previous studies in the southern coast of the Caspian Sea have detected a high-stand during the Little Ice Age period, this study presents the first evidence that this high-stand reached so far inland and at such a high altitude. Moreover, it confirms one of the very few earlier estimates of a high-stand at -21 m for the second half of the 14th century. The effects of this large-scale brackish water invasion on soil properties would have caused severe disruption to regional agriculture, thereby destabilizing local dynasties and facilitating a rapid Turko-Mongol expansion of Tamerlane's armies from the east.

Keywords

Little Ice Age, Caspian Sea, palaeo-environment, sea level change, sedimentology, palynology

APPENDIX D

Manuscript submitted

Rapid evolution of a Ramsar site in response to human interference under rapid sea level change: a south Caspian Sea case study

Safiyeh Haghani^a, Suzanne A.G. Leroy^a, Frank P. Wesselingh^b, Neil L. Rose^c,

^aEnvironmental Science, Brunel University London, London UB8 3PH, UK

^bNaturalis Biodiversity Centre, Leiden, Netherlands

^cEnvironmental Change Research Centre, University College London, London WC1E 6BT, UK

Abstract

This paper examines the interdependence of different factors in the evolution of a coastal lagoon system of the Sefidrud Delta (SW Caspian Sea) based on multi-proxy sedimentary and palaeoecological analyses and remotely sensed data. According to historical aerial photographs and multiple strands of chronology, these coastal lagoons formed between 1955 and 1964. High sediment input, longshore currents and relatively stable sea-level at that time were the main driving mechanisms that permitted the establishment of a sand spit complex. After 1964, the evolution of these coastal lagoons has been mainly controlled by changing sediment input due to dam construction and rapid sea-level fluctuation. Indeed, dam flushing operations and rapid sea-level rise (~3 m between 1977 and 1995) have accelerated the infilling of the coastal lagoon system. This rapid infilling (3.1 cm yr^{-1}) makes the whole system more prone to sediment encroachment in the short term. Because the lagoons are short-lived and have dynamic evolution, rapid natural changes interact with anthropogenic modifications of the CS environments. Therefore, the short-lived nature of these lagoonal systems (total duration of 115 years for Zibakenar Lagoon) should be considered in any conservation management decisions aimed at preserving these sensitive coastal environments.

Keywords

Short-lived coastal lagoons, rapid Caspian Sea Level change, sediment, palaeoecology, conservation